Characterising the structural, petrophysical, and geochemical properties of inverted fault zones

NATALIE DEBENHAM

Petroleum Geoscience
Australian School of Petroleum
University of Adelaide

This thesis is submitted in fulfilment of the requirements for the degree of Doctor of Philosophy

June 2019

TABLE OF CONTENTS

TABLE OF CONTENTS

TABLE OF CONTENTS

ABSTRACT

It is widely recognised that inverted fault zones form economically significant structures for subsurface fluid exploration and production. Inverted fault zones are formed by the contractional reactivation and reversal of pre-existing extensional fault zones. Recognising the reverse-reactivation of normal faults in sedimentary basins is fundamental, as the reconfiguration of fault geometries has implications for overall basin geometry, sediment accommodation and supply, and fluid flow pathways. This is particularly important for understanding the modification or creation of petroleum system elements through time, which in turn allows for increased targeted exploration.

Notwithstanding the broad economic relevance of inverted fault zones, integrated multi-scale (from micrometre-scale to outcrop-scale) studies on the structural, petrophysical, and geochemical properties of inverted fault zones within porous reservoir rocks are limited. This thesis characterises the structural, petrophysical, and geochemical properties of inverted fault zones from two localities, the Otway Basin (Australia) and Bristol Channel Basin (United Kingdom), in order to understand how inverted faults influence fluid flow at a range of scales. To address this, this thesis has two main topics of focus: (1) identify the influence of inverted faults on surrounding lithology by assessing the relationship between faults, damage zones around faults, and fractures related to fault growth; and (2) identify how subsurface fluids flow, interact, and modify their surrounds by assessing the geochemistry of fluids in fractures and thereby constraining the source, evolution, and migration of fluids preserved in fractures. An integrated, multi-scale approach is crucial for improving the prediction of subsurface fluid flow beyond the wellbore.

In order to understand the influence of inverted faults on surrounding lithology, an inverted fault (Castle Cove Fault) in the Otway Basin, southeast Australia, is the focus of the first two chapters of this thesis. The geometries and relative chronologies of natural fractures adjacent to the Castle Cove Fault are investigated. Structural mapping in the hanging wall damage zone reveals three sets of shear fractures that are geometrically related to the Castle Cove Fault. Inversion of the Castle Cove Fault has resulted in the development of an extensive network of fractures and complex fold structures, and inversion would have subsequently improved the outcrop-scale permeability structure of the damage zone for fluid migration. At the micrometre-scale, the permeability structure has also been influenced by fault inversion. Petrophysical and petrographical analyses in the hanging wall damage zone show that microstructural changes due to faulting have enhanced the micrometre-scale permeability structure of the Eumeralla Formation. These microstructural changes have been attributed to the formation of microfractures and destruction of original pore-lining chlorite morphology as a result of fault deformation. Consequently, inversion has subsequently improved the micrometre-scale permeability structure of the damage zone adjacent to the Castle Cove fault plane. Characterisation of the permeability structure adjacent to reverse-reactivated faults at a range of scales will aid with predicting fluid flow associated with inversion structures.

Structural and geochemical analyses in the next two chapters of this thesis aim to understand how subsurface fluids flow and characterise the source, evolution, and migration pathways of fluids preserved in inverted fault zones. The geochemical evolution of fluids precipitated as calcite and siderite-cemented concretions and fractures throughout the eastern Otway Basin have been investigated. Pore fluids were sourced from both meteoric water and sea water during the deposition of the Eumeralla Formation and pore fluid evolution was strongly influenced by diagenetic reactions and increased temperature during burial. Using a similar analytical approach, the geochemical evolution of fluids precipitated as calcite and gypsum-cemented fractures throughout the eastern Bristol Channel Basin have

been investigated. The main source of fluids were connate pore waters, which were altered by diagenetic reactions within their host lithologies and subsequently redistributed through migration along faults and their associated damage zones. Knowledge of the source, evolution, and migration pathways of these fluids provides valuable insights for understanding the development of inverted sedimentary basins through time. Consequently, integrated studies on the multi-scaled permeability structure of inverted fault zones and the fluids preserved within them will ultimately improve fluid exploration and monitoring strategies in sedimentary basins.

DECLARATION

I certify that this work contains no material which has been accepted for the award of any other degree or diploma in my name, in any university or other tertiary institution and, to the best of my knowledge and belief, contains no material previously published or written by another person, except where due reference has been made in the text. In addition, I certify that no part of this work will, in the future, be used in a submission in my name, for any other degree or diploma in any university or other tertiary institution without the prior approval of the University of Adelaide and where applicable, any partner institution responsible for the joint-award of this degree.

I acknowledge that copyright of published works contained within this thesis resides with the copyright holder(s) of those works.

I also give permission for the digital version of my thesis to be made available on the web, via the University's digital research repository, the Library Search and also through web search engines, unless permission has been granted by the University to restrict access for a period of time.

I acknowledge the support I have received for my research through the provision of an Australian Government Research Training Program Scholarship

28/02/2019

NATALIE DEBENHAM DATE

LIST OF PUBLICATIONS

Peer reviewed journal articles:

Debenham, N., King, R. C., and Holford, S. P. 2018. The influence of a reverse-reactivated normal fault on natural fracture geometries and relative chronologies at Castle Cove, Otway Basin. *Journal of Structural Geology* **112**, 112-130. doi: 10.1016/j.jsg.2018.05.004.

Debenham, N., Farrell, N. J. C., Holford, S. P., King, R. C., and Healy, D. 2019. Spatial distribution of micrometre-scale porosity and permeability across the damage zone of a reverse-reactivated normal fault in a tight sandstone: insights from the Otway Basin, SE Australia. *Basin Research*, 0-19. doi: 10.1111/bre.12345.

Articles written for publication:

Debenham, N., Duddy, I. R., King, R. C., and Holford, S. P. The pore fluid evolution of the mid-Cretaceous Eumeralla Formation in the eastern Otway Basin.

Debenham, N., Holford, S. P., and King, R. C. The spatial distribution and geochemical variation of calcite and gypsum cements in the eastern Bristol Channel Basin.

Conference presentations and articles:

Debenham, N., Holford, S. P, King, R. C., Tassone, D. and Healy, D. 2016, The influence of fault and fracture networks on permeability anisotropy in porous sandstones: a case study at Castle Cove, Otway Basin. Australian Earth Sciences Convention, Adelaide, June 2016, p. 108.

Debenham, N., Holford, S. P, King, R. C., and Healy, D. 2017, The influence of reverse-reactivated normal faults on fault damage zone characteristics in sandstones: a case study at Castle Cove, Otway Basin. American Association of Petroleum Geologists International Conference and Exhibition, London, October 2017.

Debenham, N., Farrell, N. J. C., Holford, S. P., King, R. C., and Healy, D. 2018. The influence of reverse-reactivated normal faults on porosity and permeability in sandstones: a case study at Castle Cove, Otway Basin. Australasian Earth Geoscience Conference, Sydney, February 2018. *Preview* **192**, 118.

Debenham, N., Farrell, N. J. C., Holford, S. P., King, R. C., and Healy, D. 2018. The permeability structure of fault zones in sedimentary basins: a case study at the Castle Cove Fault, Otway Basin. Australian Petroleum Production and Exploration Conference, Adelaide, May 2018. *The APPEA Journal* **58**, 805-808.

Debenham, N., Farrell, N. J. C., Holford, S. P., King, R. C., and Healy, D. 2018. The permeability structure of sandstones adjacent to a reverse-reactivated fault. American Association of Petroleum Geologists Geosciences Technology Workshop "Pore Pressure and Geomechanics: From Exploration to Abandonment", Perth, June 2018, p. 105-106.

ACKNOWLEDGEMENTS

The research presented in this thesis is supported by the collaboration of many people including:

My supervisors A/Prof. Simon Holford and A/Prof. Rosalind King

I would like to express my sincere gratitude to my principal supervisor, Simon Holford, and my co-supervisor, Rosalind King, for their continuous support during my studies. Both of you have been very generous with your time, guidance, enthusiasm, and encouragement, and it has been greatly appreciated. You have given me many wonderful opportunities to take my work nationally and internationally, undertake field work in exceptional locations, demonstrate undergraduate students, and pursue experiences that have allowed me to develop my geological expertise. Together you truly model an outstanding supervisory team, so thank you.

Collaborative researchers Dr. Ian Duddy, Dr. Natalie Farrell, and Dr. David Healy

I am thankful for the support and assistance of my external collaborative researchers Ian Duddy (Geotrack International) and Natalie Farrell and David Healy (University of Aberdeen). Thank you Ian for our excellent discussions on the geology of the Otway Basin and for providing me with rock samples for my studies. Thank you Natalie and Dave for your assistance with laboratory work in Aberdeen and for our insightful discussions, both in person and through email.

Field, laboratory, and research assistance

Chapter 2: Field assistants Dr. James Hall, Hugo Burgin, Dr. Rowan Hansberry, and Lachlan Furness are gratefully acknowledged for their assistance with sample collection during fieldwork. Dr. David Tassone is acknowledged for his contribution to data collection and field mapping.

Chapter 3: Gordon Holm is thanked for preparing thin sections and Colin Taylor for carrying out particle size and mercury injection capillary pressure analyses. Aoife McFadden and Dr. David Kelsey from Adelaide Microscopy, Braden Morgan, and Dr. Sophie Harland are acknowledged for their assistance with laboratory work. Field assistants Dr. James Hall, Dr. Rowan Hansberry, and Lachlan Furness are gratefully acknowledged for their assistance with sample collection during fieldwork.

Chapters 4 and 5: Field assistants Dr. James Hall, Tayallen Velayatham, Hugo Burgin, Dr. Rowan Hansberry, and Lachlan Furness are gratefully acknowledged for their assistance with sample collection during fieldwork. Mark Rollog and Kristine Nielson are thanked for their assistance with stable isotope analysis. A/Prof. Russell Drysdale and Dr. Florian Dux are also thanked for their assistance with stable isotopes. David Bruce is thanked for his assistance with strontium isotope analysis. Dr. Tony Hall is thanked for his assistance with pressure calcimeter analysis. Discussions on the research topic with Dr. Juraj Farkaš and Dr. Jonathan Tyler are greatly appreciated.

Stress, Structure, and Seismic (S^3) research group

Thank you to the members of the S^3 research group at the University of Adelaide for all of the insightful research discussions and for your support over the past three years.

Australian School of Petroleum and Department of Earth Sciences

Thank you to my colleagues in the Australian School of Petroleum and Department of Earth Sciences for your support and the opportunities that have been provided to me throughout my studies.

ACKNOWLEDGEMENTS

Sponsors

Funding support from the Australian Research Council (Discovery Project DP160101158) and the Australian Government Research Training Program Scholarship are greatly appreciated. The Petroleum Exploration Society of Australia (PESA) and the Australian Petroleum Production and Exploration Association (APPEA) are sincerely thanked for their support through the Federal Postgraduate Award and Tony Noon Memorial Scholarship, respectively. The University of Adelaide is also thanked for their travel support through the Eric Rudd Memorial Scholarship.

My family

A special thank you to my family for their love, support, and encouragement in everything that I do. Thank you for inspiring me to follow my dreams and for providing me with the opportunities to do so. Finally, thank you James for your continued and unfailing support and understanding during my pursuit of a PhD degree.

CHAPTER 1

Introduction and thesis outline

1. Rationale

The behaviour of fluids in the Earth's brittle upper crust is one of the most fundamental underlying mechanisms for addressing global resource and environmental issues. Subsurface fluid flow is a dynamic and complex process that involves mass and energy transport in the crust, primarily through the circulation of water, gases, organic liquids, and mixed-phase fluids. The movement of these fluids, and ultimately their precipitation, is critical for resource exploration and fluid monitoring strategies. An understanding of how subsurface fluids flow, interact, and modify surrounding lithologies remains one of the key prevailing research challenges in frontier geoscience research (Committee on Grand Research Questions in the Solid-Earth Sciences, 2008).

Fault zones strongly influence the hydrological and mechanical properties of the upper crust. In recent years, there has been considerable work on the structure, mechanics, and fluid flow properties of fault zones and associated deformation induced structures (e.g. Bense et al., 2013; and references therein; Faulkner et al., 2010; Wibberley et al., 2008). However, the heterogeneous nature of fault zones leads to a significant knowledge gap in understanding their influence on subsurface fluid flow. Previous studies have focussed on the permeability structure of faulted porous rocks in outcrops which have experienced simple tectonic histories (i.e. faults with a single-slip history; e.g. Antonellini and Aydin, 1994; Bauer et al., 2015; Farrell et al., 2014; Shipton et al., 2002); however, few studies have investigated the influence of complex faults (i.e. faults with a multiple-slip history) on the permeability structure of porous clastic rocks. Subsequently, fluid flow in inverted fault zones that have experienced multiple phases of deformation is less understood.

This research characterises the structural, petrophysical, and geochemical properties of inverted fault zones from two localities, the Otway Basin (Australia) and Bristol Channel Basin (United Kingdom), in order to understand how inverted faults influence fluid flow at a range of scales. The Otway and Bristol Channel Basins are Mesozoic rift basins that have experienced inversion, resulting in the reverse-reactivation of normal faults (Edwards et al., 1996; Kelly et al., 1999). These localities were chosen as they provide excellent outcrop exposures of inverted fault zones and basin sediments. This research represents the first integrated and multi-scaled (from <0.1 μm to 10 km; Fig. 1) investigation of the influence of inverted faults in porous reservoir rocks on subsurface fluid flow. An integrated, multi-scale approach is crucial for improving the prediction of subsurface fluid flow beyond the wellbore.

2. Aims of this research

The primary aim of this research is to understand how inverted faults influence fluid flow at a range of scales.

In order to address the primary aim, this thesis has two main topics of focus:

1. Identify the influence of inverted faults on surrounding lithology by assessing the relationship between faults, damage zones around faults, and fractures related to fault growth (**Chapters 2 and 3**).
2. Identify how subsurface fluids flow, interact, and modify their surrounds by assessing the geochemistry of fluids in fractures and thereby constraining the source and migration of fluids preserved in fractures (**Chapters 4 and 5**).

An integrated and multi-scale methodological approach (Fig. 1) is applied in order to identify the influence of faults on fluid flow at a range of scales. The following section provides a summary of the relevant literature and key themes concerning the topics of focus that are addressed in this thesis.

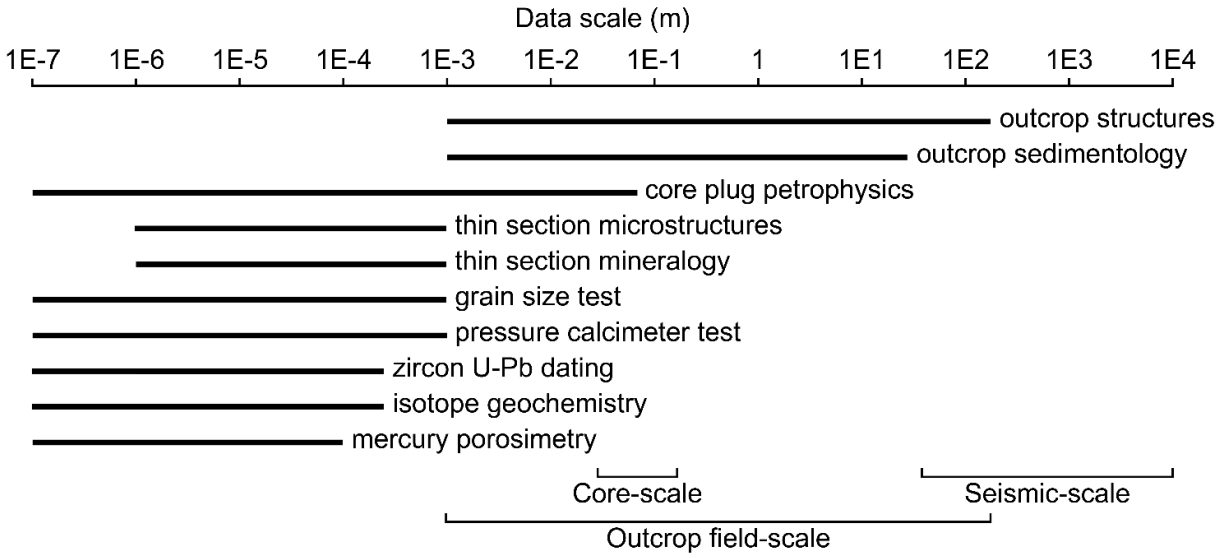

Figure 1. Scale ranges of the integrated and multi-scale structural, petrophysical, and geochemical data used in this thesis.

3. Fault zones and subsurface fluid flow

Fault zones and associated deformation induced structures control fluid flow within the Earth's brittle upper crust at a range of scales. Fault zones can serve as hydraulically conductive conduits, barriers, or conduit-barrier systems for fluid flow (Caine et al., 1996); fluids including, but not limited to, hydrocarbons, mineralising fluids, hydrothermal fluids, various gases, and groundwater. The permeability structure of fault zones is a crucial element for understanding and predicting the distribution of fluid pressure and the volume of fluids that can migrate through a fault zone (Wibberley et al., 2008). Therefore, knowledge of the permeability structure of fault zones is fundamental for developing exploration and fluid monitoring strategies in sedimentary basins.

Fault zones form through a complex interaction of mechanical and hydrological processes. Faults are commonly characterised by a fault core where high strain is localised along slip surfaces (Fig. 2; Faulkner et al., 2010). Fault zones may contain a single fault core or an anastomosing series of fault cores (e.g.

Faulkner et al., 2003). Brittle fault cores are often surrounded by a peripheral zone of fracturing and faulting, known as the fault damage zone, that accommodates low strain during deformation (Fig. 2; Caine et al., 1996; Faulkner et al., 2010). These fault zone structures occur at a range of scales, from micrometres (e.g. microfractures) to kilometres (e.g. faults). The structure of fault zones is dependent on the protolith, tectonic environment, depth of fault formation, magnitude of fault displacement, and fluid flow (Faulkner et al., 2010). As a result, the fault damage zone is typically highly heterogeneous, leading to uncertainties in characterising the mechanical and hydrological properties of fault zones.

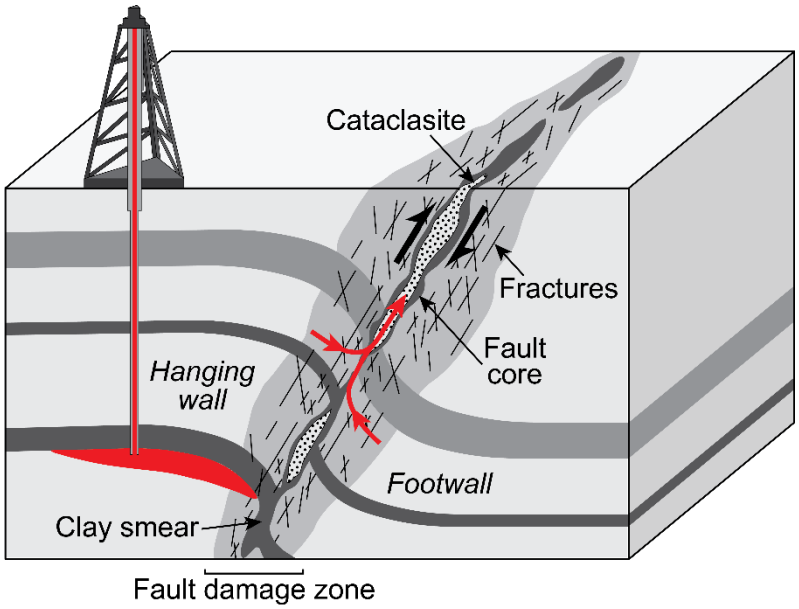

Figure 2. Typical fault zone structure of a reverse-reactivated normal fault, illustrating a high-strain fault core surrounded by a fractured damage zone. Possible fluid migration pathways are shown in red.

4. Introduction to basin inversion and reactivation of faults

Basin inversion is one of the most significant and widespread modes of compressional intraplate deformation, and has been widely documented in a number of tectonic settings (e.g. Cooper and Williams, 1989; Turner and Williams, 2004; Cooper and Warren, 2010). Positive inversion describes the compressional or transpressional crustal shortening of extensional basins (Turner and Williams, 2004) and is mainly accommodated by the contractional reactivation and reversal of pre-existing extensional faults (Hayward and Graham, 1989). Recognising the reverse-reactivation of normal faults in sedimentary basins is fundamental, as the reconfiguration of fault geometries has implications for overall basin geometry, sediment accommodation and supply, and fluid flow pathways. This is particularly important for understanding the modification or creation of petroleum system elements through time, which in turn allows for increased targeted exploration.

Inverted fault zones in the Otway Basin (Australia) and Bristol Channel Basin (United Kingdom) are described in this thesis. The complex tectonic setting and fault reactivation histories of these basins, together with excellent outcrop exposure, make them ideal natural laboratories for understanding how inverted faults influence fluid flow at a range of scales.

5. Inversion mechanics

The reactivation and inversion of pre-existing faults is highly selective, i.e. typically less than 10% of pre-existing normal faults are reactivated (Reilly et al., 2016; Sibson, 1995). Fault inversion is governed by a number of factors, including: (1) the pre-inversion dip angle of the fault plane, where faults with shallower dips are more conducive to inversion (Sibson, 1995), (2) the size of the pre-existing faults, where larger faults are more conducive to inversion (Reilly et al., 2016), (3) the orientation of fault plane relative to the inversion stress field (Del Ventisette et al., 2006), (4) the magnitude and orientation of shear and normal stresses (Sibson, 1995), (5) the coefficients of friction (Byerlee, 1978), and (6) fluid overpressure, which reduces the effective stress (Sibson, 1995; Turner and Williams, 2004). The conditions that allow for the frictional reactivation of a pre-existing cohesionless fault can be described by Amonton's Law (Equation 1):

$$\tau = \mu_s(\sigma_n - P_f) \quad (1)$$

where τ and σ_n are the resolved shear and normal stress components respectively acting on the fault plane, μ_s is the static coefficient of friction, and P_f is the formation fluid pressure. An extensive series of low-temperature rock mechanics experiments undertaken by Byerlee (1978) showed that the static coefficient of friction is mostly independent of rock type. For a pre-existing, cohesionless fault the coefficient of friction required for fault reactivation is $0.6 < \mu_s < 0.85$ (Byerlee, 1978).

6. Inverted fault geometries

Fault geometry is typically measured in two different ways: (1) as maximum displacement (d_{max}), or (2) as maximum dimensions, i.e. the length (L) and the height (H) of a fault plane (Fig. 3; Kim and Sanderson, 2005). Fault displacement varies within the fault plane, with zero displacement at the fault tips and increasing displacement toward the centre of the fault plane (Barnett et al., 1987).

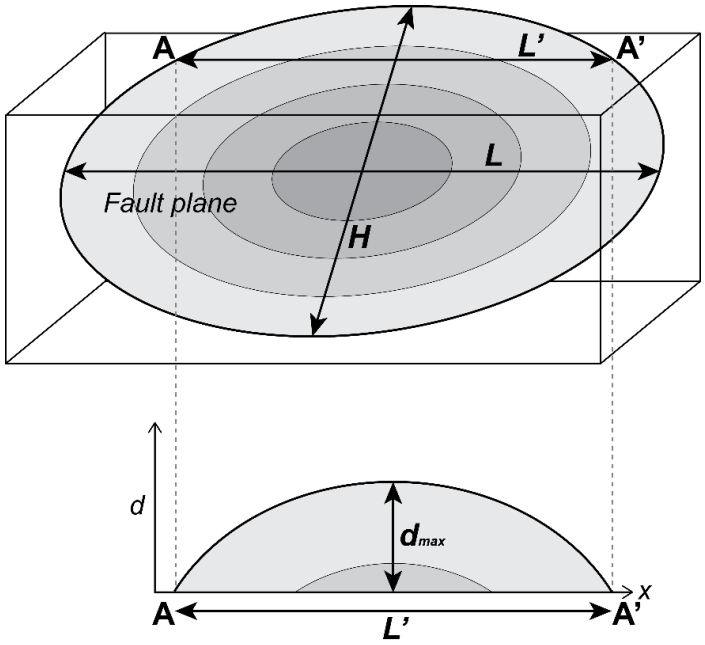

Figure 3. Displacement distribution on an elliptical fault plane, defined by length (L) and height (H), with shading increasing with increasing displacement toward the centre of the fault plane. The fault plane intersects with the upper surface along A–A' (i.e. the fault trace) and is plotted below, with displacement (d; plotted with 2x vertical exaggeration) relative to distance (x). Maximum displacement (d_{max}) at the centre of the fault plane is also illustrated. Modified after Kim and Sanderson (2005).

During fault inversion, the orientation of fault displacement will be reversed, i.e. the fault tip regions will display net reverse displacement before the centre of the fault plane displays net reverse displacement (e.g. Turner and Williams, 2004; Williams et al., 2005). This results in the progressive development of net reverse displacement along a fault plane. Sequences displaying net reverse displacement are separated from sequences displaying initial net normal displacement by a "null point" at which net fault displacement is zero (Fig. 4; Williams et al., 1989).

Physical models have been applied extensively to illustrate the structural and temporal development of inverted fault geometries (e.g. Eisenstadt and Withjack, 1995; Jagger and McClay, 2018; Keller and McClay, 1995; Mitra, 1993; Panien et al., 2005; Yamada and McClay, 2003). These models have highlighted the importance of the pre-existing fault geometry on the evolution and inversion style of inverted faults. The pre-inversion dip angle of the fault plane, together with the orientation of the fault plane relative to the inversion stress field, significantly influences the final geometry of the inverted fault zone (Del Ventisette et al., 2006; Sibson, 1995). The reactivation and inversion of planar shallow-dipping normal faults (dip angle c. 30°) during compression initially involves the vertical (± horizontal) displacement of the post-extension sequence in the hanging wall above a pre-deformation elevation and downward movement of the "null point" (Fig. 4; Williams et al., 1989). Continued compression results in the displacement of the syn-extension and pre-extension sequences in the hanging wall (Fig. 4). Steeply-dipping planar or listric normal faults (dip angle c. 60°) will reactivate and deform differently during compression, forming large-scale structures such as tightened and amplified hanging wall anticlines and shallow footwall short cut faults (Turner and Williams, 2004; Williams et al., 1989).

Chapters 2 and 3 of this thesis are focussed on an inverted fault in the eastern Otway Basin, the Castle Cove Fault. The Castle Cove Fault strikes northeast-southwest Based on outcrop data and observations, the fault plane dips steeply (c. 77°) toward the northwest (c. 334°) at shallower levels and is potentially shallow dipping at depth (Debenham et al., 2018). Similar to panel 2a in Fig. 4, adjacent to the Castle Cove Fault, a large (greater than 80m in half-wavelength) hanging wall anticline initially formed as a rollover fold during normal faulting and was subsequently amplified and tightened during compression (**Chapter 2**).

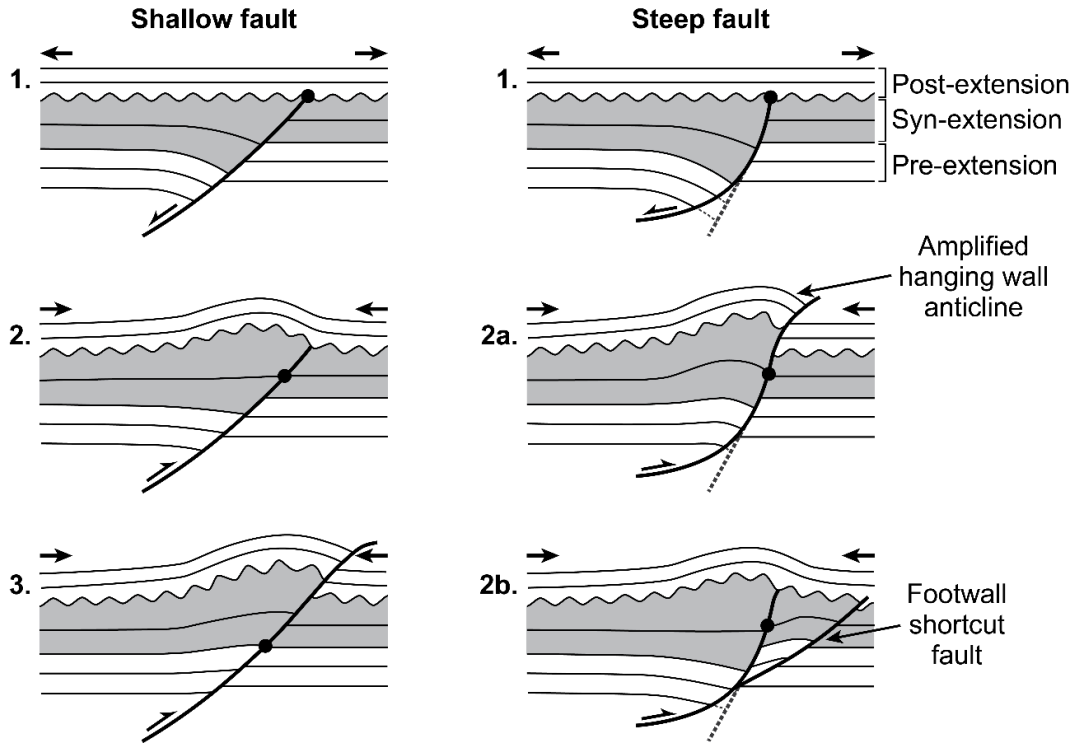

Figure 4. Sequential schematic diagrams of typical inverted fault zone geometries for shallow-dipping (left) and steeply-dipping (right) faults. The null point (black circle), described by Williams et al. (1989), moves progressively downward during increased compression. During initial compression, the shallow-dipping normal fault vertically displaces the post-extension sequence (panel 2), then with continued compression the fault displaces the syn- and pre-extension sequences (panel 3). Inversion of steeply-dipping planar and listric faults will result in a variety of geometries. Two classic examples include: an amplified hanging wall anticline with a footwall that act as buttress (panel 2a), and a shallow footwall shortcut fault which splays off the main pre-inversion fault (panel 2b).

The relationship between maximum vertical displacement and the strike length of a fault is often described by the d_{max}/L ratio (Kim and Sanderson, 2005). As inverted faults have experienced multiple phases of reactivation and deformation, their displacement-length geometrical relationships vary to that of non-inverted faults (e.g. Reilly et al., 2016; Walsh and Watterson, 1988). If faults are reactivated with an opposite sense of slip, such as normal faults that have been subsequently reversed, the net displacement will be reduced with increasing fault propagation, thereby lowering the d_{max}/L ratio (Kim and Sanderson, 2005). Therefore, in order to predict the net maximum vertical displacement of an inverted fault that is not well exposed at the surface, it is important to understand the structural and mechanical properties of the fault rock and review analogous faults that have experienced similar tectonic histories.

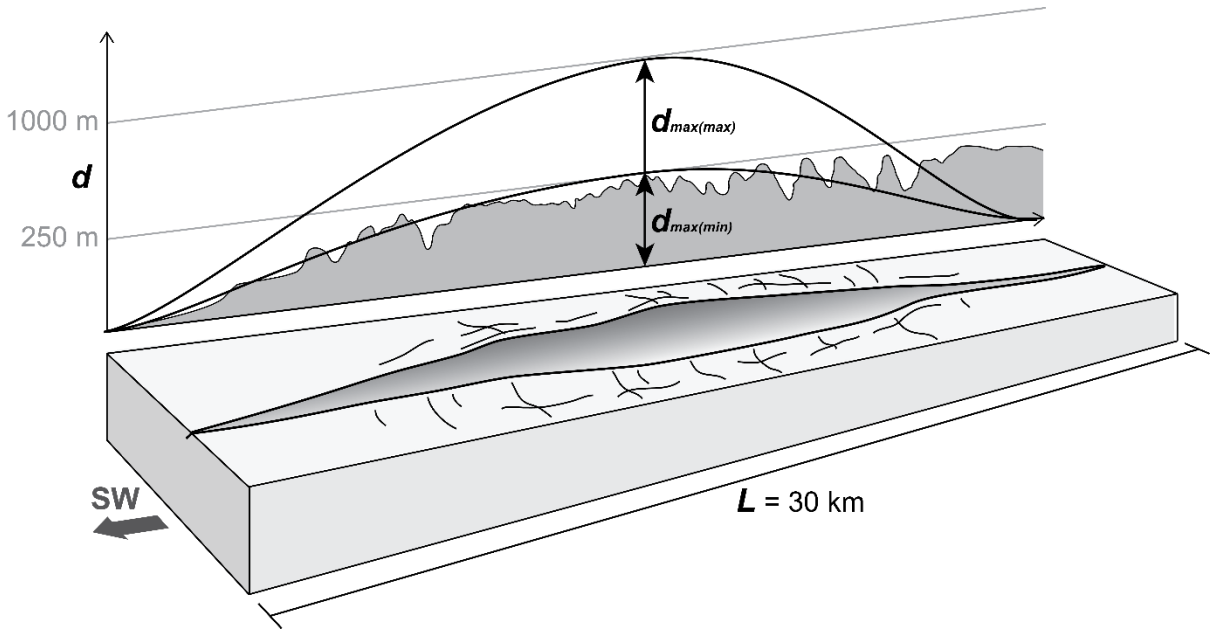

Figure 5. Displacement model of the NE–SW striking, reverse-reactivated Castle Cove Fault, Otway Basin. Maximum displacement (d_{max}) is at the centre of the fault plane and minimum displacement is at the tips of the fault. In the plot above, the present day topographic profile is shaded in grey and indicates a minimum estimate of net d_{max} of 250 m. Fault scaling relationships suggest a maximum estimate of net d_{max} of 1000 m.

In this thesis, topographic expressions of displacement provide a minimum estimate of net maximum vertical displacement ($d_{max(min)}$) of 250 m at the centre of the Castle Cove Fault (Fig. 5). Applying d_{max}/L fault scaling relationships using inverted fault data from Kim and Sanderson (2005) and Reilly et al. (2016) to the Castle Cove Fault strike length, a net maximum vertical displacement ($d_{max(max)}$) approximately up to 1 km could be inferred (Fig. 5 and 6).

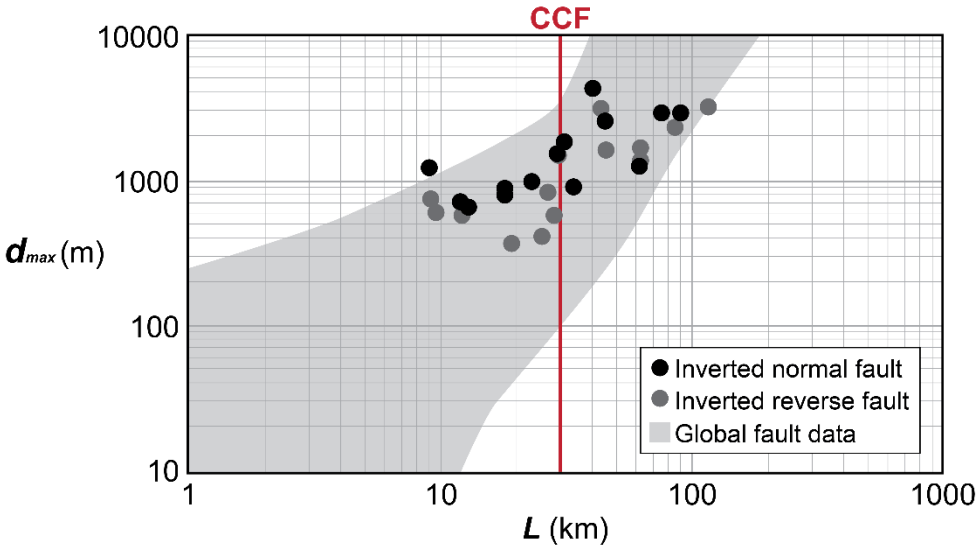

Figure 6. Fault trace length (L) relative to maximum vertical displacement (d_{max}) data from global fault data (grey shaded area), together with inverted normal fault (black circle) and inverted reverse fault (grey circle) data from the southern Taranaki Basin compiled by Reilly et al. (2016). The Castle Cove Fault (CCF) trace length (L = 30 km) is illustrated in red and can be compared to the inverted normal fault dataset.

7. Deformation associated with inversion

Deformation associated with inversion can significantly modify the pre-existing internal basin architecture. The style and distribution of deformation is dependent on factors, such as the structural setting of the basin, overall lithology, presence of decoupling sedimentary layers, geometry of pre-existing planes of weakness (e.g. faults and fractures), and the magnitude and orientation of the stress field (Bonini et al., 2012; Erickson et al., 2001). Deformation in the upper crust is dependent on the presence of fluid overpressure and basin inversion is one of the key drivers for overpressure generation (Sibson, 1995).

Inversion can result in the formation of a range of deformation structures. As inversion involves the shortening and uplift of sedimentary basins, the formation positive relief structures, such as anticlines, adjacent to faults are common. Inversion-related anticlinal structures can act as structural traps and in many instances these structures have hosted major hydrocarbon accumulations (e.g. Cooper and Warren, 2010; Cooper et al., 2001; Underhill and Stoneley, 1998). Other typical inversion-related deformation structures include small-scale faults (e.g. synthetic, antithetic, back-thrust, and shortcut faults), fractures (outcrop-scale macrofractures and grain-scale microfractures), and deformation bands within the fault damage zone (Faulkner et al., 2010). Deformation can also lead to sedimentary compaction, pore collapse, grain crushing, and cement precipitation, leading to reduced permeability within a protolith and therefore impeding the quality of a reservoir (Bense et al., 2013; Farrell and Healy, 2017; Fisher and Knipe, 1998). Consequently, deformation associated with inverted faults can be significantly different to that of typical fault geometries that have experienced simple tectonic histories.

8. Fluid flow

The permeability of fractured reservoir rocks is dependent on fluid pressure and the transport of fluids through the Earth's crust (Nelson, 2001). The temporal and spatial evolution of permeability can be assessed by using both structural and geochemical tools, such as the structural analysis of deformation-related structures at a range of scales (from thin section analysis to structural mapping) and traditional isotope analysis of precipitated pore fluids. Geochemical information from precipitated fluids provide valuable insights into past fluid transport and the pore fluid evolution of sedimentary basins (e.g. Boles et al., 2004; Meng et al., 2017; Philipp, 2008; Scotchman et al., 2002; Suchy et al., 2000). Precipitated fluids can be preserved within a basin as cements in faults and fractures (i.e. veins; Bons et al., 2012), and also as diagenetic cements within host rock pore space, concretions, and nodules (Curtis and Coleman, 1986). They preserve information on source, temperature, and timing of pore fluids from which they were precipitated (Bons et al., 2012), thereby providing insights into past fluid transport and flow networks.

9. Thesis outline

This thesis has been written as a series of individual manuscripts which address the two main topics of focus of this thesis. Two of these manuscripts have been published in peer review journals and two have been written in a publication format to be submitted for publication concurrent with this thesis submission. **Chapters 2 and 3** address the first main topic by providing a case study from the eastern Otway Basin in Australia (Fig. 7). **Chapter 2** discusses the outcrop-scale conduits for fluid flow associated with the Castle Cove Fault, while **Chapter 3** discusses the micron-scale conduits for fluid flow associated with the fault. A detailed structural and stratigraphic geological background of the Otway Basin is provided in **Chapter 2**. **Chapters 4 and 5** address the second main topic in two study locations that

are structurally analogous. **Chapter 4** identifies the pore fluid evolution and source of fluids preserved in fractures and concretions in the eastern Otway Basin, Australia (Fig. 7). **Chapter 5** utilises the techniques undertaken in previous chapters and is focussed on the source and evolution of fluids preserved in fractures and faults in the eastern Bristol Channel Basin, United Kingdom (Fig. 7), which has experienced a similar deformation history as the Otway Basin. The geological background of the Bristol Channel Basin is described in **Chapter 5**. To summarise this thesis, **Chapter 6** integrates the main findings from each chapter and includes conclusions.

Figure 7. Geological setting of the study areas described in this thesis; the Otway Basin in Australia and the Bristol Channel Basin in the United Kingdom.

9.1. Chapter 2

Chapter 2 investigates the processes governing the spatial arrangement of macrofractures surrounding an inverted fault (Castle Cove Fault) in the Otway Basin, southeast Australia. Despite the ubiquity of normal faults that have undergone compressional inversion, documentation of the structural history of natural fractures around these structures is limited. This study presents the first comprehensive investigation of the geometries and chronologies of natural fractures forming the damage zone of an inverted fault in the Otway Basin. The Castle Cove Fault damage zone preserves a complex tectonic history recording both regional and local perturbations in stress. Structural mapping within the damage zone reveals a complex tectonic history recording both regional and local perturbations in stress. A total of 11 fracture sets were identified, with three sets geometrically related to the Castle Cove Fault. **Chapter 2** highlights the need to conduct careful reconstruction of the structural histories of fault zones that experienced complex reactivation histories when attempting to define off-fault fluid flow properties.

Chapter highlights:

- Normal movement on the Castle Cove Fault occurred during late Cretaceous extension.
- Miocene–Pliocene compression resulted in reverse-reactivation and anticlinal folding.
- The width of the fault damage zone is greater than 300 m in the hanging wall.
- A total of 11 fracture sets were identified at Castle Cove.
- Three fracture sets are geometrically related to the Castle Cove Fault

This chapter is published as:

Debenham, N., King, R. C., and Holford, S. P. 2018. The influence of a reverse-reactivated normal fault on natural fracture geometries and relative chronologies at Castle Cove, Otway Basin. *Journal of Structural Geology* 112, 112-130. doi: 10.1016/j.jsg.2018.05.004.

9.2. Chapter 3

This chapter is also focussed on understanding the influence of faults on surrounding lithology by assessing micron-scale deformation associated with reverse-reactivated faulting, in comparison to the outcrop-scale deformation described in **Chapter 2**. **Chapter 3** investigates the processes controlling the micron-scale permeability structure of porous sandstones within the hanging wall of the Castle Cove Fault in the Otway Basin, southeast Australia. Studies often describe the permeability structure of low porosity host rocks that have experienced simple tectonic histories, however, few studies have investigated the influence of complex faults (i.e. faults with a multiple-slip history) on the permeability structure of porous clastic rocks. This chapter utilises detailed petrophysical, microstructural, and mineralogical analysis to provide a comprehensive investigation of porosity and permeability across the damage zone of an inverted fault in the Otway Basin. This study shows that microstructural changes as a result of faulting have improved the permeability structure of the Eumeralla Formation within the Castle Cove Fault hanging wall. Faulting resulted in the formation of microfractures and destruction of original pore-lining chlorite morphology. The results from this study have important implications for understanding fluid flow in sedimentary basins that have experienced inversion. **Chapter 3** shows that high-resolution integrated analyses of the host rock are critical for describing the permeability structure of reservoir rocks with high porosities, low permeabilities, and abundant clays that have experienced complex deformation.

Chapter highlights:

- Porosity and permeability increase toward the Castle Cove Fault.
- Enhanced connectivity toward the fault is related to an increase in microfractures.
- Destruction of chlorite morphology also contributes to enhanced connectivity.
- Macrofracture network at Castle Cove would be the most effective fluid flow conduit.

This chapter is published as:

Debenham, N., Farrell, N. J. C., Holford, S. P., King, R. C., and Healy, D. 2019. Spatial distribution of micrometre-scale porosity and permeability across the damage zone of a reverse-reactivated normal fault in a tight sandstone: insights from the Otway Basin, SE Australia. *Basin Research*, 1-19. doi: 10.1111/bre.12345.

9.3. Chapter 4

This chapter provides an analysis of the complex diagenetic and pore fluid history of the Eumeralla Formation in order to understand how diagenesis has changed the petrophysical properties over time and to understand the source and migration of pore fluids which are hosted by fractures and concretions. Geochemical data, from stable oxygen and carbon isotopes and strontium isotopes, of calcite- and siderite-cemented concretions and fractures record the evolution of pore fluids from deposition to post-diagenesis. A comprehensive and integrated geochemical analysis of both concretion-hosted cements and fracture-hosted cements has not been previously undertaken in the Otway Basin. This study shows that pore fluids were sourced from both meteoric water and sea water during the deposition of the Eumeralla Formation, and that pore fluids were influenced by diagenetic reactions and increased temperature during burial. The geochemical analyses also have implications for palaeoclimate reconstructions of the eastern Otway Basin in the mid-Cretaceous. This study demonstrates that the mean annual surface temperature during the mid-Cretaceous was approximately between 5°C and 15°C, and this is consistent with the palaeobotanical and palynological record at this time.

Chapter highlights:

- Carbonate concretions formed within the initial 688 m to 2,882 m of burial.
- Meteoric water input during led to light $\delta^{18}O$ values in calcite concretions.
- Dissolution and alteration of volcanic detritus resulted in unradiogenic $^{87}Sr/^{86}Sr$ values.
- Seawater input led to heavy $\delta^{18}O$ and radiogenic $^{87}Sr/^{86}Sr$ values in siderite concretions and calcite fractures.
- Methanogenic fermentation and oxidation of organic matter produced CO^2 for carbonate precipitation.
- Mid-Cretaceous mean annual surface temperature was 5°C to 15°C.

This chapter is written in publication format:

Debenham, N., Duddy, I. R., King, R. C., Holford, S. P. The pore fluid evolution of the mid-Cretaceous Eumeralla Formation in the eastern Otway Basin.

9.4. Chapter 5

This chapter investigates the source and spatial distribution of fluids preserved within these calcite and gypsum veins and slickensides in order to understand the geochemical evolution and migration pathways of fluids in the Bristol Channel Basin. This study utilises a similar approach to that applied in **Chapter 4**. Geochemical data, from stable oxygen and carbon isotopes and strontium isotopes, of calcite and gypsum veins record the source, evolution, and migration of fluids. This represents the first comprehensive investigation of the fluid evolution of both calcite and gypsum cements in a spatial context in the Bristol Channel Basin. This study shows that mineralising fluids in the eastern Bristol Channel Basin originated as connate pore waters that were altered through diagenesis and were subsequently precipitated along faults and fractures.

Chapter highlights:

- Mineralising fluid compositions are controlled by the lithologies in which they occur.
- The Lias Group is characterised by heavy $\delta^{18}O$ and radiogenic $^{87}Sr/^{86}Sr$ values, but light $\delta^{13}C$ values.
- The Mercia Mudstone Group is characterised by exceptionally radiogenic $^{87}Sr/^{86}Sr$ values.
- Two faults show a trend of more enriched $\delta^{18}O$ and $^{87}Sr/^{86}Sr$ values toward the west.

This chapter is written in publication format:

Debenham, N., Holford, S. P., King, R. C. The spatial distribution and geochemical variation of calcite and gypsum cements in the eastern Bristol Channel Basin.

9.5. Chapter 6: Key findings and conclusions

Chapter 6 summarises and integrates the key findings of each chapter and presents conclusions. The data collected for each chapter of this thesis has been tabulated in the Appendix.

References

Antonellini, M., Aydin, A., 1994. Effect of faulting on fluid flow in porous sandstones: Petrophysical properties. AAPG Bulletin 78, 355-377.

Barnett, J.A.M., Mortimer, J., Rippon, J.H., Walsh, J.J., Watterson, J., 1987. Displacement geometry in the volume containing a single normal fault. AAPG Bulletin 71, 925-937.

Bauer, J.F., Meier, S., Philipp, S.L., 2015. Architecture, fracture system, mechanical properties and permeability structure of a fault zone in Lower Triassic sandstone, Upper Rhine Graben. Tectonophysics 647-648, 132-145.

Bense, V.F., Gleeson, T., Loveless, S.E., Bour, O., Scibek, J., 2013. Fault zone hydrogeology. Earth-Science Reviews 127, 171-192.

Boles, J.R., Eichhubl, P., Garven, G., Chen, J., 2004. Evolution of a hydrocarbon migration pathway along basin-bounding faults: Evidence from fault cement. AAPG Bulletin 88, 947-970.

Bonini, M., Sani, F., Antonielli, B., 2012. Basin inversion and contractional reactivation of inherited normal faults: A review based on previous and new experimental models. Tectonophysics 522–523, 55-88.

Bons, P.D., Elburg, M.A., Gomez-Rivas, E., 2012. A review of the formation of tectonic veins and their microstructures. Journal of Structural Geology 43, 33-62.

Byerlee, J., 1978. Friction of rocks. Pure and Applied Geophysics 116, 615-626.

Committee on Grand Research Questions in the Solid-Earth Sciences, 2008. Origin and Evolution of Earth: Research Questions for a Changing Planet. National Research Council.

Cooper, M.A., Warren, M.J., 2010. The geometric characteristics, genesis and petroleum significance of inversion structures. Geological Society, London, Special Publications 335, 827-846.

Cooper, M.A., Weissenberger, J., Knight, I., Hostad, D., Gillespie, D., Williams, H., Burden, E., Porter-Chaudhry, J., Rae, D., Clark, E., 2001. Basin evolution in western Newfoundland: New insights from hydrocarbon exploration. AAPG Bulletin 85, 393-418.

Curtis, C.D., Coleman, M.L., 1986. Controls on the precipitation of early diagenetic calcite, dolomite, and siderite concretions in complex depositional sequences, in: Gautier, D.L. (Ed.), Roles of Organic Matter in Sediment Diagenesis. The Society of Economic Paleontologists and Mineralogists, pp. 23-33.

Debenham, N., King, R.C., Holford, S.P., 2018. The influence of a reverse-reactivated normal fault on natural fracture geometries and relative chronologies at Castle Cove, Otway Basin. Journal of Structural Geology 112, 112-130.

Del Ventisette, C., Montanari, D., Sani, F., Bonini, M., 2006. Basin inversion and fault reactivation in laboratory experiments. Journal of Structural Geology 28, 2067-2083.

Edwards, J., Leonard, J.G., Pettifer, G.R., McDonald, P.A., 1996. Colac 1:250000 Map Geological Report. Geological Survey.

Eisenstadt, G., Withjack, M.O., 1995. Estimating inversion: results from clay models. Geological Society, London, Special Publications 88, 119-136.

Erickson, S.G., Strayer, L.M., Suppe, J., 2001. Mechanics of extension and inversion in the hanging walls of listric normal faults. Journal of Geophysical Research: Solid Earth 106, 26655-26670.

Farrell, N.J.C., Healy, D., 2017. Anisotropic pore fabrics in faulted porous sandstones. Journal of Structural Geology 104, 125-141.

Farrell, N.J.C., Healy, D., Taylor, C.W., 2014. Anisotropy of permeability in faulted porous sandstones. Journal of Structural Geology 63, 50-67.

Faulkner, D.R., Jackson, C.A.L., Lunn, R.J., Schlische, R.W., Shipton, Z.K., Wibberley, C.A.J., Withjack, M.O., 2010. A review of recent developments concerning the structure, mechanics and fluid flow properties of fault zones. Journal of Structural Geology 32, 1557-1575.

Faulkner, D.R., Lewis, A.C., Rutter, E.H., 2003. On the internal structure and mechanics of large strike-slip fault zones: field observations of the Carboneras fault in southeastern Spain. Tectonophysics 367, 235-251.

Fisher, Q.J., Knipe, R.J., 1998. Fault sealing processes in siliciclastic sediments. Geological Society, London, Special Publications 147, 117-134.

Hayward, A.B., Graham, R.H., 1989. Some geometrical characteristics of inversion. Geological Society, London, Special Publications 44, 17-39.

Jagger, L.J., McClay, K.R., 2018. Analogue modelling of inverted domino-style basement fault systems. Basin Research 30, 363-381.

Keller, J.V.A., McClay, K.R., 1995. 3D sandbox models of positive inversion. Geological Society, London, Special Publications 88, 137-146.

Kelly, P.G., Peacock, D.C.P., Sanderson, D.J., McGurk, A.C., 1999. Selective reverse-reactivation of normal faults, and deformation around reverse-reactivated faults in the Mesozoic of the Somerset coast. Journal of Structural Geology 21, 493-509.

Kim, Y.-S., Sanderson, D.J., 2005. The relationship between displacement and length of faults: a review. Earth-Science Reviews 68, 317-334.

Meng, Q., Hooker, J., Cartwright, J., 2017. Genesis of natural hydraulic fractures as an indicator of basin inversion. Journal of Structural Geology.

Mitra, S., 1993. Geometry and Kinematic Evolution of Inversion Structures. AAPG Bulletin 77, 1159-1191.

Nelson, R.A., 2001. Geologic Analysis of Naturally Fractured Reservoirs, 2 ed. Gulf Professional Publishing, Woburn, p. xi.

Panien, M., Schreurs, G., Pfiffner, A., 2005. Sandbox experiments on basin inversion: testing the influence of basin orientation and basin fill. Journal of Structural Geology 27, 433-445.

Philipp, S.L., 2008. Geometry and formation of gypsum veins in mudstones at Watchet, Somerset, SW England. Geological Magazine 145, 831-844.

Reilly, C., Nicol, A., Walsh, J., 2016. Importance of pre-existing fault size for the evolution of an inverted fault system. Geological Society, London, Special Publications 439.

Scotchman, I.C., Carr, A.D., Astin, T.R., Kelly, J., 2002. Pore fluid evolution in the Kimmeridge Clay Formation of the UK Outer Moray Firth: implications for sandstone diagenesis. Marine and Petroleum Geology 19, 247-273.

Shipton, Z.K., Evans, J.P., Robeson, K.R., Forster, C.B., Snelgrove, S., 2002. Structural Heterogeneity and Permeability in Faulted Eolian Sandstone: Implications for Subsurface Modeling of Faults. AAPG Bulletin 86, 863-883.

Sibson, R.H., 1995. Selective fault reactivation during basin inversion: potential for fluid redistribution through fault-valve action. Geological Society, London, Special Publications 88, 3-19.

Suchy, V., Heijlen, W., Sykorova, I., Muchez, P., Dobes, P., Hladikova, J., Jackova, I., Safanda, J., Zeman, A., 2000. Geochemical study of calcite veins in the Silurian and Devonian of the Barrandian Basin (Czech Republic): evidence for widespread post-Variscan fluid flow in the central part of the Bohemian Massif. Sedimentary Geology 131, 201-219.

Turner, J.P., Williams, G.A., 2004. Sedimentary basin inversion and intra-plate shortening. Earth-Science Reviews 65, 277-304.

Underhill, J.R., Stoneley, R., 1998. Introduction to the development, evolution and petroleum geology of the Wessex Basin. Geological Society, London, Special Publications 133, 1-18.

Walsh, J.J., Watterson, J., 1988. Analysis of the relationship between displacements and dimensions of faults. Journal of Structural Geology 10, 239-247.

Wibberley, C.A.J., Yielding, G., Di Toro, G., 2008. Recent advances in the understanding of fault zone internal structure: A review. Geological Society Special Publication 299, 5-33.

Williams, G.A., Turner, J.P., Holford, S.P., 2005. Inversion and exhumation of the St. George's Channel basin, offshore Wales, UK. Journal of the Geological Society 162, 97-110.

Williams, G.D., Powell, C.M., Cooper, M.A., 1989. Geometry and kinematics of inversion tectonics. Geological Society, London, Special Publications 44, 3-15.

Yamada, Y., McClay, K., 2003. Application of geometric models to inverted listric fault systems in sandbox experiments. Paper 1: 2D hanging wall deformation and section restoration. Journal of Structural Geology 25, 1551-1560.

CHAPTER 2

This chapter is published as:

Debenham, N., King, R. C., and Holford, S. P. 2018. The influence of a reverse-reactivated normal fault on natural fracture geometries and relative chronologies at Castle Cove, Otway Basin. *Journal of Structural Geology* **112**, 112-130.

STATEMENT OF AUTHORSHIP

Title of Paper	The influence of a reverse-reactivated normal fault on natural fracture geometries and relative chronologies at Castle Cove, Otway Basin
Publication Status	☒ Published ☐ Accepted for publication ☐ Submitted for publication ☐ Unpublished and unsubmitted work written in manuscript style
Publication Details	Debenham, N., King, R. C., and Holford, S. P. 2018. The influence of a reverse-reactivated normal fault on natural fracture geometries and relative chronologies at Castle Cove, Otway Basin. Journal of Structural Geology 112, 112-130. doi: 10.1016/j.jsg.2018.05.004.

Principal Author

Name of Principal Author (Candidate)	Natalie Debenham		
Contribution to the Paper	Project design, fieldwork, processing and interpreting data, manuscript design and composition, creation of figures, manuscript revisions, acted as corresponding author.		
Overall Percentage	80%		
Certification	This paper reports on original research I conducted during the period of my Higher Degree by Research candidature and is not subject to any obligations or contractual agreements with a third party that would constrain its inclusion in this thesis. I am the primary author of this paper.		
Signature		Date	04/09/2018

Co-Author Contributions

By signing the Statement of Authorship, each author certifies that:

i. the candidate's stated contribution to the publication is accurate (as detailed above);
ii. permission is granted for the candidate in include the publication in the thesis; and
iii. the sum of all co-author contributions is equal to 100% less the candidate's stated contribution.

Name of Co-Author	Rosalind King		
Contribution to the Paper	Assistance with project design, assistance with interpretation, assistance manuscript design and composition, manuscript review.		
Signature		Date	04/09/2018

Name of Co-Author	Simon Holford		
Contribution to the Paper	Assistance with project design, assistance with interpretation, assistance manuscript design and composition, manuscript review.		
Signature		Date	04/09/18

ABSTRACT

Despite the ubiquity of normal faults that have undergone compressional inversion, documentation of the structural history of natural fractures around these structures is limited. In this paper, we investigate the geometries and relative chronologies of natural fractures adjacent to a reverse-reactivated normal fault, the Castle Cove Fault in the Otway Basin, southeast Australia. Local variations in strain resulted in greater deformation within the fault damage zone closer to the fault. Structural mapping within the damage zone reveals a complex tectonic history recording both regional and local perturbations in stress and a total of 11 fracture sets were identified, with three sets geometrically related to the Castle Cove Fault. The remaining fracture sets formed in response to local stresses at Castle Cove. Rifting in the late Cretaceous resulted in normal movement of the Castle Cove Fault and associated rollover folding, and the formation of the largest fracture set. Reverse-reactivation of the fault and associated anticlinal folding occurred during late Miocene to Pliocene compression. Rollover folding may have provided structural traps if seals were not breached by fractures, however anticlinal folding likely post-dated the main episodes of hydrocarbon generation and migration in the region. This study highlights the need to conduct careful reconstruction of the structural histories of fault zones that experienced complex reactivation histories when attempting to define off-fault fluid flow properties.

1. Introduction

The inversion of sedimentary basins is one of the most significant and widespread modes of compressional intraplate deformation, and has been widely documented in a number of tectonic settings (e.g. Cooper and Williams, 1989; Turner and Williams, 2004; Cooper and Warren, 2010). Positive inversion describes the compressional or transpressional crustal shortening of extensional basins (Turner and Williams, 2004) and is mainly accommodated by the contractional reactivation and reversal of pre-existing extensional faults (Hayward and Graham, 1989). In the last two decades, the impact of inversion on the prospectivity of petroleum producing basins has been increasingly recognised, resulting in an increase in targeted exploration (Macgregor, 1995; Turner and Williams, 2004; Cooper and Warren, 2010). Examples of major hydrocarbon discoveries within inversion structures include the Nam Phong gas field in northeast Thailand (Cooper and Warren, 2010), the Humber zone inversion anticline traps in Western Newfoundland, Canada (Cooper et al., 2001), the Kimmeridge oil field in the Wessex Basin, United Kingdom (Underhill and Stoneley, 1998), the gas fields in the Taranaki Basin, New Zealand (King and Funnell, 1997), and the Barracouta and Flying Fish fields in the Gippsland Basin (Hillis et al., 2008) and Minerva anticline in the Otway Basin (Schneider et al., 2004), Australia. Both the initial extensional and later compressional phases of inversion can modify or create new elements of the petroleum system. Exhumation and erosion as a result of inversion can have both positive and negative implications on the timing of hydrocarbon maturation, migration, and accumulation (Turner and Williams, 2004; Holford et al., 2010), particularly if a structural trap is present or absent. While inversion can create footwall shortcut and anticlinal traps for hydrocarbons, inversion can also destroy earlier trap geometries (Cooper and Warren, 2010). Changes in fault geometry can also lead to fluid flow, fault seal, fault leakage, and reservoir compartmentalisation (Knipe et al., 1998), and therefore an understanding of inversion structures is fundamental for developing strategies during exploration and production.

Brittle faults are commonly characterised by a fault core where high strain is localised along slip surfaces (Faulkner et al., 2010). Brittle fault cores are often surrounded by a peripheral zone of fracturing and

faulting, known as the damage zone, that accommodates low strain during deformation (Caine et al., 1996; Faulkner et al., 2010). The geometry of fracture damage zones has been well described for a wide range of fault systems, including normal, thrust and strike-slip faults (Mcgrath and Davison, 1995; Kim et al., 2004). Geometry is influenced by factors such as the protolith, burial depth, tectonic environment, magnitude of fault displacement, and fluid flow (Faulkner et al., 2010). Detailed investigations of fault damage zone geometry are often carried out through structural mapping (sections) and microstructural analyses. Notwithstanding the broad economic relevance of inverted hydrocarbon systems, documentation of the spatial arrangement of fractures around reverse-reactivated faults is surprisingly limited. Studies are typically focussed on fracture damage zones reverse-reactivated faults in mudstones and carbonates (e.g. Rawnsley et al., 1998; Engelder and Peacock, 2001; Belayneh and Cosgrove, 2004; Mynatt et al., 2009), with very few focussed on fracture damage zones reverse-reactivated faults in sandstones (e.g. Laubach and Diaz-Tushman, 2009; Mynatt et al., 2009). The structural complexity of fault systems that have undergone multiple tectonic events, and limited outcrop exposures of such systems, has limited the number of studies undertaken on the spatial arrangement of fractures around reverse-reactivated faults.

This study investigates the processes governing the spatial arrangement of fractures surrounding a fault within the Otway Basin. We present field data collected at Castle Cove in the Otway Basin, southeast Australia (Fig.1), from a well-exposed damage zone associated with the reverse-reactivated Castle Cove Fault. This study area provides the opportunity to assess the influence of a reverse-reactivated normal fault on deformation within sandstones located within the hanging wall. We aim to investigate and document the geometries and chronologies of natural fractures forming the damage zone of the Castle Cove Fault. Structural information from three sections will be used to develop a model of the structural evolution of the Castle Cove Fault and associated fractures. We show that the Castle Cove Fault damage zone preserves a complex tectonic history recording both regional and local perturbations in stress at Castle Cove, and at least three fracture sets are geometrically related to the Castle Cove Fault.

2. Tectonic setting of the Otway Basin

The Otway Basin is a north-west trending basin located along the south-eastern margin of Australia. The basin covers an area of approximately 150,000 km^2, both onshore and offshore, with a late Jurassic to Cenozoic sedimentary succession of up to 10 km in depth (Stacey et al., 2013). The Otway Basin forms part of the Southern Rift System (Stagg et al., 1990) that developed following Tithonian rifting and continental separation of Australia and Antarctica, during the break up of eastern-Gondwana (Norvick and Smith, 2001; Krassay et al., 2004). During the Barremian, fault-controlled graben structures formed as a result of initial rifting were reactivated and provided accommodation space for the deposition of the fluvial and lacustrine Crayfish Subgroup (Perincek and Cockshell, 1995; Krassay et al., 2004). There are multiple interpretations for the initial extension direction (Fig. 1) based on fault strike orientations, including NW–SE (Willcox and Stagg, 1990; O'brien et al., 1994), N–S (Lyon et al., 2007), N–S to NE–SW (Hill et al., 1994), NNE–SSW (Etheridge et al., 1985), and NE–SW extension (Perincek et al., 1994b). The onshore Otway Basin can be divided into two structural domains, the eastern and western Otway Basin, distinguished by different early Cretaceous structural trends (Hill et al., 1995a; Finlayson et al., 1996; Miller et al., 2002). The eastern Otway Basin is dominated by steep NE–SW striking, NW-dipping normal faults, with several sinistral N–S striking faults (Fig. 2) related to the upper plate margin geometry (Lister et al., 1991; Perincek and Cockshell, 1995; Miller et al., 2002). In comparison, the western Otway Basin is dominated by more complex fault arrays, with variably dipping E–W striking

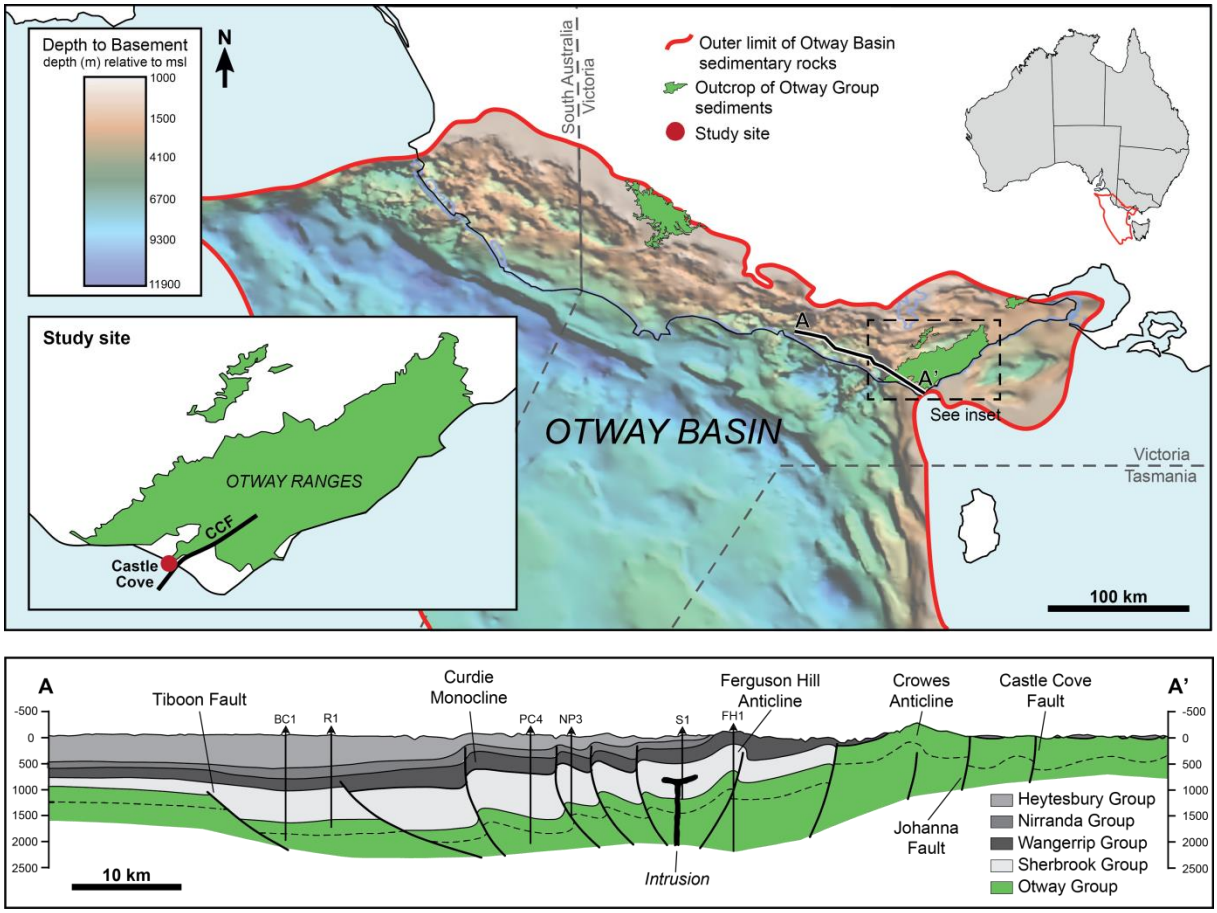

Figure 1. Regional map of the Otway Basin highlighting Castle Cove and the Castle Cove Fault (CCF), with a depth to basement map from Jorand et al. (2010). Onshore cross-section from the Port Campbell Embayment to Otway Ranges, shown by A to A′ on regional map, modified after Edwards et al. (1996) and Holford et al. (2014).

dextral faults and NW–SE striking normal faults (Fig. 2; Miller et al., 2002). This change in fault polarity, from east to west, has been attributed to a progressive change in the strike of faults rather than a fault transfer zone (Miller et al., 2002).

Post-rift subsidence during the Aptian and Albian led to the deposition of the thick volcaniclastic, fluvio-lacustrine Eumeralla Formation (Fig. 1; Hill et al., 1995a; Hall and Keetley, 2009), which is a key source rock for gas accumulations discovered in the eastern Otway Basin (Edwards et al., 1999; Boreham et al., 2004). Regional inversion and a shift to a NW–SE compression regime during the Cenomanian (Fig. 1) resulted in a basin-wide unconformity that marks the top of the Eumeralla Formation (Fig. 3), with no Cenomanian strata preserved (Partridge, 2001; Krassay et al., 2004). Contemporaneous uplift and erosion inverted most of the Otway Ranges, with final uplift of the ranges occurring in the late Miocene to Recent (Dickinson et al., 2002; Krassay et al., 2004).

Renewed rifting in the late Cretaceous resulted in N–S to NE–SW directed extension in the western and central parts of the basin (Perincek et al., 1994a), though Miller et al. (2002) proposed N–S extension due to reactivated faulting from a past N–S directed extension, while Schneider et al. (2004) suggested a significant oblique sinistral component (Fig. 1). This second stage of rifting is represented by intense fault activity and deposition of the deltaic and marine Sherbrook Group (Fig. 3), which is mostly confined to the western Otway Basin (Miller et al., 2002). The locus of rifting shifted south during the late

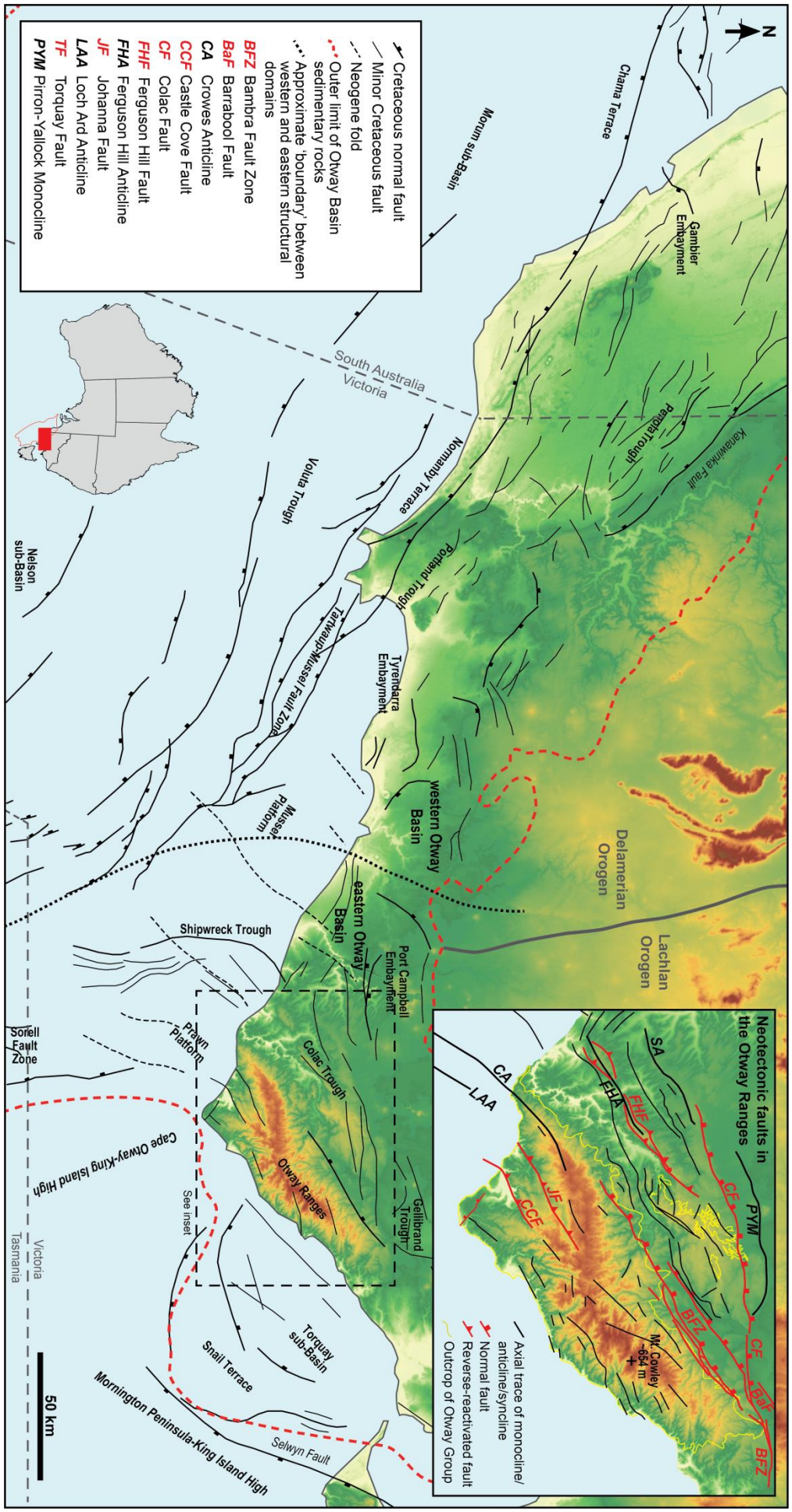

Figure 2. Regional tectonic elements map of the Otway Basin, underlain by a digital elevation model from Geoscience Australia. Locations of structural discontinuities are modified after Edwards et al. (1996), Holford et al. (2014), and Tassone et al. (2017). The inset shows the neotectonic structural discontinuities in the eastern Otway Basin.

Cretaceous, basinward of the Tartwaup-Mussel fault zone (Fig. 2; Krassay et al., 2004). Rifting and associated growth of active faults ceased by the Maastrichtian, and sedimentation was restricted to thermally subsided sag basins (Miller et al., 2002; Krassay et al., 2004).

Late Maastrichtian to mid-Eocene post-rift thermal subsidence resulted in the deposition of the deltaic to shallow marine Wangerrip Group (Fig. 3; Krassay et al., 2004). These sediments unconformably overlie the Sherbrook Group across most of the basin, consequently sealing many of the faults that were reactivated during the late Cretaceous (Perincek et al., 1994b). Following a major unconformity with significant localised erosion, the marine Nirranda Group was deposited throughout the late Eocene to early Oligocene (Krassay et al., 2004). This unconformity correlates with a change to fast seafloor spreading in the Southern Ocean and the first formation of oceanic crust near the Otway Basin at ca. 43 Ma (mid-Eocene; Veevers, 2000; Norvick and Smith, 2001). Due to subsequent changes in the plate-boundary configuration of the Indo-Australian Plate (Perincek et al., 1994b), there was a major shift to a NW–SE compressional regime (Fig. 3; Nelson et al., 2006; Holford et al., 2014). Another unconformity formed during the late Oligocene and separates the Nirranda Group from the overlying late Oligocene to late Miocene Heytesbury Group (Fig. 3), the latter of which was deposited under marine conditions (Krassay et al., 2004). Episodes of inversion and fault reactivation punctuate the Cenozoic, with periods of more intense compression-related deformation following mid-Eocene breakup and during the late Miocene to Pliocene (Holford et al., 2014). The influence of post-Albian compression was concentrated on structures in the eastern Otway Basin, particularly in the Otway Ranges and in the adjacent Torquay sub-basin (Fig. 2; Hill et al., 1995b; Perincek and Cockshell, 1995; Edwards et al., 1996; Hall and Keetley, 2009; Tassone et al., 2014).

This study is focussed on the well-exposed Castle Cove Fault, within the Otway Ranges at Castle Cove, southeast Australia (Fig. 1). Castle Cove provides excellent exposures of the youngest unit of the Eumeralla Formation, which is a fine- to medium-grained volcanogenic sandstone at this locality. The Eumeralla Formation is a porous sandstone (approximately 20%) at Castle Cove. Sections of the Eumeralla Formation that crop out in the Otway Ranges indicate that these sediments were deposited in a high-energy, complex braided fluvial system, with a vast supply of volcanogenic clastic material derived from contemporaneous dacitic volcanism to the east (Duddy, 2003). Across the basin, the Eumeralla Formation is typically 1.5 to 3 km thick, with thicker sections exceeding 6 km interpreted in the Otway Ranges. However, approximately 1 km of the thicker section was removed during mid-Cretaceous compression and uplift (Cooper and Hill, 1997; Duddy, 2003). A number of extensional faults which have been reactivated as reverse faults during compression in the Otway Basin are identified by broad monoclines, anticlines, and synclines mapped at surface (Edwards et al., 1996).

The Castle Cove Fault (Fig. 1) originated as a normal fault but was subsequently reactivated as a reverse fault during late Miocene to Pliocene compression (Duddy, 1994; Edwards et al., 1996; Holford et al., 2014). The Castle Cove Fault dips steeply to the northwest, and strikes NE–SW with a strike length of approximately 30 km. The fault appears to end at its onshore extent to the NE with a decrease in difference of topographic elevation of the fault scarp. The offshore extent of the fault to the SW appears as a 8 km linear anomaly in magnetic data (Moore, 2002). Topographic expressions of displacement provide a minimum estimate of vertical reverse displacement of 250 m at the centre of the fault. Applying fault scaling relationships using data from Kim and Sanderson (2005) and Reilly et al. (2016) to the Castle Cove Fault strike length, a maximum vertical displacement up to 1 km could be inferred. Though the fault is not exposed at the surface, a vast array of fractures and a large (greater than 80 m in half-

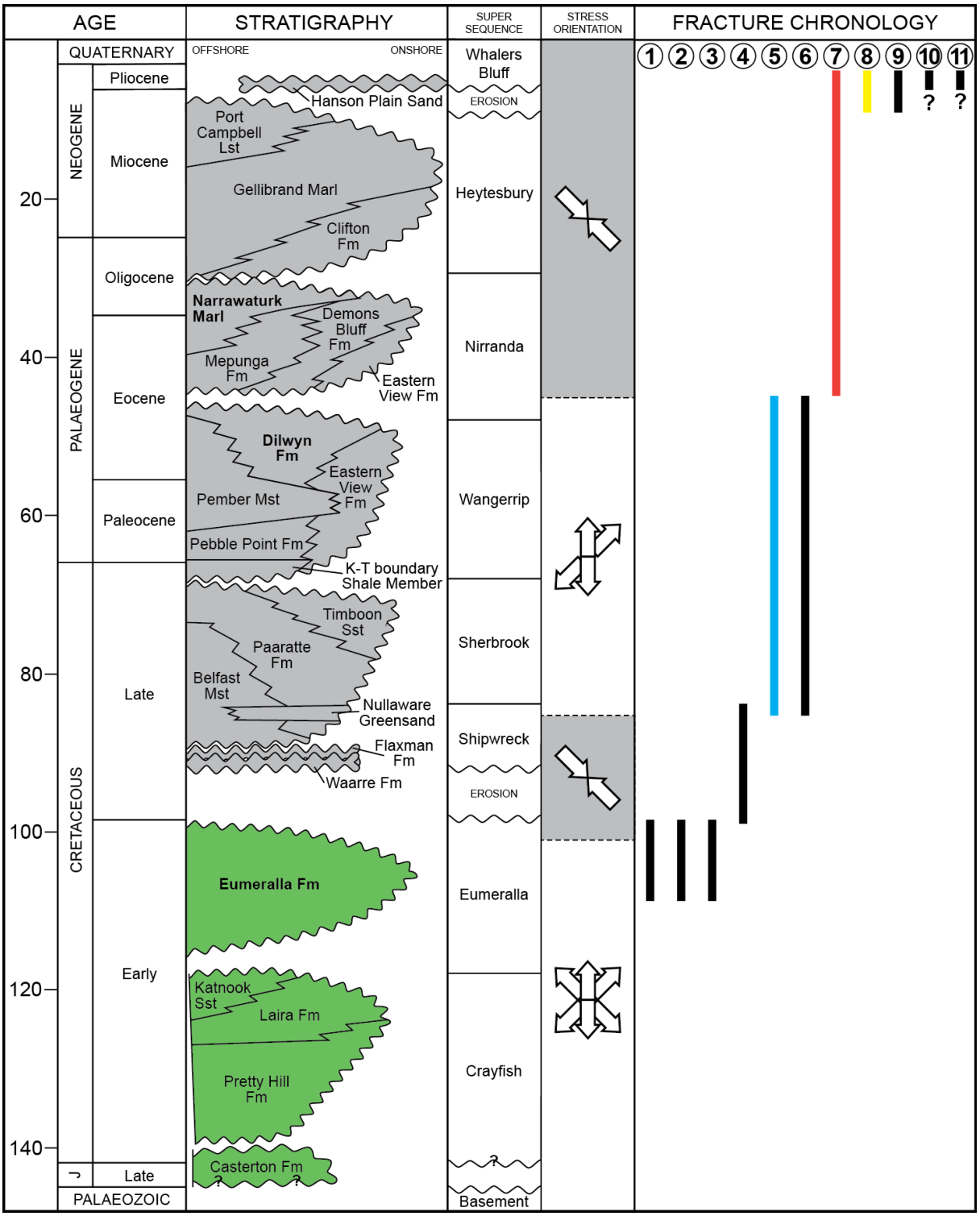

Figure 3. Stratigraphy of the Otway Basin, highlighting the Otway Group sediments with lithostratigraphy after Geary and Reid (1998). Basin phases, where grey indicates compression and white indicates extension, with maximum horizontal stress directions (arrows) from previous studies as described in the text. Vertical bars indicate the chronology and approximate timing of the fracture sets identified in this study based on cross-cutting and abutting relationships and stereographic techniques. Fracture Sets 5 (blue), 7 (orange), and 8 (yellow) have been highlighted as they have are geometrically related to the Castle Cove Fault (see text and Fig. 13).

wavelength) anticline forming an inversion structure above the Castle Cove Fault are exposed at Castle Cove, preserving the complex tectonic history of the fault and providing detailed insights of the regional tectonic history of the Otway Basin.

3. Field and structural mapping methods at Castle Cove

Detailed structural sections have been constructed to identify and map the spatial arrangement of natural fractures relative to the Castle Cove Fault. Natural fractures were mapped in the Eumeralla Formation foreshore and cliff exposures of the hanging wall, to the west of the fault (Fig. 4). Five detailed areas, comprising four sections (Sections 1, 2, 4, and 5) with extents of 2 x 8 m and one section (Section 3) of 2 x 12 m, cover an area of 88 m^2 in total. The sections were located in the same stratigraphic bed, though Sections 1 and 2 were mapped approximately 20 to 30 m shallower in the Eumeralla Formation (Fig. 4). The dip, orientation, aperture, and fracture fill of each fracture were recorded during mapping. Fractures with cement fill were identified as closed fractures. Fractures without a cement fill and no visible aperture were identified as closed fractures with no visible fill. Fractures without a cement fill but with a visible aperture were identified to be open, though open fractures may be a product of weathering. Fractures with partial cement fill were considered to be closed.

Fracture sets for Sections 1, 4, and 5 were grouped by plotting fracture data on lower hemisphere equal area projections. Insufficient data was collected at Sections 1 and 2 for these analyses. The fractures in Sections 1, 4, and 5 were rotated to show fracture geometries for horizontal bedding. The fracture data from each section was rotated using the plunge of the hanging wall anticline and bedding measurements (dip and dip directions) taken at each section. This method restores bedding to horizontal, with a vertical principal stress axis (i.e. gravity) that is Andersonian (Anderson, 1951). The rotated fracture geometries were compared to unrotated fracture geometries. Fractures with similar dips and strikes indicated a fracture set. If two fracture sets with similar dips and strikes (for extensional and compressional stress regimes) intersected at dihedral angles between 30° and 60°, conjugate shear fracture pairs were identified in accordance with Andersonian faulting theory (Anderson, 1951). Fractures within a given fracture set are assumed to have formed under similar stress conditions. For instance, fractures formed under an extensional stress regime usually have dip angles approximately 60° from horizontal, while fractures formed under a compressional stress regime typically have dip angles approximately 30° from horizontal (Sibson, 1985; Davis et al., 2011). Fractures that dip close to 90° (i.e. vertical) are assumed to have formed under strike-slip conditions (Anderson, 1951).

Shear offset information is difficult to constrain at the outcrop scale as the Eumeralla Formation is relatively homogenous (i.e. contains minor sedimentary laminations) and bedding can be on the scale of tens of metres. Therefore, the interpretation that many fractures at Castle Cove are shear fractures is based on the following reasons. Firstly, the Castle Cove Fault is itself a large shear fracture and therefore macrofractures at the outcrop scale with the similar orientations to the fault are also likely to be shear fractures. Secondly, conjugate shear fractures can be identified if a series of fractures intersect at dihedral angles, i.e. the dihedral angles of which make approximately 60°. Dihedral angles of approximately 60° have been calculated for each fracture set at Castle Cove. Thirdly, the conjugate shear fractures are bisected by a maximum compressive stress (σ_1) and the orientation of σ_1 is consistent with the geological history and orientations of stresses over time.

The relative timing of fracture set formation with respect to folding was determined by rotating stereographic projections and applying Andersonian faulting theory (Anderson, 1951). The relative timing of fracture set formation was also inferred from field observations of abutting and cross-cutting relationships. If fracture sets with Andersonian conjugate fractures were identified in unrotated stereographic projections, they were interpreted to have formed during or after tilting or folding of the

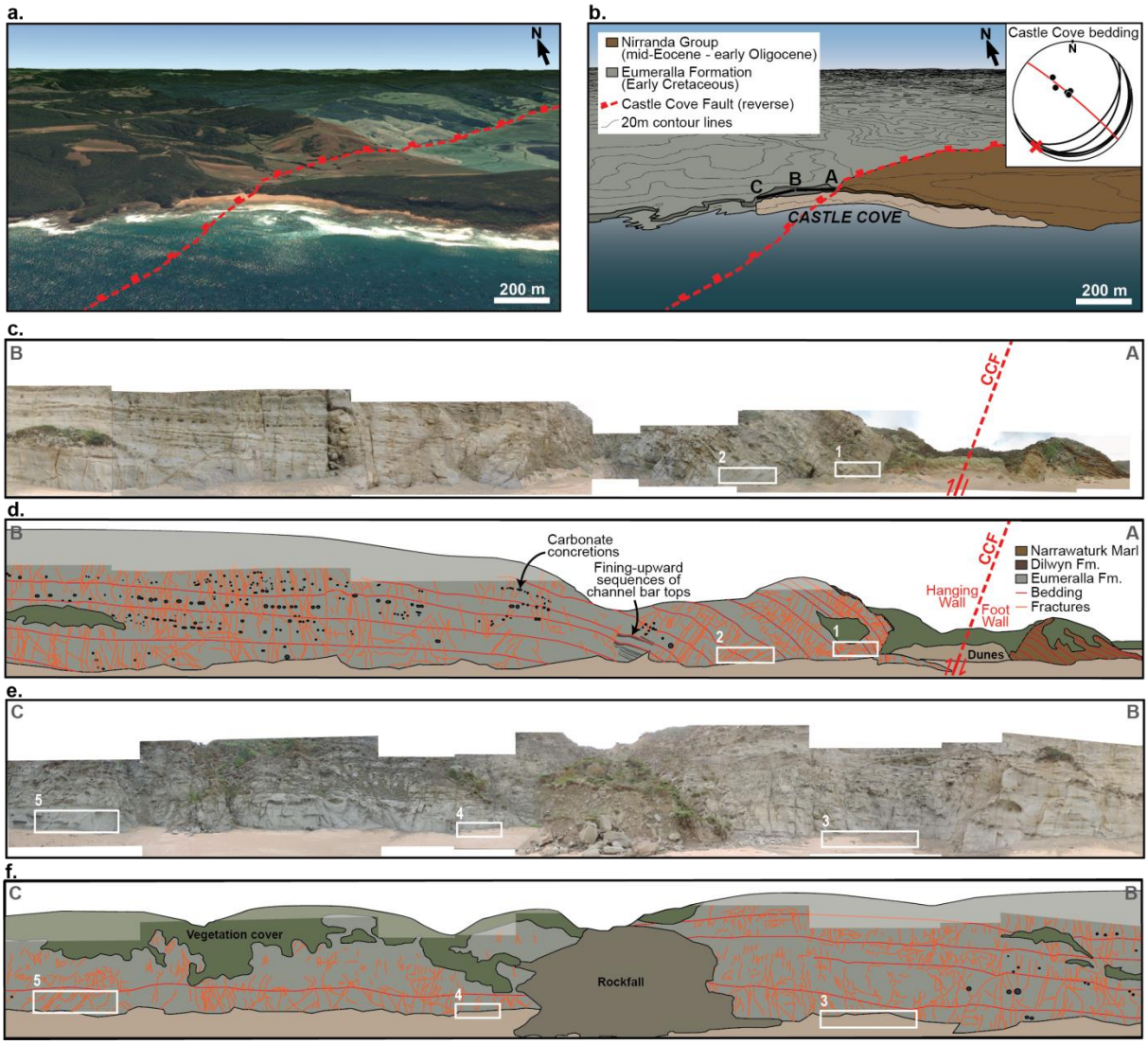

Figure 4. (a) View of the study area from 2017 Google Earth Landsat imagery; (b) illustrates the location of Castle Cove and the strike of the Castle Cove Fault. The equal area and lower hemisphere projection in the top right shows bedding planes and poles (black) of bedding measurements taken at Castle Cove, a profile plane (red; 85/040) using cylindrical best fit calculations in Stereonet 8, and the calculated fold axis (red cross; 05⟶220); (c) photo of A–B cross-section of foreshore and cliff exposures at Castle Cove. Locations of structural sections are indicated by white boxes. (d) Schematic of A–B cross-section. Red lines indicate bedding planes and orange lines indicate macrofractures visible in the photos; (e) photo of B–C cross-section.; and (f) schematic of B–C cross-section.

stratigraphic units. If fracture sets with Andersonian conjugate fractures were identified in rotated stereographic projections, they were interpreted to have formed when the bedding was horizontal. Following this, abutting and cross-cutting relationships were used to determine the relative timing of fracture set formation (Hancock, 1985). Younger stratigraphy could not be used to constrain fracture formation timing. This is because the Cenomanian unconformity has eroded the top of the Eumeralla Formation and the overlying Wangerrip Group (early Palaeogene) is not well preserved at Castle Cove. Older stratigraphy also could not be used as only the upper Eumeralla outcrops at Castle Cove. Variations in the fracture density within the Castle Cove Fault damage zone were identified by calculating linear macrofracture (i.e. fractures typically >10 cm in strike length) densities along the cliff face at Castle Cove. Fracture density is a term used to describe local variations in strain within a damage zone. To measure fracture density, the average number of fractures per metre measured was plotted against distance from the Castle Cove Fault. The total scanline length was 288 m in the Eumeralla Formation hanging wall,

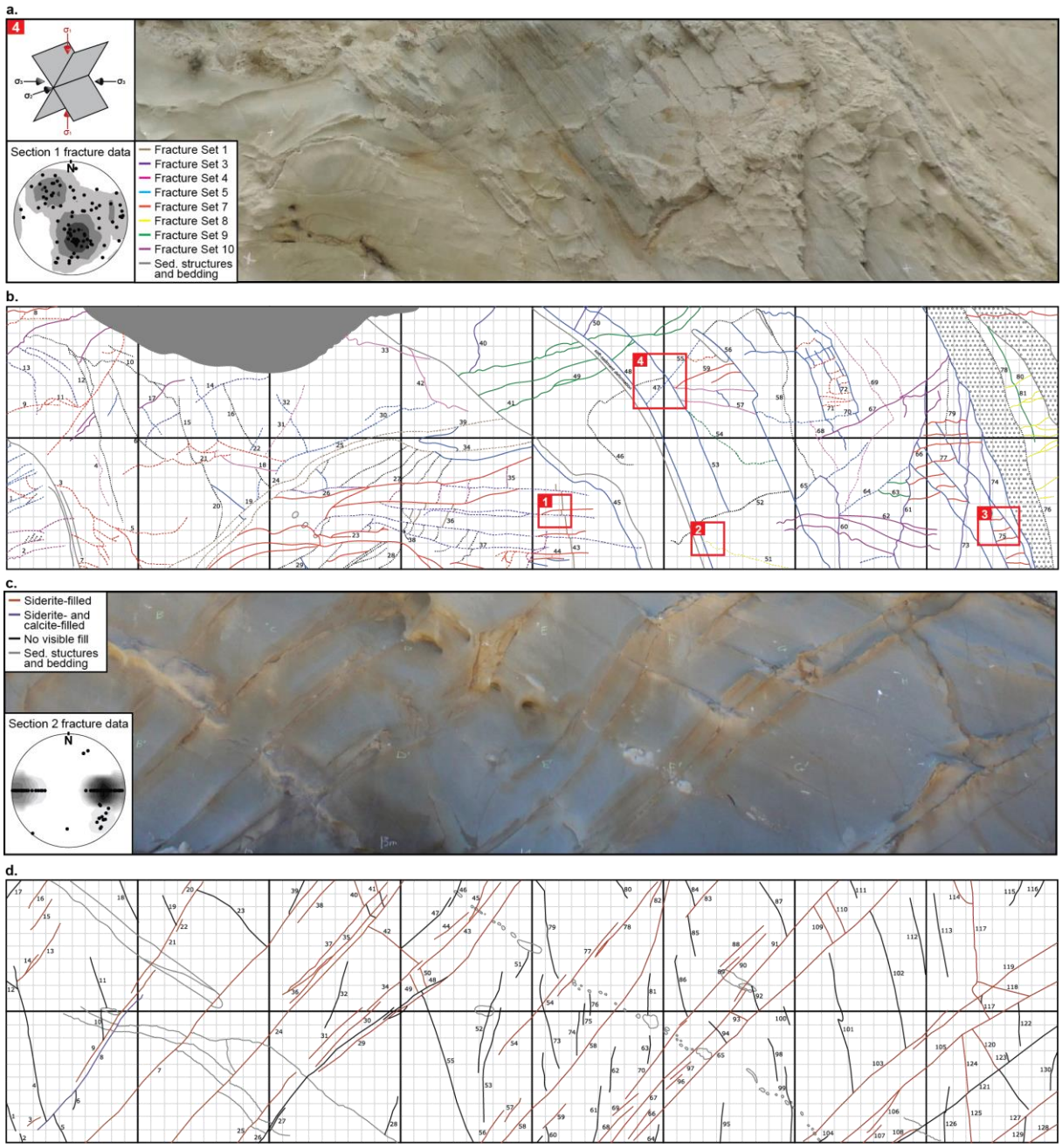

Figure 5. (a) A photo of Section 1, approximately 2–10m from the Castle Cove Fault. Insets 1, 2, and 3 are examples of abutting and cross-cutting relationships between Fracture Sets 5, 7, and 8 (see Fig. 9). Inset 4 is an example of a conjugate fracture pair (Fracture Set 5) formed during extensional stress conditions; Lower hemisphere and equal area projections of poles to fracture planes for fractures measured in Section 1 are shown in the bottom left corner; (b) a fracture trace section of Section 1. Grey shaded area indicates an area covered by rock fall. The dotted areas indicate fine-grained and pebbly overbank deposits. A synthetic fault is indicated by the largest fractures identified as Fracture Set 1; (c) a photo of Section 2, approximately 14–22m northwest of the Castle Cove Fault; Lower hemisphere and equal area projections of poles to fracture planes for fractures measured in Section 2 are shown in the bottom left corner; (d) a fracture trace section of Section 2. Each black grid is 1m×1m and the numbers on the fracture trace sections indicate the locations of fracture measurements.

orthogonal to the fault plane. The presence of small-scale faults was also noted, such as synthetic faults, antithetic faults, and vertical faults. Synthetic faults recorded similar geometries and antithetic faults recorded opposite geometries to the Castle Cove Fault.

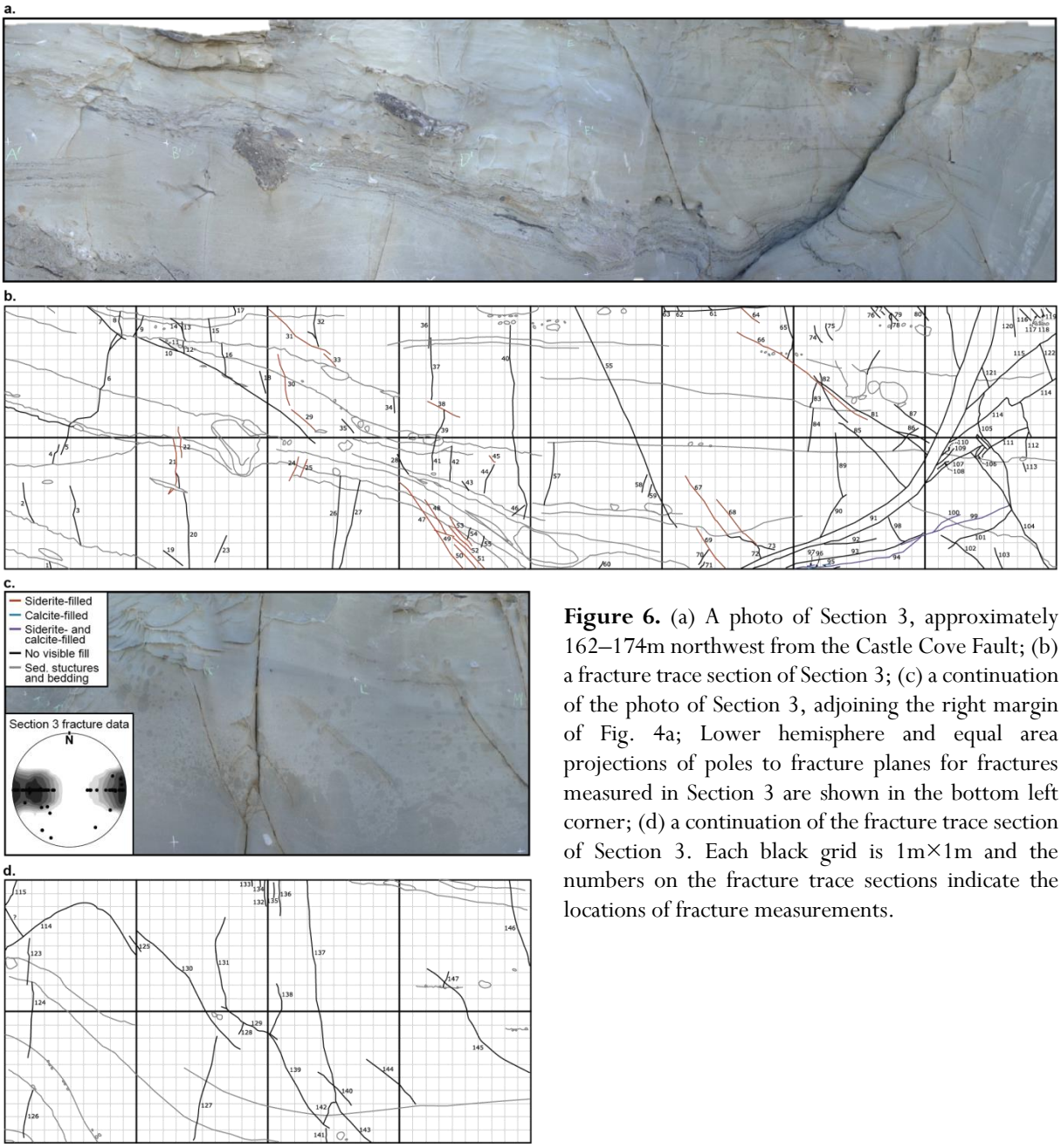

Figure 6. (a) A photo of Section 3, approximately 162–174m northwest from the Castle Cove Fault; (b) a fracture trace section of Section 3; (c) a continuation of the photo of Section 3, adjoining the right margin of Fig. 4a; Lower hemisphere and equal area projections of poles to fracture planes for fractures measured in Section 3 are shown in the bottom left corner; (d) a continuation of the fracture trace section of Section 3. Each black grid is 1m×1m and the numbers on the fracture trace sections indicate the locations of fracture measurements.

4. Results and interpretations

4.1 Fracture sections

Section 1

Section 1 covered an area of 16 m^2 and was constructed in the south-eastern dipping limb (toward 140°) of the inversion anticline at Castle Cove, approximately 2–10 m from the Castle Cove Fault (Fig. 5a and 5b). This section is closest to the Castle Cove Fault. At this locality, the beds dip 43° toward 140° and are characterised by thinly bedded (approximately 0.5 to 4 m) volcanogenic sandstones with fine-grained and pebbly overbank deposits (Fig. 5a) and thin coal laminations. A total of 271 closed fractures were mapped. There were 205 fractures filled with siderite, and 66 fractures with no visible fill. No open fractures were mapped. The spatial density of fractures in Section 1 was 17 fractures per metre. Fracture dips and strikes were measured for fracture set identification. A large synthetic fault, dipping 67° toward the northwest, is present approximately 6 m from the Castle Cove Fault in Section 1.

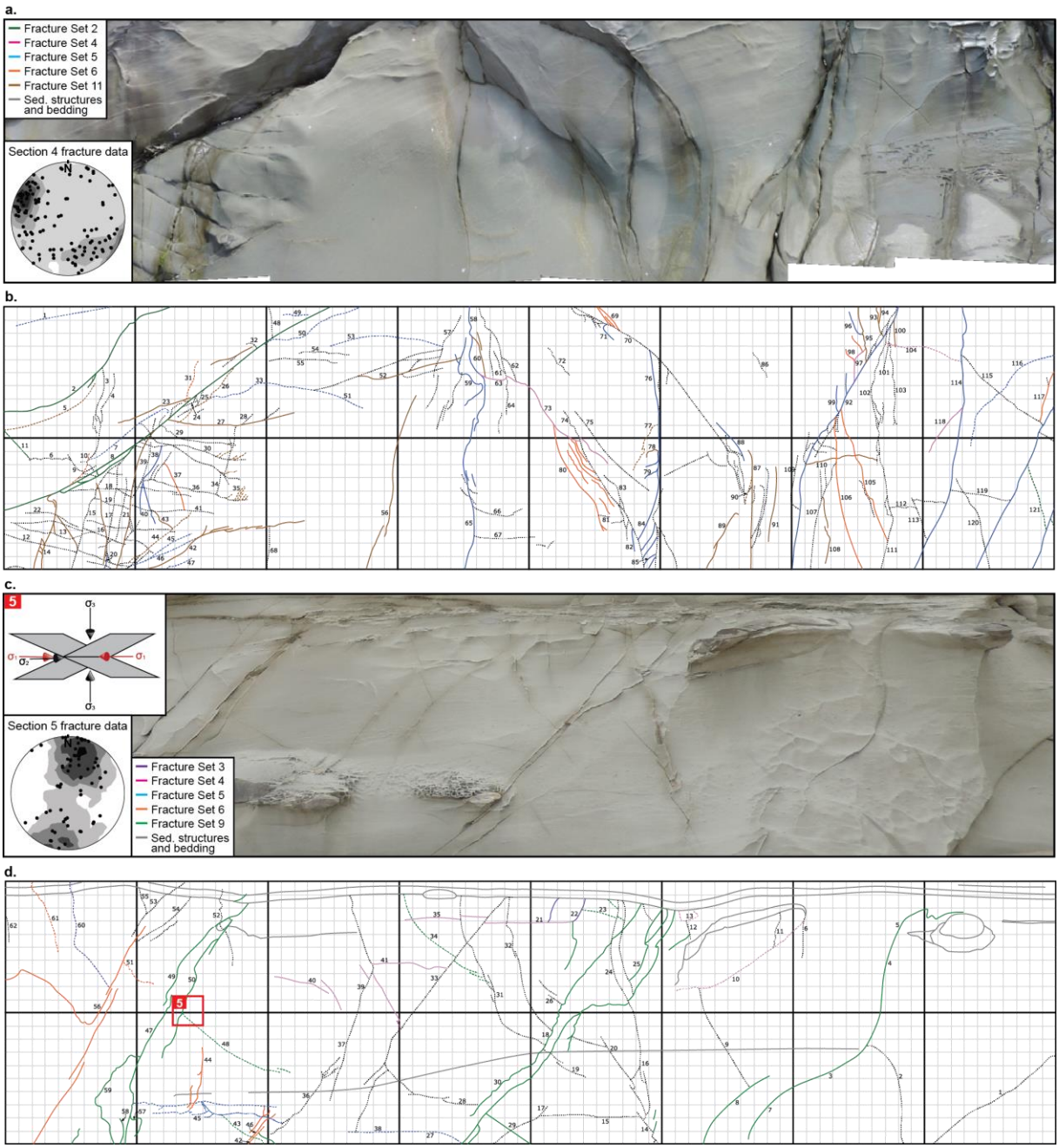

Figure 7. (a) A photo of Section 4, approximately 225–233m northwest from the Castle Cove Fault; Lower hemisphere and equal area projections of poles to fracture planes for fractures measured in Section 4 are shown in the bottom left corner; (b) a fracture trace section of Section 4. A synthetic fault is indicated by the largest fracture identified as Fracture Set 2; (c) a photo of Section 5, approximately 276–284m northwest of the Castle Cove Fault; Lower hemisphere and equal area projections of poles to fracture planes for fractures measured in Section 5 are shown in the bottom left corner; (d) a fracture trace section of Section 5. Inset 5 is an example of a conjugate fracture pair (Fracture Set 9) formed during compressional stress conditions. Each black grid is 1m×1m and the numbers on the fracture trace sections indicate the locations of fracture measurements.

Section 2

Approximately 14–22 m northwest of the Castle Cove Fault, Section 2 was constructed of beds dipping 30° to the south-east, which form the south-eastern dipping limb of the inversion anticline (Fig. 5c and 5d). Section 2 covered an area of 16 m^2. The beds are more lithologically homogenous at this locality. A total of three open fractures and 132 closed fractures were mapped. There were 67 siderite filled

fractures and 65 fractures with no visible fill. The spatial density of fractures significantly decreased away from the fault to eight fractures per metre within Section 2.

Section 3

Section 3 was a slightly larger section, covering an area of 24 m^2. It was mapped approximately 162–174 m northwest of the Castle Cove Fault (Fig. 6), in strata gently dipping (14°) toward the southeast. A total of 160 fractures were mapped, with a spatial density of 10 fractures per metre. There were 39 open fractures mapped and 121 closed fractures comprising 70 siderite filled fractures, two calcite filled fractures, six siderite and calcite filled fractures, and 43 fractures with no visible fill.

Section 4

Approximately 225–233 m northwest of the Castle Cove Fault, Section 4 was mapped in the same stratigraphic interval as Section 3 (Fig. 7a and 7b). Section 4 covered an area of 16 m^2. A total of 288 closed fractures were mapped, with a spatial density of 18 fractures per metre. There were 136 fractures filled with siderite, 102 fractures filled with calcite, and 50 fractures with no visible fill. No open fractures were mapped. This section intersects a calcite-filled synthetic fault that dips 80° toward the west-northwest.

Section 5

Section 5, was the furthest section from the Castle Cove Fault, constructed approximately 276–284 m northwest from the fault (Fig. 7c and 7d). This section covered an area of 16 m^2. Bedding gently dips 10° toward the southeast (148°) at this locality, and the section is stratigraphically aligned with Sections 3 and 4. A total of two open fractures and 117 closed fractures were mapped. There were 66 siderite filled fractures and 51 fractures with no visible fill. The spatial density of fractures was seven fractures per metre.

4.2 Fracture sets at Castle Cove

The fracture data from Sections 1, 4, and 5 were separated into fracture sets (Table 1, Fig. 8). There was insufficient fracture data from Sections 2 and 3 to identify fracture sets. Fracture sets are defined as planar features that are similar in orientation and dip (Aydin, 2000). The relative timing of fracture set formation was made using abutting and cross-cutting relationships, where younger fractures abut or cross-cut older fractures (Fig. 9; Hancock, 1985). The architectural style of the fractures was characterised following Hancock (1985), which describes the trace patterns of fractures in plan or profile and their abutting and cross-cutting relationships in reference to the shapes of capital letters in the Latin alphabet. For example, a younger fracture abutting against an older fracture will form a T-intersection. Fracture sets that are pervasive across most sections with fracture counts exceeding 20 fractures were included in this study. Fracture sets with less than 20 fractures were considered too small and not statistically representative to make reliable interpretations on their relation to local and regional tectonics. Fractures that were also structurally significant based on fracture lengths and maximum horizontal stress (σ_H) orientations were also included in this study. In order to aid chronological and structural interpretations, fracture sets have been classified into two types based on outcropping style; fracture sets that were ubiquitous across most sections and recorded large scale structural trends (Fig. 10) and fracture sets that cropped out locally (Fig. 11). Andersonian fracture sets identified after the data was rotated indicate that the fractures formed before the beds were tilted. Andersonian fracture sets identified in unrotated data indicate that they

Table 1. Summary of fracture sets with conjugate pairs documented at Castle Cove. The pervasiveness of fracture sets (local or regional), timing of formation based on stereographic projection techniques, fracture strike, orientation of maximum horizontal principle stress (σ_H), and stress regimes are listed. Fracture lengths calculated from the fracture trace maps and number of fractures (n) are also included. The colours are used to illustrate the fracture sets in fracture trace maps. Fracture sets highlighted in bold indicate the large scale fracture sets at Castle Cove.

Set	Local or Regional	Timing	Fracture Strike	Orientation of Stress Regime	Stress Regime	Fracture Length (m)	n	Map	Colour
1	Local	Pre-folding	NNE–SSW, ENE–WSW	NE–SW	Strike-slip	0.1–3	16	1	Gold
2	Local	Pre-folding	NE–SW, NW–SE	N–S	Strike-slip	0.1 – > 3	5	4	Dark green
3	**Regional**	**Pre-folding**	**NNW–SSE, E–W**	**NW–SE**	**Strike-slip**	**0.2–2.1**	**22**	**1, 5**	**Purple**
4	**Regional**	**Pre-folding**	**NW–SE to NE–SW**	**NE–SW to NW–SE**	**Compression**	**0.1–1.5**	**26**	**1, 4, 5**	**Pink**
5	**Regional**	**Post-folding**	**NE–SW**	**NW–SE**	**Extension**	**0.1 – > 2.3**	**103**	**1, 4, 5**	**Blue**
6	**Local**	**Post-folding**	**NW–SE**	**NE–SW**	**Extension**	**0.1 – > 1.2**	**30**	**4, 5**	**Orange**
7	**Local**	**Post-folding**	**NW–SE**	**NE–SW**	**Compression**	**0.05–2**	**71**	**1**	**Dark Orange**
8	Local	Post-folding	NE–SW	NW–SE	Compression	0.2–0.8	10	1	Yellow
9	**Local**	**Post-folding**	**E–W**	**N–S**	**Compression**	**0.1 – > 2.5**	**43**	**1, 5**	**Green**
10	Local	Post-folding	NW–SE	NE–SW	Extension	0.2–1.2	23	1	Violet
11	Local	Post-folding	NE–SW	NW–SE	Extension	0.01–1.1	43	4	Brown

formed after the beds were tilted. In the section below, fracture sets have been numbered in chronological order based on abutting and cross-cutting relationships and the relative timing with respect to folding indicated by rotating equal area projections. The reported mean fracture dip values below for Fracture Sets 1 to 4 have been restored to those before folding. The reported dip values for Fracture Sets 5 to 11 are present orientations.

Fracture Set 1 [gold]

Cross-cutting and abutting relationships indicate that Fracture Set 1 is the oldest set in Section 1, recording local structural trends. This fracture set was identified after the fractures were rotated to horizontal bedding (Fig. 8 and Fig. 11). The rotated orientation of the intersection of the conjugate pairs is vertical, which conforms to the Andersonian stress state for a strike-slip regime. This set has a steep mean dip of 81°. Fractures strike NNE–SSW, with conjugate fractures that strike ENE-WSW, indicating a maximum horizontal stress (σ_H) direction of NE–SW. A total of 16 closed fractures were mapped, with 11 siderite filled fractures and five fractures with no visible fill. Fracture aperture is typically <1 mm, but one fracture is up to 40 mm in width.

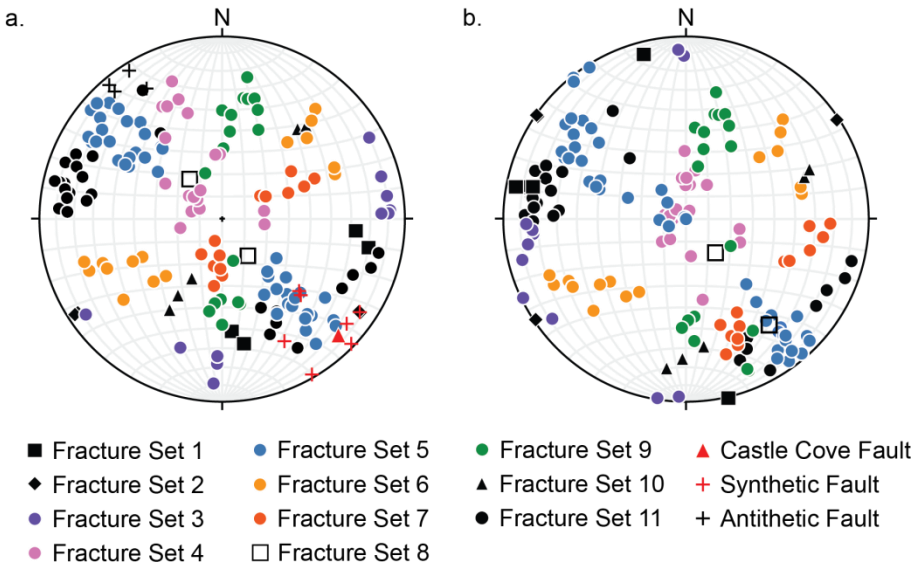

Figure 8. All unrotated data of fracture sets and faults at Castle Cove (shown as poles to planes). Coloured fracture sets are the regional sets identified in this study and black fracture sets are local fracture sets identified in this study.

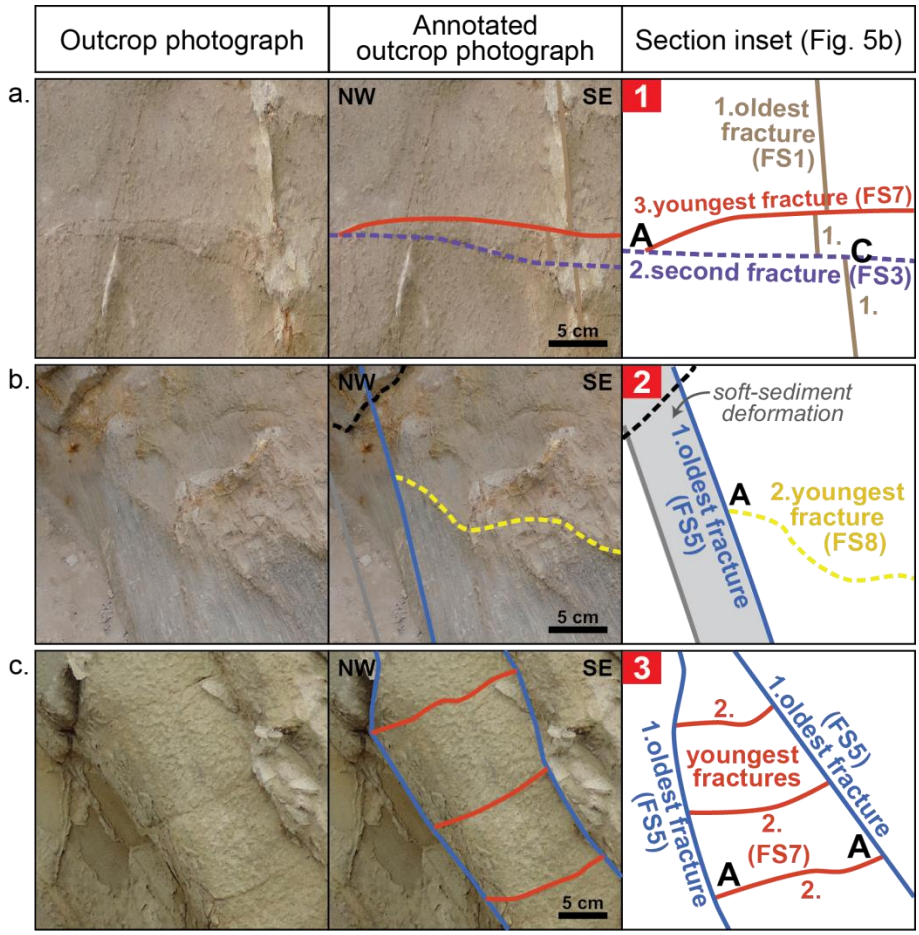

Figure 9. Examples of abutting (A) and cross-cutting (C) relationships between Fracture Sets 5, 7, and 8 (Section 1 insets in Fig. 5b). FS followed by a number indicates the Fracture Set. (a) Fracture Set 7 abutting Fracture Set 3 which in turn is cross-cutting Fracture Set 1; (b) Fracture Set 8 abutting Fracture Set 5; and (c) Fracture Set 7 abutting Fracture Set 5.

Fracture Set 2 [dark green]

Fracture Set 2 is the oldest set in Section 4 and records local structural trends. This fracture set was identified after the fractures were rotated to horizontal bedding (Fig. 8 and Fig. 11). The rotated orientation of the intersection of the conjugate pairs is vertical, which conforms to the Andersonian stress state for a strike-slip regime. This set has a steep mean dip of 89° and strikes NE–SW, with conjugate fractures that strike NW–SE, indicating a σ_H direction of N–S. A total of five closed fractures were mapped, four fractures filled with calcite and one fracture filled with siderite. The calcite filled fractures have apertures up to 10 mm. One of these fractures propagates through multiple beds and is surrounded by a damage zone (less than 2 m wide) of local fracture sets, which are not included in this paper.

Fracture Set 3 [purple]

The oldest regional fracture set identified records large scale structural trends across Sections 1 and 5. This fracture set was identified after the fractures were rotated to horizontal bedding (Fig. 8 and Fig. 10a). The rotated orientation of the intersection of the conjugate pairs is vertical, which conforms to the Andersonian stress state for a strike-slip regime. This set has a steep mean dip of 81°. Fractures strike NNW–SSE, with conjugate fractures that strike E–W, indicating a σ_H direction of NW–SE. A total of 21 closed fractures and 1 open fracture were mapped. Of the closed fractures, 14 fractures are siderite filled and 7 fractures contain no visible fill. Fracture aperture ranges between <1 to 2 mm for this set.

Geometrically, fractures typically exceed 1 m in strike length and most fractures are aligned perpendicular to bedding. In Section 1, Fracture Set 3 consistently cross-cuts and displaces Fracture Set 1 (Figure 9a).

Fracture Set 4 [pink]

Fracture Set 4 is present in all sections and records large scale structural trends. This fracture set was identified as Andersonian fractures after they were rotated to horizontal bedding (Fig. 10b). The mean dip of this set is 16° (sub-horizontal), which conforms to the Andersonian stress state for compression. Across the three sections, this fracture set mainly strikes NW–SE, though it strikes NE–SW in the furthest section from the fault (Section 5). The direction of σ_H is NW–SE for Sections 1 and 4, and NE–SW for Sections 5. A total of 26 closed fractures were mapped, with 13 siderite filled fractures and 13 fractures with no visible fill. Fracture aperture ranges between <1 to 2 mm for this set. Geometrically, these fractures occasionally appear to be abutting or cross-cutting Fracture Set 5, indicating that some fractures in Fracture Set 4 may have formed contemporaneously with Fracture Set 5.

Fracture Set 5 [blue]

This fracture set is present in all sections and records large scale structural trends. This fracture set formed after folding of the strata (Fig. 8 and Fig. 10c). In Section 1, these fractures formed along the moderately dipping beds of the inversion anticline, i.e. parallel to bedding. This set has a mean dip of 54° and strikes NE–SW, therefore this set is interpreted to have formed under an extensional stress regime with a NW–SE extension orientation. A total of 103 closed fractures were mapped, 64 fractures filled with siderite, 27 fractures filled with calcite, and 12 fractures with no visible fill. Fracture apertures typically range between <1 to 5 mm, however calcite filled fractures in Section 4 range between 5 to 20 mm. The fracture density of Fracture Set 5 decreases away from the Castle Cove Fault. In Section 1 there were 61 fractures identified, however in Sections 4 and 5 the fracture counts decreased to 35 and 7 fractures, respectively. In all sections, the fractures typically exceed 1 m in length and extend up to 2 m past the edges of the section.

Fracture Set 6 [orange]

Fracture Set 6 is only present in Sections 4 and 5 and records large scale structural trends. This fracture set formed after folding of the strata (Fig. 8 and Fig. 10d). This set has a moderate mean dip of 57° and strikes NW–SE, indicating an extensional stress regime with a NE–SW extension orientation. A total of 30 closed fractures were mapped, 24 fractures filled with siderite, one fracture filled with calcite, and five fractures had no visible fill. Fracture apertures range between <1 mm to 4 mm, with siderite cementation in fractures with larger aperture. Fractures often occur as clusters and other than abutting relationships with Fracture Sets 4 and 5, Fracture Set 6 does not show consistent geometrical relationships with other fracture sets.

Fracture Set 7 [dark orange]

This fracture set is the most pervasive set present in Section 1 and records large scale structural trends. Fracture Set 7 formed after folding of the strata (Fig. 8 and Fig. 10e). This set has a mean dip of 25° (sub-horizontal) and strikes NW–SE, indicating a compressional stress regime with a σ_H orientation of NE–SW. A total of 71 closed fractures were mapped, consisting of 56 siderite filled fractures and 15 fractures with no visible fill. Fracture aperture is typically <1 mm, but can range up to 3 mm. There is a marked

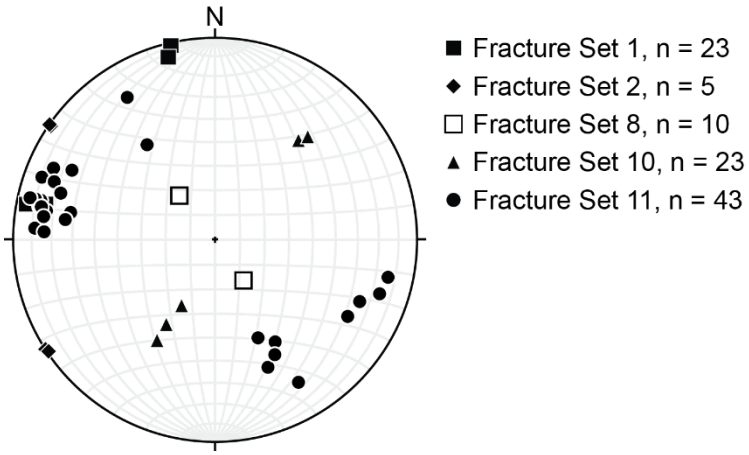

Figure 11. Lower hemisphere and equal area projections of poles to fracture planes of local fracture sets identified at Castle Cove. Fracture Sets 1 and 2 are rotated and Fracture Sets 8, 10, and 11 are unrotated.

difference in the geometry of the longer and shorter fractures of Fracture Set 7. The longer (approximately >1 m) fractures do not show consistent geometrical relationships with other fracture sets. However, the shorter (<1 m) fractures in Fracture Set 7 abut against Fracture Set 5 (Figure 9c) and Fracture Set 6, making T-intersections and forming a H-shaped pattern.

Fracture Set 8 [yellow]

Fracture Set 8 formed after the strata was folded (Fig. 8 and Fig. 11). This set dips 20° (sub-horizontal) and strikes NE–SW, therefore this set is interpreted to have formed under a compressional stress regime with a NW–SE σ_H orientation. This fracture set records local structural trends as it is only present in a small area adjacent to the Castle Cove Fault (Section 1), but it may additionally record recent regional NW–SE directed compression. A total of 10 siderite filled fractures were mapped with a fracture aperture range of <1 to 2 mm. Fracture Set 8 fractures consistently abut against the interface of soft sediment deformation and channel overbank sedimentary structures (Figure 9b), making T-intersections and forming a H-shaped pattern similar to Fracture Set 7 geometry. This reflects mechanical changes in depositional composition.

Fracture Set 9 [green]

Fracture Set 9 is present in Sections 1 and 5 and records large scale structural trends. This fracture set formed after folding of the strata (Fig. 8 and Fig. 10f). This set has a mean dip of 44° toward the north and south, and strikes E–W, indicating a compressional stress regime with a σ_H orientation of N–S. A total of 42 closed fractures and one open fracture were mapped. Of the closed fractures, 31 fractures are siderite filled and 11 fractures contain no visible fill. Fracture aperture ranges between <1 to 2 mm for this set, and one siderite filled fracture in Section 1 is up to 10 mm in width. In both sections, the fractures typically exceed 1 m in length. The fractures are clustered and most fractures terminate at bedding planes.

Fracture Set 10 [violet]

Fracture Set 10 is only present in Section 1 and records local structural trends. Fracture Set 10 formed after the strata was folded (Fig. 8 and Fig. 11). This set has a mean dip of 47° and strikes NW–SE, indicating an extensional stress regime with a NE-SW extension orientation. A total of 23 siderite filled fractures were mapped with a fracture aperture range of <1 to 2 mm, though the aperture of one siderite fracture is up to 20 mm. Several fractures in Fracture Set 10 abut against the longer fractures in Fracture Set 7, forming a H-shaped pattern.

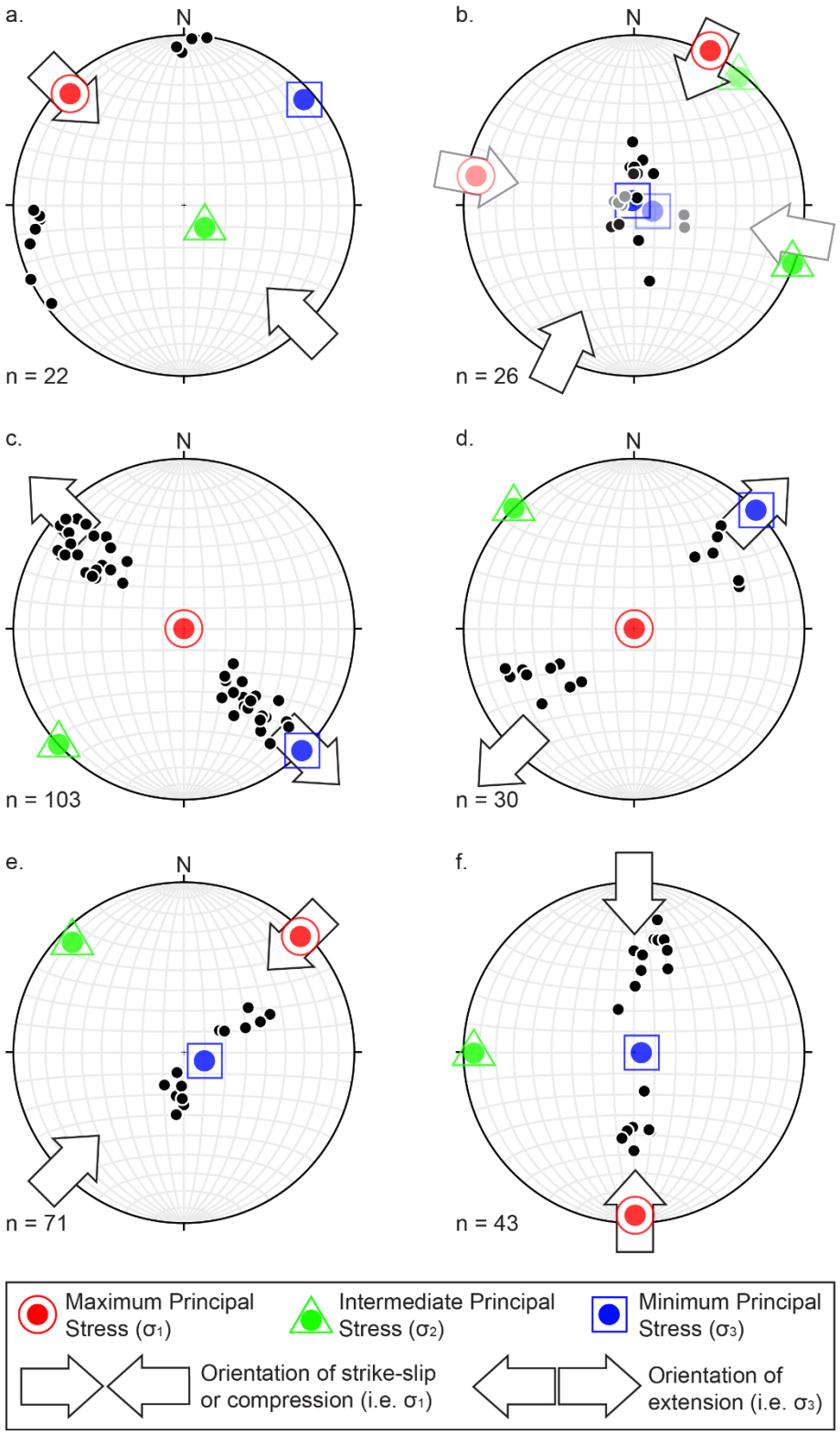

Figure 10. Lower hemisphere and equal area projections of poles to fracture planes of large scale fracture sets identified at Castle Cove. Arrows indicate the inferred stress orientations and the coloured shapes indicate the orientations of the maximum, intermediate, and minimum principal stresses. (a) Rotated projection of Fracture Set 3 recording northwest to southeast strike-slip; (b) Rotated projection of Fracture Set 4 recording northeast to southwest compression in Sections 1 and 4. Poles and arrows in grey indicate northwest to southeast compression recorded in Section 5; (c) Unrotated projection of Fracture Set 5 recording northwest to southeast extension; (d) Unrotated projection of Fracture Set 6 recording northeast to southwest extension; (e) Unrotated projection of Fracture Set 7 recording northeast to southwest compression; and (f) Unrotated projection of Fracture Set 9 recording north to south compression.

Fracture Set 11 [brown]

This fracture set is only present in Section 4 and records local structural trends. This set formed after the strata was folded (Fig. 8 and Fig. 11). Fracture Set 11 has a moderate mean dip of 70° and strikes NE–SW, therefore this set is interpreted to have formed under an extensional stress regime with a NW–SE extension orientation. A total of 43 closed fractures were mapped, consisting of 18 siderite filled fractures, 22 calcite filled fractures, and three fractures with no visible fill or a fill that could not be identified. Fracture aperture ranges between <1 to 10 mm for this set, though one fracture fill that could not be identified is up to 25 mm in width. This set is composed of two sub-sets with slight differences in dip and strike, as observed in Fig. 11. However, the timing of fracture formation of both sub-sets, indicated from abutting and cross-cutting relationships, suggests that they formed at similar times under similar stress conditions.

4.3 Castle Cove Fault damage zone

4.3.1 Extent of fault damage zone deformation at Castle Cove

The Castle Cove Fault is surrounded by a zone of fracturing and faulting, i.e. the damage zone, that accommodates strain during deformation and has significant implications for structural permeability. The width of the Castle Cove Fault damage zone cannot be determined from field observations as it extends beyond the study area (greater than 300 m in the hanging wall) to inaccessible cliff exposures. However, variations in the damage zone can be described in terms of fracture density, i.e. local variations in strain. Variations in the fracture density within the Castle Cove Fault damage zone were identified by plotting the number of macrofractures relative to distance from the fault. The number of macrofractures was measured in the hanging wall by a linear fracture count. Fractures were counted in cliff exposures orthogonal to the fault plane, between 2 to 288 m southwest of the Castle Cove Fault. The average spatial density of fractures is represented by two trend lines in Fig. 12. A zone of maximum fracture density within the damage zone (16 fractures per metre) was identified within 25 m of the Castle Cove Fault. Within this zone, eight fracture sets are recorded in Section 1. More than 25 m from the fault, the fracture density decreases to 8 fractures per metre and is represented by an approximately horizontal trend line (Fig. 12). Only five fracture sets are recorded in each of the two sections (Sections 4 and 5) in this zone.

4.3.2 Synthetic and antithetic normal faults in the fault damage zone

Northeast–southwest striking synthetic and antithetic faults were also recorded within the damage zone at Castle Cove (Fig. 12). The average dip of the synthetic faults is 75° toward the northwest and the average dip of the antithetic faults is 81° toward the southeast (Fig. 8). The length of the faults typically exceeds 10 m and several span the height of the cliffs at Castle Cove. The synthetic and antithetic faults are not evenly distributed at Castle Cove and do not show consistent amounts of offset. Many are offsetting stratigraphy by less than 20 cm of normal movement.

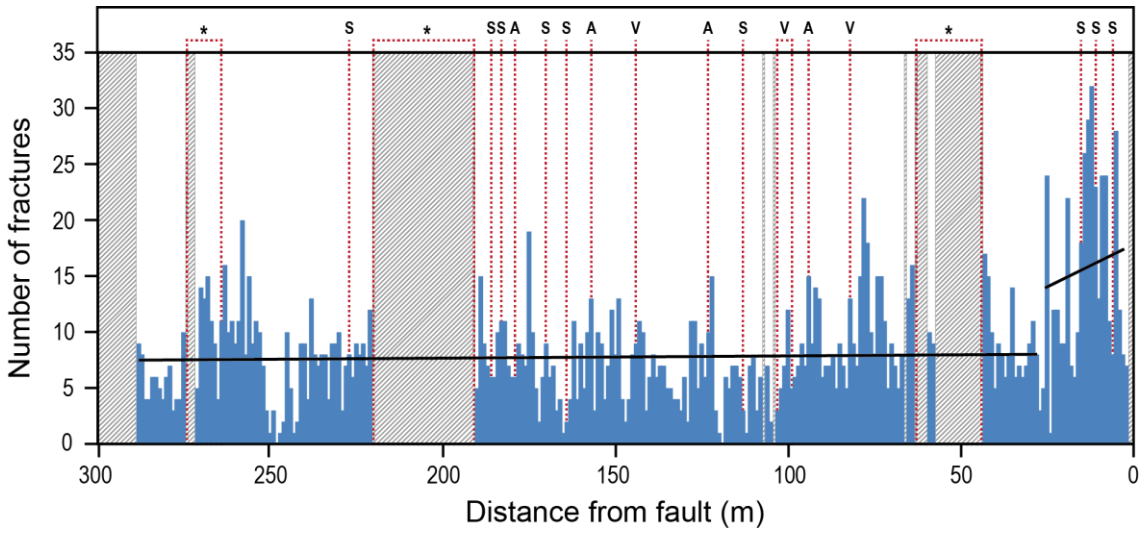

Figure 12. Number of macrofractures relative to distance from the Castle Cove Fault. The horizontal trend line more than 25 m from the Castle Cove Fault indicates background macrofracture levels and the inclined trend line indicates elevated fracture counts within 25 m of the fault. Red dashed lines indicate the locations of adjacent small-scale faults and fault zones. Letters indicate type of small-scale fault, where S is a synthetic fault, A is an antithetic fault, V is a vertical fault, and asterisks (*) indicate locations of potential fault zones. Grey shaded areas indicate sections where fractures could not be counted and there is no outcrop.

5. Discussion

5.1 Evolution of the fracture system mapped at Castle Cove

Conceptual block models illustrate the structural evolution of the geometries and chronologies of the fractures sets identified at Castle Cove (Fig. 13). The influence of mechanical stratigraphy was investigated but is not considered in these models as stratigraphy does not have a significant control on fracture set formation in the study site. The sedimentary structures described previously and the coal laminations in Section 1 will have some influence on fracture formation and propagation, however the Eumeralla Formation is largely lithologically homogenous at Castle Cove and does not exert any observable control on the fractures. The following section discusses possible fracture formation mechanisms for the fracture sets that are geometrically related to the Castle Cove Fault.

5.1.1 Fracture formation during late Cretaceous extension

A NW–SE extensional stress regime is recorded by Fracture Sets 5 (Fig. 13c). This fracture set formed after the beds at Castle Cove had been tilted. Based on the relative timing of formation (i.e. abutting and cross-cutting relationships) and the structural geometries of this fracture set, it is compatible with deformation associated with renewed rifting in the late Cretaceous. During this period, intense normal faulting and fault reactivation occurred throughout the Otway Basin (Lyon et al., 2007). However, the direction of extension during rifting in the late Cretaceous is widely debated (Perincek et al., 1994a; Miller et al., 2002; Schneider et al., 2004).

Fracture Set 5 is the most ubiquitous set identified and occurs in all mapping areas. Within the hanging wall anticline (Section 1), Fracture Set 5 occurs along many major lithology contacts, particularly along the boundaries of overbank deposits and where coal laminations are more pervasive. If planes of mechanical weakness such as lithological contacts are favourably oriented in the stress-field, fractures will nucleate and propagate along these boundaries (Welch et al., 2009). As Fracture Set 5 is the most

ubiquitous and widespread fracture set at Castle Cove and strikes parallel to the Castle Cove Fault, this fracture set likely formed during the initial formation of the Castle Cove Fault as a normal fault.

5.1.2 Fracture formation during mid-Eocene to Recent compression

Renewed compression at Castle Cove is recorded by Fracture Set 7, which is a sub-horizontal fracture set that experienced a σ_H orientation of NE–SW (Fig. 13d). This fracture set only crops out adjacent to the Castle Cove Fault (Section 1). It is the largest fracture set in Section 1 adjacent to the fault and the second largest fracture set (71 fractures) recorded at Castle Cove. As this is the second most pervasive fracture set identified at Castle Cove, it is important for characterising the Castle Cove Fault damage zone. The shift to a compressional stress regime and the relative timing (i.e. abutting and cross-cutting relationships) of Fracture Set 7 implies that this fracture set formed during mid-Eocene to Recent NW–SE directed compression. However, the structural association of Fracture Set 7 is obscure. This is because the stress orientation recorded by this fracture set is NE–SW and the fractures strike perpendicular to the hinge of the inversion anticline at Castle Cove. As this fracture set is pervasive at Castle Cove, we speculate the possible causes of fracture formation in the following section. It is possible that this fracture set formed as a result of fault rotation during the onset of compression, i.e. the orientation of σ_H can rotate and deflect adjacent to a fault as a result of the elastic properties of the fault zone (Bell, 1996). This indicates that inversion-related anticline development in the hanging wall was complex, with the axes rotating during non-coaxial inversion. This interpretation indicates that these fractures are spatially related to the fault and can be attributed to anticlinal folding in the hanging wall during inversion.

Compression is also recorded by Fracture Set 8, which is a small fracture set that only crops out adjacent to the Castle Cove Fault (Section 1). Fracture Set 8 experienced a σ_H direction of NW–SE (Fig. 13d). Though localised to a small area in Section 1, Fracture Set 8 potentially records late Miocene to Pliocene NW–SE directed compression and reverse-reactivation of the Castle Cove Fault (Duddy, 1994; Edwards et al., 1996; Holford et al., 2014). Uplift of several hundreds of metres to a kilometre or more is recorded in the Otway Ranges during this event (Dickinson et al., 2002). Fault scaling relationships (Kim and Sanderson, 2005; Reilly et al., 2016) using the strike length of the Castle Cove Fault indicate a maximum vertical displacement up to 1 km. Outcrop observations and fracture densities (Fig. 12) in the hanging wall at Castle Cove indicate a damage zone greater than 300 m in width. Therefore, given the extent of the inversion of the Castle Cove Fault it would be expected that Fracture Set 8, which is associated with the inversion, would be widespread rather than localised. A possible explanation is that strain has been accommodated by the formation of the large-scale inversion anticline rather than by fracturing.

5.2 Castle Cove Fault evolution

Early to mid-Cretaceous extension resulted in the formation of syn-rift faults and syn-sedimentary fault growth within the formations underlying the Eumeralla Formation (Perincek and Cockshell, 1995; Lyon et al., 2005). In the eastern Otway Basin, most of these faults strike NE–SW (Fig. 2) and are related to the upper plate margin geometry (Lister et al., 1991; Perincek and Cockshell, 1995; Miller et al., 2002). Faulting and fault reactivation continued during the initial stages of the deposition of the Eumeralla Formation due to sediment loading, despite the cessation of extension (Cooper, 1995; Hill et al., 1995a; Perincek and Cockshell, 1995; Finlayson et al., 1996; Lyon et al., 2005). Following a period of compression in the mid-Cretaceous, late Cretaceous rifting and extension led to intense fault activity and reactivation of several early Cretaceous syn-rift faults (Geological Survey of Victoria, 1995; Lyon et al.,

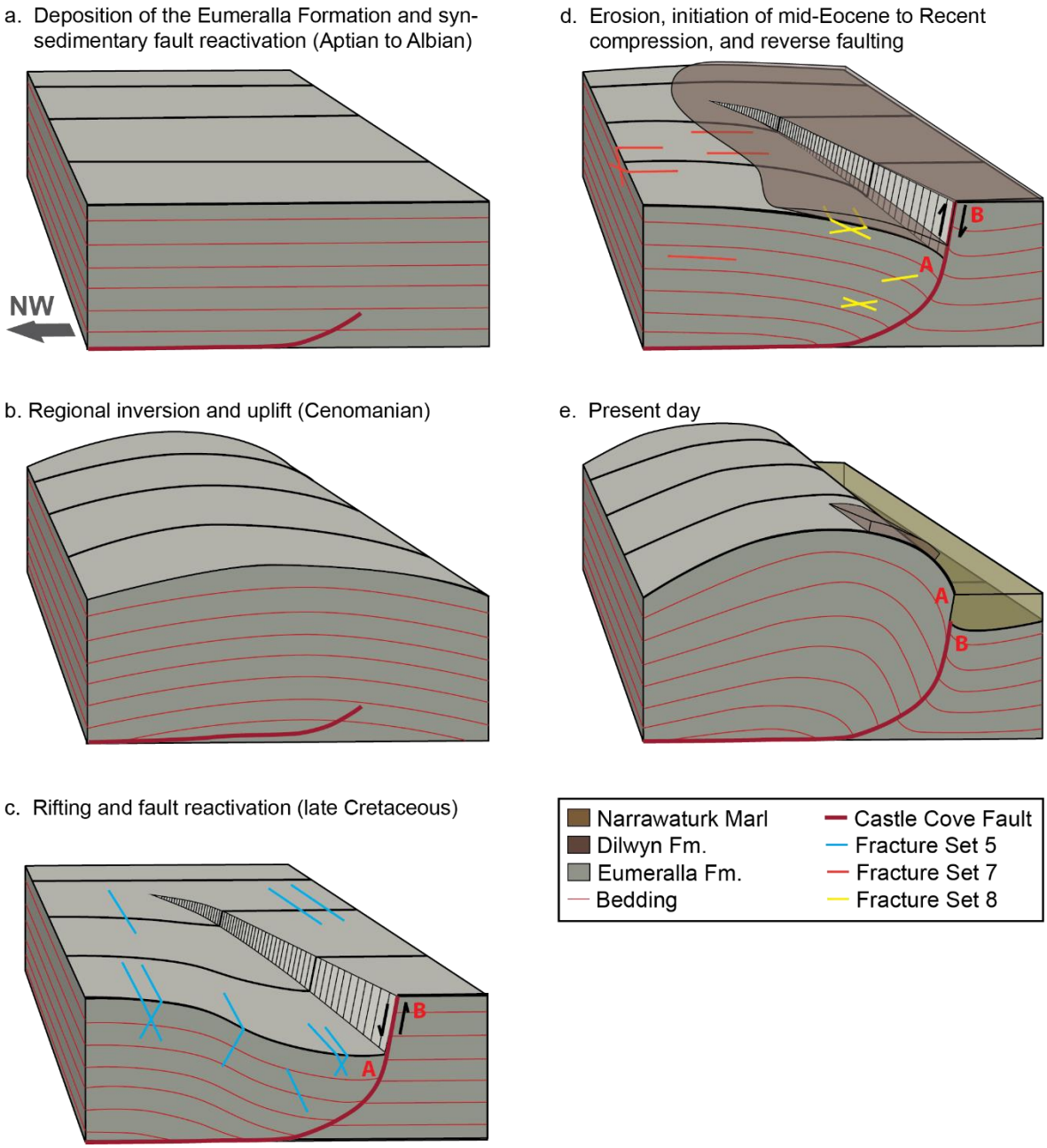

Figure 13. Structural evolution of the Castle Cove Fault and fracture sets at Castle Cove. (a) deposition of the Eumeralla Formation and syn-sedimentary fault reactivation in the Aptian to Albian, (b) regional inversion and uplift in the Cenomanian, (c) Fracture Set 5 (blue) with a NW–SE directed extensional stress regime during late Cretaceous rifting and fault reactivation, (d) Mid-Eocene to Recent compression and reverse faulting with the formation of Fracture Set 7 (dark orange) followed by Fracture Set 8 (yellow). Compressional stress regime with σ_H directions of NE–SW for Fracture Set 7 and NW–SE for Fracture Set 8. (e) A schematic of the present day geometry of the Castle Cove Fault.

2007). Given the NE–SW striking geometry of the Castle Cove Fault and timing of the deposition of the Eumeralla Formation, the fault may have formed as a result of the reactivation and propagation of an early Cretaceous normal fault. At Castle Cove, the formation of Fracture Set 5 has been attributed to the initiation of the Castle Cove Fault. The relative timing and structural geometry of this fracture set also suggests that normal faulting of the Castle Cove Fault occurred during late Cretaceous extension.

Following mid-Eocene breakup, episodes of enhanced compression-related deformation resulted in fault reactivation and inversion within the Otway Basin (Holford et al., 2014). The influence of post-Albian

compression was concentrated on structures in the eastern Otway Basin (Perincek and Cockshell, 1995; Edwards et al., 1996; Tassone et al., 2014). Normal faults that originally formed under extensional stress conditions were contractionally reactivated as reverse faults (i.e. positive inversion; Holford et al., 2011; Holford et al., 2014). At surface, these structures are identified by broad monoclines, anticlines, and synclines (Edwards et al., 1996). It is widely accepted that the Castle Cove Fault was reactivated as a reverse fault during late Miocene to Pliocene compression (Duddy, 1994; Edwards et al., 1996; Holford et al., 2014). Thermochronological data, such as apatite fission track analysis and vitrinite reflectance data, reflect the dominance of mid-Cretaceous and Cenozoic heating and cooling episodes at Castle Cove (Duddy, 2002; Duddy, 2003). Cenozoic heating reached up to 90 °C, supported by vitrinite reflectance values of 0.46%, and is thought to be related to basal heat flow and burial (Duddy, 2002; Duddy 2017, pers. comm.). Mid-Cretaceous and Cenozoic cooling may be attributed to erosion, and it is possible that Cenozoic cooling is related to cooling following reverse-reactivation of the Castle Cove Fault. Furthermore, Eocene sediments are folded within an inverse-related anticline at Castle Cove, suggesting that inversion and folding occurred after the Eocene during the Cenozoic (Duddy, 2002).

5.3 Castle Cove Fault geometry at depth

The geometry of faults at depth can be elucidated through detailed analysis of outcrop and subsurface data. Field observations on the structure of well-exposed fault zones allow for inferences to be made on the fault geometry at depth (Faulkner et al., 2010). Outcrop analogues within similar structural settings can also provide insights on the geometry of poorly exposed faults. In the subsurface, seismic reflection data can reveal structural discontinuities that are greater than 10 m (Wibberley et al., 2008). However, the Castle Cove Fault does not intersect any seismic lines and the fault core is not exposed in outcrop. Therefore, to gain an understanding of the geometry of the Castle Cove Fault at depth, field observations of the damage zone at Castle Cove and fault analogues in the eastern Otway Basin will be utilised.

In the eastern Otway Basin, the dips of inverted NNW-dipping faults typically range between 50° to 70°, and are steeper than faults in the western Otway Basin (Cooper, 1995; Hill et al., 1995a). At Castle Cove, the average dip of the synthetic and antithetic normal faults is 77°. This implies that the Castle Cove Fault was initiated as a normal fault with a steep dip. Higher dip angles require higher fluid pressure conditions and higher differential stress in order to reactivate (Sibson, 1985). However, a low fault dip angle at depth, characteristic of listric normal faults, allows for easy compressional reactivation of faults (Sibson, 1985; Sibson, 1995). At a shallower level, a steeper dip (typically dips greater than 50°) often leads to shortening that is accommodated by a build-up of strain in the hanging wall and development of a large-scale anticline (Sibson, 1995). The Castle Cove Fault has a large-scale (greater than 80 m in half-wavelength) hanging wall anticline which would imply, based on the work of Sibson (1995), that the fault may have a listric geometry. If the Castle Cove Fault is a listric fault at depth, the presence of synthetic and antithetic faults at Castle Cove indicates that folding within the hanging wall may have begun during normal faulting in the late Cretaceous (Dula, 1991). The rollover fold formed during extension would have been amplified (Sibson, 1995) into a large-scale anticlinal structure during mid-Eocene to Recent inversion.

5.4 Examples of similar reverse-reactivated fault geometries and complex fracture systems

Reverse-reactivated structures analogous to those in the Otway Basin are observed in structurally complex basins such as the Bristol Channel Basin in England (Belayneh and Cosgrove, 2004, and references therein), Wessex Basin in England (Underhill and Stoneley, 1998), Fundy rift basin in Canada (Withjack et al.,

1995), several basins in the Loei-Petchabun Fold Belt in northeast Thailand (Cooper and Warren, 2010), Gippsland Basin in Australia (Hillis et al., 2008), and the Bass Basin in Australia (Cummings et al., 2004). Anticlines forming inversion structures above reverse-reactivated normal faults are common in these basins. Examples of well-studied areas that have undergone inversion are detailed below. They illustrate the complex nature of these structures, particularly in cases where lithological variations are controlling the spatial distribution of fractures. Similar to the Otway Basin, these basins have experienced multiple events of extension and compression. Likewise, the fracture systems within these basins are equally as complex as the fracture system at Castle Cove.

The Bristol Channel Basin, particularly the southern margin of the basin, hosts a series of N–S trending reverse-reactivated normal faults with hanging wall anticlines similar in geometry and formation history to the Castle Cove Fault. These syn-rift normal faults were inverted during the N–S Alpine compression of the basin and formed concurrently with a series of strike-slip faults (Belayneh and Cosgrove, 2004). The hanging wall anticlines formed during normal faulting as rollover folds and were subsequently amplified and tightened during compression (Rawnsley et al., 1998; Belayneh and Cosgrove, 2004). This is similar to what is proposed for the Castle Cove Fault in this study. Despite the vast number of studies on the Bristol Channel Basin, the timing, spatial distributions, and causes of fracture formation is a matter of dispute (Belayneh and Cosgrove, 2004). Some authors suggest fracture formation was the result of post-compressional stress release (e.g. Rawnsley et al., 1998), whereas others suggest that fracture formation occurred during compressional inversion (e.g. Engelder and Peacock, 2001). However, unlike the Eumeralla Formation at Castle Cove, frequent sub-metre lithological variations (e.g. alternating limestone and shale) have a greater influence on fracture formation and propagation (Belayneh and Cosgrove, 2004).

The Wessex Basin records Mesozoic extension followed by N–S Cenozoic compression and associated structural inversion (Underhill and Stoneley, 1998). Similar to the Castle Cove Fault and inverted faults in the Bristol Channel Basin, the hanging wall anticlines in the Wessex Basin have been attributed to rollover folds formed during normal faulting, which were subsequently tightened and amplified during compression (Stoneley, 1992). In the Wessex Basin, the anticlines mostly formed adjacent to faults that have a more listric geometry. This has been attributed to the presence of salt detachment surfaces within the listric structures (Underhill and Stoneley, 1998), which has a significant influence on the style of inversion (Letouzey et al., 1995). In a study by Ameen and Cosgrove (1990), a total of 13 fracture sets were identified in an area that experienced major reverse faulting. The fracture system was attributed to regional N–S compression and N–S and E–W extension and the spatial distribution of fractures was lithologically controlled (Ameen and Cosgrove, 1990). The fracture system described by Ameen and Cosgrove (1990) is equally as complex as the fracture system identified at Castle Cove.

5.5 Implications for hydrocarbon exploration and development in the eastern Otway Basin

An understanding of geometries and chronologies of natural fractures (i.e. fluid flow pathways) relative to the timing of trap formation (e.g. inversion anticlines), source rock maturation, and migration is fundamental for hydrocarbon prospectivity. The structural complexity of the fracture system at Castle Cove and the examples discussed indicate that this is not straightforward in the Otway Basin. Fracture systems can act as baffles or conduits for primary hydrocarbon migration and can enhance (e.g. improve structural permeability from source to reservoir) or impede (e.g. seal failure due to structural permeability) fluid flow (Sibson, 1996; Aydin, 2000). Hydrocarbon prospectivity will be assessed based on the results of this study, with implications for similar structures in the eastern Otway Basin.

Rifting during the late Cretaceous resulted in normal faulting of the Castle Cove Fault and associated rollover folding, and led to the formation of Fracture Set 5. Similarly oriented normal faults in the eastern Otway Basin may have also formed rollover folds during extension, creating structural traps. The late Eocene to mid-Miocene experienced heating up to 90 °C as a result of up to 2 km of burial, which led to further maturation of source rocks and generation of hydrocarbons (Duddy, 1994; Duddy, 1997; Mehin and Link, 1997; Duddy, 2003). Mid-Eocene to Recent compression resulted in the reverse-reactivation of the Castle Cove Fault and the formation of Fracture Sets 7 and 8. During inversion of the fault, the large-scale hanging wall anticline was tightened and amplified. The extensive network of fractures and movement along the Castle Cove Fault would have improved structural permeability for hydrocarbon migration. Early rollover geometries may have provided sufficient structural traps for fluids if seals were not breached by fractures. However, the amplification of these structures as anticlinal folds likely post-dates the main episode of hydrocarbon generation and migration.

A study by Holford et al. (2010) suggested that hydrocarbon potential exists in areas that have experienced Neogene to Recent compression and where maximum post-depositional temperatures currently occur, e.g. the Minerva Anticline. However, erosion in the Otway Ranges has removed between 1.5 and 2.5 km of stratigraphy since the mid-Cretaceous (Duddy, 2003). Considering that the Otway Ranges have experienced significant erosion and cooling, it is likely that source rock maturation and hydrocarbon generation has ceased. Holford et al. (2010) also attribute exploration success to the timing of trap formation relative to the timing of generation and migration of hydrocarbons. In the case of the Castle Cove Fault, unless early rollover geometries acted sufficient traps, it is likely that anticlinal trap development post-dated the generation and migration of hydrocarbons.

Other influences on hydrocarbon prospectivity that should also be considered include the hydraulic properties of fractures, fracture connectivity, host rock porosity and permeability, and diagenetic history; however, these are beyond the scope of this paper. Despite the ubiquity of inverted structures, investigations of the spatial arrangement of fractures around reverse-reactivated faults are limited, with even fewer studies producing detailed structural reconstructions. This study highlights the need to conduct careful reconstruction of the structural histories of fault zones that experienced complex reactivation histories when attempting to define off-fault fluid flow properties.

6. Conclusions

In this paper, we investigated and documented the geometries and relative chronologies of natural fractures adjacent to the Castle Cove Fault in the onshore eastern Otway Basin. A total of 11 fracture sets were identified at Castle Cove. Fracture Sets 5 and 7 are the two most abundant fracture sets and are interpreted to be geometrically related to the Castle Cove Fault, together with Fracture Set 8. The fracture system mapped in this study reveals a complex tectonic history recording both regional and local perturbations in stress:

- Rifting during late Cretaceous NW–SE extension resulted in the reactivation and propagation of an early Cretaceous normal fault to form the Castle Cove Fault. The geometry of the fault, which is interpreted to be listric, led to rollover folding and associated synthetic and antithetic fault growth. The formation of Fracture Set 5 has been attributed to the initiation of the Castle Cove Fault.
- The upper Eocene to mid-Miocene experienced heating that led to further maturation of source rocks and generation of hydrocarbons. The Castle Cove Fault was reactivated as a reverse fault

during late Miocene to Pliocene NW–SE directed compression. During inversion of the fault, the rollover fold in the hanging wall was tightened and amplified to form a large-scale anticline.

- Non-coaxial inversion during anticlinal folding resulted in the formation of Fracture Set 7. Reverse-reactivation of the Castle Cove Fault and anticlinal folding also led to the formation of Fracture Set 8. The small number of fractures recording NW–SE compression suggests that strain was mainly accommodated by anticline folding in the hanging wall adjacent to the fault.
- The remaining fracture sets likely formed in response to local stresses at Castle Cove.

The results of this study show that at least three fracture sets (Fracture Sets 5, 7 and 8) at Castle Cove are geometrically related to the Castle Cove Fault. Therefore, the Castle Cove Fault damage zone is characterised by three fracture sets at Castle Cove. The remaining fracture sets likely formed in response to significant local stress regimes. In addition, we have demonstrated that rollover folding may have acted as structural traps if seals were not breached by fractures, while anticlinal folding likely post-dated the second phase of hydrocarbon migration.

Acknowledgements

This research forms part of a PhD project supported by the Australian Research Council [Discovery Project DP160101158] and through an Australian Government Research Training Program Scholarship. This study was also funded by scholarships from the Petroleum Exploration Society of Australia and the Australian Petroleum Production and Exploration Association. David Tassone is acknowledged for his contribution to data collection and field mapping. Field assistants James Hall, Hugo Burgin, Rowan Hansberry, and Lachlan Furness are gratefully acknowledged for their contribution. The S3 research group at the University of Adelaide and Ian Duddy are thanked for insightful discussions on this research topic. We thank Mike Hall and Paul Gillespie for their constructive comments and Toru Takeshita for handling the manuscript and providing feedback. This forms TRaX record 403.

References

Ameen, M. S., and Cosgrove, J. W. 1990. A kinematic analysis of meso-fractures from Studland Bay, Dorset. Proceedings of the Geologists' Association 101, 303-314. doi: 10.1016/S0016-7878(08)80164-2.

Anderson, E. M. 1951. The Dynamics of Faulting and Dyke Formation with Applications to Britain. 2. Oliver and Boyd, Edinburgh.

Aydin, A. 2000. Fractures, faults, and hydrocarbon entrapment, migration and flow. Marine and Petroleum Geology 17, 797-814. doi: 10.1016/S0264-8172(00)00020-9.

Belayneh, M., and Cosgrove, J. W. 2004. Fracture-pattern variations around a major fold and their implications regarding fracture prediction using limited data: an example from the Bristol Channel Basin. Geological Society, London, Special Publications 231, 89-102. doi: 10.1144/gsl.sp.2004.231.01.06.

Bell, J. S. 1996. In situ stresses in sedimentary rocks (part 2): Applications of stress measurements. Geoscience Canada 23, 135-153. doi.

Boreham, C. J., Hope, J. M., Jackson, P., Davenport, R., Earl, K. L., Edwards, D. S., Logan, G. A., and Krassay, A. A. 2004. Gas-oil-source correlations in the Otway Basin, southern Australia. In Boult, P. J., Johns, D. R., and Lang, S. C. (Ed.) Eastern Australian Basins Symposium II. Petroleum Exploration Society of Australia Special Publication, pp. 97-106

Caine, J. S., Evans, J. P., and Forster, C. B. 1996. Fault zone architecture and permeability structure. Geology 24, 1025-1028. doi: 10.1130/0091-7613(1996)024<1025:fzaaps>2.3.co;2.

Cooper, G. T. 1995. Seismic structure and extensional development of the eastern Otway Basin-Torquay Embayment. APPEA Journal 35, 436-450.

Cooper, G. T., and Hill, C. K. 1997. Cross-section balancing and thermochronological analysis of the Mesozoic development of the eastern Otway Basin. Journal of the Australian Petroleum Production and Exploration Association 37, 390-413.

Cooper, M. A., and Williams, G. D. 1989. Inversion Tectonics. vol. 44. Geological Society Special Publication, London.

Cooper, M. A., Weissenberger, J., Knight, I., Hostad, D., Gillespie, D., Williams, H., Burden, E., Porter-Chaudhry, J., Rae, D., and Clark, E. 2001. Basin evolution in western Newfoundland: New insights from hydrocarbon exploration. AAPG Bulletin 85, 393-418.

Cooper, M. A., and Warren, M. J. 2010. The geometric characteristics, genesis and petroleum significance of inversion structures. Geological Society, London, Special Publications 335, 827-846. doi: 10.1144/sp335.33.

Cummings, A. M., Hillis, R. R., and Tingate, P. R. 2004. New perspectives on the structural evolution of the Bass Basin: implications for petroleum prospectivity. In Boult, P. J., Johns, D. R., and Lang, S. C. (Ed.) Eastern Australian Basins Symposium II. Petroleum Exploration Society of Australia Special Publication, pp. 133-149

Davis, G. H., Reynolds, S. J., and Kluth, C. F. 2011. Structural Geology of Rocks and Regions. Wiley.

Dickinson, J. A., Wallace, M. W., Holdgate, G. R., Gallagher, S. J., and Thomas, L. 2002. Origin and Timing of the Miocene-Pliocene Unconformity in Southeast Australia. Journal of Sedimentary Research 72, 288-303.

Duddy, I. R. 1994. The Otway Basin: Thermal, Structural, Tectonic and Hydrocarbon Generation Histories. NGMA/PESA Otway Basin Symposium, Melbourne. pp. 35-42.

Duddy, I. R. 1997. Focusing exploration in the Otway Basin: Understanding timing of source rock maturation. Journal of the Australian Petroleum Production and Exploration Association 35, 178-191.

Duddy, I. R. 2002. The Otway Basin: Geology, Sedimentology, Diagenesis, AFTA Thermal History Reconstruction and Hydrocarbon Prospectivity. Field Trip Guide prepared for the National Centre for Petroleum Geology and Geophysics, Adelaide. Geotrack International Pty. Ltd.

Duddy, I. R. 2003. Mesozoic: A time of change in teconic regime. In Birch, W. D. (Ed.) Geology of Victoria. GSA Special Publication 23, pp. 239-286

Dula, W. F. 1991. Geometric models of listric normal faults and rollover folds. AAPG Bulletin 75, 1609-1625.

Edwards, D. S., Struckmeyer, H. I. M., Bradshaw, M. T., and Skinner, J. E. 1999. Geochemical characteristics of Australia's southern margin petroleum systems. The APPEA Journal 39, 297-321. doi: 10.1071/AJ98017.

Edwards, J., Leonard, J. G., Pettifer, G. R., and McDonald, P. A. 1996. Colac 1:250000 Map Geological Report. Report 98. Geological Survey.

Engelder, T., and Peacock, D. C. P. 2001. Joint development normal to regional compression during flexural-flow folding: the Lilstock buttress anticline, Somerset, England. Journal of Structural Geology 23, 259-277. doi: 10.1016/S0191-8141(00)00095-X.

Etheridge, M. A., Branson, J. C., and Stuart-Smith, P. G. 1985. Extensional basin-forming structures in Bass Strait and their importance for hydrocarbon exploration. APPEA Journal 25, 344-361.

Faulkner, D. R., Jackson, C. A. L., Lunn, R. J., Schlische, R. W., Shipton, Z. K., Wibberley, C. A. J., and Withjack, M. O. 2010. A review of recent developments concerning the structure, mechanics and fluid flow properties of fault zones. Journal of Structural Geology 32, 1557-1575. doi: 10.1016/j.jsg.2010.06.009.

Finlayson, D. M., Johnstone, D. W., Owen, A. J., and Wake-Dyster, K. D. 1996. Deep seismic images and the tectonic framework of early rifting in the Otway Basin, Australian southern margin. Tectonophysics 264, 137-152. doi: 10.1016/S0040-1951(96)00123-0.

Geary, G. C., and Reid, I. S. A. 1998. Hydrocarbon prospectivity of the offshore eastern Otway Basin, Victoria, for the 1998 acreage release. Victorian Initiative for Minerals and Petroleum Report 55. Department of Natural Resources and Environment.

Geological Survey of Victoria 1995. The stratigraphy, structure, geophysics and hydrocarbon potential of the Eastern Otway Basin. 103. Geological Survey of Victoria.

Hall, M., and Keetley, J. 2009. Otway Basin: stratigraphic and tectonic framework. GeoScience Victoria 3D Victoria Report 2. Department of Primary Industries. Victoria.

Hancock, P. L. 1985. Brittle microtectonics: principles and practice. Journal of Structural Geology 7, 437-457. doi: 10.1016/0191-8141(85)90048-3.

Hayward, A. B., and Graham, R. H. 1989. Some geometrical characteristics of inversion. Geological Society, London, Special Publications 44, 17-39. doi: 10.1144/gsl.sp.1989.044.01.03.

Hill, K. A., Finlayson, D. M., Hill, K. C., Perincek, D., and Finlayson, B. 1994. The Otway Basin: pre-drift tectonics. NGMA/PESA Otway Basin Symposium, Melbourne. pp. 43-48.

Hill, K. A., Finlayson, D. M., Hill, K. C., and Cooper, G. T. 1995a. Mesozoic tectonics of the Otway Basin: the legacy of Gondwana and the active Pacific margin- a review and ongoing research. Journal of the Australian Petroleum Production and Exploration Association 35, 467-493.

Hill, K. C., Hill, K. A., Cooper, G. T., O'Sullivan, A. J., O'Sullivan, P. B., and Richardson, M. J. 1995b. Inversion around the Bass Basin, SE Australia. Geological Society, London, Special Publications 88, 525-547. doi: 10.1144/gsl.sp.1995.088.01.27.

Hillis, R. R., Sandiford, M., Reynolds, S. D., and Quigley, M. C. 2008. Present-day stresses, seismicity and Neogene-to-Recent tectonics of Australia's 'passive' margins: intraplate deformation controlled by plate boundary forces. Geological Society, London, Special Publications 306, 71-90. doi: 10.1144/sp306.3.

Holford, P., Tuitt, A. K., Hillis, R. R., Green, P. F., Stoker, M. S., Duddy, I. R., Sandiford, M., and Tassone, D. R. 2014. Cenozoic deformation in the Otway Basin, southern Australian margin: implications for the origin and nature of post-breakup compression at rifted margins. Basin Research 26, 10-37. doi: 10.1111/bre.12035.

Holford, S. P., Hillis, R. R., Duddy, I. R., Green, P. F., Tuitt, A. K., and Stoker, M. S. 2010. Impacts of Neogene-Recent compressional deformation and uplift on hydrocarbon prospectivity of the 'passive' southern Australian margin. APPEA Journal 50, 267-284.

Holford, S. P., Hillis, R. R., Duddy, I. R., Green, P. F., Stoker, M. S., Tuitt, A. G., Backé, G., Tassone, D. R., and Macdonald, J. D. 2011. Cenozoic post-breakup compressional deformation and exhumation of the southern Australian margin. Journal of the Australian Petroleum Production and Exploration Association 51, 613-638.

Jorand, C., Krassey, A., and Hall, L. 2010. Otway Basin Hot Sedimentary Aquifers and SEEBASETM Study. Geoscience Victoria 3D Report 7. Department of Primary Industries.

Kim, Y.-S., Peacock, D. C. P., and Sanderson, D. J. 2004. Fault damage zones. Journal of Structural Geology 26, 503-517. doi: 10.1016/j.jsg.2003.08.002.

Kim, Y.-S., and Sanderson, D. J. 2005. The relationship between displacement and length of faults: a review. Earth-Science Reviews 68, 317-334. doi: 10.1016/j.earscirev.2004.06.003.

King, P. R., and Funnell, R. H. 1997. Petroleum systems of the Taranaki Basin, New Zealand: a review. Proceedings of the Petroleum Systems of SE Asia and Australasia Conference, 155-170.

Knipe, R. J., Jones, G., and Fisher, Q. J. 1998. Faulting, fault sealing and fluid flow in hydrocarbon reservoirs: an introduction. Geological Society, London, Special Publications 147, vii-xxi. doi: 10.1144/gsl.sp.1998.147.01.01.

Krassay, A. A., Cathro, D. L., and Ryan, D. J. 2004. A regional tectonostratigraphic framework for the Otway Basin. In Boult, P. J., Johns, D. R., and Lang, S. C. (Ed.) Eastern Australian Basins Symposium II. Petroleum Exploration Society of Australia Special Publication, pp. 97-106

Laubach, S. E., and Diaz-Tushman, K. 2009. Laurentian palaeostress trajectories and ephemeral fracture permeability, Cambrian Eriboll Formation sandstones west of the Moine Thrust Zone, NW Scotland. Journal of the Geological Society 166, 349-362. doi: 10.1144/0016-76492008-061.

Letouzey, J., Colletta, B., Vially, R., and Chermette, J. C. 1995. Evolution of salt related structures in compressional settings. In Jackson, M. P. A., Roberts, D. G., and Snelson, S. (Ed.) Salt tectonics: a global perspective. AAPG Memoir 65. pp. 41-60

Lister, G. S., Etheridge, M. A., and Symonds, P. A. 1991. Detachment models for the formation of passive continental margins. Tectonics 10, 1038-1064. doi: 10.1029/90TC01007.

Lyon, P., Boult, P. J., Hillis, R. R., and Mildren, S. D. 2005. Sealing by Shale Gouge and Subsequent Seal Breach by Reactivation: A Case Study of the Zema Prospect, Otway Basin. In Boult, P. J., and Kaldi, J. (Ed.) Evaluating fault and cap rock seals. AAPG Hedberg Series, no. 2, pp. 179-197

Lyon, P. J., Boult, P. J., Hillis, R. R., and Bierbrauer, K. 2007. Basement controls on fault development in the Penola Trough, Otway Basin, and implications for fault-bounded hydrocarbon traps. Australian Journal of Earth Sciences 54, 675-689. doi: 10.1080/08120090701305228.

Macgregor, D. S. 1995. Hydrocarbon habitat and classification of inverted rift basins. Geological Society, London, Special Publications 88, 83-93. doi: 10.1144/gsl.sp.1995.088.01.06.

McGrath, A. G., and Davison, I. 1995. Damage zone geometry around fault tips. Journal of Structural Geology 17, 1011-1024. doi: 10.1016/0191-8141(94)00116-H.

Mehin, K., and Link, A. G. 1997. Late Cretaceous source rocks offshore Otway Basin, Victoria and South Australia. Victorian Initiative for Minerals and Petroleum Report 43. Department of Natural Resources and Environment.

Miller, J. M., Norvick, M. S., and Wilson, C. J. L. 2002. Basement controls on rifting and the associated formation of ocean transform faults—Cretaceous continental extension of the southern margin of Australia. Tectonophysics 359, 131-155. doi: 10.1016/S0040-1951(02)00508-5.

Moore, D. H. 2002. Basement Basin Relationships in the Otway Basin, Victoria, Australia. Victorian Initiative for Minerals and Petroleum Report 79. Department of Natural Resources and Environment.

Mynatt, I., Seyum, S., and Pollard, D. D. 2009. Fracture initiation, development, and reactivation in folded sedimentary rocks at Raplee Ridge, UT. Journal of Structural Geology 31, 1100-1113. doi: 10.1016/j.jsg.2009.06.003.

Nelson, E. J., Hillis, R. R., Sandiford, M., Reynolds, S. D., and Mildren, S. D. 2006. Present-day state-of-stress of southeast Australia. APPEA Journal 46, 283-305.

Norvick, M. S., and Smith, M. A. 2001. Mapping the plate tectonic reconstruction of southern and southeastern Australia and implications for petroleum systems. Journal of the Australian Petroleum Production and Exploration Association 41, 15-35.

O'Brien, G. W., Reeves, C. V., Milligan, P. R., Morse, M. P., Alexander, E. M., Willcox, J. B., Yunxuan, Z., Finlayson, D. M., and Brodie, R. C. 1994. New ideas on the rifting history and structural architecture of the Western Otway Basin-Evidence from the integration of aeromagnetic, gravity and seismic data. APPEA Journal 34, 529-554.

Partridge, A. D. 2001. Revised stratigraphy of the Sherbrook group, Otway Basin. Eastern Australasian Basins Symposium, a Refocused Energy Perspective for the Future, pp. 455-465.

Perincek, D., Cockshell, C. D., Finlayson, D. M., and Hill, K. A. 1994a. The Otway Basin: Early Cretaceous rifting to Miocene strike-slip. NGMA/PESA Otway Basin Symposium, Melbourne. pp. 27-33.

Perincek, D., Simons, B., and Pettifer, G. R. 1994b. The tectonic framework, and associated play types of the Western Otway Basin, Victoria, Australia. APPEA Journal 34, 460-477.

Perincek, D., and Cockshell, C. D. 1995. The Otway Basin: Early Cretaceous rifting to Neogene inversion. Journal of the Australian Petroleum Production and Exploration Association 35, 451-466.

Rawnsley, K. D., Peacock, D. C. P., Rives, T., and Petit, J. P. 1998. Joints in the Mesozoic sediments around the Bristol Channel Basin. Journal of Structural Geology 20, 1641-1661. doi: 10.1016/S0191-8141(98)00070-4.

Reilly, C., Nicol, A., and Walsh, J. 2016. Importance of pre-existing fault size for the evolution of an inverted fault system. Geological Society, London, Special Publications 439. doi: 10.1144/sp439.2.

Schneider, C. L., Hill, K. C., and Hoffman, N. 2004. Compressional growth of the Minerva Anticline, Otway Basin, Southeast Australia–evidence of oblique rifting. APPEA Journal 44, 463-480.

Sibson, R. H. 1985. A note on fault reactivation. Journal of Structural Geology 7, 751-754. doi: 10.1016/0191-8141(85)90150-6.

Sibson, R. H. 1995. Selective fault reactivation during basin inversion: potential for fluid redistribution through fault-valve action. Geological Society, London, Special Publications 88, 3-19. doi: 10.1144/gsl.sp.1995.088.01.02.

Sibson, R. H. 1996. Structural permeability of fluid-driven fault-fracture meshes. Journal of Structural Geology 18, 1031-1042. doi: 10.1016/0191-8141(96)00032-6.

Stacey, A. R., Mitchell, C. H., Struckmeyer, H. I. M., and Totterdell, J. M. 2013. Geology and Hydrocarbon Prospectivity of the Deepwater Otway and Sorell Basins, Offshore Southeastern Australia. Record 2013/02. Geoscience Australia. Canberra.

Stagg, H., Willcox, J., Needham, D., O'Brien, G., Cockshell, C., Hill, A., Thomas, B., and Hough, L. 1990. Basins of the Great Australian Bight region: geology and petroleum potential. Continental Margins Program folio 5. Bureau of Mineral Resources, Geology and Geophysics, Department of Mines and Energy. South Australia.

Stoneley, R. 1992. Review of the habitat of petroleum in the Wessex Basin: Implications for exploration. Proceedings of the Ussher Society 8, 1-6.

Tassone, D. R., Holford, S. P., Duddy, I. R., Green, P. F., and Hillis, R. R. 2014. Quantifying Cretaceous–Cenozoic exhumation in the Otway Basin, southeastern Australia, using sonic transit time data: Implications for conventional and unconventional hydrocarbon prospectivity. AAPG Bulletin 98, 67-117. doi: 10.1306/04011312111.

Tassone, D. R., Holford, S. P., King, R., Tingay, M. R. P., and Hillis, R. R. 2017. Contemporary stress and neotectonics in the Otway Basin, southeastern Australia. Geological Society, London, Special Publications 458. doi: 10.1144/sp458.10.

Turner, J. P., and Williams, G. A. 2004. Sedimentary basin inversion and intra-plate shortening. Earth-Science Reviews 65, 277-304. doi: 10.1016/j.earscirev.2003.10.002.

Underhill, J. R., and Stoneley, R. 1998. Introduction to the development, evolution and petroleum geology of the Wessex Basin. Geological Society, London, Special Publications 133, 1-18. doi: 10.1144/gsl.sp.1998.133.01.01.

Veevers, J. J. 2000. Change of tectono-stratigraphic regime in the Australian plate during the 99 Ma (mid-Cretaceous) and 43 Ma (mid-Eocene) swerves of the Pacific. Geology 28, 47-50. doi: 10.1130/0091-7613(2000)28<47:cotrit>2.0.co;2.

Welch, M. J., Davies, R. K., Knipe, R. J., and Tueckmantel, C. 2009. A dynamic model for fault nucleation and propagation in a mechanically layered section. Tectonophysics 474, 473-492. doi: 10.1016/j.tecto.2009.04.025.

Wibberley, C. A. J., Yielding, G., and Di Toro, G. 2008. Recent advances in the understanding of fault zone internal structure: A review. Geological Society Special Publication 299, 5-33. doi: 10.1144/SP299.2.

Willcox, J. B., and Stagg, H. M. J. 1990. Australia's southern margin: a product of oblique extension. Tectonophysics 173, 269-281. doi: 10.1016/0040-1951(90)90223-U.

Withjack, M. O., Olsen, P. E., and Schlische, R. W. 1995. Tectonic evolution of the Fundy rift basin, Canada: Evidence of extension and shortening during passive margin development. Tectonics 14, 390-405. doi: 10.1029/94TC03087.

CHAPTER 3

This chapter is published as:

Debenham, N., Farrell, N. J. C., Holford, S. P., King, R. C., Healy, D. 2019. Spatial distribution of micrometre-scale porosity and permeability across the damage zone of a reverse-reactivated normal fault in a tight sandstone: insights from the Otway Basin, SE Australia. *Basin Research*, 1-19.

STATEMENT OF AUTHORSHIP

Title of Paper	Spatial distribution of micrometre-scale porosity and permeability across the damage zone of a reverse-reactivated normal fault in a tight sandstone: insights from the Otway Basin, SE Australia
Publication Status	☒ Published ☐ Accepted for publication ☐ Submitted for publication ☐ Unpublished and unsubmitted work written in manuscript style
Publication Details	Debenham, N., Farrell, N. J. C., Holford, S. P., King, R. C., and Healy, D. 2019. Spatial distribution of micrometre-scale porosity and permeability across the damage zone of a reverse-reactivated normal fault in a tight sandstone: insights from the Otway Basin, SE Australia. Basin Research, 0-19. doi: 10.1111/bre.12345.

Principal Author

Name of Principal Author (Candidate)	Natalie Debenham		
Contribution to the Paper	Project design, fieldwork, sample preparation, laboratory analysis, processing and interpreting, manuscript design and composition, creation of figures, manuscript revisions, acted as corresponding author.		
Overall Percentage	80%		
Certification	This paper reports on original research I conducted during the period of my Higher Degree by Research candidature and is not subject to any obligations or contractual agreements with a third party that would constrain its inclusion in this thesis. I am the primary author of this paper.		
Signature		Date	13/02/2019

Co-Author Contributions

By signing the Statement of Authorship, each author certifies that:

i. the candidate's stated contribution to the publication is accurate (as detailed above);
ii. permission is granted for the candidate in include the publication in the thesis; and
iii. the sum of all co-author contributions is equal to 100% less the candidate's stated contribution.

Name of Co-Author	Natalie Farrell		
Contribution to the Paper	Assistance with sample preparation, assistance with laboratory analysis, assistance with interpretation, assistance with manuscript design and composition, manuscript review.		
Signature		Date	21/02/2019

Name of Co-Author	Simon Holford		
Contribution to the Paper	Assistance with project design, assistance with manuscript design and composition, assistance with interpretation, manuscript review.		
Signature		Date	13/02/2019

Name of Co-Author	Rosalind King		
Contribution to the Paper	Assistance with project design, assistance with manuscript design and composition, assistance with interpretation, manuscript review.		
Signature		Date	13/02/2019

Name of Co-Author	David Healy		
Contribution to the Paper	Assistance with laboratory analysis, assistance with manuscript design and composition, provided coding for rose diagrams, manuscript review.		
Signature		Date	15/02/2019

ABSTRACT

Knowledge of the permeability structure of fault-bearing reservoir rocks is fundamental for developing robust hydrocarbon exploration and fluid monitoring strategies. Studies often describe the permeability structure of low porosity host rocks that have experienced simple tectonic histories, while investigations of the influence of faults with multiple-slip histories on the permeability structure of porous clastic rocks are limited. We present results from an integrated petrophysical, microstructural, and mineralogical investigation of the Eumeralla Formation (a tight volcanogenic sandstone) within the hanging wall of the Castle Cove Fault which strikes 30 km NE–SW in the Otway Basin, southeast Australia. This late Jurassic to Cenozoic-age basin has experienced multiple phases of extension and compression. Core plugs and thin sections oriented relative to the fault plane were sampled from the hanging wall at distances of up to 225 m from the Castle Cove Fault plane. As the fault plane is approached, connected porosities increase by approximately 10% (17% at 225 m to 24% at 0.5 m) and permeabilities increase by two orders of magnitude (from 0.04 mD at 225 m to 1.26 mD at 0.5 m). Backscattered Scanning Electron Microscope analysis shows that microstructural changes due to faulting have enhanced the micrometre-scale permeability structure of the Eumeralla Formation. These microstructural changes have been attributed to the formation of microfractures and destruction of original pore-lining chlorite morphology as a result of fault deformation. Complex deformation, i.e. formation of macrofractures, variably oriented microfractures, and a hanging wall anticline, associated with normal faulting and subsequent reverse faulting, has significantly influenced the off-fault fluid flow properties of the protolith. However, despite enhancement of the host rock permeability structure, the Eumeralla Formation at Castle Cove is still considered a tight sandstone. Our study shows that high-resolution integrated analyses of the host rock are critical for describing the micrometre-scale permeability structure of reservoir rocks with high porosities, low permeabilities, and abundant clays that have experienced complex deformation.

1. Introduction

Fault zones and their related fracture patterns control fluid flow within the Earth's brittle upper crust at a range of scales (Caine et al. 1996). Knowledge of the permeability structure of brittle fault zones is critical for predicting hydrocarbon migration, accumulation, and leakage in sedimentary basins (e.g. Knipe et al. 1998; Aydin 2000), fluid migration in geothermal plays and hydrothermal ore deposits (e.g. Sibson et al. 1975; Rowland and Sibson 2004; Fairley 2009), fluid migration in water aquifers (e.g. Bense and Person 2006; Folch and Mas-Pla 2008), and for identifying potential sites for deep-waste storage repositories for the disposal of CO_2 and radioactive waste (e.g. Bredehoeft 1997; Streit and Hillis 2004). In recent years, there has been considerable work on the structure, mechanics, and fluid flow properties of fault zones and their associated permeability structures (e.g Faulkner et al. 2010; Bense et al. 2013). However, challenges associated with predicting fluid flow in the sub-surface arise due to the complex nature of fault zones and the variable impact deformation induced features have on fluid flow.

Deformation associated with faulting can either enhance or impede the permeability of fault-bearing rocks (Caine et al. 1996; Fisher and Knipe 1998; Faulkner et al. 2010). Within a fault damage zone, macrofractures and dilational deformation bands will increase permeability (Fossen et al. 2007; Faulkner et al. 2010; Bense et al. 2013). Fluid flow within these deformation-related permeability structures occurs cyclically in a transient manner, in response to fluid pressure fluctuations associated with earthquake slip (Sibson 1994; Woodcock et al. 2007). In contrast, compartmentalisation during faulting and the

formation of compaction and shear deformation bands can impede fluid flow within a fault damage zone (Fossen et al. 2007; Bense et al. 2013). While outcrop-scale structures can be accounted for during conventional reservoir modelling of fault zone permeability structure, micrometre-scale heterogeneities are often overlooked.

At the micrometre-scale, the petrophysical properties of a host rock can also be significantly altered as a result of faulting-related deformation. For instance, the magnitude of permeability can be degraded due to pore collapse, grain crushing, and cement precipitation during deformation (Fisher and Knipe 1998; Bense et al. 2013; Farrell and Healy 2017). Alternatively, the magnitude of permeability can be enhanced through the formation of grain-scale microfractures (Anders et al. 2014) and changes in grain morphology through dilation and disaggregation (Bense et al. 2013). As effective pressure increases (i.e. increasing depth in the crust), it is predicted that microfractures will exert a greater influence on permeability than macrofractures (Nara et al. 2011). Therefore, understanding how rocks deform at the micrometre-scale is fundamental for defining off-fault fluid flow properties of reservoir rocks in sedimentary basins.

A large number of previous studies have focussed on the permeability structure of faulted porous rocks in outcrops which have experienced simple tectonic histories (i.e. faults with a single-slip history; e.g. Antonellini and Aydin 1994; Shipton et al. 2002; Farrell et al. 2014; Bauer et al. 2015); however, few studies have investigated the influence of complex faults (i.e. faults with a multiple-slip history) on the micrometre-scale permeability structure of porous clastic rocks in sedimentary basins. Motivated by this, we aim to understand the influence of inverted faults with multiple-slip histories on the micrometre-scale permeability structure of sandstones. We focus on an inverted fault that was initiated as a normal fault and was subsequently reactivated as a reverse fault. We identify the faulting-related deformation processes that control the permeability structure of the protolith within the hanging wall of the fault. Furthermore, we describe the influence of this deformation on fluid flow adjacent to the fault and the implications this has on diagenesis.

To address the aims of this study, we describe the relationships between the petrophysical, microstructural, and mineralogical properties of a porous sandstone with low permeabilities (i.e. a tight sandstone) within the damage zone of a reverse-reactivated fault, the Castle Cove Fault in the Otway Basin, southeast Australia. This study area provides an excellent opportunity to address the influence of a reverse-reactivated normal fault on the micrometre-scale permeability structure of porous sandstones. High-resolution analyses have been undertaken on core-plugs and thin sections oriented relative to the fault plane, at distances of up to 225 m from the Castle Cove Fault. We show that connected porosity, permeability, and pore connectivity increase as the fault plane is approached (from 225 to 0.5 m from the fault plane), where fracturing occurs at a range of scales and pore-lining clays become disaggregated as a result of fault-related deformation. Enhancement of the micrometre-scale permeability structure is attributed to these faulting-induced microstructural and clay morphology changes within the hanging wall.

2. Geological background

The Otway Basin is a late Jurassic to Cenozoic sedimentary basin located on the south-eastern margin of Australia (Fig. 1). The basin formed following Tithonian rifting and continental breakup of Australia and Antarctica (Norvick and Smith 2001), and has since experienced a complex tectonic history with multiple phases of extension and compression (Perincek et al. 1994; Krassay et al. 2004; Schneider et al. 2004; Tassone et al. 2012; Holford et al. 2014; Tassone et al. 2017; Debenham et al. 2018). In the eastern Otway Basin, a series of NE–SW striking faults intersect the coastline (Fig. 1). Many of these faults are

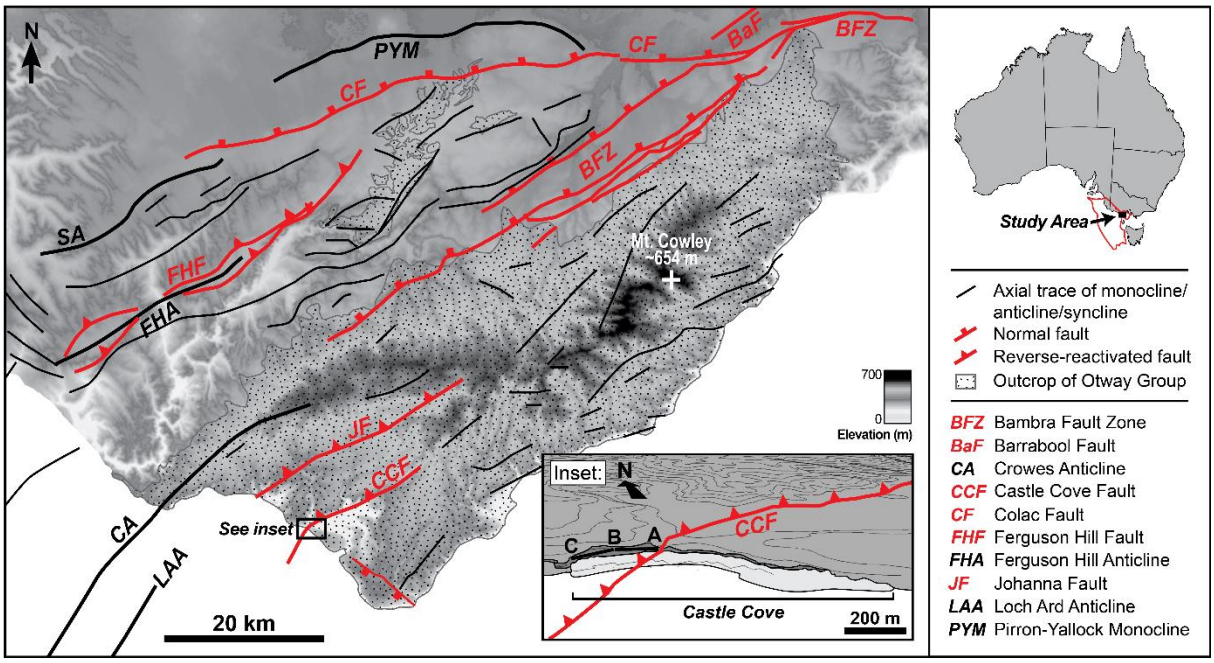

Figure 1. A structural map showing neotectonic structural discontinuities in the eastern Otway Basin, modified after Debenham et al. (2018). The map is underlain by a digital elevation model from Geoscience Australia. Note that the elevation scale only applies to the structural map. The inset illustrates the location of Castle Cove and the strike of the Castle Cove Fault. The locations of the A–B and B–C cross sections are also shown (Fig. 2).

well-exposed within the youngest unit of the Aptian to Albian Eumeralla Formation. The Eumeralla Formation is a fine- to medium-grained, compositionally immature volcanogenic sandstone with thin coal seams. The Eumeralla Formation was deposited in a high-energy, fluvial environment with braided channels, flood plains, and shallow lacustrine deposits (Krassay et al. 2004). Contemporaneous volcanism to the east of the basin formed the main source of volcanogenic clastics to the Eumeralla Formation (Duddy 2003). The formation is lithologically variable and is characterised by different diagenetic zones of alteration (Duddy 2002; Duddy 2003). Pervasive diagenesis within the Eumeralla Formation has resulted in the significant destruction of porosity and permeability under moderate burial depths of less than 1500 m (Tassone et al. 2014). Intraformational seals and interbedded coal seams within the lower section of the formation are the source of hydrocarbon accumulations discovered within the eastern Otway Basin (Edwards et al. 1999; Boreham et al. 2004), and therefore this is an important interval for petroleum exploration.

This study is focussed on a well-exposed damage zone of the seismic-scale Castle Cove Fault, located in the eastern Otway Basin, Australia (Fig. 1 and Fig. 2). The Castle Cove Fault is a NE–SW striking, reverse-reactivated normal fault with a strike length of approximately 30 km (Debenham et al. 2018). The fault plane steeply dips to the northwest (Debenham et al. 2018). The fault was initiated as a normal fault in the late Cretaceous and reactivated as a reverse fault during the late Miocene to Pliocene (Duddy 1994; Edwards et al. 1996; Holford et al. 2014; Debenham et al. 2018). Fault throw is estimated to be between 250 m to 1000 m of vertical displacement (Debenham et al. 2018).

The fault core is not exposed at the surface, but the damage zone is well-exposed and extends more than 300 m in the hanging wall to inaccessible cliff exposures (Debenham et al. 2018). Within 25 m of the fault plane, a zone of maximum macrofracture density within the fault damage zone has been identified by Debenham et al. (2018). Structural mapping also identified 11 macrofracture sets within the fault damage zone at Castle Cove, with three Andersonian shear macrofracture sets geometrically related to

the Castle Cove Fault; (1) late Cretaceous normal movement of the Castle Cove Fault resulted in the formation of the first and most spatially extensive fracture set, (2) non-coaxial inversion during anticlinal folding resulted in the formation of the second fracture set, and (3) fault reverse-reactivation and anticlinal folding also resulted in the formation of the final fracture set (Debenham et al. 2018). At Castle Cove, a series of small-scale synthetic and antithetic faults, with similar and opposite geometries to the Castle Cove Fault respectively, have been identified in the hanging wall damage zone (Debenham et al. 2018).

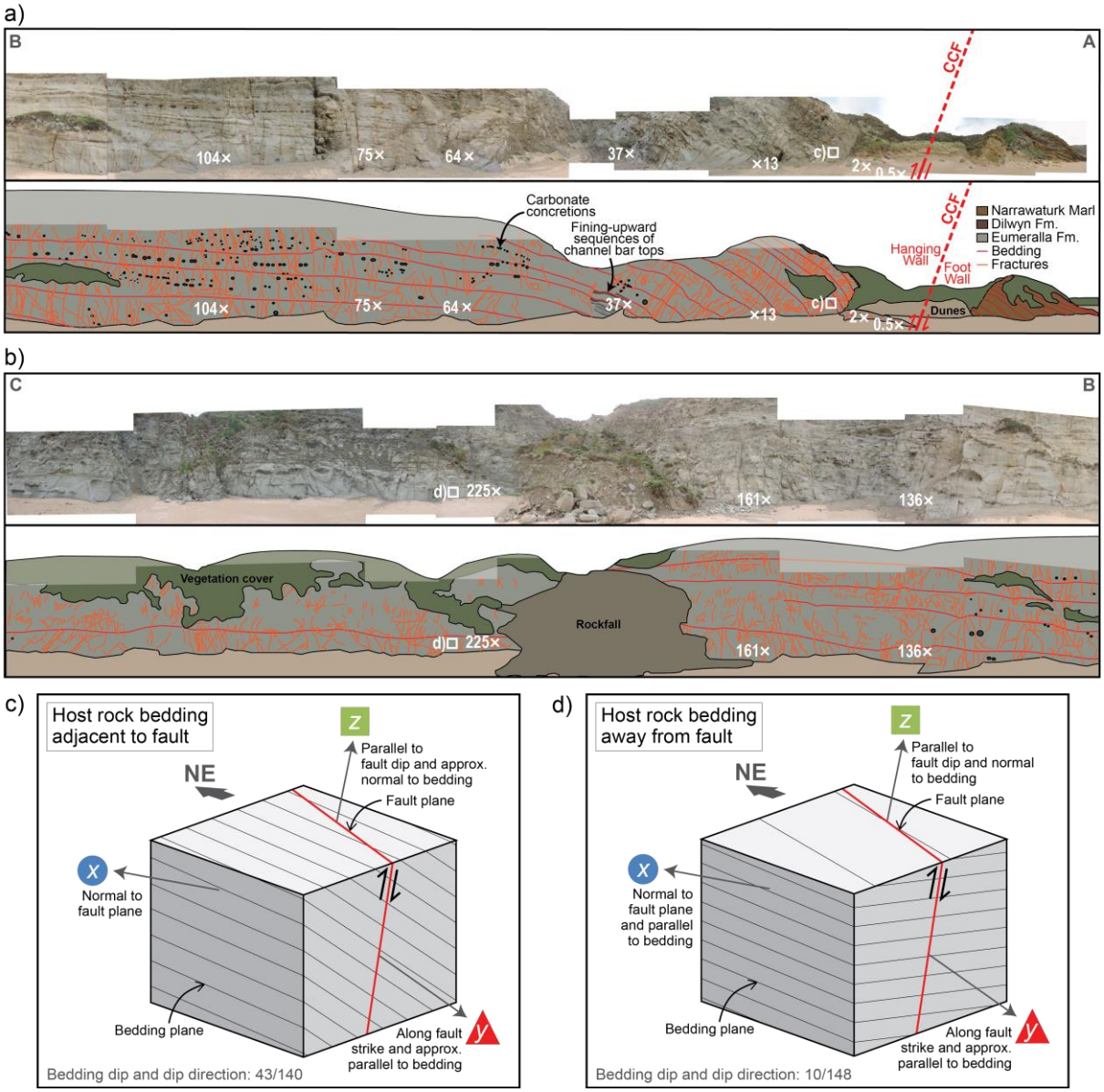

Figure 2. Photo and schematic diagram of the study site at Castle Cove in the Otway Basin, southeast Australia, after Debenham et al. (2018). (a) Photo and schematic diagram of A–B cross-section (Fig. 1) of the cliff exposures at Castle Cove. Sample locations are indicated by white crosses. Red lines indicate bedding planes and orange lines indicate macrofractures visible in the photos. (b) Photo and schematic diagram of B–C cross-section (Fig. 1). (c) Example of the host rock bedding orientation at distance from the Castle Cove Fault, and (d) example of the host rock bedding orientation adjacent to the fault.

3. Methods

3.1 Samples

Ten oriented sample blocks (approximately 20 cm cubes) were collected within the hanging wall at distances between 0.5 to 225 m from the Castle Cove Fault plane (Fig. 3). Sample blocks were carefully removed in a manner that preserves the natural appearance of the rock exposure. Macroscopic sedimentary features (such as channels, dewatering structures, and changes in lithology that could be observed at the outcrop-scale) were avoided during sampling as this study only focusses on micrometre-scale host rock petrophysical properties. Macrofractures, i.e. fractures that are visible at the outcrop scale, and deformation bands were also avoided for this reason. Micrometre-scale features (such as laminations and bedding) could not be avoided. Sample blocks collected between 64 m and 225 m were sampled from the same stratigraphic bed, however samples closer to the fault (<64 m) were collected in different stratigraphic levels as the beds were tilted up to 43° within a hanging wall anticline (greater than 80 m in half-wavelength; Fig. 2). All sample blocks were sampled from the same facies within approximately 30 m of stratigraphic height to ensure comparable host rock properties.

From the oriented sample blocks, core plugs were drilled in three orientations with respect to the fault plane, i.e. normal to the fault plane (*x*), along fault strike (*y*), and parallel to fault dip (*z*; Fig. 3). A total of 78 core plugs were drilled, which comprised of two to three repeat core plugs drilled in each orientation for each sample block. The core plugs were approximately 2.55 cm in diameter and between 2.66 cm and 8.12 cm in length. The dimensions of the core plugs were used to calculate bulk volume.

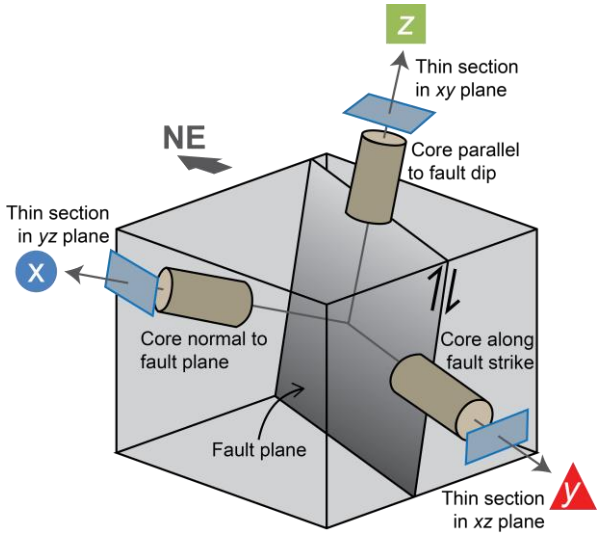

Figure 3. A schematic diagram of the oriented sample blocks with core plug and thin section orientations, relative to the Castle Cove Fault plane. Modified after Farrell et al. (2014).

3.2 Porosity

A helium injection porosimeter was used to measure the connected porosity (i.e. effective porosity) of the core plugs at room temperature. Following two temperature and pressure calibration runs, helium was injected into a reference volume and stabilised at 100 psi. Next, the helium was expanded into a chamber containing the core plugs and the pressure was recorded. The equilibrium pressure of the two chambers was derived. Based on Boyle's Law of expansion, the direct grain volume of the core plugs can

be calculated. To find the pore volume (v_{pore}), the grain volume (v_{grain}) was subtracted from the bulk volume of the core plugs. Porosity (φ, percentage) was calculated using Equation 1:

$$\varphi = 100 * v_{pore}/(v_{pore} + v_{grain}) \quad (1)$$

3.3 Permeability

A nitrogen permeameter was used to measure steady state permeability of the core plugs at ambient pressures (<2.8 MPa). A meniscus flowmeter attachment was used for core plugs with low permeabilities. Permeability (k, millidarcies) was calculated using a modified Darcy equation, which is expressed by Equation 2:

$$k = 2\mu Q\left(\frac{L}{A}\right)/(P_1^2 - P_2^2) \quad (2)$$

where μ = dynamic viscosity of the gas (centipoise), Q = gas flow rate (cm3/s), L = core plug length (cm), A = core plug cross-sectional area (cm^2), and P_1 = input gas pressure and P_2 = output gas pressure (atmospheres). Average gas pressure (P_{mean}) was calculated using a range of P_1 and P_2 values for each core plug test. To correct the permeability for gas slippage or the Klinkenberg Effect, Klinkenberg-corrected permeability was measured by plotting k against $1/P_{mean}$. The Klinkenberg-corrected permeability value was identified where the line of best fit intersected the y-axis of the plot. This value represents the permeability at which the gas is compressed by infinite pressure and acts as a liquid (Klinkenberg 1941). If the line of best fit had a coefficient of determination (R^2) that was < 0.9, the permeability was re-analysed.

3.4 Pore throat size and connectivity

Connected pore throat size and pore connectivity were determined using a Micromeritics AutoPore IV 9500 mercury intrusion porosimeter. Mercury Injection Capillary Pressure (MICP) analyses were performed on small offcuts of the core plugs. A non-wetting phase, i.e. mercury, was injected in increasing pressure increments (2 to 60,000 psi) into the sample blocks. The volume of mercury injected at each pressure increment was recorded. Pore throat size and size distributions were determined using a series of calculations described by Webb (2001). Mercury injection curves were used to determine the threshold injection pressure of mercury (Katz and Thompson 1987), which is the pressure at which the mercury forms interconnected pathways between pores, i.e. pore connectivity.

3.5 Grain size

For all 10 samples, replicate analysis of grain size was undertaken on a LS13320 Laser Diffraction Particle Size Analyser following the methods of Blott et al. (2004). Sub-samples from core plugs were dried and disaggregated through gentle physical disaggregation with a mortar and pestle, followed by ultrasonication with a chemical dispersant solution to reduce flocculation (Blott et al. 2004). The powdered samples were loaded into a holding tank and sonicated to reduce obscuration. The samples interact with an illuminating beam (Fourier lens) that focuses the scattered light. An array of photodetectors records the scattered light intensity patterns and calculates size distributions (volumes) of grains between 0.04 to 2000 μm.

3.6 Thin section analysis

Thin sections were prepared in each orientation with respect to the fault plane (Fig. 3) for mineralogical and microstructural analysis on a FEI Quanta 600 backscattered Scanning Electron Microscope (bSEM) with mineral liberation analysis capabilities and a Nikon Eclipse LV100 POL petrographic microscope, respectively. Mineral liberation analysis provided quantitative estimates of the mineralogical composition of the thin sections. Thin sections were injected with blue epoxy to highlight pore space and microstructures. The density of microfractures was calculated from thin sections oriented in the *xz* plane (Fig. 3). Within each thin section, three areas (totalling 16.37 mm²) were selected at random and the number of microfractures was counted. This yields the microfracture density in terms of the number of microfractures per squared millimetre (mm²). The microfractures were consistently counted at 25x total magnification. Microfractures were predominately counted in quartz grains as they have less fracture anisotropy in comparison to feldspars, and is therefore considered to be a good proxy for measuring grain-scale damage (c.f. Mitchell and Faulkner 2009). As microfractures were primarily counted in quartz grains, the number of fractures per mm2 will be an underestimate of the total number of fractures per mm2 within the host rock. While the density of microfractures is expected to be an underestimate, the method will identify microfracture density changes relative to distance to the fault. Microfracture type (i.e. intragranular, transgranular, and grain boundary), cement (i.e. open or sealed) and orientations were also recorded.

4. Results

4.1 Core plug porosity

Connected porosities were measured from 78 oriented core plugs sampled from 10 sample blocks of the faulted sandstone. Overall, mean porosities increase by 10% in the hanging wall as the fault plane is approached, from 17% at distance to the fault (225 m) to 24% adjacent to the fault (0.5 m); within 0.5 m of the fault plane, high porosities of up to 27% are recorded within the hanging wall. Core plug porosities are plotted relative to distance from the fault plane (Fig. 4a). Porosities are shown for three orientations (*x*, *y*, and *z*) relative to the fault plane. At distance from the fault plane (225 m and 161 m), similar porosities are recorded. This is followed by steady increase in porosities from 161 m to 75 m. There is a peak in porosities at 75 m to 64 m which drops off to lower porosities at 37 m before increasing again toward the fault plane (Fig. 4a) in the zone of maximum fracture density identified within the damage zone (Debenham et al. 2018).

4.2 Core plug permeability

Steady state permeabilities were measured from 76 oriented core plugs. Two core plugs were too short in length and consequently could not be used in this analysis. Mean permeabilities increase by two orders of magnitude from 0.04 mD at 225 m in the undeformed protolith to 1.26 mD at 0.5 m close to the fault plane. Within 0.5 m of the fault plane, permeabilities of up to 2.92 mD are recorded. Core plug permeabilities are plotted on a logarithmic scale relative to distance from the Castle Cove Fault plane (Fig. 4b). Permeabilities are shown for three orientations (*x*, *y*, and *z*) relative to the Castle Cove Fault plane orientation. Permeabilities show a dispersed data spread for each core plug orientation at different distances to the fault plane, which may be attributed to micrometre-scale heterogeneities within the core plugs, such as microscopic sedimentary features that could not be avoided during sample collection. Permeabilities increase steadily from 225 m to 64 m from the fault plane, and a peak is reached at 64 m.

Similar to the porosity trend, permeabilities drop off to lower values at 37 m before increasing again toward the fault plane (Fig. 4b) in the zone of maximum fracture density.

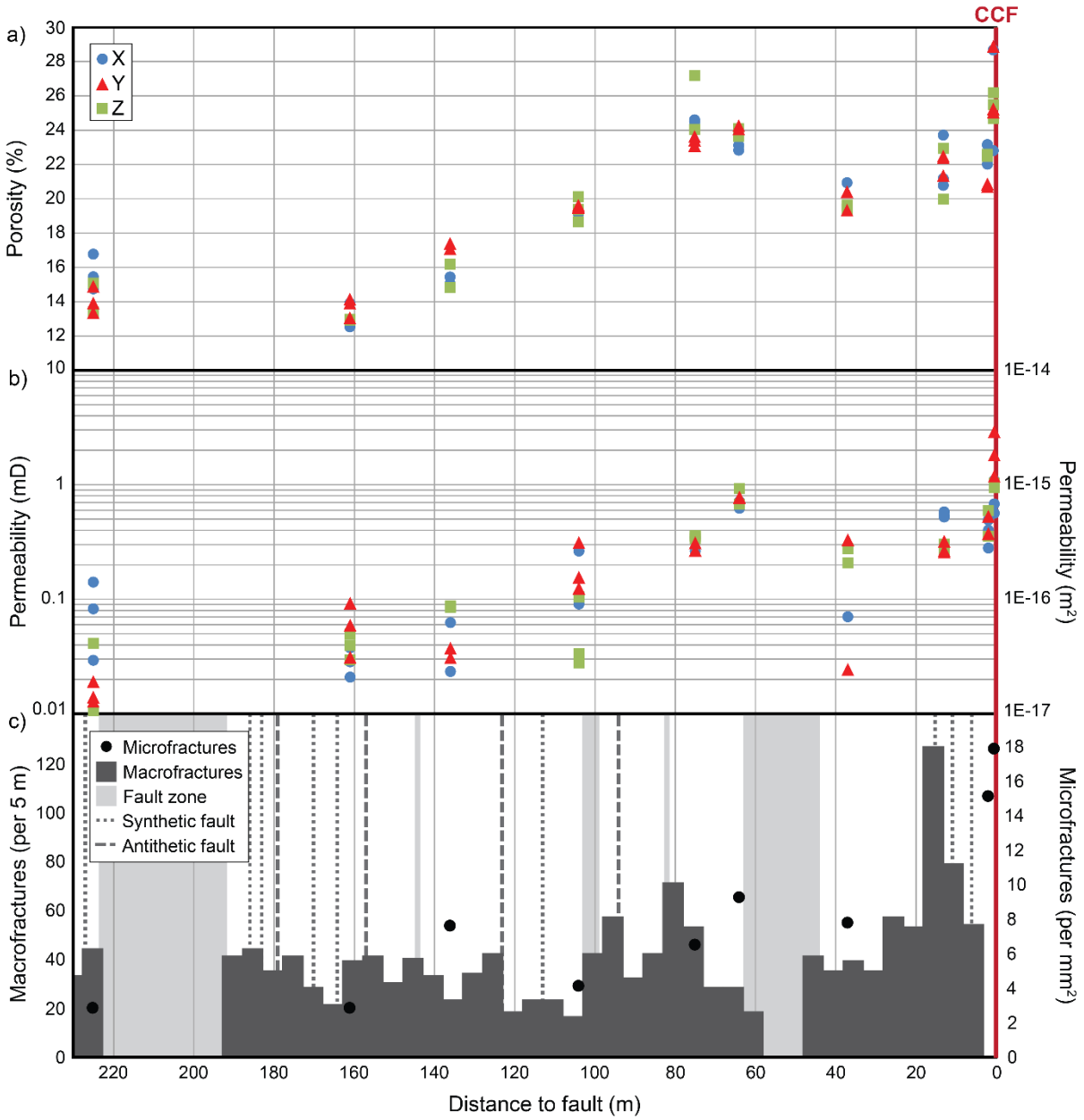

Figure 4. Changes in porosity, permeability, and fracture densities within the hanging wall relative to distance to the Castle Cove Fault (CCF). The *x*-axis has been reversed to represent the configuration of the outcrop, i.e. 230 m is northwest and 0 m is southeast. (a) Core plug porosities from three orientations (*x*, *y*, and *z*) relative to the Castle Cove Fault plane. (b) Klinkenberg-corrected, core plug permeabilities from three orientations (*x*, *y*, and *z*) relative to the Castle Cove Fault plane. Permeability is plotted on a logarithmic scale. (c) Macrofracture densities binned into 5 m intervals from Debenham et al. (2018) and microfracture densities (per mm^2, this study) relative to distance from the fault. The grey shaded areas indicate areas where there is no outcrop and fractures could not be counted due to the presence of potential fault zones. Locations of synthetic faults and antithetic faults are also shown.

The relative proportions of oriented core plug permeabilities have been plotted on a ternary plot (Fig. 5). At the greatest distance from the fault (225 m), there is minor permeability anisotropy with maximum permeability normal to the fault plane. The orientation of maximum permeability corresponds to sedimentary layers within the host rock. Permeabilities of the remaining samples are dispersed around

the centre point of the ternary plot and do not show any clear relationship to orientation. This indicates that the core plugs are relatively homogenous and do not have significant permeability anisotropy.

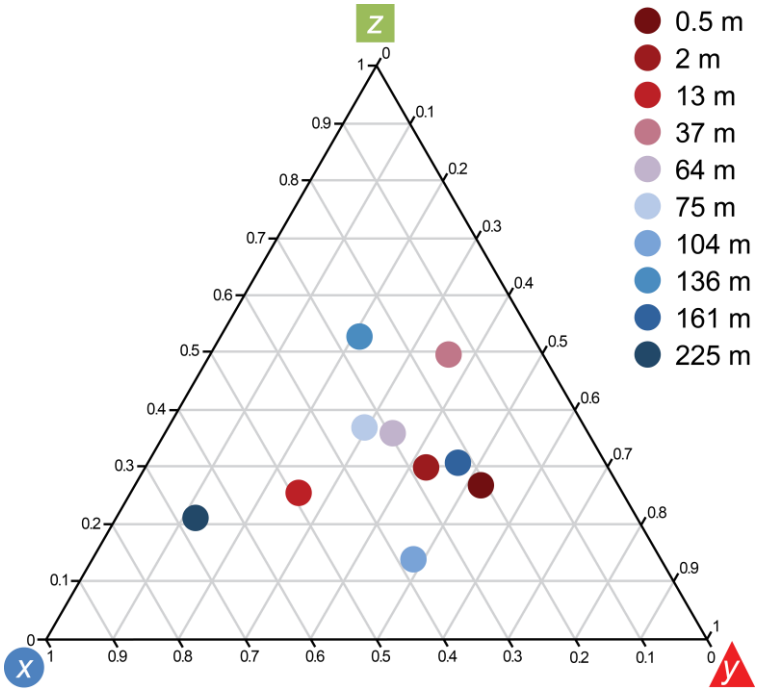

Figure 5. A triangle plot showing the ratios of mean core plug permeability. Core plugs in three orientations (*x*, *y*, and *z*) have been used for the identification of permeability anisotropy. Different colours indicate samples collected at different distances from the Castle Cove Fault.

4.3 Relationship between porosity and permeability

Core plug permeabilities are plotted on a logarithmic scale relative to core plug porosities (Fig. 6). There is a strong positive correlation (R^2 = 0.76) between connected porosity and permeability (Fig. 6). Porosity and permeability correlate with distance from the fault plane. For instance, core plugs taken from samples within the hanging wall anticline (less than 104 m from the fault plane) cluster in the higher porosity and permeability range than core plugs taken from samples beyond the hanging wall anticline (more than 104 m from the fault plane; Fig. 6).

4.4 Pore throat size and connectivity

Pore throat sizes are plotted on a logarithmic scale relative to pore volume (Fig. 7a). Pore throat size distributions show a bimodal pattern with similar pore throat size peaks and pore volume frequencies in all samples; one peak includes pore throat sizes between 0.01–0.3 μm and a second peak between 0.3–1.5 μm (Fig. 7a). At distance from the Castle Cove Fault plane (more than 104 m), there are greater volumes of smaller pore throat sizes (<0.3 μm). Closer to the fault plane, there is a shift to greater volumes of larger pore throat sizes (>1 μm; Fig. 7a).

Mercury injection curves were used to determine the mercury threshold injection pressure in small offcuts of the core plugs. There is a strong negative correlation (R^2 = 0.62) between the threshold injection pressure of mercury and distance to the Castle Cove Fault plane; the threshold injection pressure decreases by one order of magnitude (from 216 psi to 56 psi) as the fault plane is approached (Fig. 7b). Therefore, less pressure is required to form connected pathways between pores and saturate samples closer to the fault plane. Therefore, connectivity is better in more deformed rocks closer to the fault plane.

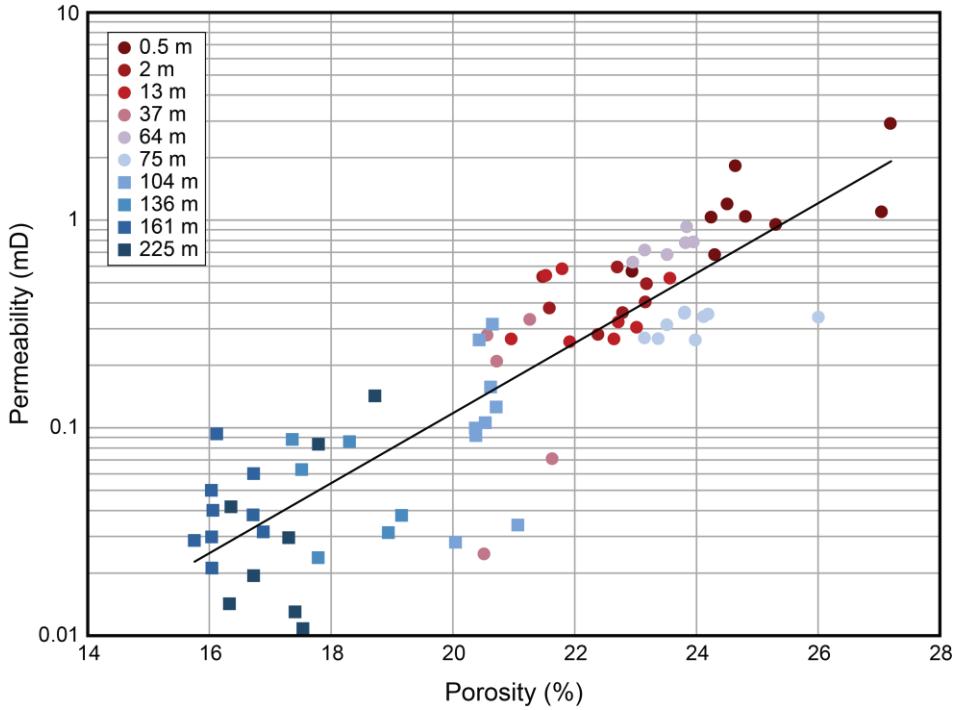

Figure 6. A cross plot of connected core plug porosity relative to core plug permeability. Permeability is plotted on a logarithmic scale. Different colours indicate samples collected at different distances from the Castle Cove Fault. Circles indicate samples collected within the Castle Cove Fault hanging wall anticline, whereas squares indicate samples collected beyond the hanging wall anticline. There is a strong positive correlation ($R^2 = 0.76$) between porosity and permeability.

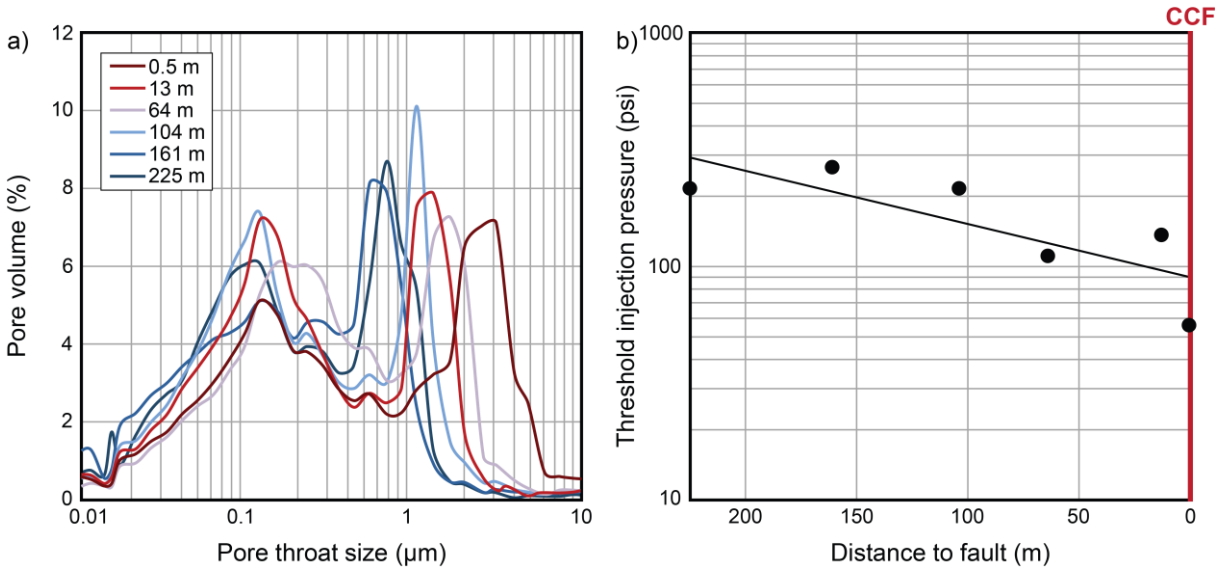

Figure 7. (a) Pore throat sizes plotted on a logarithmic scale relative to pore volume. Different colours indicate samples collected at different distances from the Castle Cove Fault. (b) The threshold injection pressure of mercury relative to distance to the Castle Cove Fault (CCF). Threshold injection pressure is plotted on a logarithmic scale. There is a strong negative correlation ($R^2 = 0.62$) between the threshold injection pressure of mercury and distance to the fault plane.

4.5 Grain size

Grain size distributions were measured from 10 core plug sub-samples using laser diffraction (Fig. 8a). The volumes of clay to coarse sand grains are plotted relative to distance to the Castle Cove Fault (Fig. 8b). There is an overall increase in the volume of clay (moderate, $R^2 = 0.44$), silt (moderate, $R^2 = 0.53$), and very-fine-sand (weak, $R^2 = 0.07$) grains (0.04–125 μm) in samples closer to the Castle Cove Fault, while there is an overall decrease in the volume of fine-sand (moderate, $R^2 = 0.44$), medium-sand (weak, R2 = 0.09), and coarse-sand (weak, $R^2 = 0.09$) grains (125–2000 μm) in samples away from the fault (Fig. 8b). The volume of different grain sizes is mostly consistent until <37 m from the fault plane where there is a peak in fine sand and a decrease in clays to very fine sands (Fig. 8b). While there is a weak to moderate linear relationship between the volumes of different grain size fractions relative to distance to the fault plane, these data indicate a progressive grain size reduction as the Castle Cove Fault plane is approached.

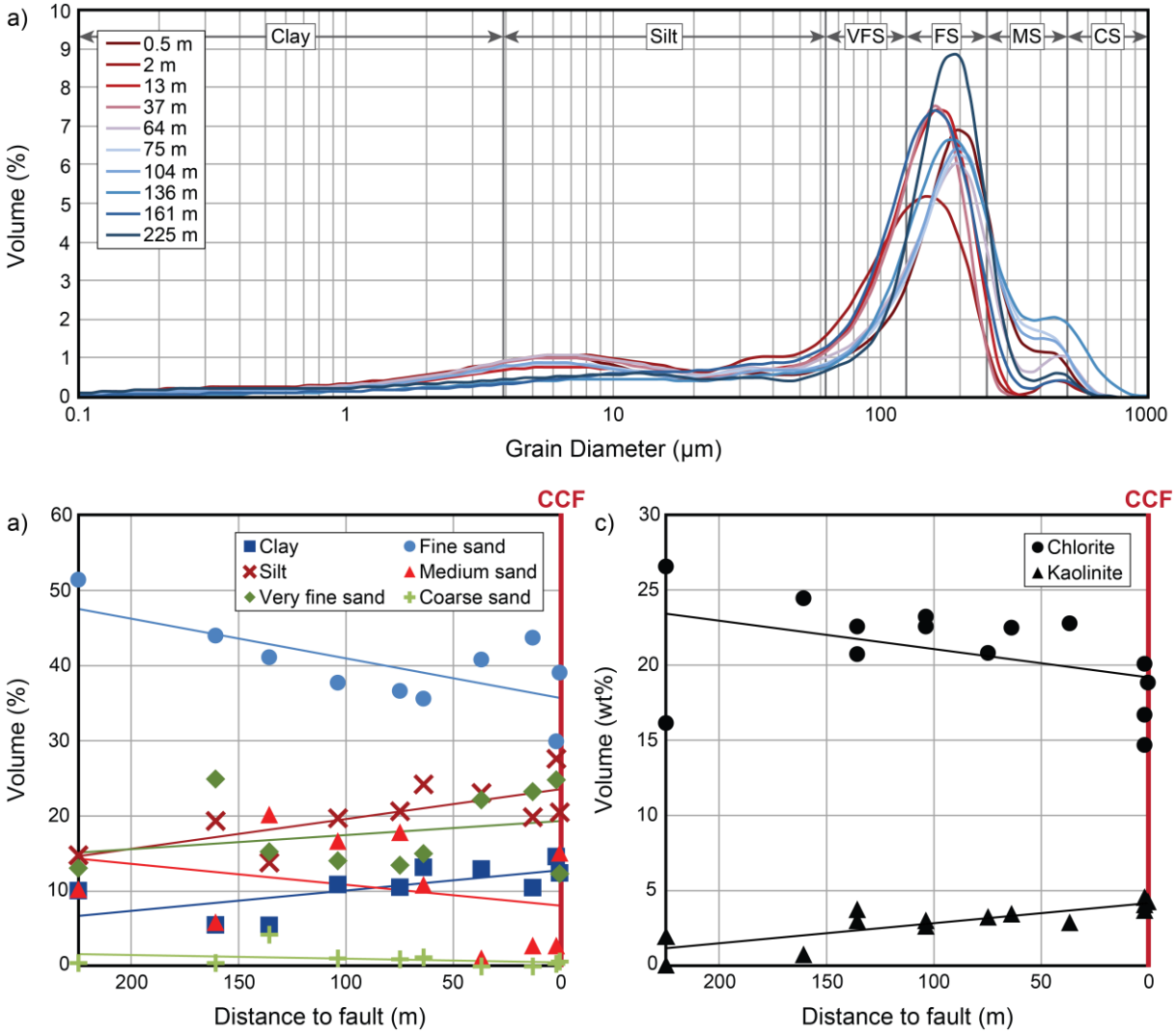

Figure 8. (a) Volume of grains relative to grain diameter identified in each sample. Different grain size (diameter) fractions are shown for clay, silt, very fine sand (VFS), fine sand (FS), medium sand (MS), and coarse sand (CS). (b) The volume of different grain sizes relative to distance to the Castle Cove Fault (CCF). Different symbols and colours indicate different grain sizes. (c) The volume of clays (chlorite and kaolinite) relative to distance to the Castle Cove Fault (CCF). Chlorite has a very weak negative correlation ($R^2 = 0.2$) with distance to the fault plane and kaolinite shows a strong positive correlation ($R^2 = 0.68$) with distance to the fault plane.

4.6 Mineralogical observations

Within the hanging wall of the Castle Cove Fault, the Eumeralla Formation is a fine- to very fine-grained volcanogenic sandstone that is moderately sorted and compositionally immature. Mineral liberation analysis indicated that all samples have a similar mineralogical composition. The framework grains are predominantly lath-shaped to sub-rounded albite (up to 48 wt%) and angular to sub-rounded quartz (up to 27 wt%). Other minerals include potassium feldspar (present as orthoclase), kaolinite, illite, muscovite, biotite, accessory minerals (such as apatite and rutile), and coal fragments. Volcanic rock fragments typical of the Eumeralla Formation are mostly altered to diagenetic clays (Duddy 2003; Tassone et al. 2014). Authigenic pore-lining chlorite (between 16–24 wt%) formed during early diagenesis is pervasive within all samples and the mean thickness of this lining is 10 μm. The pore-lining chlorite is characterised by two phases of crystallisation; a thick and poorly crystallised grain-coating chlorite that rims the grains, which transitions to a thin and well-crystallised euhedral pore-lining chlorite.

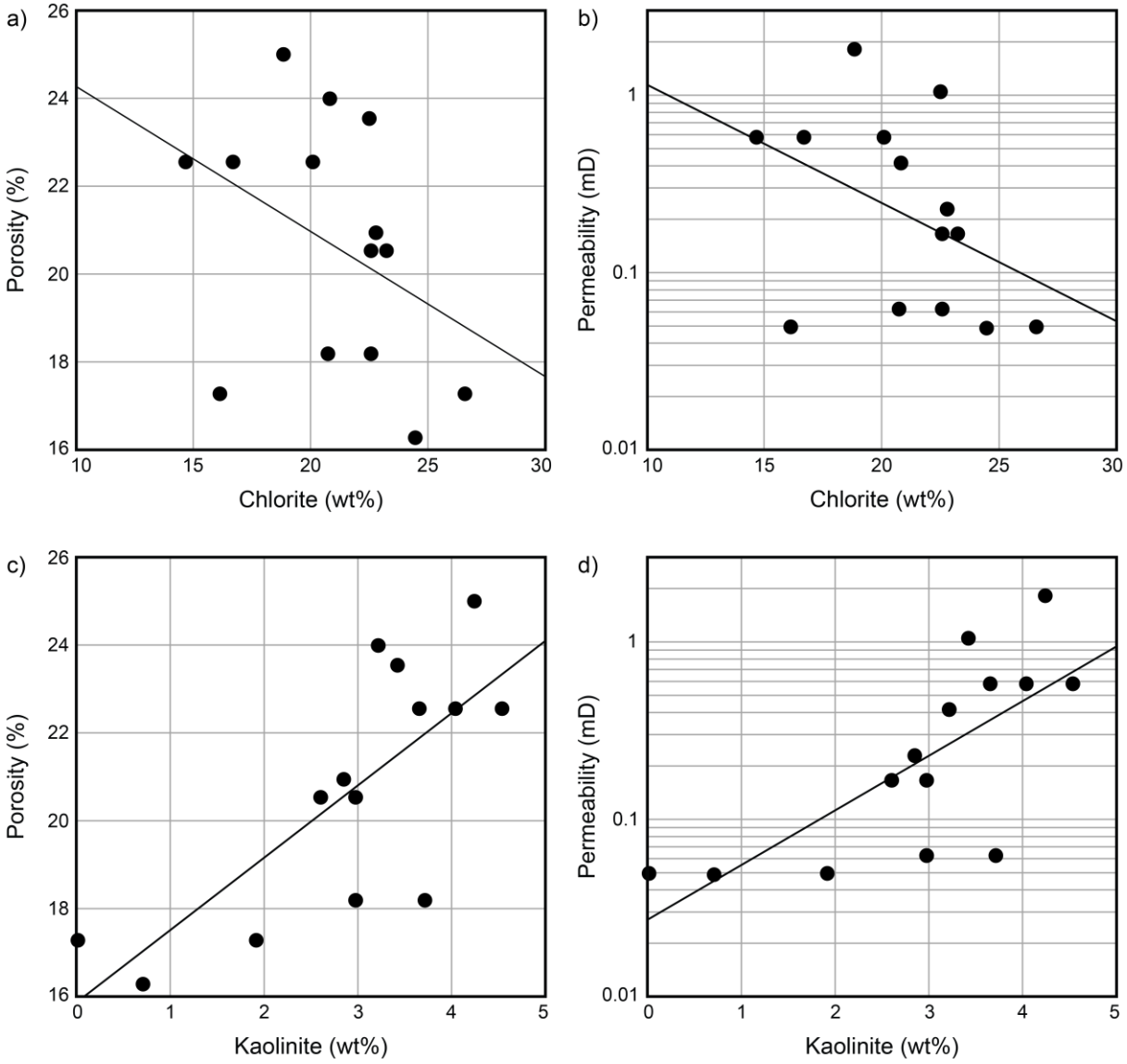

Figure 9. Relationship between volumes of clays relative to mean core plug porosity and permeability. Permeability is plotted on a logarithmic scale. (a) Chlorite relative to core plug porosity has a very weak negative correlation ($R^2 = 0.2$), and (b) chlorite relative to core plug permeability has a very weak negative correlation ($R^2 = 0.2$). (c) Kaolinite relative to core plug porosity has a strong positive correlation ($R^2 = 0.57$), and (d) kaolinite relative to core plug permeability has a strong positive correlation ($R^2 = 0.54$).

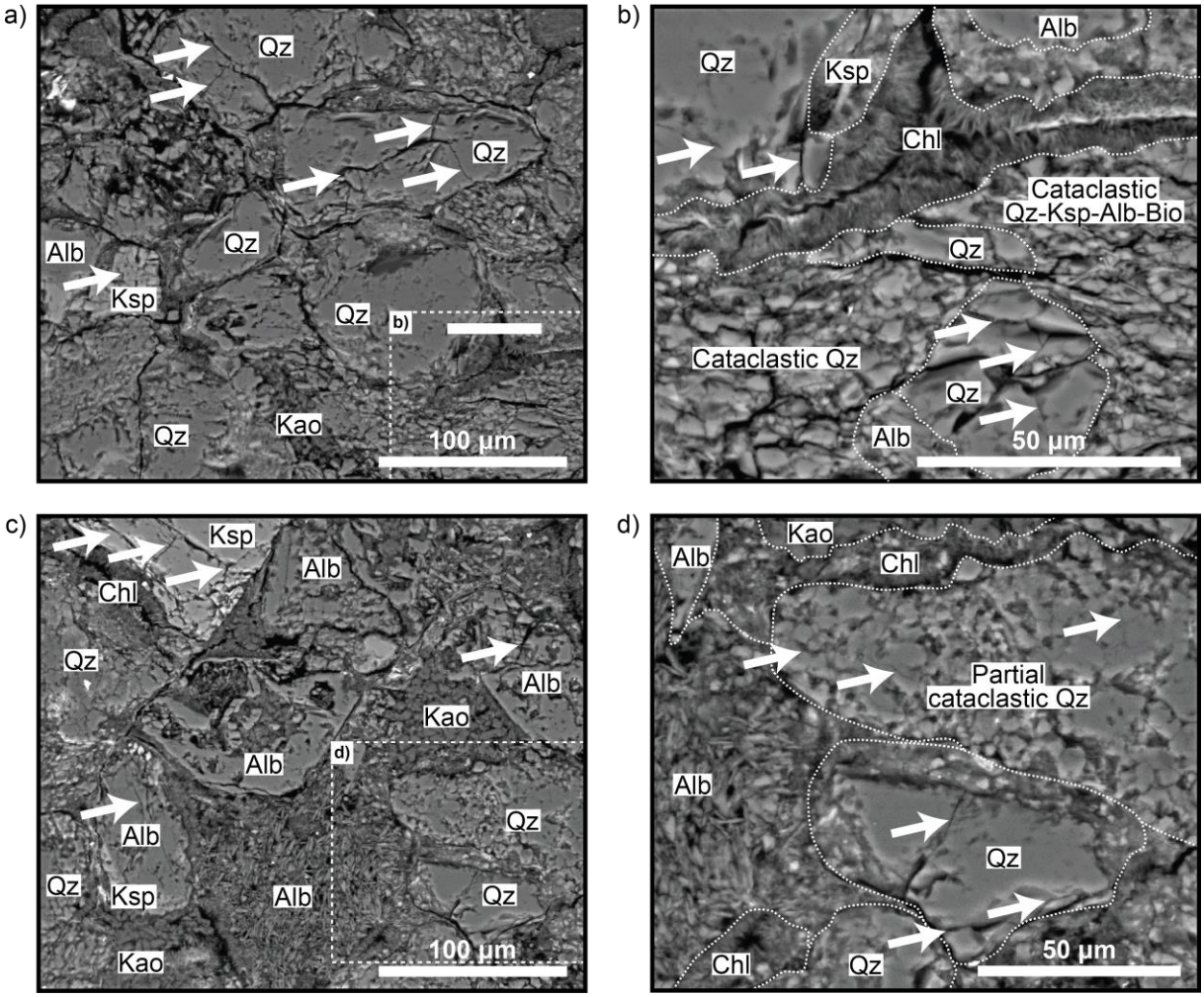

Figure 10. Backscattered SEM images of thin sections oriented in the *xz* plane at 2 m from the Castle Cove Fault plane. Larger grains of quartz and feldspar are deformed and fractured closer to the fault; examples of intragranular microfractures are indicated by the arrows. Evidence of cataclasis and subsequent grain size reduction, together with minor cataclasis of individual grains, is highlighted in (b) and (d). Diagenetic albitization and kaolinization of orthoclase is also evident in (b) and (d).

As the fault plane is approached, there is a change in the abundance of chlorite and kaolinite. For instance, chlorite decreases by approximately 4 wt% and kaolinite increases by approximately 2 wt% closer to the fault plane (Fig. 8c). While chlorite has a very weak negative correlation (R2 = 0.2) with distance to the fault plane, kaolinite shows a strong positive correlation ($R^2 = 0.68$) with distance (Fig. 8c). Similarly, chlorite has a very weak negative correlation (porosity and permeability, $R^2 = 0.2$; Fig. 9a and b), i.e. porosity and permeability decrease with an increase in chlorite, while kaolinite shows a strong positive correlation (porosity, $R^2 = 0.57$; permeability $R^2 = 0.54$; Fig. 9c and d), i.e. porosity and permeability increase with an increase in kaolinite.

Diagenetic dissolution and replacement of detrital feldspars and volcanogenic clastics by albite and clays has changed the original framework composition of the Eumeralla Formation. Diagenetic albitization and kaolinization of orthoclase is extensive and some orthoclase grains are only partially albitized in a complex "patchwork" pattern (Fig. 10c and 10d). Within partially albitized orthoclase grains, small patches of quartz occur as a product of albitization (e.g. Baccar et al. 1993). Some quartz grains are characterised by ragged textured characteristic of terminated quartz overgrowths (Fig. 11c). There is also evidence for minor quartz dissolution by the presence of small (approximately 5 µm), irregular-shaped pits and voids

that appear within detrital quartz grains. Within the quartz grains these occasionally coalesce to form larger voids and detached fragments of quartz. Orthoclase that has been kaolinized is evidenced by partial to full replacement of orthoclase grains by "books" of kaolinite.

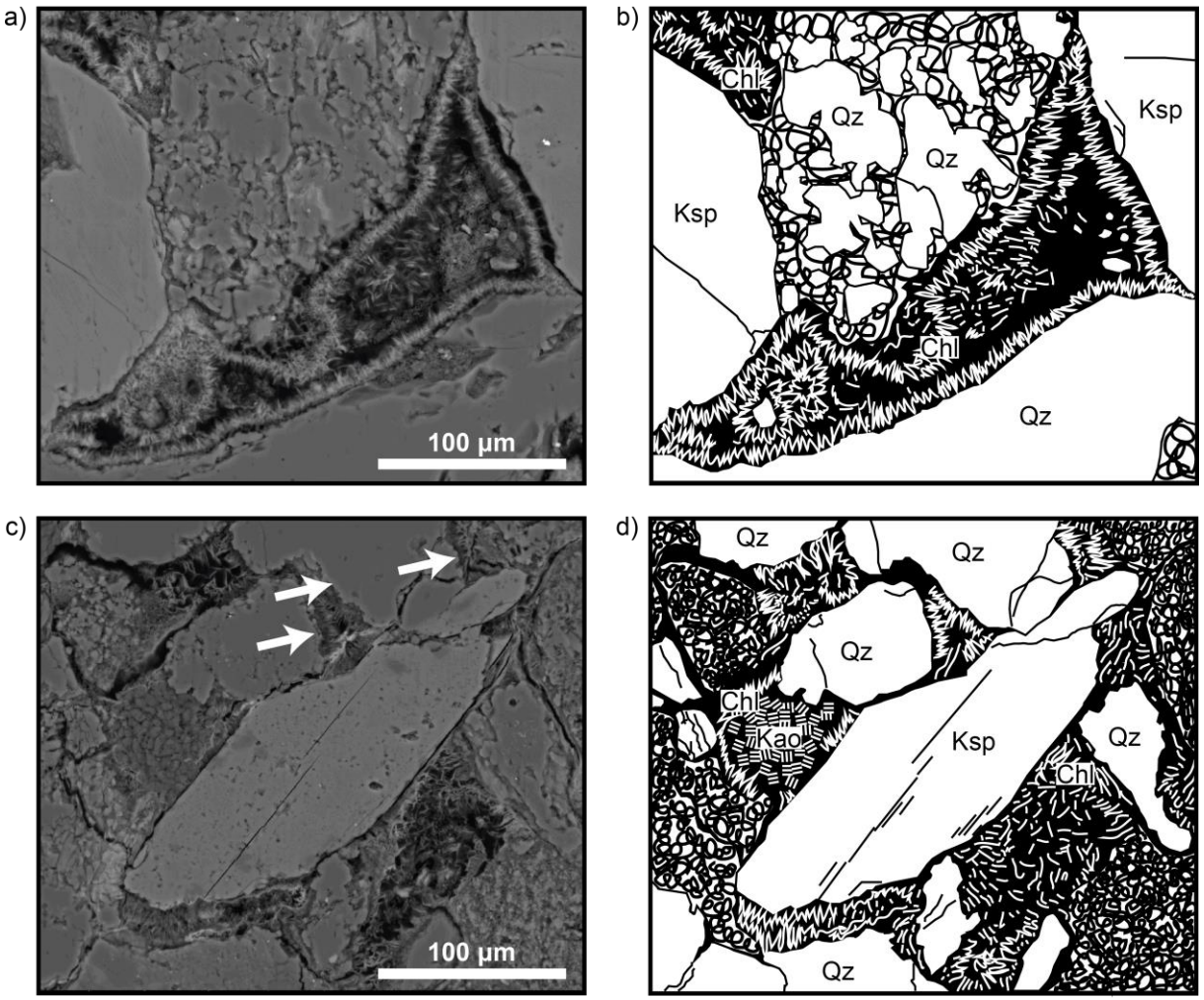

Figure 11. Backscattered SEM images of thin sections oriented in the xz plane, with schematic diagrams of the typical mineralogical and microstructural features identified within the Eumeralla Formation at Castle Cove. (a) Backscattered SEM images of 161 m from the Castle Cove Fault, and (b) schematic diagram of Fig. 11a showing well preserved intergranular porosity and filamentous pore-lining chlorite (Chl). Grains of quartz (Qz) and orthoclase (Ksp) have been identified. (c) Backscattered SEM images of 37 m from the Castle Cove Fault, and (d) schematic diagram of Fig. 11c showing a change in chlorite morphology (broken up and filling intergranular porosity) and increased microfractures within quartz and orthoclase grains. Terminated quartz overgrowth is present around some quartz grains. The diagenetic kaolinization of orthoclase in the form of kaolinite "books" (Kao) is also shown.

4.7 Microstructural observations

Microstructural features were assessed at high resolutions using bSEM imaging. Microstructural image analysis on thin sections indicate that microfractures within the Castle Cove Fault damage zone are opening-mode (Mode I) fractures, as opposed to shear fractures (Mode II) identified at the outcrop scale (i.e. macrofractures) by Debenham et al. (2018). This indicates a scale-dependence on the types of fractures that form within the Castle Cove Fault damage zone. Microstructural analysis identified three structural processes that may have influenced the porosity and permeability structure of the sandstones within the Castle Cove Fault hanging wall. These processes include disaggregation of pore-lining chlorite,

grain-scale cataclasis, and microfracturing (Fig. 10). Away from the fault, intergranular porosity is strongly preserved by pore-lining chlorite (Fig. 11a). However, closer to the fault the pore-lining chlorite is disaggregated and intergranular porosity is filled with chlorite plates (Fig. 11c). Closer to the fault there is also increased deformation and minor cataclasis of individual grains (Fig. 10). This may be controlling the progressive grain size reduction identified in laser diffraction particle size analysis.

Microstructural analysis showed a visual increase in microfracture densities closer to the Castle Cove Fault (Fig. 11), from 3 microfractures per mm^2 at 225 m from the fault plane to 18 microfractures per mm^2 at 0.5 m from the fault plane (Fig. 4c). In particular, larger grains of quartz and feldspar were deformed and fractured (Fig. 10 and Fig. 11) closer to the fault. The number of microfractures within each counting area was consistent within each sample. Due to the diagenetic albitization and kaolinization of orthoclase, there will be an underestimation of microfracture density as diagenesis may have overprinted early-formed microfractures. This is mostly avoided by the microfracture counting method used in this study, which predominantly uses quartz grains to identify microfracture density changes. There is a strong positive correlation between the density of microfractures and porosity ($R^2 = 0.54$; Fig. 12a) and the density of microfractures and permeability ($R^2 = 0.6$; Fig. 12b). Microfractures are typically intragranular and transgranular, and in transmitted light microfractures appear to be open and do not contain cements. Goethite has precipitated within a small number of wider, grain-boundary microfractures (greater than 10 μm). The orientations of the microfractures are typically variable within all samples (Fig. 13). Grains with breccia-like microfractures were attributed to grain crushing as a result of compaction or artificial processes, such as sample preparation, and were avoided in this study.

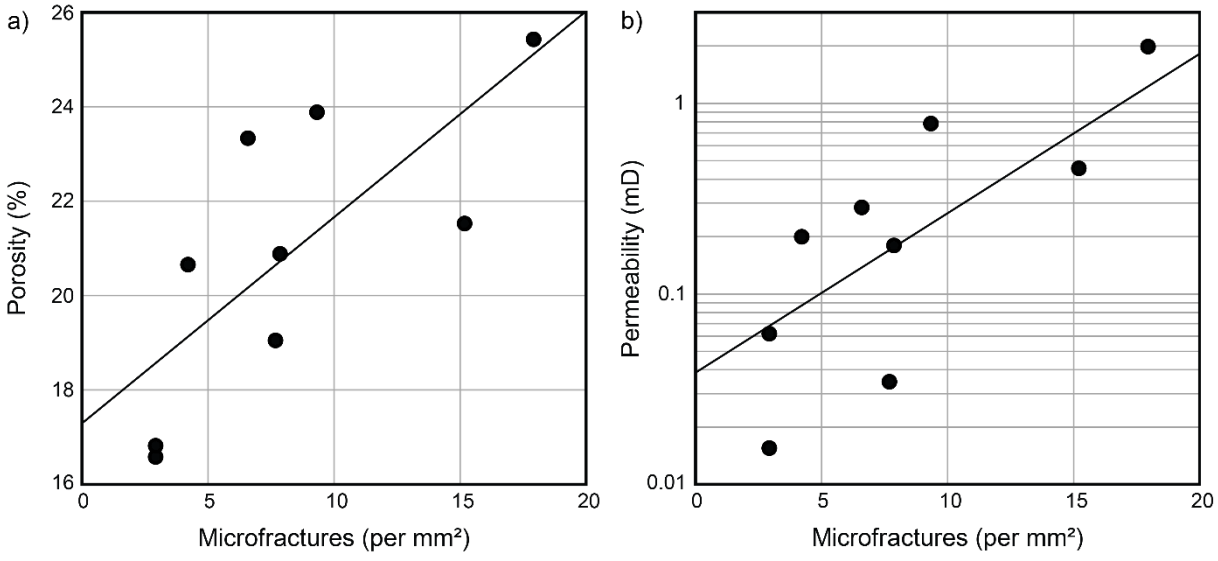

Figure 12. (a) The density of microfractures relative to mean core plug porosity has a strong positive correlation ($R^2 = 0.54$). (b) The density of microfractures relative to mean core plug permeability has a strong positive correlation ($R^2 = 0.6$). Permeability is plotted on a logarithmic scale.

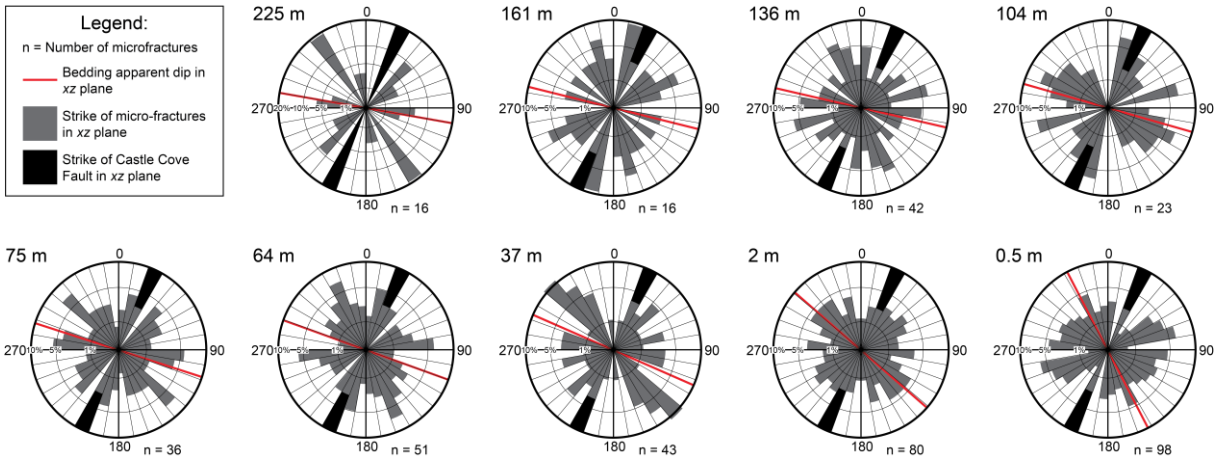

Figure 13. Equal area-scaled rose diagrams showing microfracture orientations at different distances from the Castle Cove Fault. The area of each sector of the rose diagram is proportional to the frequency of microfracture orientations (Nemec 1988) and each petal represents 10° angle increments. Microfractures were identified in thin sections oriented in the xz plane. The orientation, i.e. apparent dip, of the bedding relative to the xz plane cross-section is illustrated by the thick, red line.

5. Discussion

5.1 Microfractures within the Castle Cove Fault damage zone

Concept Microstructural analysis show that the density of microfractures increases toward the Castle Cove Fault plane (Fig. 4c). These data show two main microfracture density peaks; the first peak is adjacent to a small fault zone (<20 m wide between 45 m and 65 m from the Castle Cove Fault) and seems to be mainly influencing the sample at 64 m, and the second, largest peak is adjacent to the Castle Cove Fault plane (Fig. 4c). This positive relationship indicates that deformation, as a result of faulting, may be the main mechanism for microfracture formation. However, the microfractures do not exhibit preferential alignment to the Andersonian stresses associated with the Castle Cove Fault (Debenham et al. 2018). Microfractures are opening-mode (Mode I) fractures that are oriented parallel to the principal stress direction (Anders et al. 2014). Therefore, assuming that the microfractures formed during faulting, in the xz plane (Fig. 3) the microfractures should appear: (1) vertical, with an Andersonian vertical maximum principal stress axis (i.e. gravity) during normal faulting, and (2) horizontal and perpendicular to the horizontal maximum principal stress, with an Andersonian horizontal maximum principal stress axis during reverse faulting (Anderson 1951; Debenham et al. 2018). Given the variable microfracture orientations (Fig. 13), other processes may have also contributed to the formation of microfractures.

Structural processes such as stress heterogeneity, rotation, and changes in concentration around a fault can influence the microfracture fabric of the damage zone (e.g. Bell 1996; Wilson et al. 2003), and these could explain the variable microfracture orientations observed in this study. Anticlinal folding in the hanging wall may have contributed to the formation of microfractures (e.g. Zeng 2010). Microfractures formed during normal movement of the Castle Cove Fault and associated rollover folding in the hanging wall would have subsequently been tilted and re-oriented during amplification of the fold during reverse-reactivation. Therefore, the present day orientations of microfractures associated with the normal movement of the fault will not appear Andersonian. Other processes that can be attributed to the formation of variably oriented microfractures include; (1) pre-depositional processes, i.e. the microfractures may be inherited from the original source rock of the sediments (Laubach 1997); (2) syn-

diagenetic processes; i.e. microfractures formed during diagenesis due to compaction and subsequent cement precipitation (Boggs and Krinsley 2006); (3) near-surface processes, i.e. weathering; or (4) artificial processes, i.e. damage during thin section cutting and polishing, which was avoided as much as possible.

There are a number of processes that can lead to the formation of microfractures, and the application of analytical methods, such as three-dimensional microfracture imaging or SEM-based cathodoluminescence imaging, could further resolve these processes (Laubach 1997; Milliken and Laubach 2000). While a number of processes are contributing to microfracture formation, a comprehensive analysis of these is beyond the scope of this study; rather, this study assesses changes in microfracture density and dip orientation relative to distance to the fault plane.

5.2 The relationship between clays and the permeability structure of the Eumeralla Formation

At Castle Cove, the abundance of chlorite is mostly consistent throughout the sampled areas. Chlorite decreases by approximately 4 wt% as the Castle Cove Fault plane is approached, but only shows a weak correlation with distance (Fig. 8c). Within the Eumeralla Formation, porosity is strongly preserved by authigenic pore-lining chlorite formed during early diagenesis. The early precipitation of pore-lining chlorite has also prevented extensive quartz overgrowth and quartz grains that are rimmed by secondary quartz overgrowths are typically terminated by the growth of chlorite (Fig. 11). While the pore-lining chlorite presents potentially negative ramifications for reservoir quality, such as the closure of pore throats and subsequent reduction of permeability, deformation associated with faulting has broken up and disaggregated the authigenic chlorite closer to the Castle Cove Fault to improve the micrometre-scale permeability structure. More specifically, when the pore-lining chlorite is disaggregated during deformation, the chlorite will: (1) fill the pore space and reduce porosity slightly and (2) open up pore-throats and increase micrometre-scale permeability and connectivity.

The abundance of kaolinite is also mostly consistent across the study area. Kaolinite increases by approximately 2 wt% and has a strong positive correlation as the fault plane is approached (Fig. 8c). Similarly, kaolinite shows a strong positive correlation with porosity and permeability (Fig. 9c and d). As kaolinite only increases by a small volume as the fault plane is approached and there is evidence for the kaolinization of orthoclase, it is likely that an increase in permeability due to microfracturing is driving the precipitation of kaolinite. The precipitation of authigenic kaolinite is generally related to the presence of meteoric waters (Lanson et al. 2002). An enhanced micrometre-scale permeability structure closer to the Castle Cove Fault would provide the necessary fluid flow conduits for this reaction to occur. This suggests that an enhanced permeability structure due to faulting is leading to increased diagenesis and alteration of the protolith adjacent to the fault plane. Mineralogical changes due to diagenesis will consequently alter the mechanical properties of the protolith (Laubach et al. 2009). Diagenesis may also alter the petrophysical properties of the protolith through the precipitation of minerals and occlusion of pore space (e.g. heal microfractures) or the dissolution of minerals and creation of pore space (e.g. intragranular porosity; Pittman 1979).

5.3 Enhancement of micrometre-scale permeability structure closer to the fault plane

A positive relationship between the petrophysical properties of the host rock and distance toward the Castle Cove Fault plane has been observed (Fig. 14). The porosity, permeability, and microstructural data show two main peaks (Fig. 4). The first peak is adjacent to a small fault zone (between 45 m and 65 m) and shows enhanced petrophysical properties for samples at 64 m and 75 m from the Castle Cove fault.

The second and largest peak is adjacent to the Castle Cove Fault plane, within the zone of maximum fracture density, and the petrophysical properties of all samples in the damage zone are influenced by this fault. The zone of maximum fracture density is a zone of increased deformation within the damage zone adjacent to the Castle Cove Fault. Increased deformation within this zone would have a greater influence on the enhancement on not only the macroscale permeability structure of the damage zone (e.g. Debenham et al. 2018), but also the micrometre-scale permeability structure of the damage zone. Consistently high connected porosities (Fig. 4a) and permeabilities (Fig. 4b) due to elevated microfracture densities (Fig. 4c) and grain-scale cataclasis (Fig. 10) within this zone demonstrate this.

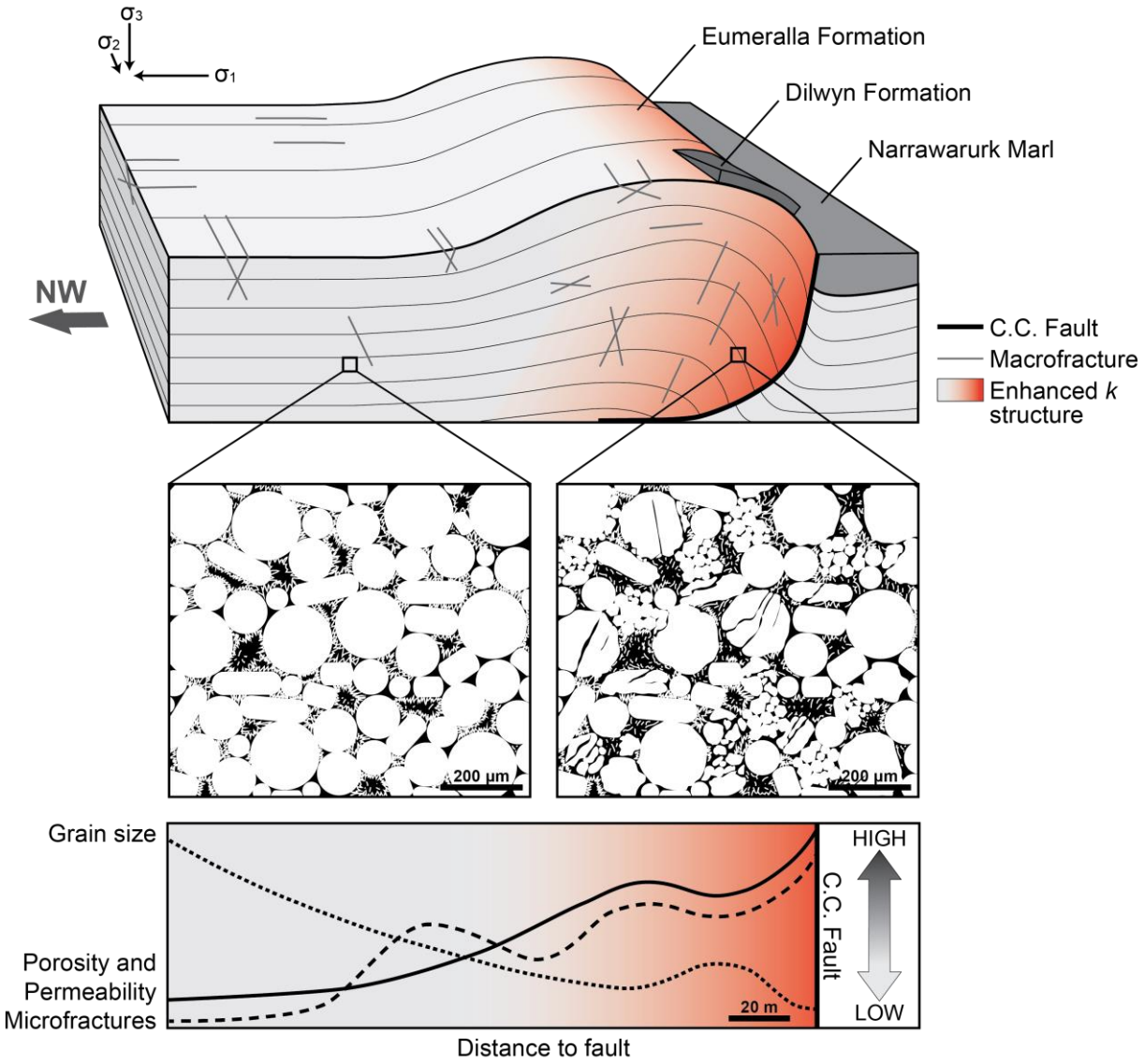

Figure 14. A summary model of the petrophysical properties of the Castle Cove Fault damage zone within the hanging wall. The block diagram illustrates the present day configuration of the Castle Cove outcrop, with macrofracture orientations from Debenham et al. (2018). This model shows an enhanced permeability structure associated with complex deformation from the Castle Cove Fault. The bottom graph summarises the porosity, permeability, macrofracture count, and grain size data from this study, where porosity, permeability, and number of macrofractures increase toward the fault and grain size decreases toward the fault.

Overall, porosity and permeability at ambient pressures increase as the Castle Cove Fault plane is approached (Fig. 4 and Fig. 14). Pore throat sizes also increase closer to the fault plane and connectivity is improved as a result (Fig. 7). However, there is a reduction in grain size as the fault plane is approached and the volume of clays to very-fine-grained sands increases toward the fault (Fig. 8 and Fig. 14). It would be expected that this would have a detrimental effect on the petrophysical properties of the host rock. However, there is a positive relationship between the petrophysical properties and distance to the fault plane. Therefore, other factors must be influencing the enhancement of the petrophysical properties of the host rock.

Thin section analyses indicate that the larger pore throat sizes measured in mercury-intrusion porosimetry can be attributed to the presence of microfractures and intergranular porosity preserved by pore-lining chlorite. Smaller pore throat sizes likely represent microporosity between clays, particularly within the filamentous and porous pore-lining chlorite. Microstructural analysis at the grain-scale has demonstrated that the density of microfractures correlates strongly with changes in porosity and permeability (Fig. 12 and Fig. 14). This indicates that an increase in connectivity adjacent to the Castle Cove Fault is related to an increase in microfractures. A change in the morphology of pore-lining chlorite, i.e. well-structured away from the fault to broken up and disaggregated adjacent to the fault, may also contribute to enhanced connectivity (Fig. 11 and Fig. 14). The increase in connected porosity toward the fault plane is attributed to the increase in microfracturing (Fig. 12a) and disaggregation of pore-lining chlorite, and this explains the strong correlation between connected porosity and permeability (Fig. 6). Despite an enhancement of the micrometre-scale permeability structure within the Castle Cove Fault damage zone, the petrophysical properties of this interval of the Eumeralla Formation indicate that the formation has the properties of a tight reservoir (i.e. permeabilities typically less than 1 mD).

5.4 Comparison of the permeability structure described in this study to other studies

Many investigations into the permeability structure of fault zones with simple tectonic histories have been undertaken on low porosity host rocks such as granites, mylonites, schists, and low porosity sandstones (e.g. Evans et al. 1997; Wibberley and Shimamoto 2003; Balsamo et al. 2010; Mitchell and Faulkner 2012; Cavailhes et al. 2013) and porous sandstones (e.g. Antonellini and Aydin 1994; Shipton et al. 2002; Farrell et al. 2014). However, studies on the influence of complex faults with multi-slip histories on the permeability structure of porous rocks are limited. It is widely recognised that the primary intrinsic control on permeability structure is the lithology of the protolith. The lithology will influence the types of fault-related deformation processes that can occur within a host rock, therefore influencing permeability structure.

Studies of fault-bearing porous sandstones have identified a number of fault-related deformation processes influencing permeability structure. Shipton et al. (2002) analysed the permeability structure of Jurassic-aged porous sandstones (Navajo Sandstone) that are intersected by a normal fault (Big Hole Fault) in Utah, western United States. The Big Hole Fault has a strike length of 4.1 km and fault throw is between 3 m to 29 m (Shipton and Cowie 2001). Shipton et al. (2002) demonstrated that centimetre- to metre-scale deformation (e.g. the formation of deformation bands), associated with faulting resulted in a decline in porosity (20% to less than 10%) and permeability (more than 2000 mD to less than 0.1 mD) as the fault is approached. A detailed study was also undertaken by Farrell et al. (2014) on Permo-Triassic porous sandstones (Hopeman Sandstone Formation) within the damage zone of a normal fault (Clashach Fault). The Clashach Fault has a strike length over 1 km and fault throw is up to 50 m (Farrell et al. 2014). While the bulk permeability of the host rock decreases as the fault plane is approached, they explained that

permeability anisotropy, i.e. preferentially oriented pore connectivity, is created as a result of faulting. Within these sandstones, permeability anisotropy is controlled by the formation of elongate pores and microfractures related to faulting, with maximum permeability oriented parallel to fault plane dip.

Unlike the faulting-related permeability structures described by Shipton et al. (2002) and Farrell et al. (2014), the results from this study show an increase in the bulk petrophysical properties of the host rock as the Castle Cove Fault plane is approached. This highlights the significant variability that faults can have on the permeability structure of fault zones in porous sandstones. The development of permeability anisotropy as a result of faulting is also not observed at Castle Cove. Minor permeability anisotropy is observed away from the fault (225 m; Fig. 5) and this is attributed to the orientation of the bedding relative to the core plugs, i.e. core plugs with permeability anisotropy are approximately parallel to bedding (Fig. 2c and d). Therefore, fine laminations and millimetre-scale coal seams within this interval of the Eumeralla Formation are controlling permeability anisotropy. The remaining samples do not show permeability anisotropy and there are a few reasons for this. For instance, the absence of preferentially oriented microfractures and pore fabrics from deformation would result in variable permeabilities. This is considered to be the main control on the isotropy of permeability. Secondly, a broad anticline (approximately 80 m in half-wavelength) in the hanging wall has tilted the beds adjacent to the Castle Cove Fault (Fig. 2). The geometry of the beds and fine laminations will influence the direction of permeability anisotropy, and as the core plugs have been drilled at an angle that is not parallel to bedding within the anticline, permeability anisotropy caused by bedding may not be identified during core plug permeability and porosity analysis. Anticlinal folding within the hanging wall of the Castle Cove Fault is an expression of a complex structural regime. Therefore, both the protolith and the structural history of the fault have influenced the permeability structure at Castle Cove.

This study describes the influence of a reverse-reactivated fault on the damage zone permeability structure of the Eumeralla Formation. Normal faulting of the Castle Cove Fault and subsequent reactivation as a reverse fault has resulted in complex deformation within the hanging wall at a range of scales, which in turn has influenced the development of the permeability structure. For instance, at the outcrop-scale, anticlinal folding in the hanging wall associated with the reversal of the Castle Cove Fault has tilted the beds and fine laminations. This would influence the direction of permeability anisotropy, as described above. Also at the outcrop-scale, the formation of macrofractures related to the multiple-slip history of the Castle Cove Fault (Debenham et al. 2018) has provided an extensive permeability network. At the micrometre-scale, the formation of variably oriented microfractures is attributed to the multiple-slip history of the fault, along with other processes as discussed previously. Complex deformation associated with normal faulting followed by reverse faulting has influenced the off-fault fluid flow properties of the host rock.

5.5 Implications for fluid flow and fluid exploration in sedimentary basins

Using insights from the Castle Cove Fault, this study aims to understand the influence of inverted faults on the micrometre-scale permeability structure, and therefore fluid flow, within tight sandstones, which are growing targets for fluid extraction and storage in sedimentary basins. The main implications for fluid flow and fluid exploration adjacent to reverse-reactivated faults are summarised here; (1) Enhanced deformation adjacent to the fault plane results in the formation of variably oriented microfractures that leads to isotropic permeability. While fluid flow is increased adjacent to the fault plane, fluid flow may occur in any direction. (2) Where pore-lining clays are present (e.g. chlorite, illite, and montmorillonite; Neasham 1977), disaggregation of the clays due to deformation can enhance the micrometre-scale

permeability structure of the protolith by opening pore-throats. However, porosity can be reduced as the disaggregated clays fill pore space during deformation and this may impede fluid flow. (3) Enhanced deformation adjacent to the fault plane results in the cataclasis of individual grains (i.e. grain size reduction) which can reduce the connected pore space, therefore impeding fluid flow (Antonellini and Aydin 1994). (4) At the outcrop scale, the reverse-reactivation of normal faults often results in anticlinal folding and uplift in the hanging wall, which would form structural highs acting as traps for fluids (c.f. Debenham et al. 2018). Alternatively, folding and uplift during inversion may result in changes in pre-existing trap configurations, thereby increasing the risk of fluid leakage (Cooper and Warren 2010). Characterisation of the micrometre-scale permeability structure adjacent to reverse-reactivated faults will aid with predicting fluid flow associated with such inversion structures.

5.6 Application of results, upscaling issues, and further work

Farrell et al. (2014) described the parameters considered to be suitable for measuring the petrophysical properties of core plugs. The use of multiple core plugs with an average core plug volume of 32.7 cm^3 is deemed to be valid for repeatable and representative results and for assessing micrometre-scale features in this study. While core plugs can be used to assess the micrometre-scale petrophysical properties of the host rock, they exclude the petrophysical properties associated with large-scale features such as macrofractures and deformation bands. On the contrary, conventional reservoir modelling workflows typically exclude the effects of micrometre-scale heterogeneity. Therefore, multiple datasets need to be considered when describing the field-scale permeability structure of a fault damage zone.

While the petrophysical properties (e.g. porosity, permeability, and pore connectivity) of the Eumeralla Formation at Castle Cove were enhanced as a result of fault-related deformation, the host rock is still considered to be a tight sandstone (i.e. a reservoir rock with permeabilities of less than 1 mD and as low as 0.001 mD; Kazemi 1982). Consequently, in order for the Castle Cove Fault damage zone to be an effective conduit for significant fluid flow, the presence of large-scale features such as macrofractures and small-scale faults are required. A complex macrofracture network exists at Castle Cove, with three fracture sets identified to be geometrically related to the Castle Cove Fault (Debenham et al. 2018). Depending on the timing of macrofracture formation and reactivation relative to fluid flow, it is expected that these would act as more effective conduits for fluid flow than the bulk permeability of the host rock. Integrating macrofracture densities associated with the Castle Cove Fault into reservoir modelling workflows would account for bulk permeability.

To further improve the applicability of the results from this study to reservoir models, it would be beneficial to carry out additional laboratory experiments under conditions that are representative of in situ temperature and confining pressure conditions. Moreover, although the Castle Cove Fault is not exposed at the surface, an investigation into the internal structure of the fault, e.g. fault core and peripheral damage zone, would result in a better understanding of the permeability structure of the Castle Cove Fault. It is also important to note that the Eumeralla Formation is lithologically variable and is characterised by different zones of diagenetic alteration (Duddy 2002) and porosity reduction as a result of over-compaction during burial (Tassone et al. 2014), and therefore the permeability structure may vary considerably depending on position in stratigraphy. While this study only focusses on the upper interval of the Eumeralla Formation, our results can be used as an analogue for sandstones that are characterised by high porosities, low permeabilities, and abundant clays.

This study highlights the importance of undertaking detailed petrophysical, structural, and mineralogical analyses of reservoir rocks that have experienced complex deformation associated with faulting. Within the hanging wall of an inverted fault, microstructural changes as a result of faulting-induced deformation have enhanced the micrometre-scale permeability structure. This study has significant implications for the future development of robust exploration and fluid monitoring strategies of similar faults in the eastern Otway Basin which have experienced similar deformation histories and other analogous faults globally.

6. Conclusions

High resolution petrophysical, microstructural, and mineralogical analyses have been undertaken on porous sandstones that have experienced complex faulting. The results from this study show that microstructural changes as a result of faulting have improved the permeability structure of the Eumeralla Formation within the hanging wall of the Castle Cove Fault:

- As the fault plane is approached, connected porosity increases by 10% and permeability at ambient pressures increases by two orders of magnitude. Pore throat sizes also increase closer to the fault plane and connectivity is improved as a result. However, there is a reduction in grain size toward the fault. An improvement of the permeability structure toward the fault plane reflects an opposite trend to other fault zones (e.g. Big Hole Fault and Clashach Fault) compared in this study. This highlights the significant variability that faults can have on the permeability structure of fault zones in porous sandstones.
- Detailed thin section analyses indicate that the larger pore throat sizes measured in mercury-intrusion porosimetry can be attributed to the presence of microfractures and intergranular porosity preserved by pore-lining chlorite.
- Microstructural analysis at the grain-scale has demonstrated that the density of microfractures correlates strongly with changes in connected porosity and permeability. This indicates that an increase in connectivity adjacent to the Castle Cove Fault is related to an increase in microfractures.
- Destruction of original authigenic pore-lining chlorite morphology may also contribute to enhanced connectivity.

Despite improvement of the permeability structure, the upper Eumeralla Formation at Castle Cove is still considered a tight sandstone. However, the extensive macrofracture network described in Debenham et al. (2018) could act as a conduit for significant fluid flow in this system. This study shows that high-resolution analyses of the protolith are fundamental for describing the permeability structure of reservoir rocks with high porosities, low permeabilities, and abundant clays. This study also has significant implications for future exploration and fluid monitoring strategies within reservoir rocks that have experienced complex structural histories.

Acknowledgements

This research forms part of a PhD project supported by the Australian Research Council [Discovery Project DP160101158] and through an Australian Government Research Training Program Scholarship. Dave Healy acknowledges the support of the Natural Environment Research Council (NERC, UK) through the award NE/N003063/1 'Quantifying the Anisotropy of Permeability in Stressed Rock'. This study was also funded by scholarships from the Petroleum Exploration Society of Australia and the Australian Petroleum Production and Exploration Association. We thank Gordon Holm for preparing

thin sections and Colin Taylor for carrying out particle size measurements and mercury injection capillary pressure analyses. Aoife McFadden and David Kelsey from Adelaide Microscopy, Braden Morgan, and Sophie Harland are acknowledged for their assistance with laboratory work. Field assistants James Hall, Rowan Hansberry, and Lachlan Furness are also gratefully acknowledged for their assistance with sample collection. Discussions with Ian Duddy on the mineralogy of the Eumeralla Formation are also greatly appreciated. This forms TRaX record 416.

References

Anders M. H., Laubach S. E. & Scholz C. H. 2014. Microfractures: A review. Journal of Structural Geology 69, Part B, 377-394. doi: 10.1016/j.jsg.2014.05.011.

Anderson E. M. 1951. The Dynamics of Faulting and Dyke Formation with Applications to Britain. 2 ed. Oliver and Boyd, Edinburgh.

Antonellini M. & Aydin A. 1994. Effect of faulting on fluid flow in porous sandstones: Petrophysical properties. AAPG Bulletin 78, 355-377.

Aydin A. 2000. Fractures, faults, and hydrocarbon entrapment, migration and flow. Marine and Petroleum Geology 17, 797-814. doi: 10.1016/S0264-8172(00)00020-9.

Baccar M. B., Fritz B. & Made B. 1993. Diagenetic albitization of K-feldspar and plagioclase in sandstone reservoirs; thermodynamic and kinetic modeling. Journal of Sedimentary Research 63, 1100-1109. doi: 10.1306/D4267CB2-2B26-11D7-8648000102C1865D.

Balsamo F., Storti F., Salvini F., Silva A. T. & Lima C. C. 2010. Structural and petrophysical evolution of extensional fault zones in low-porosity, poorly lithified sandstones of the Barreiras Formation, NE Brazil. Journal of Structural Geology 32, 1806-1826. doi: 10.1016/j.jsg.2009.10.010.

Bauer J. F., Meier S. & Philipp S. L. 2015. Architecture, fracture system, mechanical properties and permeability structure of a fault zone in Lower Triassic sandstone, Upper Rhine Graben. Tectonophysics 647-648, 132-145. doi: 10.1016/j.tecto.2015.02.014.

Bell J. S. 1996. In situ stresses in sedimentary rocks (part 2): Applications of stress measurements. Geoscience Canada 23, 135-153.

Bense V. F. & Person M. A. 2006. Faults as conduit-barrier systems to fluid flow in siliciclastic sedimentary aquifers. Water Resources Research 42. doi: 10.1029/2005WR004480.

Bense V. F., Gleeson T., Loveless S. E., Bour O. & Scibek J. 2013. Fault zone hydrogeology. Earth-Science Reviews 127, 171-192. doi: 10.1016/j.earscirev.2013.09.008.

Blott S. J., Croft D. J., Pye K., Saye S. E. & Wilson H. E. 2004. Particle size analysis by laser diffraction. Geological Society, London, Special Publications 232, 63-73. doi: 10.1144/gsl.sp.2004.232.01.08.

Boggs S. & Krinsley D. 2006 Cathodoluminescence and its causes. In Krinsley D. & Boggs S. ed. Application of Cathodoluminescence Imaging to the Study of Sedimentary Rocks. Cambridge University Press, Cambridge, pp. 7-18.

Boreham C. J., Hope J. M., Jackson P., Davenport R., Earl K. L., Edwards D. S., Logan G. A. & Krassay A. A. 2004 Gas-oil-source correlations in the Otway Basin, southern Australia. In Boult P. J., Johns D. R. & Lang S. C. ed. Eastern Australian Basins Symposium II. Petroleum Exploration Society of Australia Special Publication, pp. 97-106.

Bredehoeft J. D. 1997. Fault permeability near Yucca Mountain. Water Resources Research 33, 2459-2463. doi: 10.1029/97WR01710.

Caine J. S., Evans J. P. & Forster C. B. 1996. Fault zone architecture and permeability structure. Geology 24, 1025-1028. doi: 10.1130/0091-7613(1996)024<1025:fzaaps>2.3.co;2.

Cavailhes T., Sizun J.-P., Labaume P., Chauvet A., Buatier M., Soliva R., Mezri L., Charpentier D., Leclere H., Trave A. & Gout C. 2013. Influence of fault rock foliation on fault zone permeability: The case of deeply buried arkosic sandstones (Gres d'Annot, southeastern France). AAPG Bulletin 97, 1521-1543. doi: 10.1306/03071312127.

Cooper M. A. & Warren M. J. 2010. The geometric characteristics, genesis and petroleum significance of inversion structures. Geological Society, London, Special Publications 335, 827-846. doi: 10.1144/sp335.33.

Debenham N., King R. C. & Holford S. P. 2018. The influence of a reverse-reactivated normal fault on natural fracture geometries and relative chronologies at Castle Cove, Otway Basin. Journal of Structural Geology 112, 112-130. doi: 10.1016/j.jsg.2018.05.004.

Duddy I. R. 1994. The Otway Basin: Thermal, Structural, Tectonic and Hydrocarbon Generation Histories. NGMA/PESA Otway Basin Symposium, Melbourne. pp. 35-42.

Duddy I. R. 2002. The Otway Basin: Geology, Sedimentology, Diagenesis, AFTA Thermal History Reconstruction and Hydrocarbon Prospectivity. Field Trip Guide prepared for the National Centre for Petroleum Geology and Geophysics, Adelaide. Geotrack International Pty. Ltd.

Duddy I. R. 2003 Mesozoic: A time of change in teconic regime. In Birch W. D. ed. Geology of Victoria. GSA Special Publication 23, pp. 239-286.

Edwards D. S., Struckmeyer H. I. M., Bradshaw M. T. & Skinner J. E. 1999. Geochemical characteristics of Australia's southern margin petroleum systems. The APPEA Journal 39, 297-321. doi: 10.1071/AJ98017.

Edwards J., Leonard J. G., Pettifer G. R. & Mcdonald P. A. 1996. Colac 1:250000 Map Geological Report. Report 98. Geological Survey.

Evans J. P., Forster C. B. & Goddard J. V. 1997. Permeability of fault-related rocks, and implications for hydraulic structure of fault zones. Journal of Structural Geology 19, 1393-1404. doi: 10.1016/S0191-8141(97)00057-6.

Fairley J. P. 2009. Modeling fluid flow in a heterogeneous, fault-controlled hydrothermal system. Geofluids 9, 153-166. doi: 10.1111/j.1468-8123.2008.00236.x.

Farrell N. J. C., Healy D. & Taylor C. W. 2014. Anisotropy of permeability in faulted porous sandstones. Journal of Structural Geology 63, 50-67. doi: 10.1016/j.jsg.2014.02.008.

Farrell N. J. C. & Healy D. 2017. Anisotropic pore fabrics in faulted porous sandstones. Journal of Structural Geology 104, 125-141. doi: 10.1016/j.jsg.2017.09.010.

Faulkner D. R., Jackson C. a. L., Lunn R. J., Schlische R. W., Shipton Z. K., Wibberley C. a. J. & Withjack M. O. 2010. A review of recent developments concerning the structure, mechanics and fluid flow properties of fault zones. Journal of Structural Geology 32, 1557-1575. doi: 10.1016/j.jsg.2010.06.009.

Fisher Q. J. & Knipe R. J. 1998. Fault sealing processes in siliciclastic sediments. Geological Society, London, Special Publications 147, 117-134. doi: 10.1144/gsl.sp.1998.147.01.08.

Folch A. & Mas-Pla J. 2008. Hydrogeological interactions between fault zones and alluvial aquifers in regional flow systems. Hydrological Processes 22, 3476-3487. doi: doi:10.1002/hyp.6956.

Fossen H., Schultz R. A., Shipton Z. K. & Mair K. 2007. Deformation bands in sandstone: a review. Journal of the Geological Society 164, 755-769. doi: 10.1144/0016-76492006-036.

Holford P., Tuitt A. K., Hillis R. R., Green P. F., Stoker M. S., Duddy I. R., Sandiford M. & Tassone D. R. 2014. Cenozoic deformation in the Otway Basin, southern Australian margin: implications for the origin and nature of post-breakup compression at rifted margins. Basin Research 26, 10-37. doi: 10.1111/bre.12035.

Katz A. J. & Thompson A. H. 1987. Prediction of rock electrical conductivity from mercury injection measurements. Journal of Geophysical Research: Solid Earth 92, 599-607. doi: doi:10.1029/JB092iB01p00599.

Kazemi H. 1982. Low-Permeability Gas Sands. Journal of Petroleum Technology 34, 2229-2232. doi: 10.2118/11330-PA.

Klinkenberg L. J. 1941. The permeability of porous media to liquids and gases. American Petroleum Institute, Drilling and Production Practice, 200-213.

Knipe R. J., Jones G. & Fisher Q. J. 1998. Faulting, fault sealing and fluid flow in hydrocarbon reservoirs: an introduction. Geological Society, London, Special Publications 147, vii-xxi. doi: 10.1144/gsl.sp.1998.147.01.01.

Krassay A. A., Cathro D. L. & Ryan D. J. 2004 A regional tectonostratigraphic framework for the Otway Basin. In Boult P. J., Johns D. R. & Lang S. C. ed. Eastern Australian Basins Symposium II. Petroleum Exploration Society of Australia Special Publication, pp. 97-106.

Lanson B., Beaufort D., Berger G., Bauer A., CassagnabèRe A. & Meunier A. 2002. Authigenic kaolin and illitic minerals during burial diagenesis of sandstones: a review. Clay Minerals 37, 1-22. doi: 10.1180/0009855023710014.

Laubach S. E. 1997. A method to detect natural fracture strike in sandstones. AAPG Bulletin 81, 604-623.

Laubach S. E., Olson J. E. & Gross M. R. 2009. Mechanical and fracture stratigraphy. AAPG Bulletin 93, 1413-1426. doi: 10.1306/07270909094.

Milliken K. L. & Laubach S. E. 2000 Brittle Deformation in Sandstone Diagenesis as Revealed by Scanned Cathodoluminescence Imaging with Application to Characterization of Fractured Reservoirs. In Pagel M., Barbin V., Blanc P. & Ohnenstetter D. ed. Cathodoluminescence in Geosciences. Springer Berlin Heidelberg, Berlin, Heidelberg, pp. 225-243.

Mitchell T. M. & Faulkner D. R. 2009. The nature and origin of off-fault damage surrounding strike-slip fault zones with a wide range of displacements: A field study from the Atacama fault system, northern Chile. Journal of Structural Geology 31, 802-816. doi: 10.1016/j.jsg.2009.05.002.

Mitchell T. M. & Faulkner D. R. 2012. Towards quantifying the matrix permeability of fault damage zones in low porosity rocks. Earth and Planetary Science Letters 339-340, 24-31. doi: 10.1016/j.epsl.2012.05.014.

Nara Y., Meredith P. G., Yoneda T. & Kaneko K. 2011. Influence of macro-fractures and micro-fractures on permeability and elastic wave velocities in basalt at elevated pressure. Tectonophysics 503, 52-59. doi: 10.1016/j.tecto.2010.09.027.

Neasham J. W. 1977. The morphology of dispersed clay in sandstone reservoirs and its effect on sandstone shaliness, pore space and fluid flow properties.

Nemec W. 1988. The shape of the rose. Sedimentary Geology 59, 149-152. doi: 10.1016/0037-0738(88)90105-4.

Norvick M. S. & Smith M. A. 2001. Mapping the plate tectonic reconstruction of southern and southeastern Australia and implications for petroleum systems. Journal of the Australian Petroleum Production and Exploration Association 41, 15-35..

Perincek D., Simons B. & Pettifer G. R. 1994. The tectonic framework, and associated play types of the Western Otway Basin, Victoria, Australia. APPEA Journal 34, 460-477.

Pittman E. D. 1979. Porosity, diagenesis and productive capacity of sandstone reservoirs. SEPM Special Publication 26, 159-173.

Rowland J. V. & Sibson R. H. 2004. Structural controls on hydrothermal flow in a segmented rift system, Taupo Volcanic Zone, New Zealand. Geofluids 4, 259-283. doi: 10.1111/j.1468-8123.2004.00091.x.

Schneider C. L., Hill K. C. & Hoffman N. 2004. Compressional growth of the Minerva Anticline, Otway Basin, Southeast Australia–evidence of oblique rifting. APPEA Journal 44, 463-480.

Shipton Z. K. & Cowie P. A. 2001. Damage zone and slip-surface evolution over μm to km scales in high-porosity Navajo sandstone, Utah. Journal of Structural Geology 23, 1825-1844. doi: 10.1016/S0191-8141(01)00035-9.

Shipton Z. K., Evans J. P., Robeson K. R., Forster C. B. & Snelgrove S. 2002. Structural Heterogeneity and Permeability in Faulted Eolian Sandstone: Implications for Subsurface Modeling of Faults. AAPG Bulletin 86, 863-883. doi: 10.1306/61eedbc0-173e-11d7-8645000102c1865d.

Sibson R. H., Moore J. M. M. & Rankin A. H. 1975. Seismic pumping—a hydrothermal fluid transport mechanism. Journal of the Geological Society 131, 653-659. doi: 10.1144/gsjgs.131.6.0653.

Sibson R. H. 1994. Crustal stress, faulting and fluid flow. Geological Society, London, Special Publications 78, 69-84. doi: 10.1144/gsl.sp.1994.078.01.07.

Streit J. E. & Hillis R. R. 2004. Estimating fault stability and sustainable fluid pressures for underground storage of CO2 in porous rock. Energy 29, 1445-1456. doi: 10.1016/j.energy.2004.03.078.

Tassone D. R., Holford S. P., Hillis R. R. & Tuitt A. K. 2012. Quantifying Neogene plate-boundary controlled uplift and deformation of the southern Australian margin. Geological Society, London, Special Publications 367, 91-110. doi: 10.1144/sp367.7.

Tassone D. R., Holford S. P., Duddy I. R., Green P. F. & Hillis R. R. 2014. Quantifying Cretaceous–Cenozoic exhumation in the Otway Basin, southeastern Australia, using sonic transit time data: Implications for conventional and unconventional hydrocarbon prospectivity. AAPG Bulletin 98, 67-117. doi: 10.1306/04011312111.

Tassone D. R., Holford S. P., King R., Tingay M. R. P. & Hillis R. R. 2017. Contemporary stress and neotectonics in the Otway Basin, southeastern Australia. Geological Society, London, Special Publications 458. doi: 10.1144/sp458.10.

Webb P. A. 2001. An introduction to the physical characterization of materials by mercury intrusion porosimetry with emphasis on reduction and presentation of experimental data. Micromeritics Instrument Corp. Norcross, Georgia, U.S.A.

Wibberley C. a. J. & Shimamoto T. 2003. Internal structure and permeability of major strike-slip fault zones: the Median Tectonic Line in Mie Prefecture, Southwest Japan. Journal of Structural Geology 25, 59-78. doi: 10.1016/S0191-8141(02)00014-7.

Wilson J. E., Chester J. S. & Chester F. M. 2003. Microfracture analysis of fault growth and wear processes, Punchbowl Fault, San Andreas system, California. Journal of Structural Geology 25, 1855-1873. doi: 10.1016/S0191-8141(03)00036-1.

Woodcock N. H., Dickson J. a. D. & Tarasewicz J. P. T. 2007. Transient permeability and reseal hardening in fault zones: evidence from dilation breccia textures. Geological Society, London, Special Publications 270, 43-53. doi: 10.1144/gsl.Sp.2007.270.01.03.

Zeng L. 2010. Microfracturing in the Upper Triassic Sichuan Basin tight-gas sandstones: Tectonic, overpressure, and diagenetic origins. AAPG Bulletin 94, 1811-1825. doi: 10.1306/06301009191.

CHAPTER 4

This chapter is written in publication format:

Debenham, N., Duddy, I. R., King, R. C., Holford, S. P.
The pore fluid evolution of the mid-Cretaceous Eumeralla Formation in the eastern Otway Basin.

STATEMENT OF AUTHORSHIP

Title of Paper	The pore fluid evolution of the mid-Cretaceous Eumeralla Formation in the eastern Otway Basin.
Publication Status	☐ Published ☐ Accepted for publication ☐ Submitted for publication ☒ Unpublished and unsubmitted work written in manuscript style

Principal Author

Name of Principal Author (Candidate)	Natalie Debenham		
Contribution to the Paper	Project design, fieldwork, sample preparation, laboratory analysis, processing and interpreting, manuscript design and composition, creation of figures, manuscript revisions.		
Overall Percentage	80%		
Certification	This paper reports on original research I conducted during the period of my Higher Degree by Research candidature and is not subject to any obligations or contractual agreements with a third party that would constrain its inclusion in this thesis. I am the primary author of this paper.		
Signature		Date	26/02/2019

Co-Author Contributions

By signing the Statement of Authorship, each author certifies that:

i. the candidate's stated contribution to the publication is accurate (as detailed above);
ii. permission is granted for the candidate in include the publication in the thesis; and
iii. the sum of all co-author contributions is equal to 100% less the candidate's stated contribution.

Name of Co-Author	Ian Duddy		
Contribution to the Paper	Assistance with project design, fieldwork, assistance with sample preparation, assistance with interpretation, assistance with manuscript design and composition, manuscript review.		
Signature		Date	27/02/2019

Name of Co-Author	Rosalind King		
Contribution to the Paper	Assistance with project design, assistance with manuscript design and composition, assistance with interpretation, manuscript review.		
Signature		Date	26/02/2019

Name of Co-Author	Simon Holford		
Contribution to the Paper	Assistance with project design, assistance with manuscript design and composition, assistance with interpretation, manuscript review.		
Signature		Date	26/02/2019

ABSTRACT

Carbonate cements preserved in concretions and fractures provide valuable insights into the pore fluid evolution and diagenetic history of sedimentary basins. Geochemical data, from stable oxygen and carbon isotopes and strontium isotopes, of calcite- and siderite-cemented concretions and fractures in the eastern Otway Basin, a Jurassic–Cenozoic rift basin in south-eastern Australia, record the source and evolution of pore fluids from deposition to post-diagenesis. Concretions and fractures within the Eumeralla Formation are the focus of this study. The Aptian to Albian Eumeralla Formation is a compositionally immature volcanogenic sandstone. Carbonate concretions within the Eumeralla Formation formed within the initial ca. 700 m to 2,900 m of burial, and individual concretions formed at a similar depth over a short depth interval, i.e. concretion formation from core to rim occurs within ca. 2 m to 530 m. In this study, depleted oxygen isotopic ratios recorded in calcite-cemented concretions and fractures have been attributed to meteoric water input during early diagenesis, followed by later calcite recrystallization with increased burial. The relatively unradiogenic strontium isotopic composition of many of these concretions and fractures suggests that pore fluids were strongly influenced by the dissolution and alteration of volcanic detritus. Enriched pore fluid oxygen isotopic compositions and radiogenic strontium values suggest that there may have been a sea water input in the siderite-cemented concretions and siderite- and calcite-cemented fractures. The CO_2 required for carbonate precipitation was likely derived from both the methanogenic fermentation and oxidation of organic matter. These geochemical analyses have implications for palaeoclimate reconstructions of the eastern Otway Basin in the mid-Cretaceous. The mean annual surface temperature has been calculated from pore fluid isotopic compositions of calcite-cemented concretions together with historical continental station data. We show that the mean annual surface temperature during the mid-Cretaceous was approximately between 5°C and 15°C, and this is consistent with the palaeobotanical and palynological record at this time. This study highlights the importance of understanding the influence of diagenesis, fluid mixing, and high temperatures on pore fluids during deep burial when attempting to describe the pore fluid evolution of sedimentary basins.

1. Introduction

Geochemical information from precipitated fluids provide valuable insights into the pore fluid evolution of sedimentary basins (e.g. Suchy et al. 2000; Scotchman et al. 2002; Boles et al. 2004; Philipp 2008; Meng et al. 2017b). Precipitated fluids can be preserved within a basin as cements in faults and fractures (i.e. veins; Bons et al. 2012), and also as diagenetic cements within host rock pore space, concretions, and nodules (Curtis and Coleman 1986). They preserve information on source, temperature, and timing of pore fluids from which they were precipitated (Bons et al. 2012), thereby providing insights into past fluid transport and flow networks. Cements preserved in fractures typically represent fluids that have travelled through pore and fracture networks (Bons et al. 2012), whilst concretions can provide insights into the early geochemical evolution of pore fluids during burial diagenesis (e.g. Gregory et al. 1989; Scotchman 1991; Scotchman et al. 2002). Analysis of the early pore fluid chemistry preserved in concretions together with later fracture-hosted precipitated fluids can be used to understand the geochemical evolution of a sedimentary basin. As the oxygen isotope composition of pore fluids is related to surface temperature conditions, studies on the pore fluid evolution of sedimentary basins can also have profound implications for regional palaeoclimate reconstructions (Dansgaard 1964; Joussaume et al. 1984; Gat 1996).

There are many studies in which traditional isotope and fluid inclusion analyses have been used to successfully reconstruct pore fluid evolution and the diagenetic histories of sedimentary basins (e.g. Ayalon and Longstaffe 1988; Evans 1995; Pagel et al. 1997; Scotchman et al. 2002; Meng et al. 2017a). These studies have utilised high resolution geochemical techniques on carbonate cements to understand the source, temperature, and timing of fluid flow in sedimentary basins. However, geochemical analyses on both concretion-hosted cements and fracture-hosted cements in order to gain a comprehensive understanding of the pore fluid evolution of a basin, from deposition to post-diagenesis, are less common.

This study investigates the geochemical evolution of fluids precipitated as calcite and siderite-cemented concretions and fractures in eastern Otway Basin, southeast Australia. A series of geochemical analyses have been undertaken on carbonate cements from concretions and fractures in the Eumeralla Formation, including carbon and oxygen stable isotope and strontium isotope analysis. The Aptian to Albian Eumeralla Formation is a compositionally immature volcanogenic sandstone. Stable isotope analyses provide insights into the source of the pore fluids (e.g. meteoric water or seawater) and strontium analyses identify processes influencing the geochemistry of the fluids. The geochemical analyses carried out in this study have not been previously undertaken on fractures or siderite concretions within the Otway Basin, though previous studies involving stable isotope analysis have been undertaken on calcite concretions within the Otway Basin by Gregory et al. (1989) and Ferguson et al. (1999). Gregory et al. (1989) and Ferguson et al. (1999) concluded that pore fluids within the calcite concretions were sourced from meteoric water and precipitated at shallow depths. In this study we show that pore fluids were sourced from both meteoric water and sea water during the deposition of the Eumeralla Formation, and that pore fluids were influenced by diagenetic reactions and increased temperature during burial.

2. Geological background

2.1 Structural setting

The Otway Basin is a late Jurassic to Cenozoic rift basin located in southeast Australia (Fig. 1), formed following the rifting and continental separation of Australia and Antarctica during the breakup of eastern Gondwana (Norvick and Smith 2001). The basin has experienced a complex tectonic history, with initial rifting during the late Jurassic to early Cretaceous, regional inversion during the mid-Cretaceous, renewed rifting in the late Cretaceous, and compression since the mid-Eocene (Perincek et al. 1994; Krassay et al. 2004; Schneider et al. 2004; Holford et al. 2014; Debenham et al. 2018). The onshore part of the basin can be divided into two main structural domains, the eastern and western Otway Basin, which are characterised by differing structural trends (Hill et al. 1995; Finlayson et al. 1996; Miller et al. 2002; Burgin et al. 2018). This study is focussed on outcrop exposures in the Otway Ranges, in the eastern Otway Basin (Fig. 1).

2.2 Eumeralla Formation

In the eastern Otway Basin, the Aptian to Albian Eumeralla Formation crops out in cliff exposures along the coastline (Fig. 1). The Eumeralla Formation is a fine- to medium-grained volcanogenic sandstone that is compositionally immature. The formation was deposited at high palaeolatitudes (between 70° to 80°; Fig. 2) in a fluvial to deltaic environment characterised by braided channels, flood plains, and shallow lacustrine deposits (Krassay et al. 2004). There is a shift from fluvial and deltaic dominated facies in the Eumeralla Formation to marine dominated facies at the Cenomanian unconformity, which marks the top of the Eumeralla Formation (Duddy 2003). The Eumeralla Formation is the thickest stratigraphic unit in the Otway Basin, with up to 3 km intersected during drilling, and thicker sections exceeding 6 km have

been interpreted from pre-exhumation stratigraphic reconstructions of the Otway Ranges using thermochronological data (Duddy 2003). In the Otway Ranges, approximately 1.5 to 3 km of the Eumeralla Formation has been eroded since the mid-Cretaceous, with up to 5 km removed at Cape Otway (Duddy 1994).

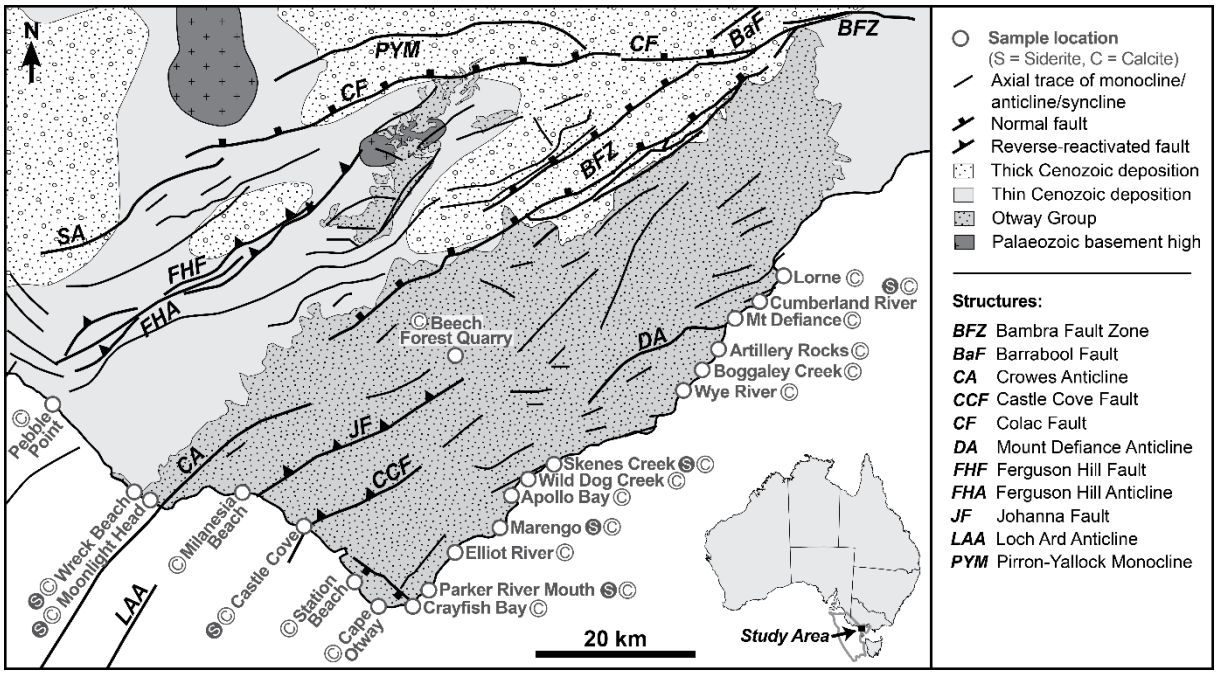

Figure 1. A map showing neotectonic structural discontinuities and sedimentary packages in the eastern Otway Basin, modified after Debenham et al. (2018) and Edwards et al. (1996). Sample locations are shown with the corresponding cement types (siderite or calcite) analysed in this study.

Pervasive diagenesis of volcanic detritus (e.g. volcanic glass, olivine, and orthopyroxene) within the Eumeralla Formation by connate pore water commenced immediately after burial (Duddy 1983; Duddy 2003). Pore-lining clays (e.g. chlorite and smectite) coated the remaining detrital grains within 10 m of burial (Duddy 2003). During early burial and prior to significant compaction, concretions containing manganese-bearing calcite and siderite cements precipitated throughout the formation (Gregory et al. 1989; Duddy 2003). These concretions preserve early pore fluid chemistry and original mineral compositions, particularly amphibole, plagioclase, and clinopyroxene (Duddy 2003), and protect these labile minerals from the influence of later pore fluids. The precipitation of calcite and siderite allowed zeolites (i.e. heulandite and clinoptilolite) to precipitate in the remaining pore space by reducing the partial pressure of CO_2 in the pore fluids (Duddy 2002). Upper sections of the Eumeralla Formation are characterised by a less than 1.5 km diagenetic zone of Ca-rich plagioclase and heulandite, identified as the andesine–heulandite diagenetic zone by Duddy (2003). Eumeralla Formation rocks buried to depths greater than 1.2 to 1.5 km are characterised by a zone of albitized Ca-rich plagioclase and K-rich feldspar, resulting from reaction with Na-rich fluids, and is identified as the albite–laumontite diagenetic zone by Duddy (2003).

2.3 Eastern Otway Basin palaeotemperatures

A study by Duddy (1994) using vitrinite reflectance analysis showed that maximum post-depositional palaeotemperatures of the Eumeralla Formation in the eastern Otway Basin varied between 60°C to more than 350°C. Palaeotemperatures are largely controlled by burial and elevated geothermal gradients, and show a spatial correlation with major faults and folds. Most locations in the eastern Otway Basin have

experienced temperatures above 100°C (Duddy 1994). The upper Eumeralla Formation at Moonlight Head has not been heated to significant temperatures (vitrinite reflectance temperature = 56°C) due to a lack of burial, and therefore preserves the original volcanogenic lithology and has not been albitized. Therefore, Moonlight Head is a site of interest for this study.

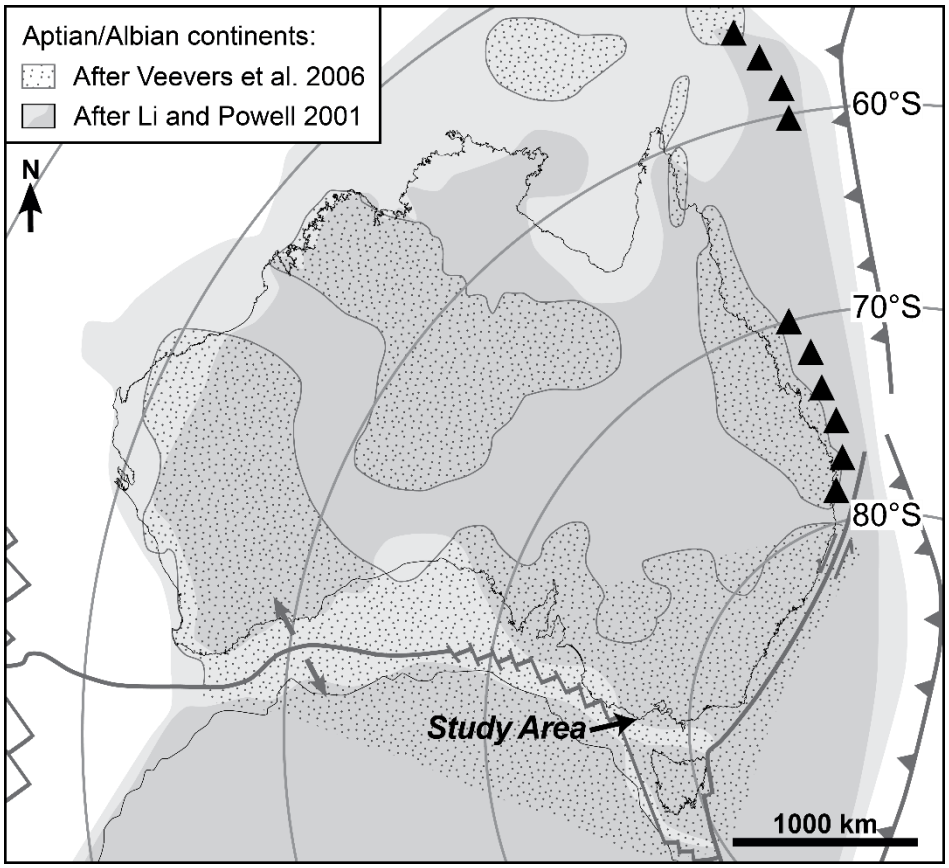

Figure 2. Aptian to Albian palaeogeographic reconstruction of Australia during the deposition of the Eumeralla Formation, with continents (shaded) after Veevers (2006) and Li and Powell (2001). Palaeolatitudes after Veevers et al. (1991).

2.4 Concretion and fracture samples in this study

The main aim for this study is to assess the source and precipitation temperature of carbonate cements in concretions and fractures in order to understand pore fluid evolution in the Eumeralla Formation. This can be investigated by assessing pore fluid chemistry preserved in concretions together with later fracture-hosted precipitated fluids and sedimentary fill. In the eastern Otway Basin, the Eumeralla Formation contains abundant manganese-bearing calcite- and siderite-cemented concretions. Calcite-cemented concretions are more common than siderite-cemented concretions. The concretions occur in a range of sizes, from the millimetre-scale to greater than 50 cm in diameter. They typically only contain one phase of cement, either calcite or siderite, in a single concretion. Some concretions transition from an earlier-formed calcite core to a later-formed siderite rim (Gregory et al. 1989). The relative timing of the events leading to the cementation of the calcite and siderite concretions is difficult to constrain based on textural relationships.

A complex array of brittle deformation structures, such as faults and fractures, have been documented in the eastern Otway Basin (Tassone et al. 2014; Bailey et al. 2015; Burgin et al. 2018; Debenham et al. 2018). Fractures are typically filled with either siderite, calcite, or quartz cements. In some instances,

both siderite and calcite cements occur in a single fracture (e.g. Parker River Mouth; Fig. 1). The relative formation timing of some of these fractures has been linked to deformation associated with faulting and fault reactivation (Debenham et al. 2018) reflecting both local stress regimes (Tassone et al. 2014) and basin-wide stress regimes (Burgin et al. 2018). Knowledge of the diagenetic, thermochronological, and structural history of a basin can be used to understand the causes and extent of fracture-hosted fluid flow events.

This study focuses specifically on concretions and fractures sampled from Moonlight Head and Castle Cove (Fig. 1). Stable isotope data and carbonate quantification data from concretions and fractures sampled throughout the eastern Otway Basin by Gregory et al. (1989) will also be utilised in this study. As the Eumeralla Formation at Moonlight Head has only experienced shallow burial, this location preserves the early diagenetic and original mineralogical composition of the Eumeralla Formation. Therefore, Moonlight Head is important for determining the baseline strontium isotopic composition of the Eumeralla Formation. The baseline will help determine the pore fluid evolution preserved in the concretion and fracture cement samples, which have been collected in the eastern Otway Basin, i.e. whether the fluids are sourced from a closed system (e.g. pore fluids that have been altered by diagenesis but have remained within the Eumeralla Formation) or an open system (e.g. influx of external sources of fluids). Stable isotopic analysis on the carbonate cements will also identify the source of the fluids, e.g. meteoric water, seawater, or upwelling hydrothermal fluids. Carbonate quantification analysis of the concretions (i.e. volume percent of carbonate in a concretion) can be used to calculate the original void space (i.e. porosity) of the rock (e.g. Lippmann 1955; Oertel and Curtis 1972; Gautier 1982). Porosity, in turn, is a proxy for burial depth (Gautier 1982), and therefore carbonate quantification analysis will help contextualise the geochemical data collected in this study in terms of depth and temperature.

3. Methods

3.1 Sample preparation

Calcite-cemented and siderite-cemented fracture and concretion samples were collected from cliff exposures and shore platforms throughout the eastern Otway Basin (Fig. 1) for carbon and oxygen stable isotope and strontium isotope analysis. Powdered samples were extracted from fracture cements using a dental technician's drill. The concretions were drilled in 1 cm increments from rim to core (Fig. 3). Carbonate mineralogy (i.e. calcite and siderite) was confirmed by mineralogical analysis on a FEI Quanta 600 backscattered Scanning Electron Microscope (BSEM) and a standard petrographic microscope, and no dolomite was identified.

3.2 Carbonate quantification in concretions and calculated burial depth

A modified pressure-calcimeter test was carried out following the method of Sherrod et al. (2002) in order to determine the percentage of carbonate present within the concretions. A 4 *M* hydrochloric acid was used to react with carbonate in 17 powdered rock samples (200 mg), 8 calcium carbonate standards of varying weights, and 2 blanks. A handheld manometer was used to record maximum pressure after 4 hours. The pressure measured from the standards and blanks was plotted against mass to calculate the polynomial regression trend line. The regression trend line was used to normalise the mass of the weighed samples and calculate the percentage of carbonate in each sample. The percentage of carbonate is equivalent to the initial porosity in the rock (Gautier 1982), and this porosity value was used to calculate burial depth. This method assumes that burial-related compaction follows a predictable trend with no overpressure effects. First, a burial depth trend was plotted on a compaction curve specifically determined

for the Eumeralla Formation by converting sonic transit time (Δt, µsec/ft) from Tassone et al. (2014) to porosity (φ, percentage) using Equation 1:

$$\varphi = (\Delta t - \Delta t_{ma})/(\Delta t_f - \Delta t_{ma}) \quad (1)$$

where Δt_{ma} = sonic transit time of the rock matrix (µsec/ft) and Δt_f = sonic transit time of the interstitial fluids (µsec/ft). Burial depth (m), in turn, was calculated using the logarithmic regression trend line of the burial depth trend (Equation 2):

$$\text{Burial depth} = -1196 \ln(\varphi) + 5469.5 \quad (2)$$

Equation 2 is consistent with porosities measured at different depths in a number of wells in the Otway Basin (e.g. Port Campbell-4, Heathfield-1, and Flaxmans-1).

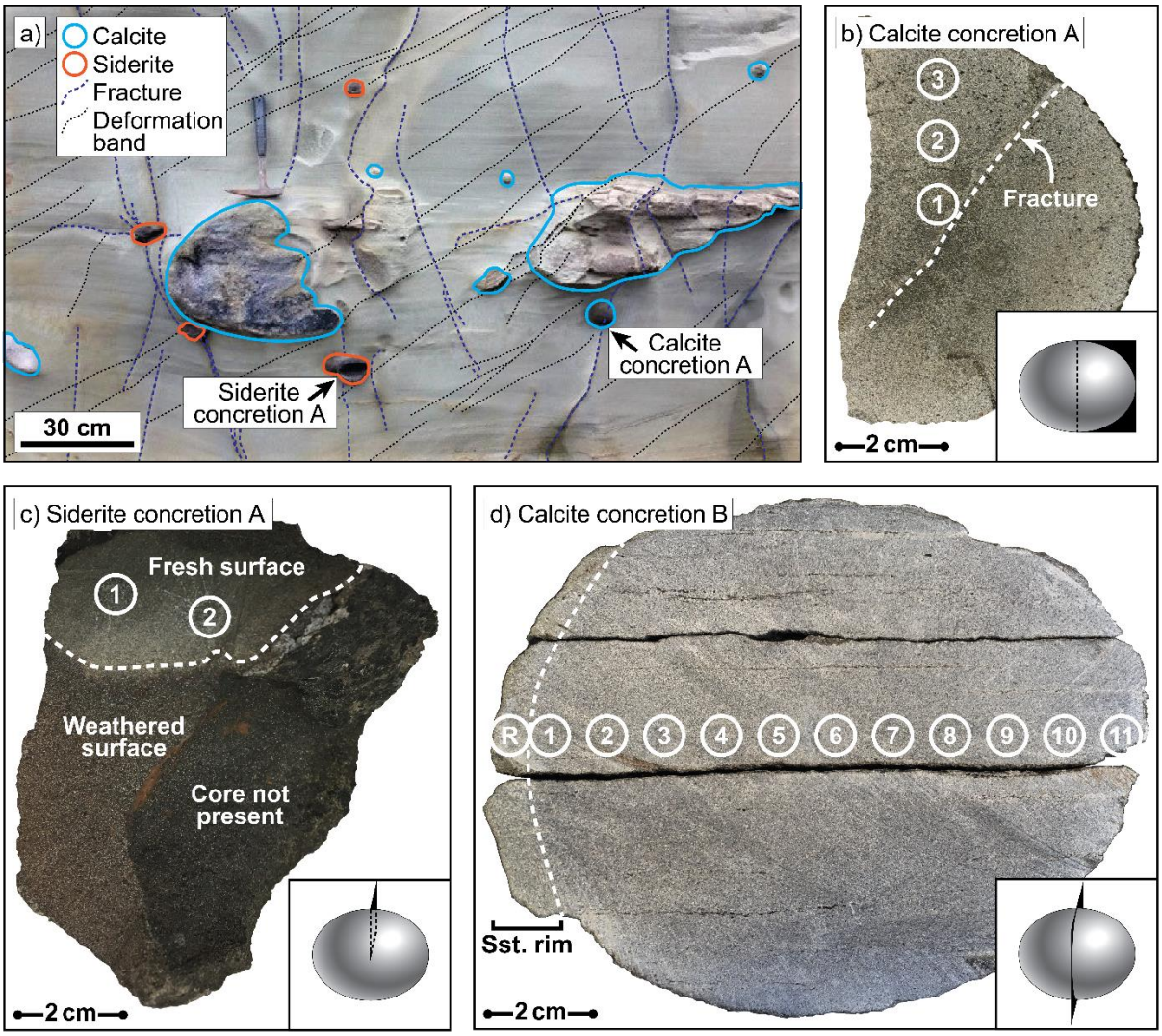

Figure 3. (a) Field photograph of the Eumeralla Formation at Castle Cove, showing the location of two concretions used in this study. Cross-section photographs and sub-sample locations for (b) a calcite concretion (RD14-372), (c) a siderite concretion (RD14-371), and (d) a calcite concretion (RD14-373) at Castle Cove. Calcite concretion B was sampled below the view of the field photograph.

3.3 Carbon and oxygen isotope analysis of fracture cements and concretions

A selection of 41 samples were measured for carbon ($\delta^{13}C$) and oxygen ($\delta^{18}O$) isotopes following a method that was modified from Spötl and Vennemann (2003). Powdered samples (0.001 mg) were placed into glass septa vials and purged with helium. Ten drops of 1 *M* phosphoric acid were manually added to the vials. The vials were left for approximately 24 hours at 70°C to react with the carbonates and produce carbon dioxide gas (CO_2). The isotopic ratio of the CO_2 gas was measured using a Nu Instruments Dual Inlet Isotope Ratio Mass Spectrometer (DI-IRMS) at the University of Adelaide. The ANU P3 (*Tridacna gigas* aragonite shell; literature value = $\delta^{13}C$: 2.23‰, $\delta^{18}O$: –0.31‰), UAC-1 (calcium carbonate; literature value = $\delta^{13}C$: –15‰, $\delta^{18}O$: –18.4‰), and IAEA CO-8 1 (marble; literature value = $\delta^{13}C$: –5.76‰, $\delta^{18}O$: –22.7‰) reference materials were used as internal accuracy standards. $\delta^{13}C$ and $\delta^{18}O$ values are reported in per mille (‰) units relative to the Vienna Pee Dee Belemnite (VPDB) standard and Standard Mean Ocean Water (SMOW), respectively. $\delta^{13}C$ and $\delta^{18}O$ values of calcite-cemented concretion and fracture samples from Gregory et al. (1989) are also compared in this study. Two concretion samples from Gregory et al. (1989) were re-analysed and this ensured that the stable isotope data from Gregory et al. (1989) was comparable to the data collected in this study.

3.4 Strontium isotope analysis of fracture cements and concretions

A selection of 25 samples were measured for strontium ($^{87}Sr/^{86}Sr$) isotope tracers. Powdered samples (0.001 mg) were placed into clean polytetrafluoroethylene (PTFE) vials and 2 mL of 1 *M* hydrochloric acid was manually added to the vials containing calcite cements. The samples were leached for approximately 24 hours at room temperature. Samples containing siderite cements were leached with 6 *M* hydrochloric acid for 48 hours at 140°C. All samples were centrifuged and the supernatant was transferred to a clean PTFE vial and left to dry. Whole rock sandstone samples, several whole concretion samples (sub-sampled from the core of the concretions), and two mineral separate samples (heulandite and hornblende) from Moonlight Head and Castle Cove were further dissolved 28 *M* hydrofluoric acid in order to extract strontium from the whole rock. The samples were transferred in 8 *M* nitric acid to chromatographic columns that contained Eichrom strontium resin SPS (particle diameter: 50–100 μm). The samples were cleaned with 8 *M* nitric acid and the strontium fraction was extracted with 0.05 *M* nitric acid. The purified strontium fraction was loaded on to degassed rhenium filaments and the $^{87}Sr/^{86}Sr$ isotopic ratio was measured using a Phoenix Isotopx Thermal Ionisation Mass Spectrometer (TIMS) at the University of Adelaide. Two standards, i.e. JDo-1 (Kuzuu dolomite) and JLs-1 (Garo limestone) reference materials issued by the Geological Survey of Japan, and two blank vials spiked with strontium were used as internal accuracy standards. The average $^{87}Sr/^{86}Sr$ isotopic ratio for JDo-1 was 0.707547 ± 0.000003 (2σ; n = 2; GeoReM literature value = 0.70752) and the average $^{87}Sr/^{86}Sr$ isotopic ratio for JLs-1 was 0.707826 ± 0.000003 (2σ; n = 2; GeoReM literature value = 0.70783). The spiked blanks contained less than 2 ng of strontium and the total contribution of strontium was less than 0.1%, therefore no correction for the blanks were made in this study. NISTSRM-987 was also used to test external reproducibility, which yielded an average $^{87}Sr/^{86}Sr$ isotopic ratio of 0.710244 ± 0.000012 (2σ; n = 14; literature value = 0.710248).

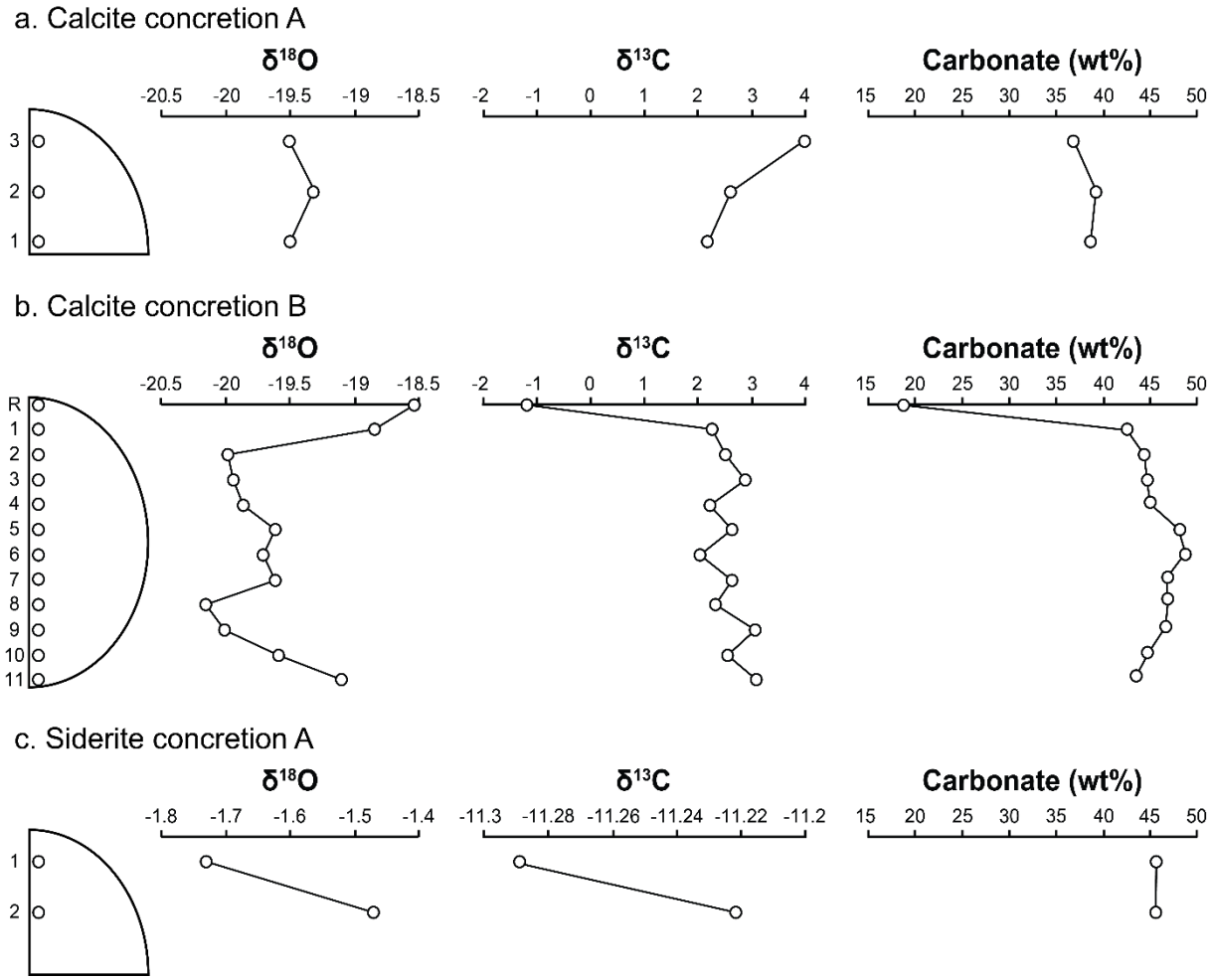

Figure 4. $\delta^{18}O$ SMOW, $\delta^{13}C$ VPDB, and carbonate weight percentage values of subsamples taken from rim to core in transects across the carbonate concretions in Figure 3. Calcite concretion B (panel b) shows the radial symmetry of the isotope compositions across the concretion.

4. Results

4.1 Carbonate quantification in concretions

Calcite in concretions analysed in this study ranges from 19% to 55% by volume, and siderite in concretions ranges from 42% to 46% by volume. Comparatively, the calcite in concretions analysed by Gregory et al. (1989) ranges between 9% and 55% by volume. While sub-samples taken from the core of the concretions (i.e. centre of the concretions) are characterised by the highest percentages of carbonates and the carbonate percentage is often lower at the rim of the concretions, the percentage of carbonate generally does not vary significantly from core to rim (Fig. 4). Therefore, this indicates that individual concretions formed at a similar depth over a short depth interval, i.e. concretion formation from core to rim occurs within ca. 2 m to 530 m.

4.2 Carbon and oxygen isotopes

The carbon and oxygen isotopic composition of calcite- and siderite-cemented concretions and fractures are highly variable (Fig. 5a). The $\delta^{18}O$ values of the calcite concretions analysed in this study range between 10.1‰ and 15.0‰ SMOW, while the $\delta^{13}C$ values are between –8.6‰ and 4.0‰ VPDB. The isotopic composition of the siderite concretions is heavier than that of the calcite concretions; they are

enriched in ^{18}O and ^{13}C relative to SMOW and VPDB, respectively (Fig. 5a). The $\delta^{18}O$ values of the siderite concretions range between 27.8‰ and 29.4‰ SMOW, while the $\delta^{13}C$ values are between –11.3‰ and 10.9‰ VPDB. The isotopic composition of the fracture-hosted cements is more variable than that of the concretion-hosted cements. The $\delta^{18}O$ values of the calcite-filled fractures analysed in this study range between 5.4‰ and 29.6‰ SMOW, while the $\delta^{13}C$ values are between –38.8‰ and 2.2‰ VPDB. The siderite-filled fractures have similar stable isotope values as the siderite concretions (Fig. 5a). The $\delta^{18}O$ values of the siderite-filled fractures range between 23.4‰ and 29.9‰ SMOW, while the $\delta^{13}C$ values are between –16.8‰ and –3.7‰ VPDB. Overall, the siderite-cemented concretions and fractures have heavier mean $\delta^{18}O$ values and lighter mean $\delta^{13}C$ values than calcite-cemented concretions and fractures.

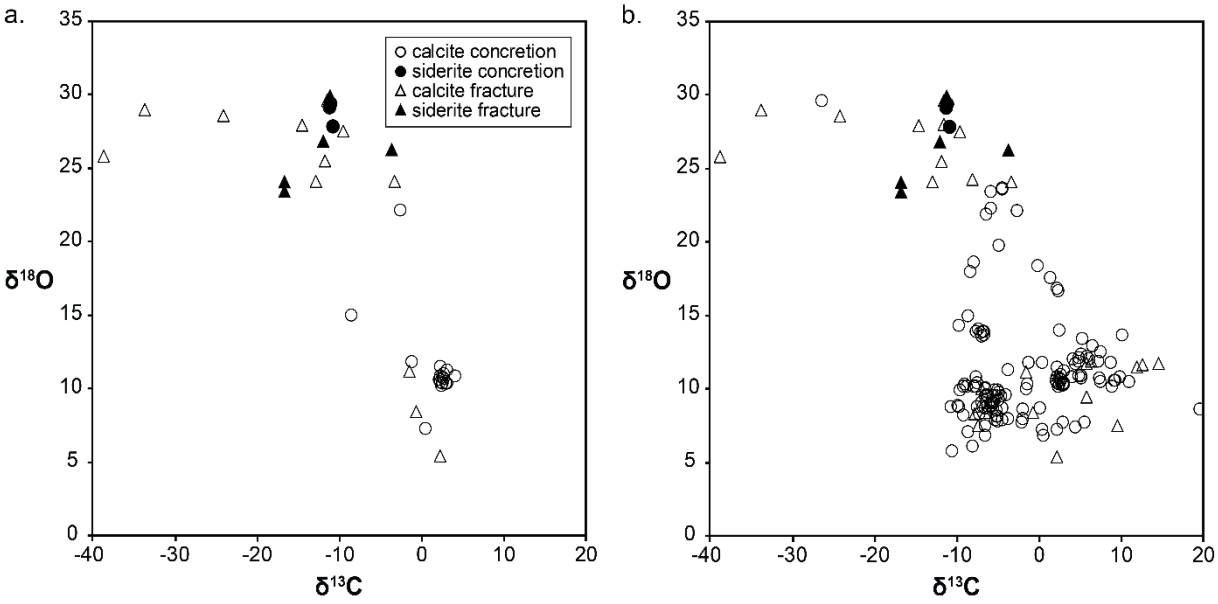

Figure 5. $\delta^{18}O$ SMOW values relative to $\delta^{13}C$ VPDB values for calcite- and siderite-cemented concretions and fractures from (a) this study, and (b) this study and Gregory et al. (1989).

The range of $\delta^{13}C$ and $\delta^{18}O$ values from concretions and fractures collected in this study are comparable to the values measured by Gregory et al. (1989) (Fig. 5b). The $\delta^{18}O$ values plot in two distinct groups (Fig. 5b): (1) approximately 5‰ to 15‰ SMOW, and (2) approximately 22‰ to 30‰ SMOW. The first group is composed of calcite concretions from this study and from Gregory et al. (1989), together with calcite-cemented fractures sampled from Castle Cove, Cape Otway, and Skenes Creek, and calcite-cemented fractures within concretions collected by Gregory et al. (1989). The calcite-cemented concretions have exceptionally light oxygen isotope ratios in comparison to siderite-cemented concretions. The second group is composed of calcite-cemented fractures from the remaining study locations, together with all the siderite-cemented concretion and fracture samples analysed in this study. Siderite-cemented concretions analysed by Gregory et al. (1989) also plotted in this range. Approximately four calcite concretion samples and two calcite-cemented fractures within concretions from Gregory et al. (1989) are also included in this group (Fig. 5b). This group is characterised by heavier oxygen isotope ratios and lighter carbon isotope ratios relative to the first group.

Oxygen and carbon isotopic compositions have been plotted relative to the percentage of carbonates in the concretions (Fig. 6). There is an overall trend of decreasing $\delta^{18}O$ values (by approximately 10‰)

with increasing percentage of carbonates (Fig. 6a), i.e. the oxygen isotopic composition of carbonates in the concretions becomes lighter with increasing burial depth. The $\delta^{18}O$ values within individual concretions, however, can be variable, but typically shows an increase in $\delta^{18}O$ values as the percentage of carbonates decreases from the core to the rim, i.e. the oxygen isotopic composition of carbonates in the concretions becomes lighter toward the rim. The $\delta^{13}C$ values are considerably more scattered and there appears to be only a weak overall trend of decreasing $\delta^{13}C$ values with increasing percentage of carbonates, particularly in the cores of concretions, (Fig. 6b), i.e. the carbon isotopic composition of carbonates in the concretion cores becomes lighter with increasing burial depth. Within individual concretions, the $\delta^{13}C$ values either decrease with a decreasing percentage of carbonates or are variable and do not exhibit a relationship with the percentage of carbonates.

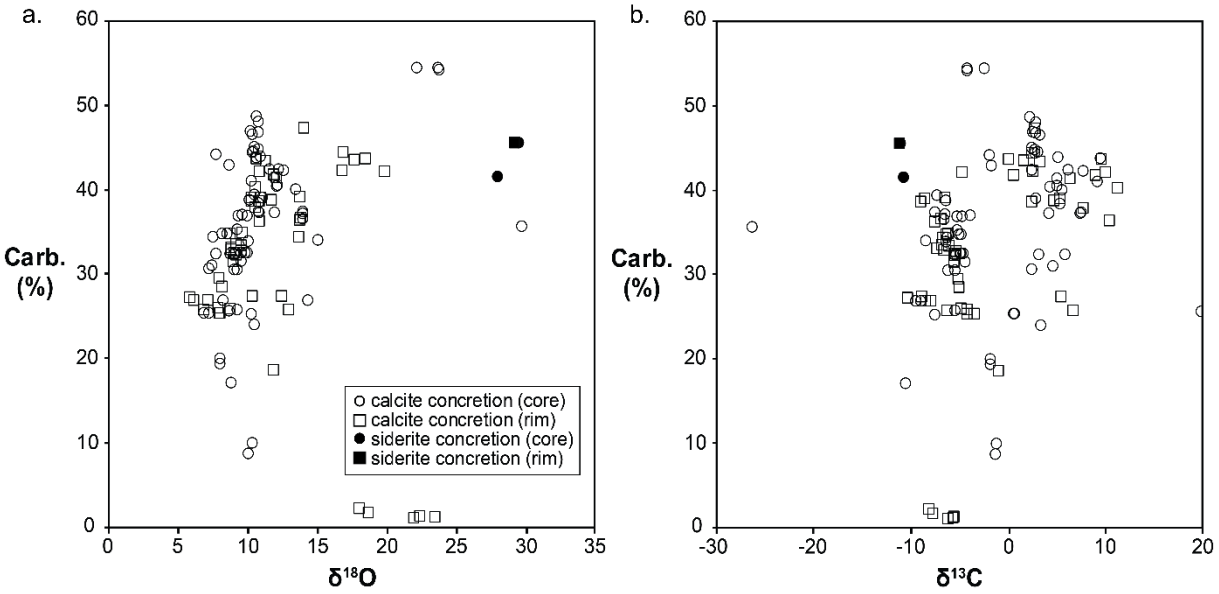

Figure 6. Weight percentage of carbonates relative to (a) $\delta^{18}O$ SMOW values from this study and Gregory et al. (1989), and (b) $\delta^{13}C$ VPDB values from this study and Gregory et al. (1989).

4.3 Strontium isotopes

The strontium isotopic composition of the Eumeralla Formation at Moonlight Head is 0.706061, and the $^{87}Sr/^{86}Sr$ values for hornblende and zeolite (heulandite group) mineral separates from this sandstone are 0.704761 and 0.705987, respectively. The $^{87}Sr/^{86}Sr$ values of the whole rock mineral matrix (without carbonates) within calcite- and siderite-cemented concretions at Moonlight Head are 0.705733 and 0.705960, respectively. These values are very similar and they are also similar to that of the Eumeralla Formation at Moonlight Head (Fig. 7). As concretions preserve the early mineralogical composition of the Eumeralla Formation, this similarity shows that the Eumeralla Formation sandstone at Moonlight Head also reflects an early diagenetic, mineralogical composition. At Moonlight Head, the $^{87}Sr/^{86}Sr$ value of the calcite concretion is 0.708174, while the $^{87}Sr/^{86}Sr$ value of the siderite concretion is 0.706759 (Fig. 7).

The strontium isotopic composition of the Eumeralla Formation at Castle Cove is 0.710463, which is more radiogenic than that of the Eumeralla Formation at Moonlight Head; it is enriched in ^{87}Sr relative to ^{86}Sr (Fig. 7). The $^{87}Sr/^{86}Sr$ values of the whole rock mineral matrix (without carbonates) within calcite- and siderite-cemented concretions at Castle Cove are 0.707373 and 0.707238, respectively. These values

are significantly less radiogenic than that of the Eumeralla Formation at Castle Cove, but more radiogenic than the $^{87}Sr/^{86}Sr$ values observed in the concretions at Moonlight Head (Fig. 7). The $^{87}Sr/^{86}Sr$ values of the calcite fractures in the eastern Otway Ranges range between 0.704317 and 0.709327, while the siderite fractures range between 0.705873 and 0.709882 (Fig. 7). Overall, the mean $^{87}Sr/^{86}Sr$ value of siderite-cemented concretions and fractures is more radiogenic than that of calcite-cemented concretions and fractures.

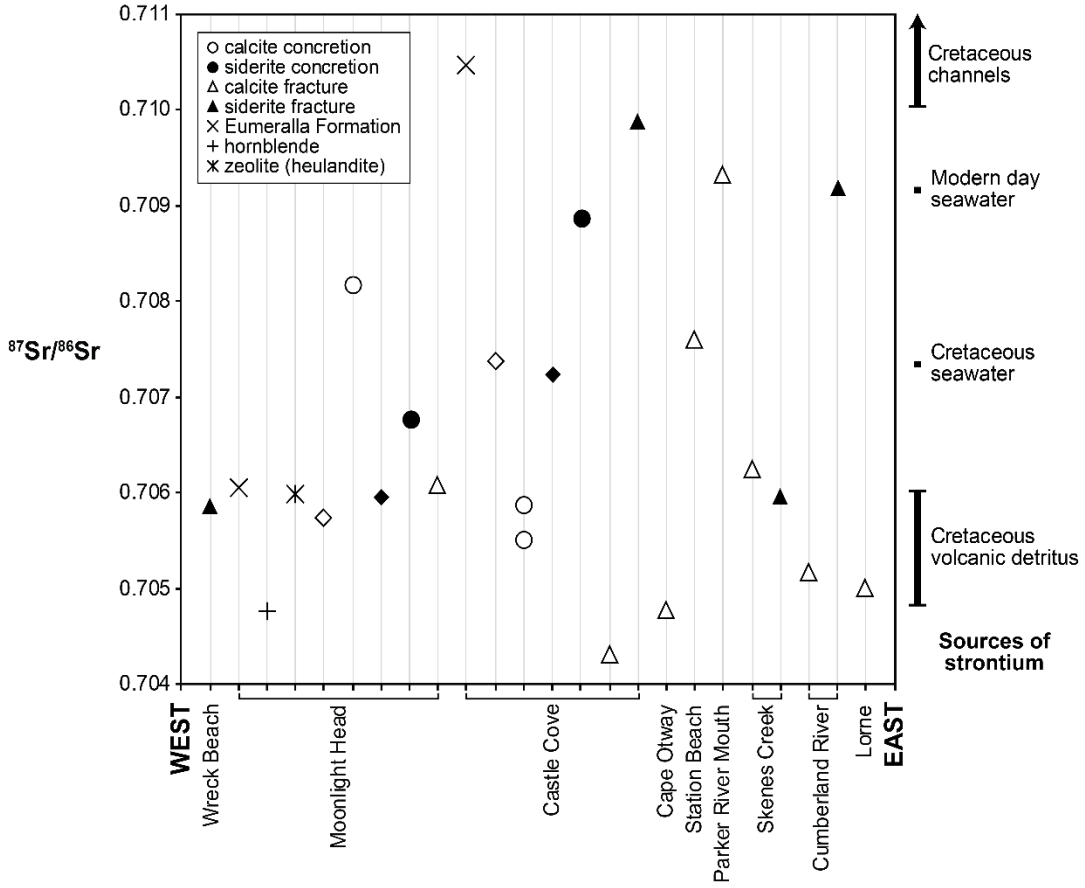

Figure 7. The $^{87}Sr/^{86}Sr$ values of concretion, fracture, and sandstone samples from locations in the eastern Otway Basin, from west to east. The range of $^{87}Sr/^{86}Sr$ values of various sources of strontium are indicated on the right. The $^{87}Sr/^{86}Sr$ values are derived from: Bralower et al. (1997) for Cretaceous seawater values; Palmer and Edmond (1989) for Cretaceous fluvial channel values; hornblende and zeolite separates in this study for volcanic detritus; and Herut et al. (1993) for modern sea water.

Strontium isotopic composition has been plotted relative to oxygen and carbon isotopic compositions (Fig. 8). This plot shows that siderite cemented-concretions and fractures typically have heavier oxygen and carbon isotope ratios and more radiogenic strontium values than calcite-cemented concretions and fractures. While there is only a weak correlation (coefficient of determination, $R^2 = 0.22$) between the $^{87}Sr/^{86}Sr$ values and $\delta^{18}O$ values of calcite- and siderite-cemented concretions and fractures, siderite-cemented samples consistently have more radiogenic $^{87}Sr/^{86}Sr$ values, heavier $\delta^{18}O$ values, and moderately enriched $\delta^{13}C$ values relative to calcite-cemented samples. A siderite concretion from Castle Cove and a calcite fracture from Parker River Mouth have exceptionally heavy oxygen isotope ratios (greater than 29.1‰) and radiogenic strontium values (greater than 0.708858; Fig. 8). There is no clear relationship between the $^{87}Sr/^{86}Sr$ values and $\delta^{13}C$ values of calcite- and siderite-cemented concretions and fractures.

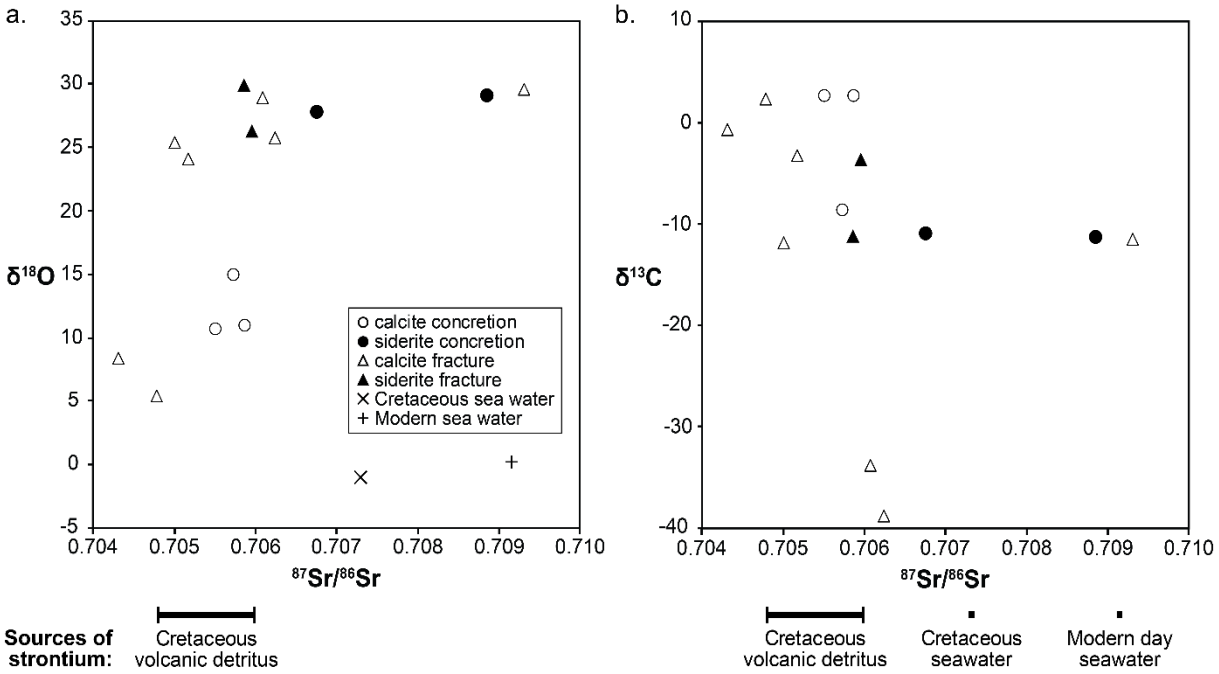

Figure 8. $^{87}Sr/^{86}Sr$ values relative to (a) $\delta^{18}O$ SMOW values, and (b) $\delta^{13}C$ VPDB values. The $^{87}Sr/^{86}Sr$ values are derived from: Bralower et al. (1997) for Cretaceous seawater values; and zeolite separates in this study for volcanic detritus; and Herut et al. (1993) for modern sea water.

5. Interpretation and discussion

5.1 Depth of concretion formation

The concretions in the eastern Otway Basin are characterised by an internal structure that is concentrically zoned, with radial growth from the core to an outer rim (Gill et al. 1977). Stable isotopic data from concretions collected in this study (Fig. 4) and by Gregory et al. (1989) also supports radial growth, i.e. stable isotopic compositions are symmetrical across the concretions. As the carbonate cements fill pore space and do not appear to replace detrital grains, the percentage of carbonates is a proxy for the initial porosity of the rock. Given that the percentage of carbonates indicates the initial porosity, and porosity in turn is a proxy for burial depth (Gautier 1982), concretions with the highest percentage of carbonates are interpreted to have formed at shallow burial depths, while concretions with the lowest percentage of carbonates formed at greater burial depths. The burial depth trend on the compaction curve derived from Tassone et al. (2014) shows that, based on the percentage of carbonates in concretions collected in this study together with Gregory et al. (1989), the concretions formed within the initial ca. 700 m to 2,900 m of burial (Fig. 9).

5.2 Sources of carbon and oxygen

5.2.1 Oxygen isotopic compositions

The oxygen isotopic composition of carbonate cements in the eastern Otway Basin show two distinct groups; i.e. a group that is characterised by exceptionally light $\delta^{18}O$ values and a group that has relatively heavier $\delta^{18}O$ values (Fig. 5b). The latter group will be discussed first. Siderite-cemented concretions and fractures, and most (75%) of the calcite-cemented fractures analysed in this study, have heavy oxygen isotope ratios (approximately 22‰ to 30‰ SMOW) and light carbon isotope ratios (less than –2‰ VPDB). These values plot within the range of $\delta^{18}O$ and $\delta^{13}C$ values typical of seawater-derived cements preserved in marine concretions (Mozley and Burns 1993).

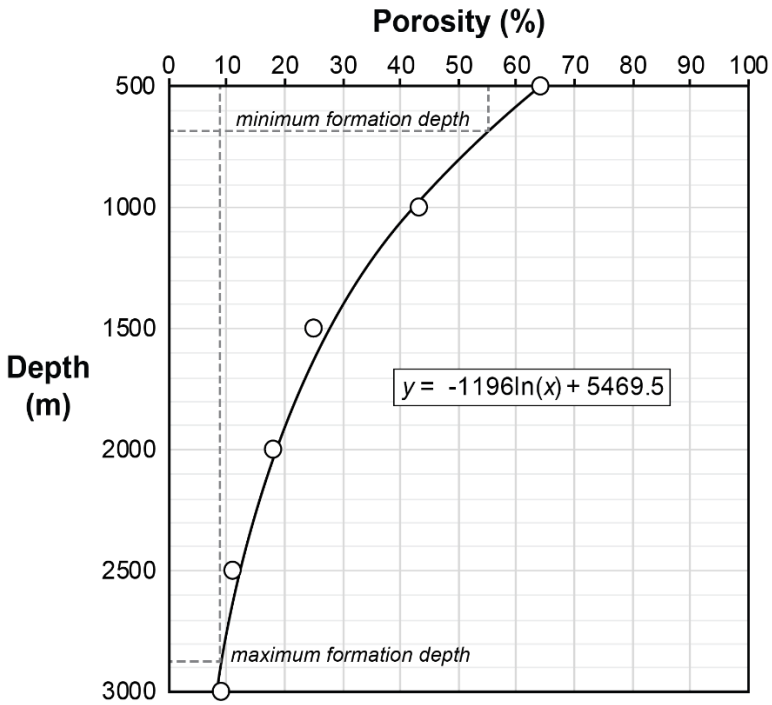

Figure 9. A compaction curve of the Eumeralla Formation in the eastern Otway Basin calculated from Tassone et al. (2014). This compaction curve has been derived from the fine-grained Eumeralla Formation in the Otway Basin. The formation depths of the concretions are calculated using the weight percentage of carbonates in the concretions as a proxy for porosity. The minimum and maximum formation depths of the concretions in this study and Gregory et al. (1989) are indicated on the burial trend and are 688 m (55% porosity) to 2,882 m (9% porosity), respectively. The circles indicate porosities at 500 m intervals.

Calcite-cemented concretions have exceptionally light oxygen isotope ratios (approximately 5‰ to 15‰ SMOW) in comparison to siderite-cemented concretions (Fig. 5b), and low $\delta^{18}O$ values such as these are not often observed in concretions (Mozley and Burns 1993). Calcite-cemented fractures from Castle Cove, Cape Otway, and Skenes Creek also have light oxygen isotopic compositions. The oxygen isotopic composition of carbonate cements is predominantly controlled by the source of the pore fluids and the temperature of carbonate precipitation. Mozley and Burns (1993) and Bojanowski et al. (2014) have speculated a number of processes that can lower the $\delta^{18}O$ values of pore fluids, and three main processes are described here;

(1) Meteoric water input during diagenesis is the most commonly described process for depleted pore fluid $\delta^{18}O$ values (e.g. Hudson 1978; Thyne and Boles 1989; Bloch 1990). Given the fluvial and deltaic depositional environment of the Eumeralla Formation, it is not surprising that meteoric water was present within the sediment during diagenesis and resulted in depleted $\delta^{18}O$ values.

(2) Alteration of volcanic detritus (e.g. volcanic glass) to clay minerals (e.g. smectite) results in the depletion of $\delta^{18}O$ values in pore fluids (Lawrence and Gieskes 1981; Pirrie and Marshall 1991). Pervasive diagenesis and alteration of volcanic detritus to pore-lining clays (e.g. chlorite and smectite) within the Eumeralla Formation immediately after burial has been previously described by Duddy (1983) and Duddy (2003). Fig. 6a shows a moderate deflection in $\delta^{18}O$ values at approximately 34 wt% carbonate to low values at greater depths, which is equivalent to 1.25 km depth (Fig. 9). This depth correlates with a transition to the albite–laumontite diagenetic zone from the andesine–heulandite diagenetic zone (Duddy 2003). This thus suggests that continued diagenetic alteration of the volcanic detritus may have influenced the oxygen isotopic composition of pore fluids at a range of depths.

(3) Carbonate recrystallization of concretions with increased burial and elevated temperatures which can re-equilibrate the oxygen isotopic composition, resulting in depleted $\delta^{18}O$ values (Mozley and Burns 1993; Morad 1998). The oxygen isotopic composition of carbonate cements in the concretions analysed in this study, together with the stable isotope data collected by Gregory et al. (1989), becomes lighter with increasing burial depth, and therefore increasing temperature (Fig. 6a). High palaeotemperatures (>105 °C) can explain the oxygen isotope depletion observed in some calcite-cemented fractures. Cape Otway records the highest palaeotemperatures associated with former burial depths in the eastern Otway Basin (>350 °C) based on vitrinite reflectance analysis by Duddy (1994) and the calcite-cemented fracture from this location records the lightest $\delta^{18}O$ value (Fig. 5b). Therefore, all three processes may have contributed to a depletion in the oxygen isotope ratios.

5.2.2 Calculated oxygen isotopic compositions of original pore fluids

The oxygen isotopic composition of the original pore fluids from which the cements in the concretions and fractures formed from can be calculated using the measured isotopic composition of the cements together with estimates of the cement precipitation temperature. The oxygen isotopic composition of pore fluids in equilibrium with calcite and siderite cements can be calculated using equations from O'Neil et al. (1969) and Carothers et al. (1988), respectively:

$$\text{Calcite–water}: \delta^{18}O_{water} = \delta^{18}O_{calcite} - ((2780000/T^2) - 2.89) \quad (3)$$

$$\text{Siderite–water}: \delta^{18}O_{water} = \delta^{18}O_{siderite} - ((3130000/T^2) - 2.89) \quad (4)$$

The $\delta^{18}O$ of the original pore fluids ($\delta^{18}O_{water}$) has been calculated for a range of subsurface temperatures (T) in order to capture the range of possible temperatures for carbonate precipitation (Fig. 10). Firstly, the $\delta^{18}O_{water}$ was calculated at 15°C as a minimum estimate for carbonate precipitation temperature. The $\delta^{18}O_{water}$ values of pore fluids precipitated at 15°C range from –25‰ to –1‰ for calcite cements based on fractionation Equation 3, and from –11‰ to –5‰ for siderite cements based on Equation 4 (Fig. 10a). The $\delta^{18}O_{water}$ of the original fluids (of concretion cements) has also been calculated using temperatures derived from the formation depths of the concretions (Fig. 9) and the geothermal gradient of the eastern Otway Basin during the mid-Cretaceous (i.e. approximately 60°C/km; Duddy 2003). The $\delta^{18}O_{water}$ values of the fluids precipitated at temperatures derived the formation depths of the concretions are considerably more variable, and range from –26‰ to 18‰ for calcite cements, and from 3‰ to 4‰ for siderite cements (Fig. 10b). Finally, the $\delta^{18}O_{water}$ was calculated at maximum vitrinite reflectance temperatures from Duddy (1994) as a maximum estimate for carbonate precipitation temperature. The $\delta^{18}O_{water}$ values of the fluids precipitated at estimates of maximum temperatures range from –13‰ to 15‰ for calcite cements, and from –2‰ to 12‰ for siderite cements (Fig. 10c).

As the concretions formed at depths between 688 m and 2,882 m and not near the surface, the pore fluid temperatures would have been similar to the subsurface temperatures at these depths. Therefore, the $\delta^{18}O_{water}$ values calculated from subsurface temperatures during concretion formation are considered to be the best estimate of the pore fluid isotopic compositions of the concretion cements. The $\delta^{18}O_{water}$ values suggest that most (75%) calcite-cemented concretions and some (25%) calcite-cemented fractures formed from pore fluids that were lighter than Cretaceous seawater, i.e. meteoric water (Fig. 10). Meteoric water is depleted in heavy oxygen isotopes relative to seawater (Gat 1996), and considering the fluvial and deltaic depositional environment of the Eumeralla Formation, it would be expected that meteoric

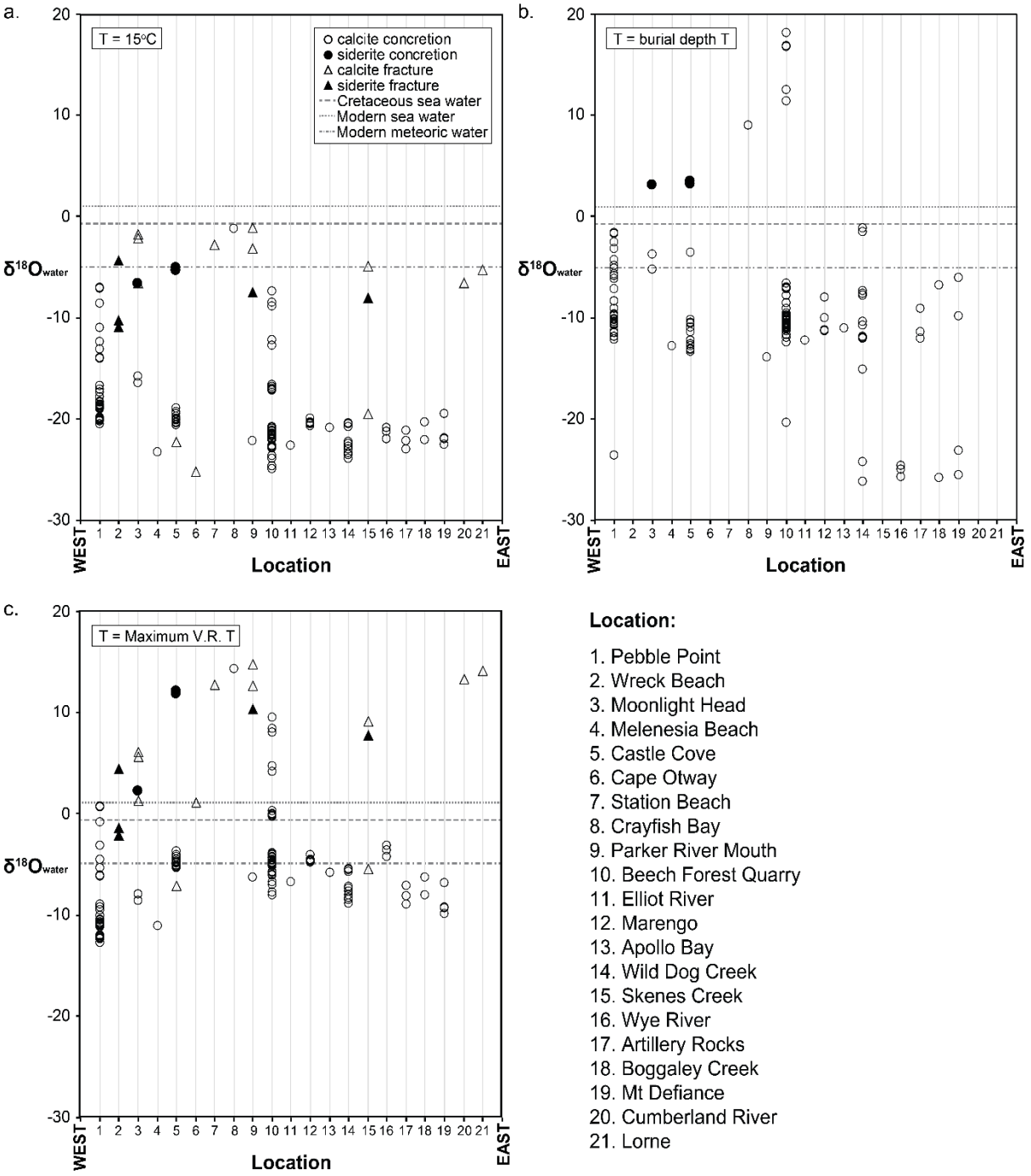

Figure 10. The $\delta^{18}O$ values of the original pore fluids ($\delta^{18}O_{water}$) for a range of subsurface temperatures (*T*) for carbonate precipitation in concretions and fractures, using fractionation equations from O'Neil et al. (1969) and Carothers et al. (1988) for calcite and siderite, respectively. (a) $\delta^{18}O_{water}$ calculated at 15°C as a minimum estimate for carbonate precipitation temperature. (b) $\delta^{18}O_{water}$ calculated using temperatures derived from the formation depths of the concretions and the geothermal gradient of the eastern Otway Basin during the mid-Cretaceous (approximately 60°C/km). (c) $\delta^{18}O_{water}$ calculated at maximum vitrinite reflectance temperatures from Duddy (1994) as a maximum estimate for carbonate precipitation temperature.

water was present within the pore space. A meteoric water source for the calcite-cemented concretions is consistent with interpretations made by Gregory et al. (1989). The $\delta^{18}O_{water}$ values calculated from both minimum and maximum estimates of precipitation temperature represent the range from which the fracture-hosted cements may have formed. The heavier $\delta^{18}O_{water}$ values preserved within all siderite-cemented concretions and fractures and most calcite-cemented fractures indicates that they were derived

from fluids similar to Cretaceous seawater (Fig. 10). The siderite-cemented concretions analysed in this study formed approximately within the first kilometre of burial (mean = 938 m; 1σ = 64 m), at shallower depths than most calcite-cemented concretions (mean = 1,241 m; 1σ = 340 m). A marine incursion during deposition (equivalent to shallow formation depths) could explain the enriched isotope values. Indeed, a marine incursion during the Albian has been indicated by the presence of dinoflagellates (Korasidis et al. 2016). However, given that the Eumeralla Formation is dominated by a fluvial and deltaic depositional environment, and as the siderite-cemented concretions are far less common than calcite-cemented concretions, this interpretation remains speculative.

5.2.3 Carbon isotopic compositions

The carbon isotopic composition of carbonate cements hosted within the concretions and fractures is highly variable (Fig. 6b). The carbon isotopic composition of carbonate cements reflects local variations related to the depositional environment and the types of organic reactions occurring simultaneously with carbonate formation (Mozley and Burns 1993). Therefore trends of $\delta^{13}C$ values may be location specific. This explains the high variability exhibited by the $\delta^{13}C$ values (Fig. 5). Calcite-cemented concretions are characterised by a range of carbon isotopic compositions (approximately –26‰ to 20‰), but most have relatively heavy carbon isotopic compositions (approximately –11‰ to 11‰). Enriched carbon isotopic compositions suggest that CO_2 from dissolved inorganic carbon, which was derived from the methanogenic fermentation of organic matter, was the primary source of carbon in these cements (Curtis and Coleman 1986; Morad 1998). However, given the range of $\delta^{13}C$ values, the carbon isotopic composition of these cements may not necessarily be derived from a single source, rather, the composition could represent an integration of signals from a range of sources (Raiswell and Fisher 2000). The siderite-cemented concretions and fractures have lighter $\delta^{13}C$ values (approximately –17‰ to –4‰) than the calcite-cemented concretions. Most calcite-cemented fractures also have light $\delta^{13}C$ values (approximately –2‰ to –15‰) and some fractures have exceptionally light $\delta^{13}C$ values (approximately –24‰ to –39‰). Light carbon isotopic compositions such as these suggest that these cements could have formed from CO_2 derived from the oxidation of methane (Raiswell 1987).

5.3 Sources of strontium

The potential source materials that may be responsible for strontium enrichment and strontium isotopic compositions of pore fluids include: (1) continental detritus imported by Cretaceous fluvial channels, estimated to be $^{87}Sr/^{86}Sr$ = 0.71 to 0.72 (Fig. 11; Palmer and Edmond 1989); (2) volcanic detritus from contemporaneous volcanism, estimated to be approximately $^{87}Sr/^{86}Sr$ = 0.7048 to 0.7060, based on the strontium isotopic compositions of mineral separates in this study, i.e. the lower range $^{87}Sr/^{86}Sr$ value for unaltered hornblende separates and the higher value for zeolite (heulandite group) separates from the Eumeralla Formation at Moonlight Head (Fig. 11). The zeolites have precipitated following the diagenesis of volcanic detritus (Duddy 2002); and (3) Cretaceous seawater, $^{87}Sr/^{86}Sr$ = 0.7073 (Fig. 11; Bralower et al. 1997). Each of the potential source materials is discussed in detail below.

Only one sample, from the Eumeralla Formation at Castle Cove, reflects a radiogenic strontium isotopic composition that is analogous to continental detritus imported by channels during the Cretaceous (Fig. 7). This indicates that continental detritus was not the dominant source of the strontium isotopic composition of pore fluids. Most samples have $^{87}Sr/^{86}Sr$ values that are less radiogenic than Cretaceous seawater, and half of the samples analysed in this study have strontium isotopic compositions that are

representative of contemporaneous volcanic detritus (Fig. 7). Therefore, the relatively unradiogenic strontium isotopic composition of many concretion and fracture cements in the eastern Otway Basin suggests that pore fluids were strongly influenced by the dissolution and alteration of volcanic detritus.

Mineral separate samples of volcanic detritus (hornblende) and volcanic-derived minerals (zeolites) from Moonlight Head have been used to determine the approximate range of the strontium isotopic composition of volcanic detritus (i.e. $^{87}Sr/^{86}Sr = 0.7048$ to 0.7060). This $^{87}Sr/^{86}Sr$ value, together with the strontium isotopic compositions from samples of the Eumeralla Formation and concretion mineral matrix at Moonlight Head, is important for determining the baseline isotopic composition of the upper Eumeralla Formation. This baseline can help determine the source of the fluids in the concretion and fracture cement samples at Moonlight Head and other locations in the eastern Otway Basin. Calcite-cemented fracture samples from Moonlight Head, Cape Otway, Cumberland River, and Lorne, siderite-cemented fracture samples from Wreck Beach and Skenes Creek, and calcite-cemented concretion samples from Castle Cove, preserve a strontium isotopic composition representative of volcanic detritus (Fig. 7). Calcite-cemented fracture samples from Castle Cove and Skenes Creek also have similar $^{87}Sr/^{86}Sr$ values to that of volcanic detritus (Fig. 7). This suggests that pore fluids were strongly influenced by the dissolution and alteration of volcanic detritus at these locations, which indicates that the pore fluids were sourced locally in a closed system.

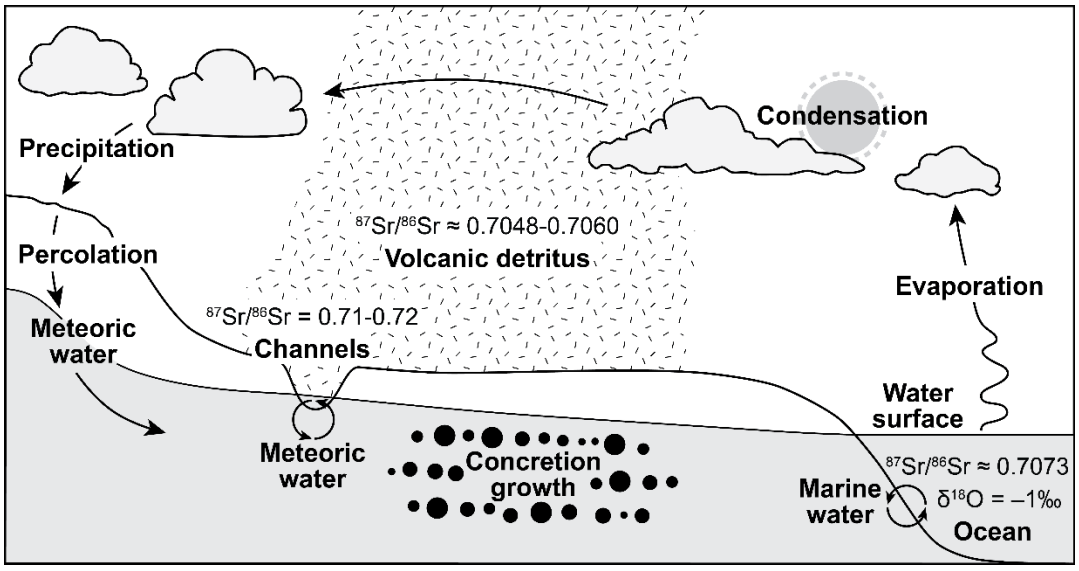

Figure 11. Schematic representation of stable isotope and strontium isotope processes in the water cycle, including external input from volcanoes, during the deposition of the Eumeralla Formation in the mid-Cretaceous. $\delta^{18}O$ values assume a temperature of 10–15°C following Price et al. (2012). The $\delta^{18}O$ values of different processes are derived from: Price et al. (2012) for Cretaceous seawater values. The $^{87}Sr/^{86}Sr$ isotopic ratio of different processes are derived from: Bralower et al. (1997) for Cretaceous seawater values; Palmer and Edmond (1989) for Cretaceous fluvial channel values; and hornblende and zeolite separates in this study for volcanic detritus values.

The remaining samples are more radiogenic than the baseline strontium isotopic composition measured at Moonlight Head. This suggests that pore fluids may be mixed with external and more radiogenic strontium sources, such as seawater or continental detritus (e.g. siliciclastics and clays) imported by fluvial channels (Fig. 11). Concretion mineral matrix samples from Castle Cove have radiogenic strontium isotopic compositions of 0.7072 to 0.7074, which is almost identical to Cretaceous seawater strontium isotopic compositions of 0.7073 (Fig. 7; Bralower et al. 1997), however, only the siderite-cemented concretion has heavy oxygen isotopic compositions similar to coeval seawater. The carbonate cements

within the siderite-cemented concretions analysed in this study also have radiogenic $^{87}Sr/^{86}Sr$ values similar to that of Cretaceous seawater (Fig. 8) and this is consistent with the heavy $\delta^{18}O_{water}$ values calculated from these concretions.

5.4 Synthesis of the pore fluid evolution of the carbonate cements in the Eumeralla Formation

In this section, we aim to integrate the results and interpretations made in this study with the diagenetic history of the Eumeralla Formation described by Duddy (2003), in order to understand the evolution of pore fluids from early deposition to post-diagenesis. Carbonate concretions within sedimentary basins typically form as a result of the cementation of circulating interstitial fluids during burial diagenesis (Irwin et al. 1977). Therefore, stable oxygen and carbon isotopes, together with strontium isotopes, from carbonate cements within concretions have been analysed in order to identify the source and temperature of these pore fluids. Fractures can also preserve carbonate cements that have precipitated from circulating fluids migrated through pore space and connected fracture networks (Bons et al. 2012).

Diagenesis of labile volcanic detritus by connate pore water to form grain-coating clays (i.e. smectite and chlorite) began immediately after burial (Duddy 1983). These pore fluids were sourced from meteoric water in a fluvial and deltaic depositional environment (Duddy 2003). Based on light $\delta^{18}O_{water}$ values calculated from most calcite-cemented concretions and some calcite-cemented fractures in this study, these fluids were the primary source of the pore fluids that precipitated these carbonates. These carbonates also have similar $^{87}Sr/^{86}Sr$ values to that of volcanic detritus, suggesting that these pore fluids were strongly influenced by the dissolution and alteration of volcanic detritus, which indicates that the pore fluids remained in a closed system. Calcite-cemented concretions are characterised by a range of carbon isotopic compositions, but most typically have heavy $\delta^{13}C$ values. These heavy carbon isotopic compositions suggest that CO_2 was derived from the methanogenic fermentation of organic matter during burial diagenesis (Curtis and Coleman 1986; Morad 1998).

Heavy $\delta^{18}O_{water}$ values and radiogenic $^{87}Sr/^{86}Sr$ values suggest that there may have been a sea water input in the siderite-cemented concretions and siderite- and calcite-cemented fractures. The presence of dinoflagellates (Korasidis et al. 2016) in the Eumeralla Formation is consistent with this interpretation. Considering that the Eumeralla Formation was deposited on a flat delta plain, there may have been periods of reduced volcanic sediment input resulting in shallow marine incursions. These marine incursion events may have fluxed sufficient amounts of sea water in the sediment to allow for a source of iron in the siderite-cemented concretions, thereby providing a source of iron in the sediments for siderite precipitation in fractures. During burial diagenesis, organic matter was oxidized by these oxygen-bearing sea water to form CO_2 (Raiswell 1987), allowing for the precipitation of siderite in the siderite-cemented concretions, and later the fractures.

The precipitation of carbonate cements in the concretions protected labile volcanic minerals (e.g. clinopyroxene, amphibole, and calcic plagioclase) within the concretions from further alteration by diagenetic reactions. The precipitation of calcite and siderite cements also reduced the partial pressure of CO_2 in the pore fluids, thereby promoting the precipitation of zeolites (Duddy 2002). Brittle deformation (i.e. the formation of fractures) due to local and basin-scale tectonic events resulted in structural permeability (e.g. Debenham et al. 2018). The formation of structural conduits would have promoted the migration of remaining pore fluids and subsequent cement precipitation.

5.5 Implications for basin-scale palaeoclimate reconstructions in the mid-Cretaceous

The mean annual surface temperature of eastern Australia in the mid-Cretaceous can be calculated from historical isotopic composition data of meteoric water collected at continental stations together with the calculated oxygen isotopic compositions of original pore fluids (i.e. $\delta^{18}O_{water}$) preserved in concretions. The $\delta^{18}O_{water}$ value used in this calculation assumed carbonate precipitation temperatures that were equivalent to the temperatures at the depth of concretion formation. Equations from Gregory et al. (1989) and Ferguson et al. (1999), both derived from regression curves from different continental stations for <15°C, were used to calculate mean annual surface temperature ($T_{surface}$) with a standard deviation of approximately ±5°C, respectively:

$$T_{surface} = (0.91 * \delta^{18}O_{water}) + 16.9 \quad (5)$$

$$T_{surface} = (1.05 * \delta^{18}O_{water}) + 18.1 \quad (6)$$

Carbonate cements formed by recrystallization at high temperatures are characterised by lower oxygen isotopic compositions, and therefore $\delta^{18}O_{water}$ values. Depletion in $\delta^{18}O$ due to recrystallization therefore must be considered when making palaeoclimate reconstructions (Morad 1998). Therefore, $\delta^{18}O_{water}$ values of concretions from locations that have experienced high maximum temperatures related to deep burial (vitrinite reflectance temperatures >56°C) have not been used for mean annual surface temperature calculations. The formation depths, and therefore formation temperatures, of concretions are also considered in these calculations, and we have only used $\delta^{18}O_{water}$ values from concretions that have formed at shallow burial depths (less than 1.5 km). The concretions sampled from Moonlight Head, which did not undergo severe diagenesis, are of particular interest for these calculations as they preserve relatively unaltered $\delta^{18}O_{water}$ values.

While Equations 5 and 6 use different continental station data, they are similar and therefore both have been used to capture a range of possible mean annual surface temperatures. Using Equation 5, the mean annual surface temperature calculated from calcite concretions is 9.5°C, with temperatures ranging between 5.9°C and 15.5°C. Using Equation 6, the temperature calculated from calcite concretions is 9.6°C, with temperatures ranging between 5.5°C and 16.5°C. These temperatures are consistent with palaeotemperatures values presented by Price et al. (2012), who calculated temperatures between 10°C and 15°C during the mid-Cretaceous from belemnite rostra specimens at palaeolatitudes between 75°S and 50°S (Fig. 2). The temperature estimates are also consistent with the palaeobotanical and palynological record which supports mid-Cretaceous warming (Douglas and Williams 1982; Douglas 1986; Wagstaff et al. 2013; Korasidis et al. 2016). However, the mean annual surface temperatures calculated from calcite concretions by Gregory et al. (1989) and Ferguson et al. (1999) are not consistent with temperatures between 5°C and 15°C calculated in this study and Price et al. (2012), and conflict with the palaeobotanical and palynological record. Gregory et al. (1989) have argued colder mean annual surface temperatures during the mid-Cretaceous of less than 5°C to below freezing. Gregory et al. (1989) assume that the calcite concretions in the eastern Otway Basin formed near the surface at low temperatures and that the pore fluids were sourced directly from meteoric water without further alteration. They did not calculate the burial depth of the concretions, and they also did not consider how diagenesis, fluid mixing, and temperature through time have altered the $\delta^{18}O_{water}$ values of the carbonate cements in the concretions. Any disregard of these factors will lead to erroneous estimations of mean annual surface temperatures.

6. Conclusions

Geochemical data, from stable oxygen and carbon isotope and strontium isotope analyses, of calcite- and siderite-cemented concretions and fractures provide valuable insights into the source of pore fluids and their evolution in the Eumeralla Formation within the eastern Otway Basin.

- The depth of concretion formation has been calculated by using the percentage of carbonates within the concretions, which indicates the initial porosity of the sediments and subsequently burial depth. The burial depth trend shows that, based on the percentage of carbonates in concretions collected in this study together with Gregory et al. (1989), the concretions formed within the initial ca. 700 m to 2,900 m of burial. Individual concretions formed at a similar depth over a short depth interval, short depth interval, i.e. concretion formation from core to rim occurs within ca. 2 m to 530 m.
- Depleted oxygen isotopic ratios (approximately 5‰ to 15‰ SMOW) recorded in all calcite-cemented concretions and some fractures indicates a meteoric water input during early diagenesis, followed by later calcite recrystallization with increased burial. The relatively unradiogenic strontium isotopic composition ($^{87}Sr/^{86}Sr$ = less than 0.707) of the carbonate cements in these concretions and fractures indicates that the dissolution and alteration of volcanic detritus was strongly influencing the composition of pore fluids.
- Heavy pore fluid oxygen isotopic compositions (approximately 22‰ to 30‰ SMOW) and radiogenic strontium values suggest that there may have been sea water input in the siderite-cemented concretions and siderite- and calcite-cemented fractures. A marine incursion during deposition of the Eumeralla Formation sediments has been proposed to explain this.
- Methanogenic fermentation and oxidation of organic matter produced the CO_2 required for carbonate precipitation of calcite and siderite cements.
- Pore fluids were influenced by diagenetic reactions and increased temperature during burial. Increased temperature may have led to calcite recrystallization, thereby further depleting the oxygen isotopic compositions preserved in the calcite-cemented concretions.
- The mean annual surface temperature has been calculated from pore fluid isotopic compositions of low-temperature calcite-cemented concretions together with historical continental station data. The mean annual surface temperature during the mid-Cretaceous in the eastern Otway Basin was approximately between 5°C and 15°C.

Acknowledgements

This research forms part of a PhD project supported by the Australian Research Council [Discovery Project DP160101158] and through an Australian Government Research Training Program Scholarship. This study was also funded by scholarships from the Petroleum Exploration Society of Australia and the Australian Petroleum Production and Exploration Association. Lachlan Furness and Rowan Hansberry are also gratefully acknowledged for sample collection during fieldwork. Mark Rollog and Kristine Nielson are thanked for their assistance with stable isotope analysis. David Bruce is thanked for his assistance with strontium isotope analysis. A/Prof. Russell Drysdale and Dr. Florian Dux are thanked for analysing several samples for stable isotopes. Dr. Tony Hall is thanked for his assistance with pressure calcimeter analysis. Discussions on the research topic with Dr. Juraj Farkaš and Dr. Jonathan Tyler are greatly appreciated.

References

Ayalon A. & Longstaffe F. J. 1988. Oxygen isotope studies of diagenesis and pore-water evolution in the Western Canada sedimentary basin; evidence from the Upper Cretaceous basal Belly River Sandstone, Alberta. Journal of Sedimentary Research 58, 489-505. doi: 10.1306/212F8DCD-2B24-11D7-8648000102C1865D.

Bailey A. H. E., King R. C., Holford S. P., Sage J., Hand M. & Backé G. 2015. Defining structural permeability in Australian sedimentary basins. APPEA Journal, 119-147. doi.

Bloch J. 1990. Stable isotopic composition of authigenic carbonates from the Albian Harmon Member (Peace River Formation): evidence of early diagenetic processes. Bulletin of Canadian Petroleum Geology 38, 39-52. doi.

Bojanowski M. J., Barczuk A. & Wetzel A. 2014. Deep-burial alteration of early-diagenetic carbonate concretions formed in Palaeozoic deep-marine greywackes and mudstones (Bardo Unit, Sudetes Mountains, Poland). Sedimentology 61, 1211-1239. doi: 10.1111/sed.12098.

Boles J. R., Eichhubl P., Garven G. & Chen J. 2004. Evolution of a hydrocarbon migration pathway along basin-bounding faults: Evidence from fault cement. AAPG Bulletin 88, 947-970. doi.

Bons P. D., Elburg M. A. & Gomez-Rivas E. 2012. A review of the formation of tectonic veins and their microstructures. Journal of Structural Geology 43, 33-62. doi: 10.1016/j.jsg.2012.07.005.

Bralower T. J., Fullagar P. D., Paull C. K., Dwyer G. S. & Leckie R. M. 1997. Mid-Cretaceous strontium-isotope stratigraphy of deep-sea sections. GSA Bulletin 109, 1421-1442. doi: 10.1130/0016-7606(1997)109<1421:MCSISO>2.3.CO;2.

Burgin H. B., Amrouch K., Rajabi M., Kulikowski D. & Holford S. P. 2018. Determining paleo-structural environments through natural fracture and calcite twin analyses- a case study in the Otway Basin, Australia. The APPEA Journal 58, 238-254. doi.

Carothers W. W., Adami L. H. & Rosenbauer R. J. 1988. Experimental oxygen isotope fractionation between siderite-water and phosphoric acid liberated CO2-siderite. Geochimica et Cosmochimica Acta 52, 2445-2450. doi: 10.1016/0016-7037(88)90302-X.

Curtis C. D. & Coleman M. L. 1986 Controls on the precipitation of early diagenetic calcite, dolomite, and siderite concretions in complex depositional sequences. In Gautier D. L. ed. Roles of Organic Matter in Sediment Diagenesis. The Society of Economic Paleontologists and Mineralogists, pp. 23-33.

Dansgaard W. 1964. Stable isotopes in precipitation. Tellus 16, 436-468. doi: 10.1111/j.2153-3490.1964.tb00181.x.

Debenham N., King R. C. & Holford S. P. 2018. The influence of a reverse-reactivated normal fault on natural fracture geometries and relative chronologies at Castle Cove, Otway Basin. Journal of Structural Geology 112, 112-130. doi: 10.1016/j.jsg.2018.05.004.

Douglas J. G. & Williams G. E. 1982. Southern polar forests: The Early Cretaceous floras of Victoria and their palaeoclimatic significance. Palaeogeography, Palaeoclimatology, Palaeoecology 39, 171-185. doi: 10.1016/0031-0182(82)90021-9.

Douglas J. G. 1986 The Cretaceous vegetation, and palaeoenvironment of Otway Group sediments. In Glenie R. C. ed. Second South-Eastern Australia Oil Exploration Symposium—Technical Papers. Petroleum Exploration Society of Australia, Melbourne, Australia, pp. 233-240.

Duddy I. R. 1983. The geology, petrology and geochemistry of the Otway formation volcanogenic sediments. PhD Thesis. The University of Melbourne (unpubl.).

Duddy I. R. 1994. The Otway Basin: Thermal, Structural, Tectonic and Hydrocarbon Generation Histories. NGMA/PESA Otway Basin Symposium, Melbourne. pp. 35-42.

Duddy I. R. 2002. The Otway Basin: Geology, Sedimentology, Diagenesis, AFTA Thermal History Reconstruction and Hydrocarbon Prospectivity. Field Trip Guide prepared for the National Centre for Petroleum Geology and Geophysics, Adelaide. Geotrack International Pty. Ltd.

Duddy I. R. 2003 Mesozoic: A time of change in teconic regime. In Birch W. D. ed. Geology of Victoria. GSA Special Publication 23, pp. 239-286.

Edwards J., Leonard J. G., Pettifer G. R. & Mcdonald P. A. 1996 Colac 1:250000 Map. In ed.^eds. pp. 2 ed. Victoria, Australia: Geological Survey of Victoria.

Evans M. A. 1995. Fluid inclusions in veins from the Middle Devonian shales: A record of deformation conditions and fluid evolution in the Appalachian Plateau. GSA Bulletin 107, 327-339. doi: 10.1130/0016-7606(1995)107<0327:FIIVFT>2.3.CO;2.

Ferguson K. M., Gregory R. T. & Constantine A. 1999. Lower Cretaceous (Aptian-Albian) secular changes in the oxygen and carbon isotope record from high paleolatitude, fluvial sediments, Southeast Australia: Comparisons to the marine record. Geological Society of America Special Papers 332, 59-72. doi: 10.1130/0-8137-2332-9.59.

Finlayson D. M., Johnstone D. W., Owen A. J. & Wake-Dyster K. D. 1996. Deep seismic images and the tectonic framework of early rifting in the Otway Basin, Australian southern margin. Tectonophysics 264, 137-152. doi: 10.1016/S0040-1951(96)00123-0.

Gat J. R. 1996. Oxygen and hydrogen isotopes in the hydrologic cycle. Annual Review of Earth and Planetary Sciences 24, 225-262. doi: 10.1146/annurev.earth.24.1.225.

Gautier D. L. 1982. Siderite concretions; indicators of early diagenesis in the Gammon Shale (Cretaceous). Journal of Sedimentary Research 52, 859-871. doi: 10.1306/212F8076-2B24-11D7-8648000102C1865D.

Gill E. D., Segnit E. R. & Mcneill N. H. 1977. Concretions in Otway Group sediments, South-East Australia. Proceedings of the Royal Society of Victoria 89, 51-55. doi.

Gregory R. T., Douthitt C. B., Duddy I. R., Rich P. V. & Rich T. H. 1989. Oxygen isotopic composition of carbonate concretions from the lower Cretaceous of Victoria, Australia: implications for the evolution of meteoric waters on the Australian continent in a paleopolar environment. Earth and Planetary Science Letters 92, 27-42. doi.

Herut B., Starinsky A. & Katz A. 1993. Strontium in rainwater from Israel: Sources, isotopes and chemistry. Earth and Planetary Science Letters 120, 77-84. doi: 10.1016/0012-821X(93)90024-4.

Hill K. A., Finlayson D. M., Hill K. C. & Cooper G. T. 1995. Mesozoic tectonics of the Otway Basin: the legacy of Gondwana and the active Pacific margin- a review and ongoing research. Journal of the Australian Petroleum Production and Exploration Association 35, 467-493. doi.

Holford P., Tuitt A. K., Hillis R. R., Green P. F., Stoker M. S., Duddy I. R., Sandiford M. & Tassone D. R. 2014. Cenozoic deformation in the Otway Basin, southern Australian margin: implications for the origin and nature of post-breakup compression at rifted margins. Basin Research 26, 10-37. doi: 10.1111/bre.12035.

Hudson J. D. 1978. Concretions, isotopes, and the diagenetic history of the Oxford Clay (Jurassic) of central England. Sedimentology 25, 339-370. doi: doi:10.1111/j.1365-3091.1978.tb00317.x.

Irwin H., Curtis C. & Coleman M. 1977. Isotopic evidence for source of diagenetic carbonates formed during burial of organic-rich sediments. Nature 269, 209-213. doi: 10.1038/269209a0.

Joussaume S., Sadourny R. & Jouzel J. 1984. A general circulation model of water isotope cycles in the atmosphere. Nature 311, 24-29. doi: 10.1038/311024a0.

Korasidis V. A., Wagstaff B. E., Gallagher S. J., Duddy I. R., Tosolini A.-M. P., Cantrill D. J. & Norvick M. S. 2016. Early angiosperm diversification in the Albian of southeast Australia: implications for flowering plant radiation across eastern Gondwana. Review of Palaeobotany and Palynology 232, 61-80. doi: 10.1016/j.revpalbo.2016.04.005.

Krassay A. A., Cathro D. L. & Ryan D. J. 2004 A regional tectonostratigraphic framework for the Otway Basin. In Boult P. J., Johns D. R. & Lang S. C. ed. Eastern Australian Basins Symposium II. Petroleum Exploration Society of Australia Special Publication, pp. 97-106.

Lawrence J. R. & Gieskes J. M. 1981. Constraints on water transport and alteration in the oceanic crust from the isotopic composition of pore water. Journal of Geophysical Research: Solid Earth 86, 7924-7934. doi: doi:10.1029/JB086iB09p07924.

Li Z. X. & Powell C. M. 2001. An outline of the palaeogeographic evolution of the Australasian region since the beginning of the Neoproterozoic. Earth-Science Reviews 53, 237-277. doi: 10.1016/S0012-8252(00)00021-0.

Lippmann F. 1955. Ton, Geoden und Minerale des Barrême von Hoheneggelsen. Geologische Rundschau 43, 475-503. doi: 10.1007/bf01764034.

Meng Q., Hooker J. & Cartwright J. 2017a. Early overpressuring in organic-rich shales during burial: evidence from fibrous calcite veins in the Lower Jurassic Shales-with-Beef Member in the Wessex Basin, UK. Journal of the Geological Society. doi: 10.1144/jgs2016-146.

Meng Q., Hooker J. & Cartwright J. 2017b. Genesis of natural hydraulic fractures as an indicator of basin inversion. Journal of Structural Geology. doi: 10.1016/j.jsg.2017.07.001.

Miller J. M., Norvick M. S. & Wilson C. J. L. 2002. Basement controls on rifting and the associated formation of ocean transform faults—Cretaceous continental extension of the southern margin of Australia. Tectonophysics 359, 131-155. doi: 10.1016/S0040-1951(02)00508-5.

Morad S. 1998 Carbonate Cementation in Sandstones: Distribution Patterns and Geochemical Evolution. In Morad S. ed. Carbonate Cementation in Sandstones. pp. 1-26.

Mozley P. S. & Burns S. J. 1993. Oxygen and carbon isotopic composition of marine carbonate concretions; an overview. Journal of Sedimentary Research 63, 73-83. doi: 10.1306/D4267A91-2B26-11D7-8648000102C1865D.

Norvick M. S. & Smith M. A. 2001. Mapping the plate tectonic reconstruction of southern and southeastern Australia and implications for petroleum systems. Journal of the Australian Petroleum Production and Exploration Association 41, 15-35. doi.

O'neil J. R., Clayton R. N. & Mayeda T. K. 1969. Oxygen Isotope Fractionation in Divalent Metal Carbonates. The Journal of Chemical Physics 51, 5547-5558. doi: 10.1063/1.1671982.

Oertel G. & Curtis C. D. 1972. Clay-Ironstone Concretion Preserving Fabrics Due to Progressive Compaction. GSA Bulletin 83, 2597-2606. doi: 10.1130/0016-7606(1972)83[2597:CCPFDT]2.0.CO;2.

Pagel M., Braun J.-J., Disnar J. R., Martínez L., Renac C. & Vasseur G. 1997. Thermal history constraints from studies of organic matter, clay minerals, fluid inclusions, and apatite fission tracks at the Ardeche paleo-margin (BA1 drill hole, GPF program), France. Journal of Sedimentary Research 67, 235-245. doi.

Palmer M. R. & Edmond J. M. 1989. The strontium isotope budget of the modern ocean. Earth and Planetary Science Letters 92, 11-26. doi: 10.1016/0012-821X(89)90017-4.

Perincek D., Simons B. & Pettifer G. R. 1994. The tectonic framework, and associated play types of the Western Otway Basin, Victoria, Australia. APPEA Journal 34, 460-477. doi.

Philipp S. L. 2008. Geometry and formation of gypsum veins in mudstones at Watchet, Somerset, SW England. Geological Magazine 145, 831-844. doi: 10.1017/s0016756808005451.

Pirrie D. & Marshall J. D. 1991. Field relationships and stable isotope geochemistry of concretions from James Ross Island, Antarctica. Sedimentary Geology 71, 137-150. doi: 10.1016/0037-0738(91)90098-X.

Price G. D., Williamson T., Henderson R. A. & Gagan M. K. 2012. Barremian–Cenomanian palaeotemperatures for Australian seas based on new oxygen-isotope data from belemnite rostra. Palaeogeography, Palaeoclimatology, Palaeoecology 358-360, 27-39. doi: 10.1016/j.palaeo.2012.07.015.

Raiswell R. 1987. Non-steady state microbiological diagenesis and the origin of concretions and nodular limestones. Geological Society, London, Special Publications 36, 41-54. doi: 10.1144/gsl.Sp.1987.036.01.05.

Raiswell R. & Fisher Q. J. 2000. Mudrock-hosted carbonate concretions: a review of growth mechanisms and their influence on chemical and isotopic composition. Journal of the Geological Society 157, 239-251. doi: 10.1144/jgs.157.1.239.

Schneider C. L., Hill K. C. & Hoffman N. 2004. Compressional growth of the Minerva Anticline, Otway Basin, Southeast Australia–evidence of oblique rifting. APPEA Journal 44, 463-480. doi.

Scotchman I. C. 1991. The geochemistry of concretions from the Kimmeridge Clay Formation of southern and eastern England. Sedimentology 38, 79-106. doi: 10.1111/j.1365-3091.1991.tb01856.x.

Scotchman I. C., Carr A. D., Astin T. R. & Kelly J. 2002. Pore fluid evolution in the Kimmeridge Clay Formation of the UK Outer Moray Firth: implications for sandstone diagenesis. Marine and Petroleum Geology 19, 247-273. doi: 10.1016/S0264-8172(02)00016-8.

Sherrod L., Dunn G., Peterson G. & Kolberg R. 2002. Inorganic carbon analysis by modified pressure-calcimeter method. Soil Science Society of America Journal 66, 299-305. doi.

Spötl C. & Vennemann T. W. 2003. Continuous-flow isotope ratio mass spectrometric analysis of carbonate minerals. Rapid Communications in Mass Spectrometry 17, 1004-1006. doi: 10.1002/rcm.1010.

Suchy V., Heijlen W., Sykorova I., Muchez P., Dobes P., Hladikova J., Jackova I., Safanda J. & Zeman A. 2000. Geochemical study of calcite veins in the Silurian and Devonian of the Barrandian Basin (Czech Republic): evidence for widespread post-Variscan fluid flow in the central part of the Bohemian Massif. Sedimentary Geology 131, 201-219. doi: 10.1016/S0037-0738(99)00136-0.

Tassone D. R., Holford S. P., Duddy I. R., Green P. F. & Hillis R. R. 2014. Quantifying Cretaceous–Cenozoic exhumation in the Otway Basin, southeastern Australia, using sonic transit time data: Implications for conventional and unconventional hydrocarbon prospectivity. AAPG Bulletin 98, 67-117. doi: 10.1306/04011312111.

Thyne G. D. & Boles J. R. 1989. Isotopic evidence for origin of the Moeraki septarian concretions, New Zealand. Journal of Sedimentary Research 59, 272-279. doi: 10.1306/212f8f6c-2b24-11d7-8648000102c1865d.

Veevers J. J., Powell C. M. & Roots S. R. 1991. Review of seafloor spreading around Australia. I. synthesis of the patterns of spreading. Australian Journal of Earth Sciences 38, 373-389. doi: 10.1080/08120099108727979.

Veevers J. J. 2006. Updated Gondwana (Permian–Cretaceous) earth history of Australia. Gondwana Research 9, 231-260. doi: 10.1016/j.gr.2005.11.005.

Wagstaff B. E., Gallagher S. J., Norvick M. S., Cantrill D. J. & Wallace M. W. 2013. High latitude Albian climate variability: Palynological evidence for long-term drying in a greenhouse world. Palaeogeography, Palaeoclimatology, Palaeoecology 386, 501-511. doi: 10.1016/j.palaeo.2013.06.018.

CHAPTER 5

This chapter is written in publication format:

Debenham, N., Holford, S. P., King, R. C.
The spatial distribution and geochemical variation of calcite and gypsum cements in the eastern Bristol Channel Basin.

STATEMENT OF AUTHORSHIP

Title of Paper	The spatial distribution and geochemical variation of calcite and gypsum cements in the eastern Bristol Channel Basin.
Publication Status	☐ Published ☐ Accepted for publication ☐ Submitted for publication ☒ Unpublished and unsubmitted work written in manuscript style

Principal Author

Name of Principal Author (Candidate)	Natalie Debenham		
Contribution to the Paper	Project design, fieldwork, sample preparation, laboratory analysis, processing and interpreting, manuscript design and composition, creation of figures, manuscript revisions.		
Overall Percentage	80%		
Certification	This paper reports on original research I conducted during the period of my Higher Degree by Research candidature and is not subject to any obligations or contractual agreements with a third party that would constrain its inclusion in this thesis. I am the primary author of this paper.		
Signature		Date	26/02/2019

Co-Author Contributions

By signing the Statement of Authorship, each author certifies that:

i. the candidate's stated contribution to the publication is accurate (as detailed above);
ii. permission is granted for the candidate in include the publication in the thesis; and
iii. the sum of all co-author contributions is equal to 100% less the candidate's stated contribution.

Name of Co-Author	Simon Holford		
Contribution to the Paper	Assistance with project design, assistance with manuscript design and composition, assistance with interpretation, manuscript review.		
Signature		Date	26/02/2019

Name of Co-Author	Rosalind King		
Contribution to the Paper	Assistance with project design, assistance with manuscript design and composition, assistance with interpretation, manuscript review.		
Signature		Date	26/02/2019

ABSTRACT

The spatial distribution and geochemical variation of fault- and fracture-hosted cements can be used to reconstruct the evolution and migration of pore fluids in sedimentary basins. Geochemical data, from stable oxygen and carbon isotope and strontium isotope analyses, of calcite and gypsum cements provide valuable insights into the source of pore fluids and their evolution in the eastern Bristol Channel Basin. Overall, at both an outcrop-scale and a basin-scale there were no observable relationships between the dip angle and orientation of fractures with the oxygen and carbon isotopic composition of calcite cements, indicating that the movement and distribution of fluids in fractures is not controlled by the orientation of fracture opening. Radiogenic strontium isotopic compositions of calcite and gypsum cements indicate at least two different mineralising fluid compositions that are strongly controlled by the lithologies (fossiliferous limestones and shales and marls with gypsum nodules, respectively) in which they occur. These fluids originated as connate pore fluids that were altered during the diagenesis of their host lithologies. Mineralising fluids within the Lower Jurassic Lias Group are characterised by enriched oxygen and strontium isotopic compositions and relatively depleted carbon isotopic compositions, associated with the alteration of labile minerals and carbonaceous fossils. Mineralising fluids within the underlying Mercia Mudstone Group have exceptionally radiogenic strontium isotopic compositions as a result of the interaction of fluids with evaporitic intervals. The mineralising fluids were redistributed through migration along faults and their associated damage zones. Previous studies typically utilise one geochemical analytical technique to characterise mineralising fluids, however this study highlights the importance of integrating a range of geochemical analyses when attempting to understand the source of fluids and their evolution through time.

1. Introduction

The composition of fluids in sedimentary basins provides valuable information on the geochemistry, hydrogeology, thermal history, and tectonic structure of the earth's upper crust. Defining the spatial extent and geochemical properties of fluids that have influenced sedimentary basins has important implications for developing strategies during commodity exploration and production. For instance, understanding hydrocarbon generation and migration in petroleum plays (e.g. Aydin, 2000; Knipe et al., 1998) and fluid migration in geothermal plays, and ore mineralisation (e.g. Fairley, 2009; Rowland and Sibson, 2004; Sibson et al., 1975). Therefore, knowledge of the processes involved with fluid flow events in basins is fundamental for understanding large-scale crustal processes and for formulating basin-specific models and prediction strategies for exploration.

Fluids can be preserved within sedimentary basins as diagenetic cements within pore space and within faults and fractures (Bons et al., 2012; Curtis and Coleman, 1986). Traditional isotope (e.g. oxygen and carbon isotopes) and fluid inclusion analyses are two techniques that are commonly utilised in order to reconstruct pore fluid evolution and fluid flow history of sedimentary basins (e.g. Ayalon and Longstaffe, 1988; Bixler et al., 1998; Evans, 1995; Meng et al., 2017a; Pagel et al., 1997; Scotchman et al., 2002). Typically studies only utilise one geochemical analytical technique to characterise pore fluids. However, an understanding of the evolution and pathways for fluid flow requires an integrated approach, involving a combination of structural geology, sedimentology, and geochemical methods.

This study aims to assess the source and spatial distribution of fluids in order to understand the geochemical evolution and migration pathways of fluids in the eastern Bristol Channel Basin. Although the basin does

not contain commercial quantities of hydrocarbons (Kamerling, 1979), exposures of inverted fault zones along the exhumed southern margin of the basin that host precipitated fluids can be used to gain a better understanding of fluid flow in the subsurface. Exceptionally well exposed outcrops preserved along the Somerset coastline in the eastern Bristol Channel Basin allow for detailed structural mapping and high-resolution geochemical analyses. A series of integrated geochemical analyses have been undertaken on calcite and gypsum veins and slickencrysts (i.e. elongate mineral precipitates formed in slickensides), including carbon and oxygen stable isotope and strontium isotope analysis. Structural mapping and sampling along fault zones have also been utilised to understand geochemical relationships in a spatial context. This study builds on previous geochemical analyses which have been mainly focused on calcite veins at Kilve (e.g. Bixler et al., 1998; Davison, 1995; Logan and Decker, 1994), however, this represents the first comprehensive and integrated investigation of the fluid evolution of both calcite and gypsum cements in the Bristol Channel Basin. We show that mineralising fluids in the eastern Bristol Channel Basin originated as connate pore waters that were altered through diagenesis and were subsequently precipitated along faults and fractures.

2. Geological background

This study is focussed on coastal exposures of a series of fault systems on the southern margin of the eastern Bristol Channel Basin, in north Somerset, United Kingdom (Fig. 1). Faulted and fractured Upper Triassic and Lower Jurassic beds are exposed in the study area, which spans from Blue Anchor to Lilstock (Fig. 1 and Fig. 2). The Bristol Channel Basin is an east–west trending basin that developed following Permian–Triassic rifting during the break-up of Pangaea (Coward, 1995; Van Hoorn, 1987). Rifting resulted in the development of east–west trending and south dipping normal faults above a normal-reactivated Variscan thrust fault within the Palaeozoic basement (Brooks et al., 1988; Van Hoorn, 1987). Sedimentation within the Bristol Channel Basin was strongly controlled by subsidence related to rifting, changes in sea level, and climate fluctuations (Ruffell and Shelton, 1999). The coarse-grained, arenaceous Sherwood Sandstone Group was deposited during the early Triassic in a continental environment (Fig. 2).

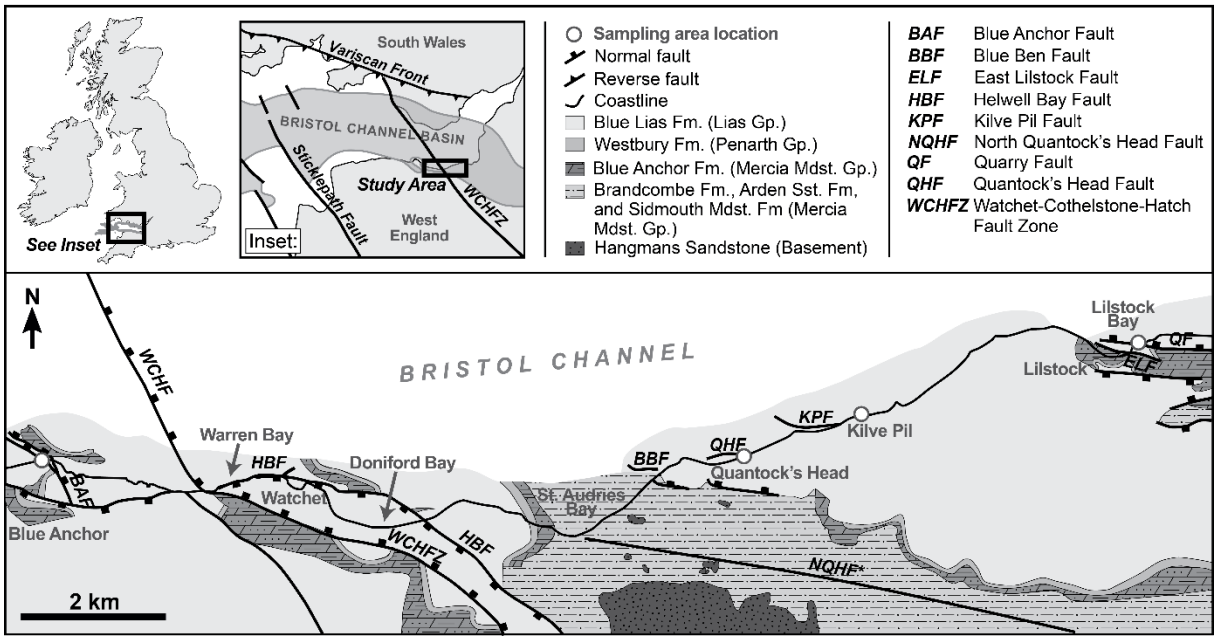

Figure 1. Geological map of north Somerset, Bristol Channel Basin. Major faults are shown and faults with estimated fault strikes are indicated by an asterisk. Note that there are many other faults exposed along the coastline that have not been illustrated. The inset, geological boundaries, and fault strikes are modified after Glen et al. (2005) with permission and Alistair Beach (1993).

These sediments were succeeded by the deposition of fine-grained sediments and an interval of evaporites that form the Mercia Mudstone Group (Fig. 2). Rifting continued throughout the Jurassic and into the early Cretaceous, and many of these faults remained active during this period, particularly along the basin margins (Dart et al., 1995; Kamerling, 1979). This period was characterised by a transition to an open marine environment, resulting in the deposition of interbedded mudstones and limestones to form the Lower Jurassic Lias Group (Fig. 2).

The damage zones of faults in the western section of the study area are often characterised by sub-parallel calcite veins formed as a result of hydraulic fracturing, particularly in the limestone beds within the Lias Group (Fig. 1; Philipp, 2012). North–south contraction, associated with the Alpine orogeny during the late Cretaceous to Palaeogene, led to basin inversion and the formation of east–west trending thrust faults and the reverse reactivation of pre-existing normal faults (Kelly et al., 1999; Nemčok et al., 1995; Peacock and Sanderson, 1999). Similar deformation in the Wessex Basin, located southeast to the Bristol Channel Basin, has been dated to the Eocene to Oligocene based on U–Pb dating of calcite veins (Parrish et al., 2018). Sub-parallel calcite veins associated with faults in the western section of the study area often cross-cut earlier formed veins (Philipp, 2012), and the youngest veins have been dated to have formed prior to the Pliocene based on radiometric and palaeomagnetic dating techniques (Gutmanis et al., 1991). In the eastern section of the study area (Fig. 1), gypsum veins within the evaporite-rich Mercia Mudstone Group are thought to have formed as a result of hydraulic fracturing by either: (a) overpressure generated by the hydration of anhydrite to gypsum (Philipp, 2008), or (b) overpressure due to compression resulting from tectonism and disequilibrium compaction, during the last stage of basin uplift in the late Cretaceous to the Palaeogene (Cosgrove, 2001; Meng et al., 2017b).

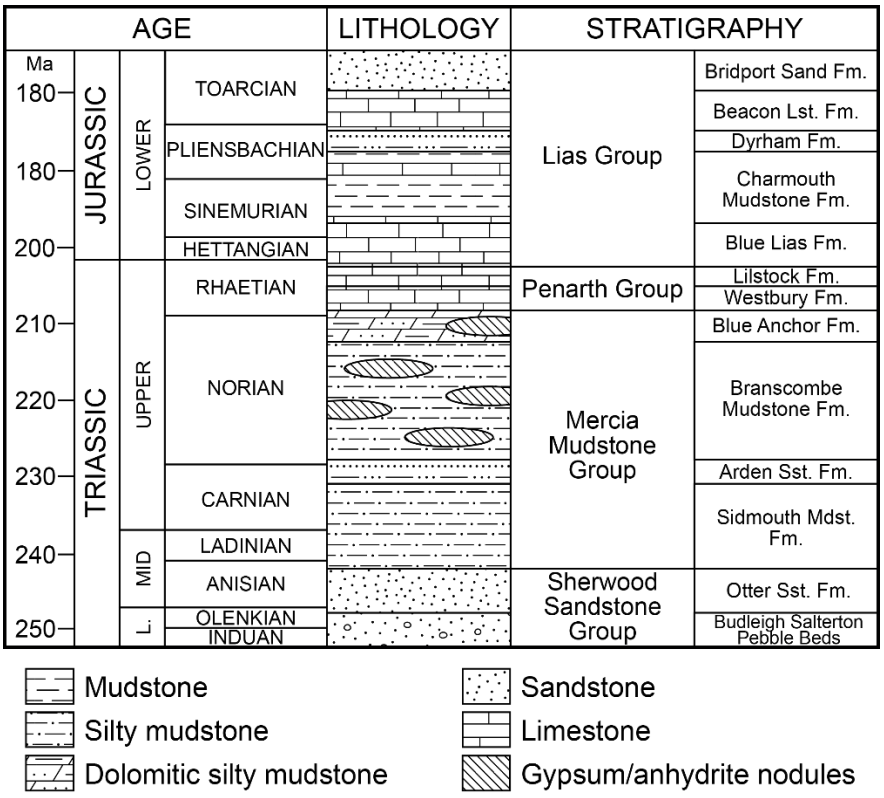

Figure 2. Stratigraphic table of the Triassic–Jurassic strata within the Bristol Channel Basin. Lias Group stratigraphy after Cox et al. (1999), Penarth Group stratigraphy after Dart et al. (1995), Mercia Mudstone Group stratigraphy after Howard et al. (2008), and Sherwood Sandstone Group stratigraphy after Hounslow and Ruffell (2006).

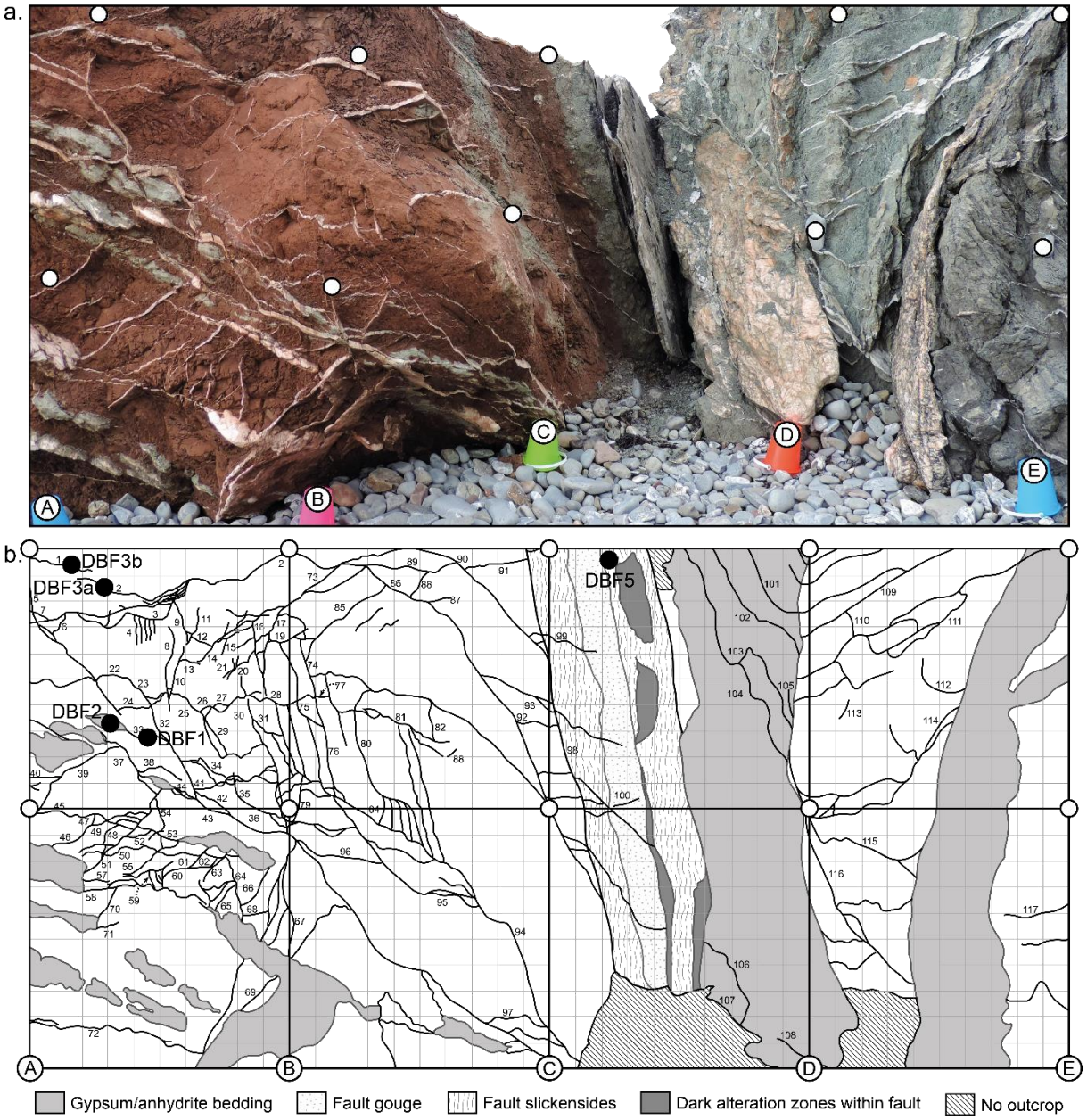

Figure 3. (a) An outcrop photo of the structural section of the Doniford Bay Fault at Warren Bay, Watchet. The red rocks in the footwall are the Mercia Mudstone Group and the grey rocks in the hanging wall are the Lias Group. (b) A gypsum vein trace section with sample locations (black circles). Each black grid is 1 m × 1 m and the numbers on the vein trace sections indicate the locations of vein measurements.

3. Methods

3.1 Structural sections and sample preparation

A total of 26 calcite and 18 gypsum veins and slickencrysts were sampled from cliff exposures and wave cut platforms along the Somerset coastline in the Bristol Channel Basin (Fig. 1) for oxygen and carbon stable isotope and strontium isotope analyses. Most veins and slickencrysts were sampled from areas that were mapped in this study. Detailed structural sections were constructed to map and identify the spatial arrangement of veins relative to faults at Watchet (Fig. 3; Helwell Bay Fault, also called the Doniford Bay Fault), Kilve (Fig. 4; Kilve Pil Fault), Quantock's Head (Fig. 5; Quantock's Head Fault), and Lilstock (Fig. 6; East Lilstock Fault). The faults were surrounded by a peripheral zone of veins and folds, i.e. the

damage zone. The dip, orientation, aperture, and cement type of each vein were recorded during mapping.

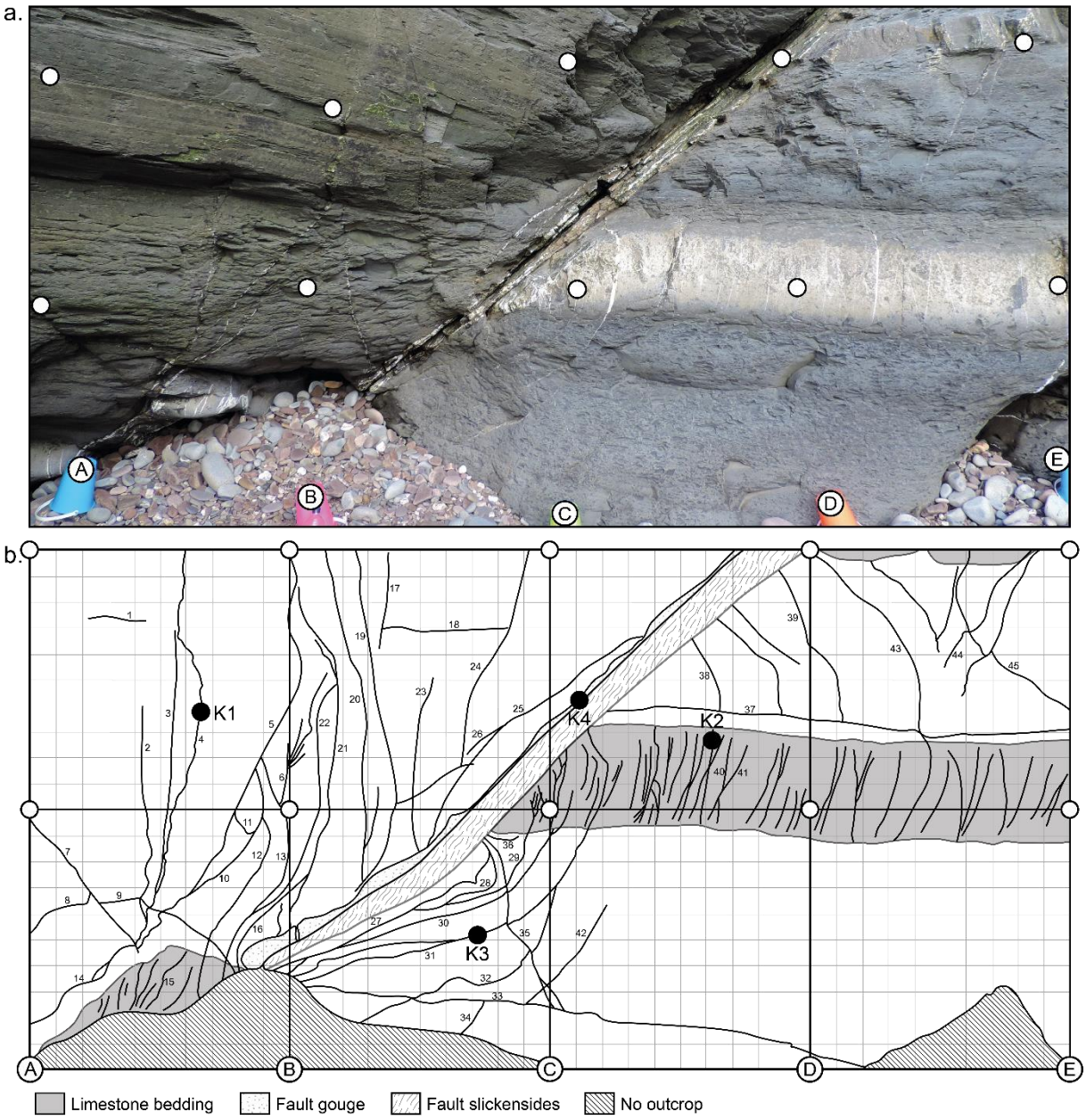

Figure 4. (a) An outcrop photo of the structural section of the Kilve Pil Fault at Kilve. The grey rocks in the footwall and hanging wall are the Lias Group, with alternating layers of shales and limestones. (b) A calcite vein trace section with sample locations (black circles). Each black grid is 1 m × 1 m and the numbers on the vein trace sections indicate the locations of vein measurements.

Samples of veins and slickencrysts were also collected in transects along the Helwell Bay Fault plane in Warren Bay at Watchet and the Kilve Pil Fault at Kilve (Fig. 7). The Helwell Bay Fault is a south-dipping normal fault that downthrows the Blue Lias Formation (Lias Group) against the Mercia Mudstone Group. At Warren Bay, veins were collected from the footwall of the Helwell Bay Fault damage zone. These veins were sampled from different fracture stratigraphic units (i.e. changes in fracture attributes related to the mechanical properties of the unit; c.f. Laubach et al., 2009) identified by Meng et al. (2017c) within the Mercia Mudstone Group. Fracture Unit 1 corresponds to the oldest stratigraphic unit at Warren Bay and crops out in the western part of the bay, while Fracture Units 2 to 4 sequentially crop out toward the

eastern section of the bay and represent younger units (Meng et al., 2017c). At Kilve, slickencrysts and one vein sample were collected from foreshore exposures of the core of the Kilve Pil Fault. The Kilve Pil Fault is a north-dipping normal fault with minor reverse-reactivation identified by folding in the hanging wall. The cliff face exposure of this fault and its hanging wall and footwall damage zone was also mapped.

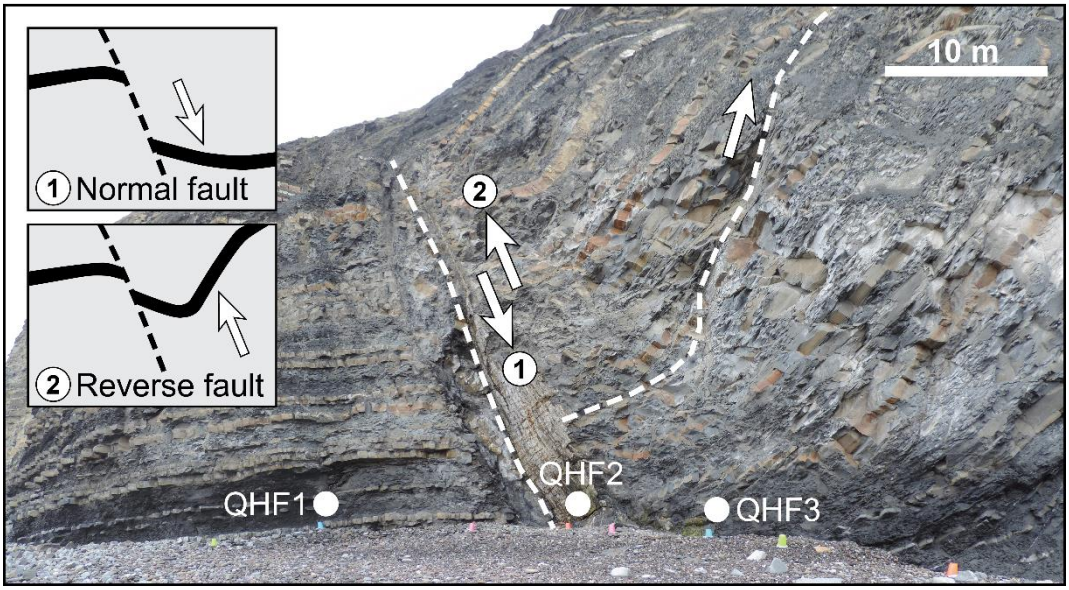

Figure 5. An outcrop photo of the Quantock's Head Fault at Quantock's Head. Sample locations (white circle) and strike of the main fault and an antithetic fault (white dashed lines) are shown. The movement of the fault, which has been reverse-reactivated, is illustrated by the schematic images.

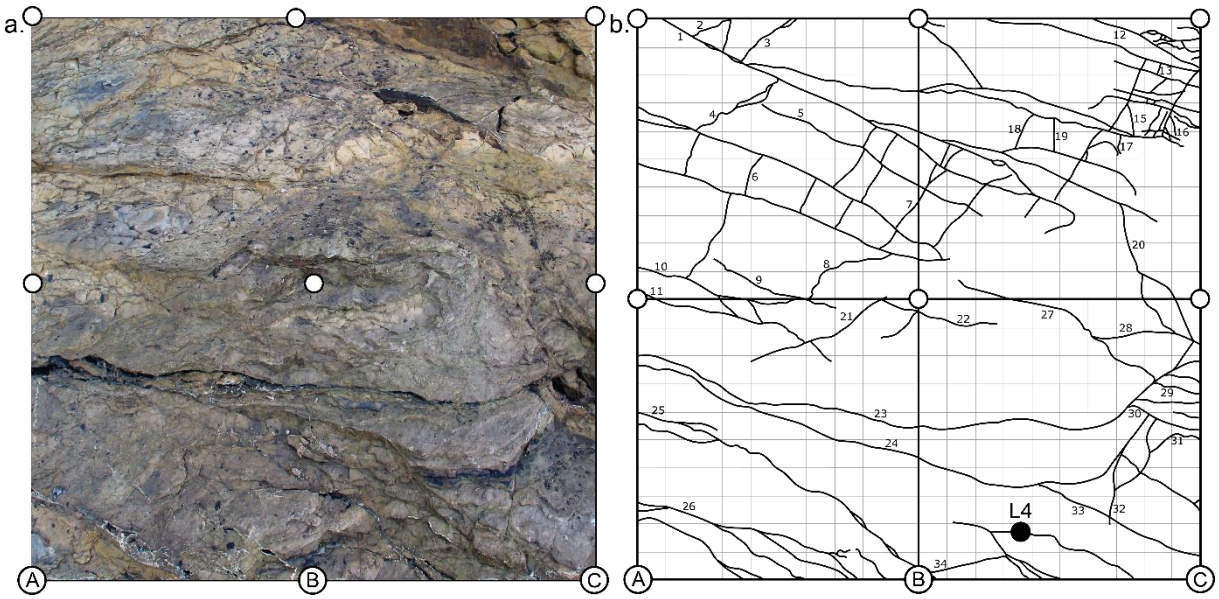

Figure 6. (a) An outcrop photo of the structural section of the East Lilstock Fault at Lilstock. The fault gouge is shown here. (b) A calcite vein trace section with sample locations (black circles). Each black grid is 0.5 m × 0.5 m and the numbers on the vein trace sections indicate the locations of vein measurements.

Calcite cements in the hanging wall, footwall and fault slickencrysts of the Quantock's Head Fault at Quantock's Head were sampled. The Quantock's Head Fault dips to the south with approximately 40 to 50 m of net normal slip and shows minor reverse-reactivation identified by folding in the hanging wall (Fig. 5). Calcite veins within the fault gouge of the East Lilstock Fault at Lilstock were also sampled. The East Lilstock Fault is a north-dipping normal fault that downthrows the Blue Lias Formation (Lias Group)

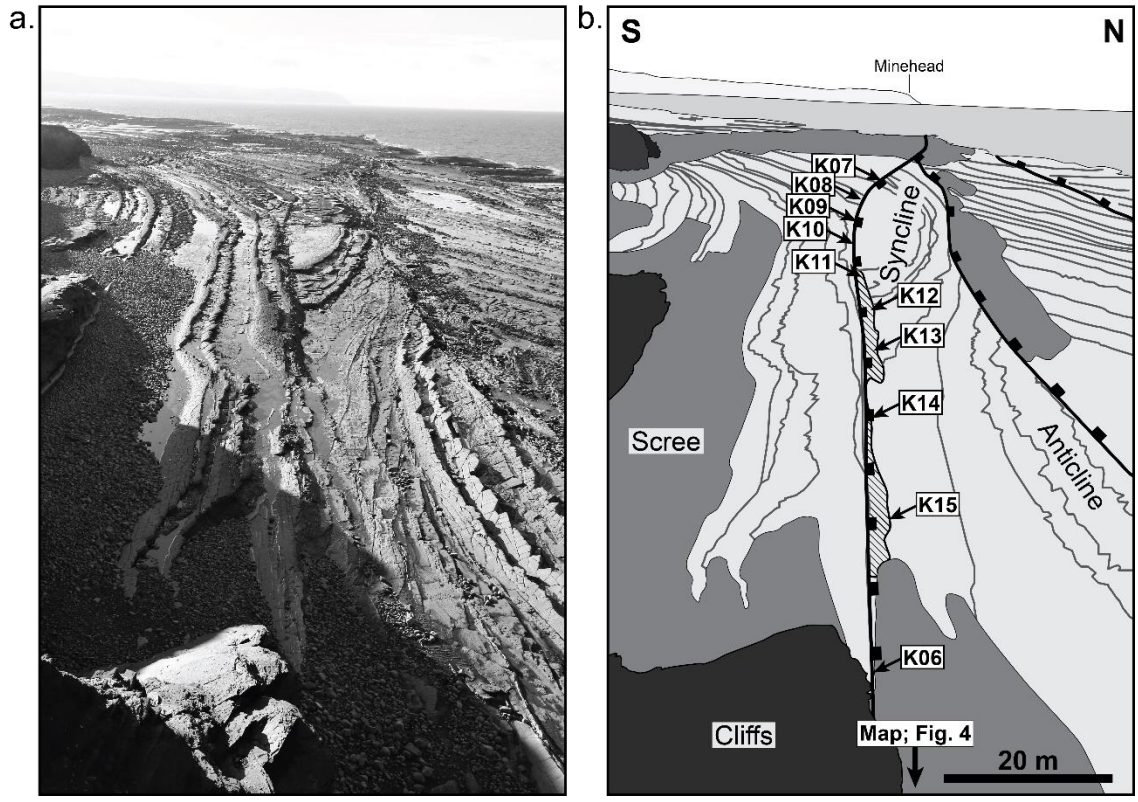

Figure 7. (a) An outcrop photo along the strike of the Kilve Pil Fault plane at Kilve. (b) Sample locations are shown (black arrows) and the location of the structural section of the Kilve Pil Fault (Figure 4) is indicated. Minehead indicates the west of the study area.

by approximately 60 m against the Mercia Mudstone Group. Reverse-reactivation is identified by anticlinal folding in the hanging wall.

3.2 Oxygen and carbon stable isotopes

Powdered samples were extracted from veins using a dental technician's drill and prepared for geochemical analyses. A selection of 19 calcite vein and slickencryst samples were measured for oxygen ($\delta^{18}O$) and carbon ($\delta^{13}C$) isotopes following a method described in Chapter 4 that was modified from Spötl and Vennemann (2003). The isotopic ratio of the CO_2 gas was measured using a Nu Instruments Dual Inlet Isotope Ratio Mass Spectrometer (DI-IRMS) at the University of Adelaide. The ANU P3 (Tridacna gigas aragonite shell; $\delta^{18}O$: –0.31‰, $\delta^{13}C$: 2.23‰), UAC-1 (calcium carbonate; $\delta^{18}O$: –18.4‰, $\delta^{13}C$: –15‰), and IAEA CO-8 1 (marble; $\delta^{18}O$: –22.7‰, $\delta^{13}C$: –5.76‰) reference materials were used as internal accuracy standards. The $\delta^{18}O$ and $\delta^{13}C$ values have been measured relative to the Vienna Pee Dee Belemnite (VPDB) standard. However, in this study we report $\delta^{13}C$ values relative to VPDB and $\delta^{18}O$ values relative to Standard Mean Ocean Water (SMOW) in per mille (‰) units, where $\delta^{18}O$ values have been calculated by converting VPDB values to SMOW values following Friedman and O'Neil (1977). The analytical uncertainties of the isotope measurements are tabulated in Appendix 4.

3.3 Strontium isotopes

A selection of 11 gypsum and 14 calcite vein and slickencryst samples were measured for strontium ($^{87}Sr/^{86}Sr$) isotope tracers. Powdered samples (0.001 mg) were placed into clean polytetrafluoroethylene (PTFE) vials and 2 mL of 1 M hydrochloric acid was manually added to the vials. The powdered samples

were leached at room temperature for approximately 24 hours. The strontium fraction was extracted following the methods of Chapter 4. The ratio of $^{87}Sr/^{86}Sr$ was measured using a Phoenix Isotopx Thermal Ionisation Mass Spectrometer at the University of Adelaide. Two standards, i.e. JDo-1 (Kuzuu dolomite) and JLs-1 (Garo limestone) reference materials issued by the Geological Survey of Japan, and two blank vials spiked with strontium were used as internal accuracy standards. The average $^{87}Sr/^{86}Sr$ isotopic ratio for JDo-1 was 0.707547 ± 0.000003 (2σ; n = 2; GeoReM literature value = 0.70752) and the average $^{87}Sr/^{86}Sr$ isotopic ratio for JLs-1 was 0.707826 ± 0.000003 (2σ; n = 2; GeoReM literature value = 0.70783). The spiked blanks contained less than 2 ng of strontium and the total contribution of strontium was less than 0.1%, therefore no correction for the blanks were made in this study. NISTSRM-987 was also used to test external reproducibility, which yielded an average $^{87}Sr/^{86}Sr$ isotopic ratio of 0.710244 ± 0.000012 (2σ; n = 14; literature value = 0.710248). The analytical uncertainties of the isotope measurements are tabulated in Appendix 4.

4. Results

4.1 Oxygen and carbon stable isotopes

The oxygen and carbon isotopic composition of calcite veins and slickencrysts in the Lias Group are similar at individual study locations (i.e. local scale) but vary across the study area (i.e. basin scale; Appendix 4 and Fig. 8). Overall, at both a local scale and a basin scale there were no observable relationships between the dip angle and orientation of fractures with the oxygen and carbon isotopic composition of calcite cements, indicating that the movement and distribution of fluids in fractures is not controlled by the orientation of fracture opening.

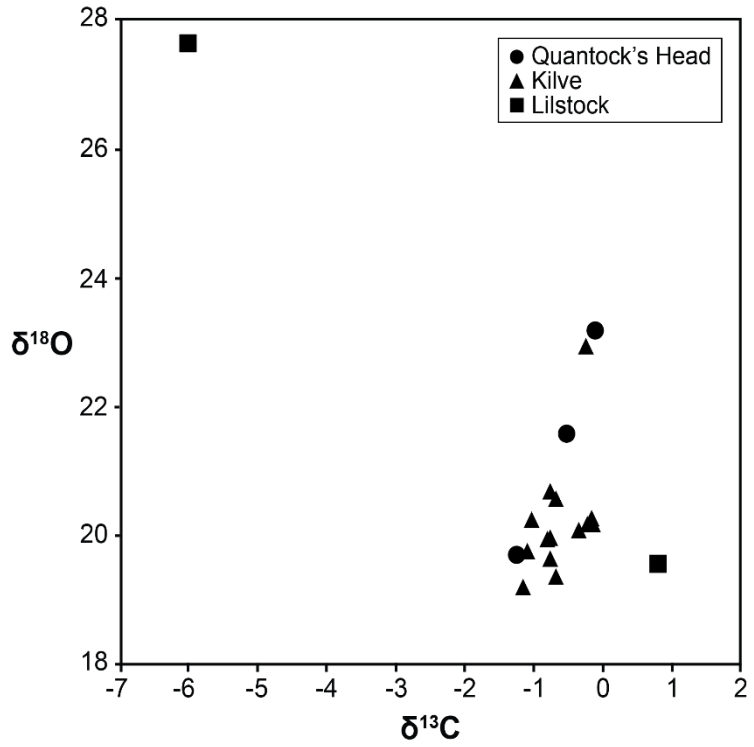

Figure 8. $\delta^{18}O$ SMOW values relative to $\delta^{13}C$ VPDB values for calcite veins from Quantock's Head, Kilve, and Lilstock.

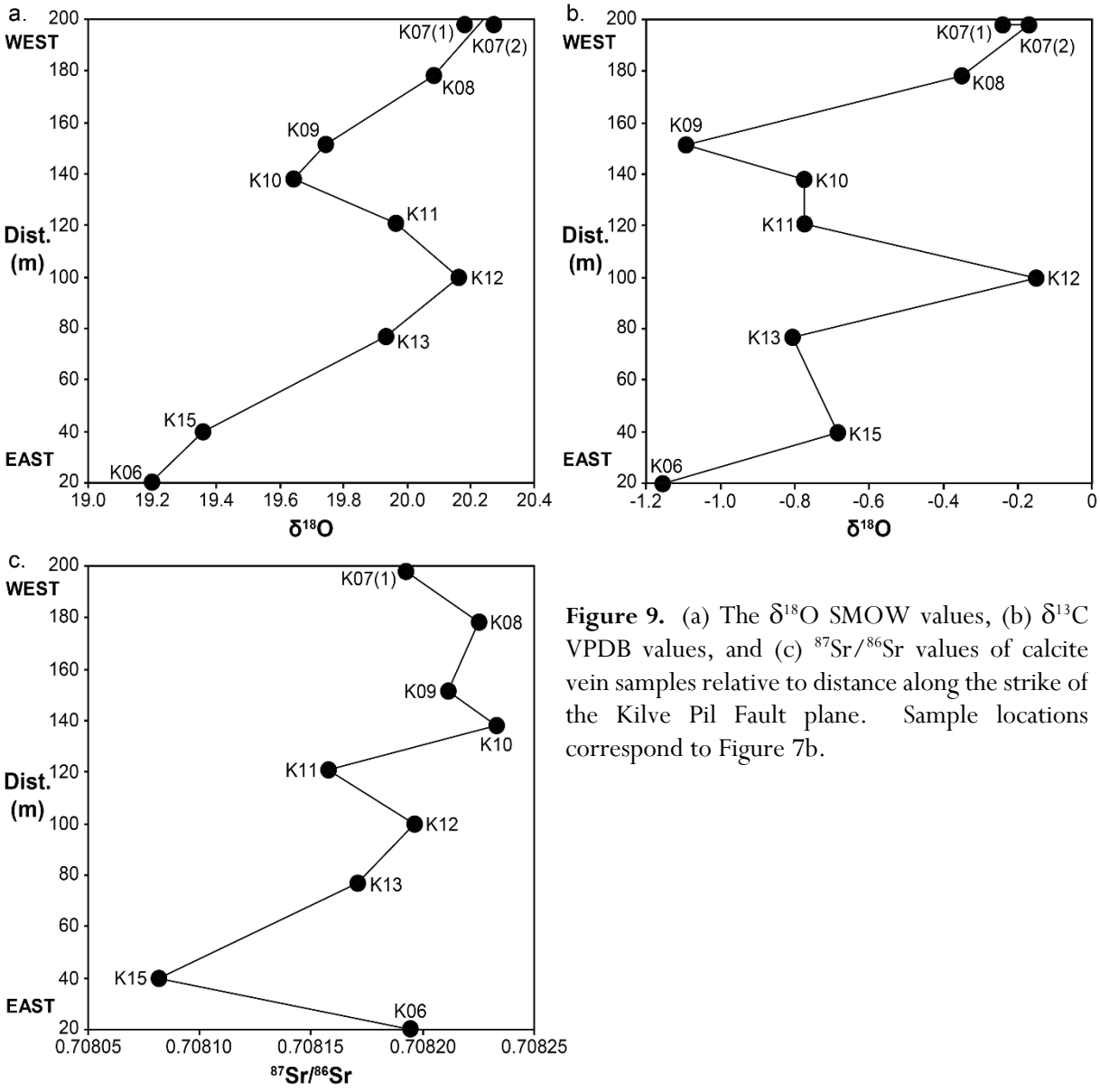

Figure 9. (a) The $\delta^{18}O$ SMOW values, (b) $\delta^{13}C$ VPDB values, and (c) $^{87}Sr/^{86}Sr$ values of calcite vein samples relative to distance along the strike of the Kilve Pil Fault plane. Sample locations correspond to Figure 7b.

4.1.1 Quantock's Head Fault

At the Quantock's Head Fault (Fig. 5), the calcite slickencrysts in the fault plane have a slightly depleted isotopic composition ($\delta^{18}O$: 19.7‰, $\delta^{13}C$: –1.3‰) relative to calcite veins in the footwall ($\delta^{18}O$: –21.6‰, $\delta^{13}C$: –0.6‰) and the hanging wall ($\delta^{18}O$: –23.2‰, $\delta^{13}C$: –0.1‰; Fig. 8).

4.1.2 Kilve Pil Fault

At the Kilve Pil Fault, the $\delta^{18}O$ values of the calcite slickencrysts in the fault plane are similar, but gradually become heavier, lighter, then heavier toward the west (i.e. from 19.2‰ in the east to 20.2‰ in the west; Fig. 7 and Fig. 9a). There is a strong positive correlation (coefficient of determination, $R^2 = 0.61$) between the $\delta^{18}O$ values and distance along the fault plane. The $\delta^{13}C$ values are considerably more scattered and there appears to be only a moderate overall trend ($R^2 = 0.33$) of increasing $\delta^{13}C$ values with distance along the fault plane to the west (Fig. 9b). Within the damage zone of the Kilve Pil Fault (Fig. 4), the oxygen and carbon isotopic compositions of the calcite veins are similar. The $\delta^{18}O$ values range between 20.2‰ and 20.7‰ SMOW, while the $\delta^{13}C$ values are between –1.0‰ and –0.7‰ VPDB. The

calcite slickencrysts in the fault plane in the mapping area (Fig. 4), however, have a slightly heavier oxygen and carbon isotopic composition of 22.9‰ SMOW and –0.3‰ VPDB, respectively.

4.1.3 East Lilstock Fault

At the East Lilstock Fault, a calcite vein within the fault gauge (Fig. 6) has a very heavy $\delta^{18}O$ value of 27.7‰ SMOW and a very light $\delta^{13}C$ value of –6.0‰ VPDB. A nearby fault that is parallel to the East Lilstock Fault strike, located further to the east, records a similar $\delta^{18}O$ value but a slightly heavier $\delta^{13}C$ value ($\delta^{18}O$: 19.6‰, $\delta^{13}C$: 0.78‰) to calcite cements located in Quantock's Head and Kilve.

4.2 Strontium isotopes

The strontium isotopic composition of calcite and gypsum veins and slickencrysts plot in two distinct groups (Fig. 10). The calcite cements have $^{87}Sr/^{86}Sr$ values between 0.708027 and 0.708233, and one calcite vein sample from the East Lilstock Fault records a radiogenic $^{87}Sr/^{86}Sr$ value of 0.709465. The gypsum cements have highly radiogenic $^{87}Sr/^{86}Sr$ values between 0.708992 and 0.709794. There is a strong negative correlation ($R^2 = 0.72$) between the $^{87}Sr/^{86}Sr$ values of gypsum cements and the horizontal distance (i.e. the $^{87}Sr/^{86}Sr$ values become more radiogenic toward the west), however there is no correlation ($R^2 = 0.07$) between the $^{87}Sr/^{86}Sr$ values of all calcite cements and the horizontal distance (Fig. 10).

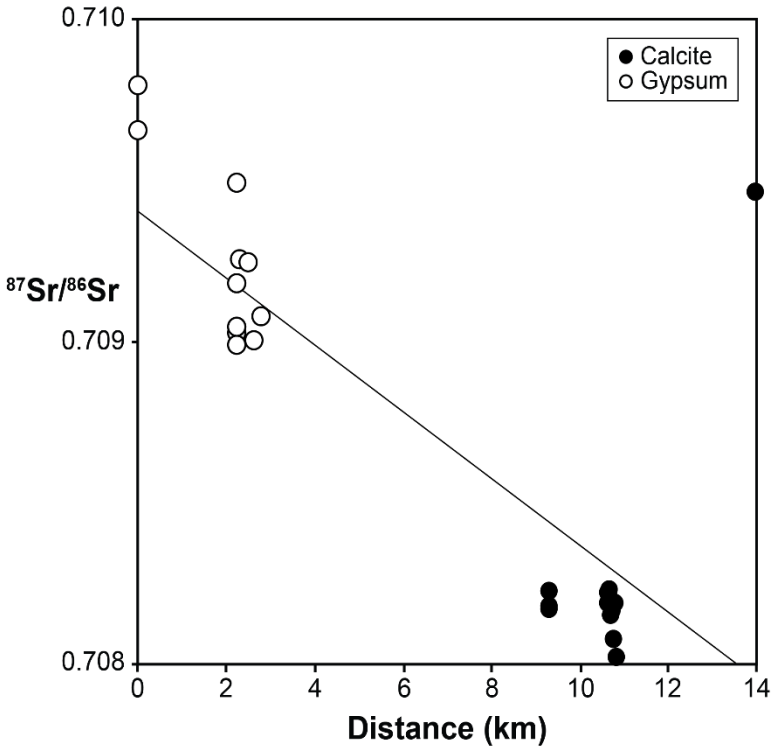

Figure 10. The $^{87}Sr/^{86}Sr$ values of calcite and gypsum vein samples from locations in the eastern Bristol Channel Basin, from west (at 0 km) to east (at 14 km). The overall correlation between the $^{87}Sr/^{86}Sr$ values of veins and horizontal distance is $R^2 = 0.63$.

Gypsum vein samples from Blue Anchor have the most radiogenic strontium isotopic composition ($^{87}Sr/^{86}Sr$: 0.709656 to 0.709794) in the study area (Table 1 and Fig. 10). At the Helwell Bay Fault, the $^{87}Sr/^{86}Sr$ values of the gypsum veins adjacent to the fault plane are similar, but gradually become more radiogenic toward the west (i.e. from 0.709079 in the east to 0.709259 in the west). Within the damage

zone of the Helwell Bay Fault (Fig. 3), the strontium isotopic compositions of the gypsum veins are similar (0.708992 to 0.709182). The gypsum slickencrysts in the fault plane in the mapping area (Fig. 3) also have a similar $^{87}Sr/^{86}Sr$ value of 0.709047. The gypsum nodules in the bedding at Warren Bay have the most radiogenic strontium values ($^{87}Sr/^{86}Sr$: 0.709493; Table 1 and Fig. 3) relative to gypsum veins and slickencrysts within the fault damage zone. At the Quantock's Head Fault (Fig. 5), the calcite slickencrysts in the fault plane have a more radiogenic strontium isotopic composition ($^{87}Sr/^{86}Sr$: 0.708229) relative to the calcite veins in the footwall ($^{87}Sr/^{86}Sr$: 0.708172) and the hanging wall ($^{87}Sr/^{86}Sr$: 0.708184). At the Kilve Pil Fault, the $^{87}Sr/^{86}Sr$ values of the calcite slickencrysts in the fault plane overall become more radiogenic toward the west (Fig. 7 and Fig. 9c) and follow a similar pattern to the $\delta^{18}O$ values (Fig. 9a). The calcite slickencrysts in the fault plane in the mapping area (Fig. 7) have a less radiogenic strontium isotopic composition of 0.708027 relative to the slickencrysts toward the west. At the East Lilstock Fault, a calcite vein within the fault gauge (Fig. 6) has a very radiogenic $^{87}Sr/^{86}Sr$ value of 0.709465 and is similar to the most radiogenic gypsum vein samples located to the west in the study area (i.e. Lilstock and Watchet).

5. Discussion

5.1 Sources of oxygen: calculated oxygen isotopic compositions of original pore fluids

The calcite veins and slickencrysts collected at different locations in this study have similar oxygen isotopic compositions (19.2‰ to 27.7‰ SMOW; Fig. 8). This range of $\delta^{18}O$ values are comparable to the values measured by Bixler et al. (1998), who presented $\delta^{18}O$ values between 22.6‰ and 27.4‰ SMOW from calcite veins at Kilve. The oxygen isotopic composition of the original pore fluids from which the calcite cements formed can be calculated using the measured isotopic composition of the cements in this study together with estimates of the cement precipitation temperature from other studies. Fluid inclusion analysis by Logan and Decker (1994) has identified a range of cement precipitation temperatures that can be utilised in this study. Homogenisation temperatures of fluid inclusions measured in calcite veins at Kilve range from 70°C to 130°C (Logan and Decker, 1994). These temperatures indicate that the fluids were sourced at depth and geochemical analyses by Davison (1995) suggest that the mineralising fluids at Kilve were sourced from approximately 1 km below present day exposures. Additionally, Davison (1995) suggest that the mineralising fluids were hotter than the surrounding protolith, which was approximately 80°C during the Jurassic to early Cretaceous based on vitrinite reflectance data (Cornford, 1986). Using the temperature estimations for calcite precipitation from Logan and Decker (1994) and the measured oxygen isotopic composition of the calcite cements in this study, the original oxygen isotopic composition of pore fluids ($\delta^{18}O_{water}$) in equilibrium with calcite cements can be calculated using a fractionation equation from O'Neil et al. (1969):

$$\text{Calcite–water}: \delta^{18}O_{water} = \delta^{18}O_{calcite} - ((2780000/T^2) - 2.89) \quad (1)$$

The $\delta^{18}O_{water}$ values of pore fluids in this study precipitated at 70°C (i.e. minimum temperature estimate) range from –1.6‰ to 2.5‰ SMOW for most calcite cements based on Equation 1, and up to 6.9‰ SMOW for a calcite vein within the fault gauge of the East Lilstock Fault. The $\delta^{18}O_{water}$ values of pore fluids in this study precipitated at 130°C (i.e. maximum temperature estimate) are heavier and range from 5.0‰ to 9.0‰ SMOW for most calcite cements based on Equation 1, and up to 13.44‰ SMOW for the calcite vein sampled at Lilstock. Overall, the range of calculated $\delta^{18}O_{water}$ values are relatively heavy, and they are heavier than that of coeval seawater (–1.0‰ SMOW; Shackelton and Kennett, 1975). The

calculated $\delta^{18}O_{water}$ values are consistent with calcite precipitation from fluids that have undergone oxygen isotope exchange with the host rock, i.e. Lias Group shales and limestones. As the Lias Group contains abundant carbonaceous fossils, the most likely source of enriched $\delta^{18}O$ values is input from heavy marine bicarbonate during the dissolution of carbonate fossils (Marshall, 1982).

5.2 Sources of carbon

The calcite veins and slickencrysts sampled from the Lias Group in this study have light carbon isotopic compositions. The $\delta^{13}C$ values of calcite veins and slickencrysts at Quantock's Head and Kilve are similar (–1.3‰ to –0.1‰ VPDB; Fig. 8). The calcite vein samples from Lilstock are more variable (–6.0‰ to 0.8‰ VPDB; Fig. 8). The carbon isotopic composition of calcite is controlled by variations related to the depositional environment, presence of particulate and fossiliferous calcite, and the types of organic reactions occurring simultaneously with calcite formation (Mozley and Burns, 1993). Therefore variations in the carbon isotopic composition of calcite would be location specific, and may also vary within a location. The range of $\delta^{13}C$ values of calcite cements analysed in this study are within the range commonly found for marine fossils (Hudson, 1975, 1977). The main calcite source for the veins was likely particulate and fossiliferous calcite within the Lias Group. The Lias Group also crops out along the Dorset coast, located south of the study area, and the source of calcite preserved in veins has been linked to carbonate fossils within the Lias Group (Nemčok et al., 1995). The Lias Group in the eastern Bristol Channel Basin also contains abundant carbonate fossils. Nemčok et al. (1995) suggest that the nucleation of calcite cements first occurred in fossil-rich beds and was subsequently transported to veins through diffusion and this mechanism is also plausible in the Bristol Channel Basin.

5.3 Sources of strontium

The strontium isotopic composition of calcite and gypsum cements in the eastern Bristol Channel Basin represent radiogenic values ($^{87}Sr/^{86}Sr$ = >0.708; Fig. 10). These strontium isotope values are more radiogenic than those of coeval seawater. The strontium isotopic composition of early Jurassic seawater ranged between 0.7075 and 0.7078 (Jones et al., 1994; Koepnick et al., 1990). Elevated levels of $^{87}Sr/^{86}Sr$ in veins indicate a continental-derived source of strontium (Wierzbowski, 2013). This suggests the migration of radiogenic basinal fluids through the fault systems and their associated damage zones, and this interpretation is consistent with Logan and Decker (1994) and Bixler et al. (1998). Gypsum cements from Blue Anchor and Watchet in the western section of the study area, and one calcite vein from the East Lilstock Fault, have exceptionally radiogenic strontium isotopic compositions (Fig. 10). The gypsum nodules in the bedding at Watchet have the most radiogenic strontium values measured in this study. This suggests that the evaporitic intervals within the Mercia Mudstone Group are also contributing to the mineralising fluid composition and are resulting in enriched $^{87}Sr/^{86}Sr$ values in gypsum veins and slickencrysts. In the eastern section of the study area, extensive diagenetic alteration of the Lias Group has resulted in enriched $^{87}Sr/^{86}Sr$ values within the limestone intervals (0.70808 to 0.70824; c.f. Bixler et al., 1998). The strontium isotopic composition of these limestone intervals is comparable to those measured in calcite veins and slickencrysts in this study (0.708027 to 0.708233; Fig. 10). The dissolution and alteration of labile minerals and fossils within the Lias Group may be controlling the strontium isotopic composition of the mineralising fluids.

5.4 Fluid evolution and migration

The oxygen, carbon, and strontium isotopic compositions of veins and slickencrysts in this study can be used to understand fluid evolution and the migration pathways of fluids in the Bristol Channel Basin. The strontium isotopic composition of calcite and gypsum cements in this study indicate at least two different mineralising fluid compositions that are strongly controlled by the lithologies in which they occur. These fluids originated as connate pore fluids, i.e. fluids buried at the time of deposition, which were altered during the diagenesis of their host lithologies. The diagenesis, alteration, and the dissolution of labile minerals and carbonaceous fossils within the Lias Group resulted in enriched oxygen and strontium isotopic compositions and relatively depleted carbon isotopic compositions of pore fluids. The evaporitic intervals (e.g. gypsum nodules) within the Mercia Mudstone Group led to exceptionally radiogenic strontium isotopic compositions of pore fluids. This indicates that the mineralising fluids in the Mercia Mudstone Group and Lias Group in the eastern Bristol Channel Basin were supplied locally from pore space and were redistributed through migration along faults and their associated damage zones.

There is a spatial trend of oxygen and strontium isotopic compositions relative to distance, from east to west. More radiogenic strontium isotope compositions relative to distance was observed in the overall gypsum cement dataset, the gypsum veins along the Helwell Bay Fault plane, and the calcite slickencrysts along the Kilve Pil Fault plane. Calcite slickencrysts on the Kilve Pil Fault plane also record a trend of increasing $\delta^{18}O$ values toward the west (Fig. 9a). There are two plausible explanations for this spatial trend: (1) the exposed outcrops in each study location are generally stratigraphically deeper to the west, and (2) a contrasting origin of fluids migrating along the fault systems, indicating that different fluid flow regimes have interacted with the faults. The former explanation suggests that depth, and therefore temperature, have contributed to geochemical changes in the pore fluids along the fault. Alternatively, changes in lithology associated with changes in stratigraphic depth may be contributing to this trend. As the geochemical signature of the pore fluids potentially reflects changes associated with changes in depth, this implies that the fluids have not travelled far vertically. The latter explanation suggests that the interaction of different sources of fluids may have contributed to the spatial trend. However, this seems unlikely given that similar trends between the geochemistry of the pore fluids relative to distance are observed in different locations. Without further geochemical and structural analysis these explanations remain speculative.

5.5 Comparison of the results from this study with other studies

The results in this study indicate that the mineralising fluids are of local origin, and this is consistent with other studies in the Bristol Channel Basin. For instance, field observations at Kilve by Philipp (2012) suggest the calcite veins were of local origin and potentially migrated from sill-like sources of water at depth. At Watchet, Meng et al. (2017b) suggest that the mineralising fluids preserved as gypsum veins migrated through diffusion that was driven by concentration gradients. Elemental analysis and strontium isotope analysis by Meng et al. (2017c) indicate that gypsum veins are sourced from fluids derived from evaporitic intervals within the Mercia Mudstone Group, and this is also consistent with this study.

However, not all studies suggest a local origin of mineralising fluids in the Bristol Channel Basin. For example, fluid inclusion analysis by Logan and Decker (1994) suggests that the fluids preserved in some faults in the study area experienced elevated temperatures (up to 200°C). Therefore, they concluded that these fluids migrated up faults from a greater depth, rather than being sourced locally from the adjacent rock. Similarly, the presence of hydrocarbon inclusions and exceptionally radiogenic strontium isotopic

compositions in some calcite veins analysed by Bixler et al. (1998) indicate that fluids have a basinal origin and may have migrated from greater depths. Similar radiogenic strontium isotopic compositions in this present study have been attributed to the dissolution and alteration of labile minerals and fossils. Oxygen isotopic compositions also suggest calcite precipitation from fluids that have undergone oxygen isotope exchange with the host rock. Therefore, the results from this study highlight the importance of integrating a range of geochemical analyses when attempting to understand the source of pore fluids and their evolution through time.

6. Conclusions

Geochemical data, from stable oxygen and carbon isotope and strontium isotope analyses, of calcite and gypsum cements provide valuable insights into the source of pore fluids and their evolution and migration in the eastern Bristol Channel Basin.

- Radiogenic strontium isotopic compositions indicate at least two different mineralising fluid compositions that are strongly controlled by the lithologies in which they occur.
- The alteration of labile minerals and carbonaceous fossils within the Lias Group resulted in enriched oxygen (19.2‰ to 27.7‰ SMOW) and strontium isotopic compositions (0.708027 to 0.709465) and relatively depleted carbon isotopic compositions (–6.0‰ to 0.8‰ VPDB) of pore fluids.
- The evaporitic intervals within the Mercia Mudstone Group led to exceptionally radiogenic strontium isotopic compositions (0.708992 to 0.709794) of pore fluids.
- A spatial trend of more radiogenic strontium and enriched oxygen isotope compositions relative to distance, from east to west, was observed along fault strike for two faults (Helwell Bay Fault and Kilve Pil Fault).
- Mineralising fluids in the eastern Bristol Channel Basin were supplied locally from pore space and redistributed through migration along faults and their associated damage zones.
- There were no observable relationships between the dip angle and orientation of fractures with the oxygen and carbon isotopic composition of calcite cements, indicating that the movement and distribution of fluids in fractures is not controlled by the orientation of fracture opening. This is important for understanding the movement of economic fluids, such as hydrocarbons and mineral deposits, in basins that have experienced similar tectonic histories.

This study shows that the composition of the lithology that hosts the pore fluids can have a strong control on pore fluid chemistry. Fault zones act as conduits for the migration of fluids, however if changes in the isotopic composition of fluids within the fault zones reflect changes in depth, the fluids in the eastern Bristol Channel Basin may not have travelled great distances within these fault zones.

Acknowledgements

This research forms part of a PhD project supported by the Australian Research Council [Discovery Project DP160101158] and through an Australian Government Research Training Program Scholarship. This study was also funded by scholarships from the Petroleum Exploration Society of Australia and the Australian Petroleum Production and Exploration Association. Permission was granted by Natural England for field work and sampling in the Blue Anchor to Lilstock Site of Special Scientific Interest (SSSI). Field assistants James Hall and Tayallen Velayatham are gratefully acknowledged for their contribution.

References

Alistair Beach, 1993. Extensional and Inversion Tectonics, West Somerset: A Field Trip Guide, Glasgow, Scotland, UK.

Ayalon, A., Longstaffe, F.J., 1988. Oxygen isotope studies of diagenesis and pore-water evolution in the Western Canada sedimentary basin; evidence from the Upper Cretaceous basal Belly River Sandstone, Alberta. Journal of Sedimentary Research 58, 489-505.

Aydin, A., 2000. Fractures, faults, and hydrocarbon entrapment, migration and flow. Marine and Petroleum Geology 17, 797-814.

Bixler, W.G., Elmore, R.D., Engel, M.H., 1998. The origin of magnetization and geochemical alteration in a fault zone, Kilve, England. Geological Journal 33, 89-105.

Bons, P.D., Elburg, M.A., Gomez-Rivas, E., 2012. A review of the formation of tectonic veins and their microstructures. Journal of Structural Geology 43, 33-62.

Brooks, M., Trayner, P.M., Trimble, T.J., 1988. Mesozoic reactivation of Variscan thrusting in the Bristol Channel area, UK. Journal of the Geological Society 145, 439-444.

Cornford, C., 1986. The Bristol Channel Graben: organic chemical limits on subsidence and speculation on the origin of inversion. Proceedings of the Ussher Society 6, 360-367.

Cosgrove, J.W., 2001. Hydraulic fracturing during the formation and deformation of a basin: A factor in the dewatering of low-permeability sediments. AAPG Bulletin 85, 737-748.

Coward, M.P., 1995. Structural and tectonic setting of the Permo-Triassic basins of northwest Europe. Geological Society, London, Special Publications 91, 7-39.

Cox, B.M., Sumbler, M.G., Ivimey-Cook, H.C., 1999. A Formational framework for the Lower Jurassic of England and Wales (Onshore Area). British Geological Survey, Nottingham, United Kingdom.

Curtis, C.D., Coleman, M.L., 1986. Controls on the precipitation of early diagenetic calcite, dolomite, and siderite concretions in complex depositional sequences, In: Gautier, D.L. (Ed.), Roles of Organic Matter in Sediment Diagenesis. The Society of Economic Paleontologists and Mineralogists, pp. 23-33.

Dart, C.J., McClay, K.R., Hollings, P.N., 1995. 3D analysis of inverted extensional fault systems, southern Bristol Channel basin, UK. Geological Society, London, Special Publications 88, 393-413.

Davison, I., 1995. Fault slip evolution determined from crack-seal veins in pull-aparts and their implications for general slip models. Journal of Structural Geology 17, 1025-1034.

Evans, M.A., 1995. Fluid inclusions in veins from the Middle Devonian shales: A record of deformation conditions and fluid evolution in the Appalachian Plateau. GSA Bulletin 107, 327-339.

Fairley, J.P., 2009. Modeling fluid flow in a heterogeneous, fault-controlled hydrothermal system. Geofluids 9, 153-166.

Friedman, I., O'Neil, J.R., 1977. Compilation of stable isotope fractionation factors of geochemical interest, Professional Paper, p. 117.

Glen, R.A., Hancock, P.L., Whittaker, A., 2005. Basin inversion by distributed deformation: the southern margin of the Bristol Channel Basin, England. Journal of Structural Geology 27, 2113-2134.

Gutmanis, J.C., Hailwood, E.A., Maddock, R.H., Vita-Finzi, C., 1991. The use of dating techniques to constrain the age of fault activity: a case history from north Somerset, United Kingdom. Quarterly Journal of Engineering Geology and Hydrogeology 24, 363-374.

Hounslow, M., Ruffell, A., 2006. Triassic: seasonal rivers, dusty deserts and saline lakes, In: Rawson, P.F., Brenchley, P. (Eds.), The Geology of England and Wales. Geological Society of London, United Kingdom, pp. 295-325.

Howard, A.S., Warrington, G., Ambrose, K., Rees, J.G., 2008. A formational framework for the Mercia Mudstone Group (Triassic) of England and Wales. British Geological Survey, Nottingham, United Kingdom.

Hudson, J.D., 1975. Carbon isotopes and limestone cement. Geology 3, 19-22.

Hudson, J.D., 1977. Stable isotopes and limestone lithification. Journal of the Geological Society 133, 637-660.

Jones, C.E., Jenkyns, H.C., Hesselbo, S.P., 1994. Strontium isotopes in Early Jurassic seawater. Geochimica et Cosmochimica Acta 58, 1285-1301.

Kamerling, P., 1979. The geology and hydrocarbon habitat of the Bristol Channel Basin. Journal of Petroleum Geology 2, 75-93.

Kelly, P.G., Peacock, D.C.P., Sanderson, D.J., McGurk, A.C., 1999. Selective reverse-reactivation of normal faults, and deformation around reverse-reactivated faults in the Mesozoic of the Somerset coast. Journal of Structural Geology 21, 493-509.

Knipe, R.J., Jones, G., Fisher, Q.J., 1998. Faulting, fault sealing and fluid flow in hydrocarbon reservoirs: an introduction. Geological Society, London, Special Publications 147, vii-xxi.

Koepnick, R.B., Denison, R.E., Burke, W.H., Hetherington, E.A., Dahl, D.A., 1990. Construction of the Triassic and Jurassic portion of the Phanerozoic curve of seawater 87Sr/86Sr. Chemical Geology: Isotope Geoscience section 80, 327-349.

Laubach, S.E., Olson, J.E., Gross, M.R., 2009. Mechanical and fracture stratigraphy. AAPG Bulletin 93, 1413-1426.

Logan, J.M., Decker, C.I., 1994. Cyclic fluid flow along faults, In: Jacobson, M.L.H., S. H., Sibson, R.H., Bruhn, R.L. (Eds.), Proceedings of Workshop LXIII: USGS Red-Book conference on the mechanical involvement of fluids in faulting. U.S. Geological Survey Open-File Report, United States of America, pp. 190-203.

Marshall, J.D., 1982. Isotopic composition of displacive fibrous calcite veins; reversals in pore-water composition trends during burial diagenesis. Journal of Sedimentary Research 52, 615-630.

Meng, Q., Hooker, J., Cartwright, J., 2017a. Early overpressuring in organic-rich shales during burial: evidence from fibrous calcite veins in the Lower Jurassic Shales-with-Beef Member in the Wessex Basin, UK. Journal of the Geological Society.

Meng, Q., Hooker, J., Cartwright, J., 2017b. Genesis of natural hydraulic fractures as an indicator of basin inversion. Journal of Structural Geology.

Meng, Q., Hooker, J., Cartwright, J.O.E., 2017c. Lithological control on fracture cementation in the Keuper Marl (Triassic), north Somerset, UK. Geological Magazine, 1-15.

Mozley, P.S., Burns, S.J., 1993. Oxygen and carbon isotopic composition of marine carbonate concretions; an overview. Journal of Sedimentary Research 63, 73-83.

Nemčok, M., Gayer, R., Miliorizos, M., 1995. Structural analysis of the inverted Bristol Channel Basin: implications for the geometry and timing of fracture porosity. Geological Society, London, Special Publications 88, 355-392.

O'Neil, J.R., Clayton, R.N., Mayeda, T.K., 1969. Oxygen Isotope Fractionation in Divalent Metal Carbonates. The Journal of Chemical Physics 51, 5547-5558.

Pagel, M., Braun, J.-J., Disnar, J.R., Martínez, L., Renac, C., Vasseur, G., 1997. Thermal history constraints from studies of organic matter, clay minerals, fluid inclusions, and apatite fission tracks at the Ardeche paleo-margin (BA1 drill hole, GPF program), France. Journal of Sedimentary Research 67, 235-245.

Parrish, R.R., Parrish, C.M., Lasalle, S., 2018. Vein calcite dating reveals Pyrenean orogen as cause of Paleogene deformation in southern England. Journal of the Geological Society, jgs2017-2107.

Peacock, D.C.P., Sanderson, D.J., 1999. Deformation history and basin-controlling faults in the Mesozoic sedimentary rocks of the Somerset coast. Proceedings of the Geologists' Association 110, 41-52.

Philipp, S.L., 2008. Geometry and formation of gypsum veins in mudstones at Watchet, Somerset, SW England. Geological Magazine 145, 831-844.

Philipp, S.L., 2012. Fluid overpressure estimates from the aspect ratios of mineral veins. Tectonophysics 581, 35-47.

Rowland, J.V., Sibson, R.H., 2004. Structural controls on hydrothermal flow in a segmented rift system, Taupo Volcanic Zone, New Zealand. Geofluids 4, 259-283.

Ruffell, A., Shelton, R., 1999. The control of sedimentary facies by climate during phases of crustal extension: examples from the Triassic of onshore and offshore England and Northern Ireland. Journal of the Geological Society 156, 779-789.

Scotchman, I.C., Carr, A.D., Astin, T.R., Kelly, J., 2002. Pore fluid evolution in the Kimmeridge Clay Formation of the UK Outer Moray Firth: implications for sandstone diagenesis. Marine and Petroleum Geology 19, 247-273.

Shackelton, N.J., Kennett, J.P., 1975. Paleotemperature history of the Cenozoic and the initiation of Antarctic glaciation: oxygen and carbon isotope analyses in DSDP sites 277, 279 and 281, In: Kennett, J.P., Houtz, R.E. (Eds.), Initial Reports of the Deep Sea Drilling Project 29, U.S. Government Printing Office, Washington, pp. 743-756.

Sibson, R.H., Moore, J.M.M., Rankin, A.H., 1975. Seismic pumping—a hydrothermal fluid transport mechanism. Journal of the Geological Society 131, 653-659.

Spötl, C., Vennemann, T.W., 2003. Continuous-flow isotope ratio mass spectrometric analysis of carbonate minerals. Rapid Communications in Mass Spectrometry 17, 1004-1006.

Van Hoorn, B., 1987. The south Celtic Sea/Bristol Channel Basin: origin, deformation and inversion history. Tectonophysics 137, 309-334.

Wierzbowski, H., 2013. Strontium isotope composition of sedimentary rocks and its application to chemostratigraphy and palaeoenvironmental reconstructions. The Annales UMCS Sectio AAA – Physica 68, 23-37.

CHAPTER 6

Key findings and conclusions

This thesis endeavoured to characterise the structural, petrophysical, and geochemical properties of inverted fault zones in order to understand how inverted faults influence fluid flow at a range of scales. To address this, this thesis had two main topics of focus:

1. Identify the influence of inverted faults on surrounding lithology by assessing the relationship between faults, damage zones around faults, and fractures related to fault growth.
2. Identify how subsurface fluids flow, interact, and modify their surrounds by assessing the geochemistry of fluids in fractures and thereby constraining the source, evolution, and migration of fluids preserved in fractures.

These topics of focus will be discussed below in relation to the key findings of each chapter in this thesis.

1. The influence of inverted faults on surrounding lithology

Chapters 2 and 3 used a combination of structural, petrophysical, and petrographical analyses with the aim of characterising the conduits for fluid flow associated with fault inversion. **Chapter 2** discussed the outcrop-scale conduits for fluid flow associated with the reverse-reactivated Castle Cove Fault in the eastern Otway Basin, while **Chapter 3** discussed the micrometre-scale conduits for fluid flow associated with the fault.

The geometries and chronologies of natural macrofractures (i.e. fractures typically >10 cm in strike length) forming the damage zone of the Castle Cove Fault were investigated (**Chapter 2**). The damage zone of the Castle Cove Fault extends greater than 300 m in the hanging wall. Structural mapping in the hanging wall damage zone revealed three sets of shear fractures that are geometrically related to the Castle Cove Fault. Late Cretaceous NW–SE rifting and normal faulting led to led to rollover folding and associated synthetic and antithetic fault growth within the hanging wall. This resulted in the formation of the first, and most extensive, fracture set in the Castle Cove Fault damage zone. The fault was reactivated as a reverse fault during late Miocene to Pliocene NW–SE directed compression. During inversion of the fault, the rollover fold in the hanging wall was tightened and amplified to form a large-scale anticline. Non-coaxial inversion during anticlinal folding resulted in the formation of the second, extensive fracture set in the hanging wall damage zone. Reverse-reactivation of the fault also led to the formation of the third fracture set. The third fracture set was not extensive in the hanging wall and this suggests that strain was mainly accommodated by anticline folding in the hanging wall adjacent to the fault. Therefore, inversion of the Castle Cove Fault has resulted in the development of an extensive network of fractures and complex fold structures, and inversion would have subsequently improved the permeability structure of the damage zone for fluid migration.

At the micrometre-scale, the permeability structure has also been influenced by fault inversion (**Chapter 3**). Petrophysical and petrographical analyses in the hanging wall damage zone have shown that microstructural changes due to faulting have enhanced the micrometre-scale permeability structure of the Eumeralla Formation. These microstructural changes have been attributed to the formation of microfractures (i.e. grain-scale fractures identifiable in thin sections) and destruction of original pore-lining chlorite morphology as a result of fault deformation. More specifically, fault inversion has influenced the micrometre-scale permeability structure of the hanging wall damage zone in three main ways: (1) the formation of variably oriented microfractures that leads to isotropic permeability; (2) disaggregation of pore-lining clays due to deformation, which can enhance the micrometre-scale permeability structure of the protolith by opening pore-throats; and (3) cataclasis of individual grains

and grain size reduction, which can reduce the connected pore space and therefore impede fluid flow. Consequently, inversion has subsequently improved the permeability structure of the damage zone adjacent to the Castle Cove fault plane.

Therefore, complex deformation associated with normal faulting and subsequent reverse reactivation, (e.g. the formation of macrofractures, variably oriented microfractures, a hanging wall anticline, grain cataclasis, and changes in clay morphology) has significantly influenced the off-fault fluid flow properties of the protolith (**Chapters 2 and 3**). Characterisation of the permeability structure adjacent to reverse-reactivated faults at a range of scales will aid with predicting fluid flow associated with inversion structures.

2. How subsurface fluids flow, interact, and modify their surrounds

Chapters 4 and 5 used a combination of structural and geochemical analyses with the aim of understanding how subsurface fluids flow and characterising the source, evolution, and migration pathways of fluids preserved in deformation structures (e.g. faults and fractures). **Chapter 4** identified the pore fluid evolution and source of fluids preserved in fractures and concretions in the eastern Otway Basin, Australia, while **Chapter 3** identified the source and evolution of fluids preserved in fractures and faults in the eastern Bristol Channel Basin, United Kingdom.

The geochemical evolution of fluids precipitated as calcite and siderite-cemented concretions and fractures throughout the eastern Otway Basin was investigated (**Chapter 4**). Geochemical data from oxygen, carbon and strontium isotope analyses record the source and evolution of pore fluids from deposition to post-diagenesis. Two main sources of fluids were identified: (1) meteoric water, which was sourced locally and remained in a closed system, and (2) seawater, which was incorporated into the sediments during marine incursions. Depleted oxygen isotopic ratios recorded in all calcite-cemented concretions and some fractures indicated a meteoric water input during early diagenesis, followed by later calcite recrystallization with increased burial. The relatively unradiogenic strontium isotopic composition of these cements indicated that the dissolution and alteration of volcanic detritus was strongly influencing the composition of pore fluids. Heavy pore fluid oxygen isotopic compositions and radiogenic strontium values in the siderite-cemented concretions and siderite- and calcite-cemented fractures suggested a sea water input. Carbon dioxide for carbonate precipitation was sourced from methanogenic fermentation and oxidation of organic matter. This chapter showed that pore fluids were sourced from both meteoric water and sea water during the deposition of the Eumeralla Formation, and that pore fluid evolution was strongly influenced by diagenetic reactions and increased temperature during burial.

The geochemical evolution of fluids precipitated as calcite and gypsum-cemented fractures (i.e. veins) throughout the eastern Bristol Channel Basin was also investigated (**Chapter 5**). Following a similar approach to **Chapter 4**, geochemical data from oxygen, carbon and strontium isotope analyses record the source and evolution of fluids. The main source of fluids was connate pore waters, which were subsequently altered by diagenetic reactions within their host lithologies. Therefore, the two formations that were analysed in this study, i.e. the Mercia Mudstone Group and the Lias Group, host fluids with differing geochemical signatures. Mineralising fluids within the Lias Group are characterised by enriched oxygen and strontium isotopic compositions and relatively depleted carbon isotopic compositions, associated with the alteration of labile minerals and carbonaceous fossils. Mineralising fluids within the underlying Mercia Mudstone Group have exceptionally radiogenic strontium isotopic

compositions as a result of the interaction of fluids with evaporitic intervals. This chapter showed that mineralising fluids were sourced from pore waters incorporated into the sediment during deposition, and that these fluids were altered by diagenetic reactions and subsequently redistributed through migration along faults and their associated damage zones.

Inverted sedimentary basins that have experienced multiple phases of deformation, such as the eastern Otway Basin and eastern Bristol Channel Basin, host complex structures at a range of scales that can be preserved through the precipitation of fluids as cements. Knowledge of the source, evolution, and migration pathways of these fluids provides valuable insights for understanding the development of sedimentary basins through time. Integrated studies on the multi-scaled permeability structure of inverted fault zones (**Chapters 2 and 3**) and the fluids preserved within them (**Chapters 4 and 5**) will ultimately improve fluid exploration and monitoring strategies in sedimentary basins.

RESEARCH STANZA

The focus of my PhD dissertation

is faults and associated deformation.

Faults are large fractures in the crust,

they can be normal, strike-slip, or thrust.

My research looks at an extensive fault,

that went normal and thrust – then came to a halt.

The fault's found in the Otway Basin,

and has experienced one phase of inversion.

I study a lithic sandstone,

within this fault damage zone.

The sandstone's called the Eumeralla Formation;

a key source rock for gas accumulation.

I identify how subsurface fluids flow;

where they're from and where they go.

To do this I make fracture maps,

collect samples, and identify fault traps.

The maps show fracture formation timing,

and identify fractures from faulting.

I take small cores plugs from sample blocks,

and look at the properties of the rocks.

I look at pore space – both large and small,

and fractures – both short and tall.

I also look at the fracture cement,

to see fluid evolution from past to present.

Then with all this geological information,

We can predict fluid flow and migration.

Ultimately this has significant implication

for off-fault petroleum exploration.

APPENDIX 1

Chapter 2 data

Section 1 fracture data (GPS Location: 0710866 E, 5704543333 N) Mapped by Natalie Debenham

Map grid	Fracture	Dip	Dip Direction	Open/Closed	Fill	Aperture (mm)
H'	1	44	319	Closed	Siderite	< 1
H'	2	09	195	Closed	Siderite	< 1
H'	3	39	210	Closed	Siderite	1
H'	4	59	152	Closed	Siderite	< 1
H'	5	32	248	Closed	Siderite	3
H'	6	43	120	Closed	Siderite	< 1
H'	7	46	246	Closed	Siderite	< 1
H	8	21	010	Closed	No fill	< 1
H	9	40	248	Closed	Siderite	< 1
H	10	41	185	Closed	Siderite	2
H	11	38	235	Closed	Siderite	< 1
H	12	70	138	Closed	Siderite	< 1
H	13	63	018	Closed	Siderite	< 1
G	14	68	002	Closed	Siderite	2
G	15	72	091	Closed	Siderite	< 1
G	16	46	179	Closed	Siderite	< 1
G	17	40	030	Closed	Siderite	< 1
G'	18	19	078	Closed	Siderite	2
G'	19	59	350	Open/Closed	Siderite	40
G'	20	78	100	Closed	Siderite	1
G'	21	20	238	Closed	Siderite	< 1
G'	22	48	322	Closed	Siderite	< 1
F'	23	16	004	Closed	Siderite	< 1
F'	24	71	019	Closed	Siderite	1
F'	25	71	018	Open/Closed	Siderite	20
F'	26	10	019	Closed	Siderite	< 1
F'	27	80	147	Closed	Siderite	< 2
F'	28	41	270	Closed	Siderite	< 3
F'	29	60	140	Closed	Siderite	< 4
F	30	32	321	Closed	Siderite	2
F	31	59	160	Closed	Siderite	< 1
F	32	50	321	Closed	No fill	< 1
F	33	45	145	Closed	No fill	< 1
E'	34	52	355	Closed	Siderite	< 1
E'	35	58	222	Closed	Siderite	< 1
E'	36	63	275	Closed	Siderite	< 1
E'	37	64	002	Closed	Siderite	< 1
E'	38	78	321	Closed	Siderite	< 1
E	39	58	359	Closed	Siderite	1
E	40	81	241	Closed	No fill	< 1
E	41	44	339	Closed	Siderite	1
E	42	69	160	Closed	No fill	-
D'	43	71	281	Closed	Siderite	3-5
D'	44	25	000	Closed	Siderite	< 1
D'	45	44	140	Closed	No fill	-
D'	46	50	108	Closed	Siderite	2
D	47	44	289	Closed	Siderite	1

D	48	51	128	Closed	Siderite	< 1
D	49	39	348	Closed	Siderite	1-10
D	50	81	267	Closed	No fill	-
D	51	23	141	Closed	Siderite	2
D	52	64	250	Closed	Siderite	< 1
D	53	43	140	Closed	Siderite	1-2
C	54	30	190	Closed	Siderite	1
C	55	39	322	Closed	Siderite	< 1
C	56	54	138	Closed	Siderite	1
C	57	30	122	Closed	Siderite	< 1
C	58	77	186	Closed	No fill	-
C	59	22	002	Closed	Siderite	< 1
B'	60	79	255	Closed	No fill	-
B'	61	80	262	Closed	No fill	-
B'	62	03	211	Closed	Siderite	< 1
B'	63	38	349	Closed	Siderite	< 1
B'	64	49	330	Closed	Siderite	1-2
B'	65	38	331	Closed	Siderite	1-3
B'	66	18	029	Closed	Siderite	< 1
B	67	30	352	Closed	Siderite	5-20
B	68	58	154	Closed	Siderite	1-2
B	69	51	162	Closed	Siderite	< 1
B	70	30	319	Closed	Siderite	< 1
B	71	22	242	Closed	No fill	-
B	72	46	129	Closed	No fill	-
A'	73	80	268	Closed	Siderite	< 1
A'	74	76	268	Closed	Siderite	< 1
A'	75	30	007	Closed	Siderite	< 1
A'	76	65	309	Closed	No fill	< 1
A'	77	18	031	Closed	Siderite	< 1
A	78	79	269	Closed	No fill	-
A	79	83	295	Closed	Siderite	< 1
A	80	20	325	Closed	Siderite	< 1
A	81	19	345	Closed	Siderite	< 1
A	82	78	129	Closed	No fill	-

Section 2 fracture data Mapped by David Tassone

Map grid	Fracture	Dip	Dip Direction	Open/Closed	Fill	Aperture (mm)
A'	1	70	90	Open/Closed	-	<1
A'	2	80	90	Open/Closed	-	<1
A'	3	48	270	Closed	Siderite	<1
A'	4	76	90	Closed	No fill	-
A'	5	71	90	Open/Closed	-	1.5
A'	6	63	270	Closed	No fill	<1
A'	7	66	294	Closed	Siderite	< 3
A'	8	48	270	Closed	Calcite, siderite	< 2
A'	9	44	270	Closed	Siderite	1.5
A'	10	82	90	Closed	No fill	<1
A	11	80	90	Closed	No fill	<1
A	12	44	90	Open/Closed	-	1
A	13	60	270	Closed	Siderite	1
A	14	57	270	Closed	Siderite	<1
A	15	52	270	Closed	Siderite	1
A	16	52	270	Closed	Siderite	1
A	17	40	270	Open	-	2
A	18	72	90	Closed	No fill	<1
B	19	48	90	Closed	No fill	<1
B	20	52	270	Closed	Siderite	<1
B	21	54	270	Closed	Siderite	<1
B	22	62	270	Closed	Siderite	<1
B	23	40	90	Closed	No fill	<1
B'	24	50	294	Closed	Siderite	1
B'	25	48	270	Closed	Siderite	1
B'	26	40	270	Open/Closed	-	< 5
C'	27	40	270	Open/Closed	-	< 5
C'	28	58	270	Open/Closed	-	<1
C'	29	40	270	Closed	Siderite	1
C'	30	43	270	Closed	Siderite	1
C'	31	38	270	Closed	Siderite	1
C'	32	54	270	Closed	No fill	<1
C'	33	88	40	-	-	-
C	34	40	270	Closed	Siderite	1
C	35	48	270	Closed	Siderite	1
C	36	36	270	Closed	Siderite	1
C	37	50	270	Closed	Siderite	1
C	38	55	270	Closed	Siderite	1
C	39	52	270	Open/Closed	1.5	
C	40	68	90	Closed	Siderite	<1
C	41	66	90	Closed	Siderite	<1
C	42	38	90	Closed	Siderite	1
D	43	35	270	Closed	Siderite	<1
D	44	36	270	Closed	Siderite	1

D	45	76	320	Closed	Siderite	1
D	46	49	270	Closed	No fill	<1
D	47	40	270	Closed	No fill	<1
D	48	37	270	Closed	No fill	<1
D	49	64	90	Closed	Siderite	2-3
D	50	71	90	Closed	Siderite	2-3
D	51	69	310	Closed	No fill	<1
D'	52	50	270	Closed	No fill	<1
D'	53	61	270	Closed	No fill	<1
D'	54	62	312	Closed	Siderite	3
D'	55	54	90	-	-	-
D'	56	62	270	Closed	Siderite	<1
D'	57	52	270	Closed	Siderite	<1
E'	58	52	270	Closed	Siderite	2
E'	59	42	270	Closed	Siderite	<1
E'	60	70	270	Closed	No fill	<1
E'	61	82	270	Closed	No fill	<1
E'	62	79	270	Closed	No fill	<1
E'	63	70	270	Closed	No fill	<1
E'	64	69	270	Closed	No fill	<1
E'	65	50	270	Closed	Siderite	1-2
E'	66	52	270	Closed	Siderite	2
E'	67	52	295	Closed	Siderite	2
E'	68	40	270	Closed	Siderite	<1
E'	69	36	270	Closed	Siderite	<1
E'	70	45	270	Closed	Siderite	<1
E'	71	76	270	Closed	No fill	<1
E'	72	68	90	-	-	-
E'	73	85	90	Closed	No fill	<1
E'	74	78	270	Closed	No fill	<1
E'	75	78	270	Closed	No fill	<1
E'	76	78	270	Closed	No fill	<1
E'	77	64	270	Closed	Siderite	1
E'	78	64	270	Closed	Siderite	1
E'	79	80	90	Closed	No fill	<1
E'	80	72	90	Closed	No fill	<1
E'	81	79	270	Closed	No fill	<1
E'	82	72	270	Closed	Siderite	<1
F	83	62	270	Closed	Siderite	<1
F	84	80	90	Open	-	<1
F	85	80	90	Open	-	<1
F	86	84	270	Closed	No fill	<1
F	87	63	90	Open/Closed	-	1
F	88	50	270	Closed	Siderite	<1
F	89	50	270	Closed	Siderite	<1
F	90	50	270	Closed	Siderite	1

F	91	64	318	Closed	Siderite	1
F	92	78	90	Closed	No fill	<1
F'	93	34	90	Closed	Siderite	<1
F'	94	48	90	Closed	No fill	<1
F'	95	88	90	Closed	No fill	<1
F'	96	43	270	Closed	Siderite	2
F'	97	41	270	Closed	Siderite	2
F'	98	82	90	Closed	No fill	<1
F'	99	84	90	Closed	No fill	<1
F'	100	72	90	Closed	No fill	<1
G'	101	71	90	Closed	No fill	<1
G'	102	67	90	Closed	No fill	<1
G'	103	71	308	Closed	Siderite	4
G'	104	32	270	Closed	No fill	<1
G'	105	66	301	Closed	Siderite	5
G'	106	64	308	Closed	Siderite	5
G'	107	35	270	Closed	Siderite	1
G'	108	44	270	Closed	Siderite	1
G	109	60	202	Closed	Siderite	1
G	110	60	202	Closed	Siderite	1
G	111	60	202	Closed	No fill	<1
G	112	68	90	Closed	No fill	<1
H	113	72	90	Closed	No fill	<1
H	114	68	90	Closed	Siderite	< 2
H	115	70	270	Closed	No fill	<1
H	116	70	270	Closed	No fill	<1
H	117	67	206	Closed	Siderite	< 2
H	118	57	2	Closed	Siderite	< 2
H	119	75	318	Closed	Siderite	< 2
H'	120	60	90	Closed	Siderite	1
H'	121	62	312	-	-	-
H'	122	82	270	Closed	No fill	<1
H'	123	88	90	Closed	No fill	<1
H'	124	84	90	Closed	Siderite	1
H'	125	68	90	Closed	Siderite	1.5
H'	126	74	90	Closed	No fill	-
H'	127	61	270	Closed	Siderite	2-3
H'	128	25	270	Closed	Siderite	1
H'	129	70	270	Closed	No fill	-
H'	130	72	270	Closed	No fill	-

Section 3 fracture data Mapped by David Tassone

Map grid	Fracture	Dip	Dip Direction	Open/Closed	Fill	Aperture (mm)
A'	1	78	270	Closed	Siderite	2
A'	2	70	90	Closed	No fill	< 1
A'	3	84	90	Closed	No fill	1.5
A'	4	60	270	Open	-	< 1
A'	5	66	270	Open	-	1
A	6	62	270	Open	-	1
A	7	40	53	Closed	No fill	1
A	8	82	258	Open	-	1
B	9	62	-	Open	-	< 1
B	10	48	58	Open/Closed		1
B	11	38	-	Closed	No fill	< 1
B	12	78	270	Closed	No fill	< 1
B	13	84	90	Open	-	< 1
B	14	44	40	Open	-	1
B	15	82	264	Open	-	1.5
B	16	70	90	Closed	No fill	< 1
B	17	69	252	Open	-	3
B	18	52	90	Closed	No fill	< 1
B'	19	32	90	Closed	No fill	< 1
B'	20	86	90	Closed	No fill	1.5
B'	21	84	90	Closed	Siderite	1
B'	22	88	90	Closed	Siderite	< 1
B'	23	77	270	-	-	2
C'	24	64	270	Closed	Siderite	1
C'	25	66	270	Closed	Siderite	1
C'	26	83	90	Open	-	1
C'	27	70	270	Open	-	2
C'	28	61	90	Closed	No fill	< 1
C	29	37	90	Closed	Siderite	< 1
C	30	30	90	Closed	Siderite	< 1
C	31	40	90	Closed	Siderite	1
C	32	77	270	Open	-	1
C	33	37	-	Closed	Siderite	< 1
C	34	84	270	Open	-	< 1
C	35	56	90	Open	-	1
D	36	79	270	Open	-	1
D	37	81	270	Open	-	1
D	38	36	90	Closed	Siderite	1
D	39	70	270	Closed	No fill	< 1
D	40	72	90	Open	-	1.5
D'	41	84	270	Open	-	< 1
D'	42	82	90	Open	-	< 1
D'	43	59	90	Open	-	< 1
D'	44	68	270	Open	-	< 1

D'	45	58	90	Closed	Siderite	< 1
D'	46	40	270	Open	-	< 1
D'	47	47	90	Closed	Siderite	1
D'	48	36	90	Closed	Siderite	< 1
D'	49	24	90	Closed	Siderite	< 1
D'	50	40	90	Closed	Siderite	< 1
D'	51	42	90	Closed	Siderite	< 1
D'	52	42	90	Closed	Siderite	< 1
D'	53	44	90	Closed	Siderite	< 1
D'	54	68	270	Open	-	< 1
D'	55	68	270	Open	-	< 1
E	56	70	74	Open	-	3
E'	57	54	270	Open	-	< 1
E'	58	82	270	Closed	No fill	< 1
E'	59	84	270	Closed	-	< 1
E'	60	62	270	Closed	No fill	< 1
F	61	42	92	Open	-	2
F	62	42	92	Closed	No fill	< 1
F	63	42	92	Open	-	1
F	64	54	90	Closed	Siderite	1
F	65	82	90	Open	-	< 1
F	66	40	90	Closed	Siderite	< 1
F'	67	50	90	Closed	Siderite	< 1
F'	68	52	90	Closed	Siderite	< 1
F'	69	64	90	Closed	Siderite	1
F'	70	31	270	Open	-	2
F'	71	26	270	Closed	Siderite	1
F'	72	62	90	Open	-	1
F'	73	22	90	Closed	Siderite	1
G	74	74	34	Closed	Siderite	1
G	75	74	34	Closed	Siderite	1
G	76	50	90	Closed	Siderite	< 1
G	77	50	90	Closed	Siderite	< 1
G	78	79	90	Closed	Siderite	< 1
G	79	66	90	Closed	Siderite	< 1
G	80	56	90	Closed	Siderite	1
G	81	40	90	Closed	Siderite	< 1
G	82	79	21	Closed	Siderite	< 1
G	83	81	270	Closed	No fill	< 1
G	84	83	270	Closed	No fill	< 1
G	85	72	-	Closed	Siderite	1
G	86	30	270	Closed	Siderite	< 1
G	87	34	90	Closed	Siderite	< 1
G	88	30	270	Closed	No fill	< 1
G'	89	80	90	Closed	Siderite	< 1
G'	90	69	296	Closed	Siderite	< 1

G'	91	69	325	Open	-	< 50-100
G'	92	-	-	Closed	Siderite	1
G'	93	-	-	Closed	Siderite	1
G'	94	-	-	Closed	Calcite, siderite	2
G'	95	-	-	Closed	Calcite	1
G'	96	-	-	Closed	Calcite	3
G'	97	-	-	Closed	Calcite, siderite	1
G'	98	-	-	Closed	Siderite	< 1
H'	99	82	181	Closed	Calcite, siderite	1
H'	100			Closed	Calcite, siderite	1
H'	101	52	166	Closed	Siderite	1
H'	102	-	-	Closed	Siderite	1
H'	103	-	-	Closed	No fill	< 1
H'	104	-	-	Open	-	2
H'	105	32	90	Closed	Siderite	< 1
H'	106	80	90	Closed	Siderite	1
H'	107	25	270	Closed	Siderite	1
H'	108	22	270	Closed	Siderite	1
H'	109	18	270	Closed	No fill	< 1
H'	110	31	270	Closed	No fill	< 1
H'	111	42	270	Closed	No fill	< 1
H'	112	81	90	Closed	Siderite	1
H'	113	68	90	Open	-	< 1
H	114	78	348	Closed	Siderite	1-2
H	115	70	9	Open/Closed	-	3-4
H	116	49	90	Closed	Siderite	< 1
H	117	49	90	Closed	Siderite	< 1
H	118	49	90	Closed	Siderite	< 1
H	119	49	90	Closed	Siderite	< 1
H	120	82	270	Closed	Siderite	1
H	121	72	90	Closed	No fill	< 1
H	122	60	90	Open/Closed		1
I	123	72	90	Closed	No fill	< 1
I	124	74	90	Open	-	< 1
I	125	60		Closed	Siderite	1
I'	126	62	270	Open	-	1
J'	127	74	270	Closed	No fill	1.5
J'	128	64	270	Closed	Siderite	< 1
J'	129	62	35	Closed	Siderite	1
J	130	68	46	Closed	Quartz, siderite	1
J	131	80	274	Open/Closed	-	-
J	132	80	84	Closed	Siderite	< 1
K	133	80	84	Closed	Siderite	< 1
K	134	80	84	Closed	Siderite	< 1
K	135	80	84	Closed	Siderite	< 1
K	136	80	84	Closed	Siderite	< 1

K	137	84	80	Open	-	1-3
K	138	60	270	Closed	Siderite	< 1
K'	139	71	90	Closed	No fill	2
K'	140	64	35	Closed	Siderite	1
K'	141	84	80	Open	-	1-3
K'	142	80	312	Open	-	1
K'	143	64	90	Closed	Quartz, siderite	1-3
K'	144	40	90	Closed	Siderite	< 1
L'	145	80	25	Closed	Siderite	1.5
L	146	80	80	Open/Closed	-	3
L	147	80	90	Closed	Siderite	1

Section 4 fracture data Mapped by Natalie Debenham

Map grid	Fracture	Dip	Dip Direction	Open/Closed	Fill	Aperture (mm)
A	1	38	312	Closed	Siderite	4
A	2	81	304	Closed	Calcite	4
A	3	66	210	Closed	Siderite	1
A	4	84	208	Closed	Calcite	1
A	5	67	293	Closed	Calcite	1-2
A'	6	83	345	Closed	Calcite	1
A'	7	70	312	Closed	Calcite	1-3
A'	8	80	304	Closed	Calcite	1-10
A'	9	48	348	Closed	Calcite	1-2
A'	10	56	248	Closed	Calcite	1-2
A'	11	84	057	Closed	Siderite	1
A'	12	63	020	Closed	Calcite	1-8
A'	13	76	100	Closed	Calcite	1
A'	14	80	103	Closed	Calcite	1
A'	15	84	118	Closed	Calcite, siderite	1-5
A'	16	83	110	Closed	Calcite	2
A'	17	86	116	Closed	Calcite	1
A'	18	46	012	Closed	Calcite	< 8
A'	19	58	022	Closed	Calcite	< 3
A'	20	84	130	Closed	Siderite	1
A'	21	79	114	Closed	Calcite, siderite	1-10
B	22	53	030	Closed	Siderite	< 1
B	23	49	330	Closed	Calcite	< 5
B	24	38	296	Closed	Calcite	1-10
B	25	65	269	Closed	Calcite, siderite	1-2
B	26	75	288	Closed	Calcite	< 8
B	27	58	338	Closed	Calcite	1-3
B	28	44	290	Closed	Calcite	< 1
B'	29	46	351	Closed	Siderite?	1
B'	30	59	348	Closed	Calcite	1-5
B	31	57	245	Closed	Calcite, siderite	1
B'	32	72	351	Closed	Siderite	1
B'	33	70	295	Closed	Calcite	1
B'	34	82	116	Closed	Siderite	1
B'	35	65	300	Closed	Calcite	< 1
B'	36	57	350	Closed	Calcite	2-3
B'	37	59	070	Closed	Siderite	1-2
B'	38	77	130	Closed	Calcite	2-3
B'	39	80	117	Closed	Calcite	1-2
B'	40	73	121	Closed	Siderite	1-2
B'	41	50	025	Closed	Calcite	1
B'	42	71	330	Closed	Siderite	1
B'	43	70	116	Closed	Calcite	1-2

B'	44	77	282	Closed	Calcite	1-2
B'	45	73	313	Closed	Calcite	2-3
B'	46	73	323	Closed	Calcite	5-8
B'	47	64	323	Closed	Siderite	1
C	48	81	209	Closed	Siderite	1
C	49	48	313	Closed	Calcite	2
C	50	59	307	Closed	Calcite	< 10
C	51	48	317	Closed	Calcite	1
C	52	44	337	Closed	Calcite	< 1
C	53	60	317	Closed	Calcite	1
C	54	67	354	Closed	Calcite	1
C	55	88	142	Closed	Calcite	< 1
C'	56	80	101	Closed	Siderite	1
D	57	82	231	Closed	Siderite	< 1
D	58	72	127	Closed	Calcite	2-20
D	59	65	136	Closed	Siderite	1-2
D	60	64	098	Closed	Calcite	1-2
D	61	48	088	Closed	Calcite	1
D	62	55	094	Closed	Siderite	2
D	63	14	104	Closed	Siderite	1
D	64	69	080	Closed	Calcite	2
D'	65	50	120	Closed	Calcite	1-3
D'	66	61	000	Closed	Siderite	1-2
D'	67	70	351	Closed	Siderite	1-2
C'	68	82	243	Closed	Siderite?	1-2
E	69	67	069	Closed	Siderite	1-2
E	70	63	058	Closed	Siderite	2-5
E	71	37	127	Closed	Siderite	< 1
E	72	79	172	Closed	Siderite	1
E	73	22	063	Closed	Siderite	2-3
E	74	80	071	Closed	Siderite	1-2
E	75	73	052	Closed	Siderite	1
E	76	74	137	Closed	Siderite?	2-5
E	77	74	148	Closed	Siderite	1
E'	78	76	110	Closed	Siderite	1
E'	79	79	136	Closed	Siderite	< 1
E'	80	58	067	Closed	Siderite	1
E'	81	77	173	Closed	Siderite	1
E'	82	56	120	Closed	Calcite?	1
E'	83	67	197	Closed	Siderite	1-2
E'	84	76	122	Closed	Siderite	1-2
E'	85	71	122	Closed	Siderite	1
F	86	44	091	Closed	Siderite	1-2
F'	87	83	103	Closed	Siderite	1-2
F'	88	52	124	Closed	Siderite	1
F'	89	81	094	Closed	Siderite?	1-3

F'	90	50	144	Closed	Siderite	1
F'	91	71	107	Closed	Siderite	1-2
F'	92	84	133	Closed	Unsure	5-100
G	93	64	101	Closed	Siderite	1-2
G	94	76	093	Closed	Siderite	1
G	95	86	103	Closed	Unsure	2-5
G	96	52	120	Closed	Siderite	1
G	97	29	178	Closed	Siderite	1-2
G	98	40	065	Closed	Siderite	1-2
G	99	65	125	Closed	Siderite	1
G	100	79	101	Closed	Siderite	1-2
G	101	84	202	Closed	Siderite	1-2
G	102	85	200	Closed	Unsure	1-5
G	103	67	182	Closed	Siderite	1
G	104	11	115	Closed	Siderite?	1
G'	105	45	065	Closed	Siderite	1
G'	106	68	073	Closed	Siderite	1-2?
G'	107	53	116	Closed	Siderite	1-2
G'	108	66	098	Closed	Siderite?	1
G'	109	33	095	Closed	Siderite	1
G'	110	54	333	Closed	Siderite	< 1
G'	111	77	098	Closed	Unsure	2-25
G'	112	36	352	Closed	Siderite	1
G'	113	89	038	Closed	Siderite	1
H	114	73	137	Closed	Siderite	2
H	115	70	039	Closed	Siderite	1
H	116	29	305	Closed	Siderite	1-2
H	117	79	118	Closed	Siderite	1
H	118	29	174	Closed	Siderite	1
H'	119	87	349	Closed	Siderite	< 1
H'	120	88	233	Closed	Siderite	1
H'	121	86	057	Closed	Calcite	1

Section 5 fracture data (GPS Location: 0710595 E, 5704594 N) Mapped by Natalie Debenham

Map grid	Fracture	Dip	Dip Direction	Open/Closed	Fill	Aperture (mm)
H'	1	29	220	Closed	Siderite	1
G'	2	88	140	Closed	No fill	< 1
G'	3	30	220	Closed	No fill	< 1
G'	4	68	190	Closed	No fill	< 1
G	5	79	192	Closed	No fill	< 1
G	6	88	178	Closed	No fill	< 1
F'	7	40	169	Closed	No fill	< 1
F'	8	44	202	Closed	No fill	< 1
F'	9	86	151	Closed	No fill	< 1
F	10	19	259	Closed	No fill	< 1
F	11	89	190	Closed	No fill	< 1
F	12	88	198	Closed	No fill	< 1
F	13	19	277	Closed	No fill	< 1
E'	14	62	018	Closed	No fill	< 1
E'	15	59	305	Closed	No fill	< 1
E'	16	88	194	Closed	Siderite	1-5
E'	17	38	169	Closed	No fill	< 1
E'	18	49	185	Closed	Siderite	< 1
E'	19	88	175	Closed	No fill	< 1
E'	20	61	022	Closed	No fill	< 1
E	21	14	128	Closed	No fill	< 1
E	22	80	055	Closed	No fill	< 1
E	23	36	001	Closed	No fill	< 1
E	24	88	195	Closed	Siderite	< 1
E	25	40	185	Closed	No fill	< 1
E	26	26	022	Closed	Siderite	< 1
D'	27	60	342	Closed	No fill	< 1
D'	28	61	341	Closed	No fill	< 1
D'	29	32	181	Closed	No fill	< 1
D'	30	48	185	Closed	Siderite	1-2
D	31	86	195	Closed	Siderite	< 1
D	32	88	202	Closed	Siderite	< 1
D	33	53	245	Closed	Siderite	1-3
D	34	38	005	Closed	Siderite	< 1
D	35	18	125	Closed	No fill	< 1
D	36	53	245	Closed	Siderite	1
D	37	61	228	Closed	Siderite	1
D	38	59	320	Closed	No fill	< 1
D	39	65	241	Closed	Siderite	< 1
D	40	16	128	Closed	No fill	< 1
D	41	16	143	Closed	No fill	< 1
D	42	42	048	Closed	Siderite	< 1
D	43	42	008	Closed	Siderite	< 1
D	44	68	220	Closed	No fill	< 1
D	45	58	318	Closed	Siderite	< 1
D	46	54	226	Closed	Siderite	< 1
D	47	46	220	Open/Closed	Siderite	< 1

D	48	48	000	Closed	No fill	< 1
D	49	58	195	Closed	Siderite	1-2
D	50	57	190	Closed	Siderite	1
D	51	36	045	Closed	No fill	< 1
D	52	88	009	Closed	No fill	< 1
D	53	38	248	Closed	Siderite	< 1
D	54	50	260	Closed	Siderite	< 1
D	55	78	019	Closed	No fill	< 1
D	56	62	222	Closed	Siderite	0-5
D	57	53	198	Closed	Siderite	< 1
D	58	57	192	Open	No fill	< 1
D	59	50	180	Closed	Siderite	< 1
D	60	79	003	Open	No fill	1
D	61	59	051	Closed	No fill	< 1
D	62	78	020	Closed	No fill	< 1

APPENDIX 2

Chapter 3 data

Core plug data: core plug measurements, porosity, and permeability

Sample	Distance to fault (m)	Average length (cm)	Average width (cm)	Weight (g)	Porosity (%)	Klinkenberg Permeability (mD)
10BX1	-20	7.85	2.57	89.8	17.99	0.41
10BX2	-20	7.64	2.58	87.0	19.04	0.58
10BX3	-20	7.84	2.58	91.2	17.64	0.39
10AY1	-20	5.26	2.56	65.5	10.41	0.01
10AY2	-20	5.98	2.58	74.8	11.27	0.04
10AY3	-20	5.27	2.57	62.7	12.91	0.18
10AZ1	-20	7.55	2.58	87.8	17.80	0.07
10AZ2	-20	7.48	2.56	90.9	11.76	0.02
10AZ3	-20	5.28	2.56	59.8	18.33	0.13
9AX1	0.5	6.89	2.55	70.6	24.30	0.68
9AX2	0.5	6.24	2.54	64.3	22.94	0.57
9AX3	0.5	2.98	2.54	30.0	27.04	1.09
9AY1	0.5	2.86	2.53	28.6	24.64	1.83
9AY2	0.5	2.66	2.55	26.1	27.19	2.92
9AY3	0.5	2.81	2.54	28.5	24.51	1.20
9AZ1	0.5	7.84	2.55	79.6	25.30	0.95
9AZ2	0.5	7.73	2.54	78.2	24.81	1.04
9AZ3	0.5	7.61	2.53	77.0	24.24	1.03
8AX1	2	4.67	2.54	48.4	23.16	0.40
8AX2	2	2.91	2.53	30.1	23.18	0.49
8AX3	2	2.49	2.54	25.8	22.87	-
8AX4	2	3.87	2.54	40.7	22.38	0.28
8AY1	2	6.19	2.55	65.1	21.58	0.38
8AY2	2	6.13	2.54	64.0	21.48	0.53
8AZ1	2	6.12	2.54	63.5	22.70	0.59
8AZ2	2	1.88	2.53	19.2	22.77	-
8AZ3	2	4.94	2.55	51.8	22.79	0.36
7.5AX1	13	8.07	2.56	86.4	23.57	0.53
7.5AX2	13	2.84	2.55	30.2	21.52	0.54
7.5AX3	13	2.78	2.56	29.6	21.80	0.58
7.5AY1	13	7.64	2.56	81.6	22.65	0.27
7.5AY2	13	6.80	2.56	73.1	22.72	0.32
7.5AY3	13	6.14	2.56	65.7	21.92	0.26
7.5AZ1	13	8.12	2.57	86.5	23.02	0.30
7.5AZ2	13	7.76	2.55	83.4	20.96	0.27
7AX1	37	4.69	2.52	49.2	21.63	0.07
7AY1	37	6.12	2.53	64.7	20.51	0.02
7AY2	37	4.67	2.53	49.3	21.26	0.33
7AZ1	37	4.41	2.52	46.8	20.56	0.28
7AZ2	37	4.42	2.53	47.0	20.72	0.21
6CX1	104	7.45	2.56	81.3	20.43	0.26
6CX2	104	7.44	2.56	81.0	20.38	0.09
6CX3	104	7.31	2.56	79.7	20.37	0.10
6CY1	104	7.86	2.56	85.7	20.65	0.32
6CY2	104	7.78	2.56	84.9	20.62	0.16
6CY3	104	7.51	2.56	82.1	20.71	0.13

6CZ1	104	7.32	2.56	80.1	21.07	0.03
6CZ2	104	6.65	2.55	72.9	20.04	0.03
6CZ3	104	6.57	2.56	72.1	20.53	0.11
5AX1	64	6.00	2.52	61.0	23.15	0.72
5AX2	64	6.05	2.55	62.7	22.95	0.63
5AY1	64	6.19	2.54	63.1	23.82	0.78
5AY2	64	5.08	2.53	51.3	23.95	0.78
5AZ1	64	6.08	2.53	61.7	23.84	0.93
5AZ2	64	6.14	2.54	62.8	23.52	0.68
4BX1	75	5.31	2.56	55.1	24.19	0.35
4BX2	75	5.23	2.55	54.6	23.98	0.27
4BX3	75	5.18	2.56	54.0	24.12	0.34
4BY1	75	6.55	2.55	68.7	23.15	0.27
4BY2	75	6.50	2.55	68.4	23.37	0.27
4BY3	75	6.46	2.55	67.6	23.52	0.31
4BZ1	75	6.50	2.56	67.8	23.81	0.36
4BZ2	75	6.03	2.56	63.3	26.00	0.34
4BZ3	75	5.99	2.55	62.4	23.80	0.36
3BX1	136	6.59	2.56	74.8	17.52	0.06
3BX2	136	6.01	2.55	67.9	17.79	0.02
3BY1	136	6.50	2.57	73.2	18.94	0.03
3BY2	136	6.05	2.57	68.3	19.16	0.04
3BZ1	136	7.83	2.56	88.8	18.30	0.09
3BZ2	136	7.73	2.55	87.8	17.36	0.09
2CX1	161	6.61	2.56	75.5	16.04	0.02
2CX2	161	6.50	2.55	74.5	15.75	0.03
2CX3	161	5.98	2.56	68.2	16.72	0.04
2CY1	161	7.52	2.55	85.5	16.89	0.03
2CY2	161	7.52	2.55	85.6	16.73	0.06
2CY3	161	6.56	2.56	75.1	16.12	0.09
2CZ1	161	7.35	2.55	84.1	16.03	0.05
2CZ2	161	6.57	2.56	75.3	16.04	0.03
2CZ3	161	6.02	2.55	68.7	16.06	0.04
1AX1	225	4.52	2.55	51.5	17.30	0.03
1AX2	225	3.81	2.55	43.2	17.79	0.08
1AX3	225	2.86	2.54	31.8	18.72	0.14
1AY1	225	6.23	2.55	70.6	16.73	0.02
1AY2	225	5.96	2.55	67.7	16.33	0.01
1AY3	225	4.66	2.55	53.1	17.41	0.01
1AZ1	225	6.17	2.56	70.4	16.35	0.04
1AZ2	225	2.93	2.54	33.0	17.54	0.01

Core plug data: volumes (%) of different grain sizes. N.B. No grains are >1000 µm.

Sample	**Distance to fault (m)**	**Clay** <3.9 µm	**Silt** 3.9-62.5 µm	**Very fine sand** 62.5-125 µm	**Fine sand** 125-250 µm	**Medium sand** 250-500 µm	**Coarse sand** 500-1000 µm
1AY2	225	10.05	14.79	13.04	51.42	10.26	0.44
2CY	161	5.50	19.33	24.90	43.98	5.86	0.43
3BY	136	5.45	13.81	15.22	41.11	20.19	4.21
6CY	104	10.87	19.69	14.02	37.73	16.65	1.04
4BY	75	10.51	20.62	13.45	36.64	17.85	0.93
5AY	64	13.17	24.20	14.99	35.60	10.85	1.19
7AY2	37	12.94	23.06	22.14	40.79	1.08	0.00
7.5AY	13	10.46	19.85	23.23	43.70	2.76	0.00
8AY2	2	14.60	27.61	24.80	29.91	2.77	0.31
9AY	0.5	12.41	20.49	12.29	39.07	15.10	0.64

Core plug data: mercury intrusion porosimetry

Sample	**Distance to fault (m)**	**Porosity (%)**	**Pore throat size (µm)** at first major peak	**Pore throat size (µm)** at second major peak	**Mercury threshold injection pressure (psi)**
1AY1	225	16.99	0.12	0.68	216.23
2CY	161	16.09	0.12	0.54	266.34
6CY	104	18.61	0.12	1.04	216.38
5AY1	64	23.72	0.19	1.65	111.16
7.5AY	13	19.70	0.15	1.30	136.70
9AY	0.5	23.63	0.12	2.55	56.17

APPENDIX 3

Chapter 4 data

Sample data: concretions, veins, and sandstone

Sample	Location	W-E distance (km)	Mineralogy	Comments
8642-113A (repeat 1b)	Pebble Point	0	Calcite concretion	Core, carbonate only
LFWB02 (1)	Wreck Beach	5.00	Siderite vein	Cross-cutting siderite, cataclastic deformation, tensile fracture behaviour
LFWB02 (2)	Wreck Beach	5.00	Siderite vein	Cross-cutting siderite, cataclastic deformation, tensile fracture behaviour
LFWB04	Wreck Beach	5.00	Siderite vein	Cross-cutting siderite, cataclastic deformation, tensile fracture behaviour
RD14-378 (Loc 204)	Moonlight Head	5.72	Sandstone (whole rock)	Eumeralla Formation
RD14-378 (Hbl)	Moonlight Head	5.72	Hornblende	Mineral separate from Eumeralla Formation
RD14-378 (Zeo)	Moonlight Head	5.72	Zeolite (heulandite group)	Mineral separate from Eumeralla Formation
LFMH01	Moonlight Head	5.72	Calcite with siderite halo	Crack-seal with calcite precipitation, cross-cutting siderite, tensile fracture behaviour
LFMH04	Moonlight Head	5.72	Calcite vein	Crack-seal with calcite precipitation, tensile fracture behaviour
JS-01	Moonlight Head	5.72	Calcite vein	Multiple (3?) stages of crystallisation
R25366a	Moonlight Head	5.72	Calcite concretion	Carbonate only
R25366b	Moonlight Head	5.72	Calcite concretion (whole rock)	Whole rock only, no carbonate
R25367a	Moonlight Head	5.72	Siderite concretion	Carbonate only
R25367b	Moonlight Head	5.72	Siderite concretion (whole rock)	Whole rock only, no carbonate
RD14-365	Castle Cove	23.89	Sandstone (whole rock)	Eumeralla Formation
NDCC(Ca)01	Castle Cove	23.89	Calcite vein	-
LFCC02	Castle Cove	23.89	Siderite vein	-
RD14-372 (1) (core)	Castle Cove	23.89	Calcite concretion	Carbonate only
RD14-372 (2) (mid)	Castle Cove	23.89	Calcite concretion	Carbonate only
RD14-372 (3) (rim)	Castle Cove	23.89	Calcite concretion (whole rock)	Whole rock only, no carbonate
RD14-373 (rim)	Castle Cove	23.89	Calcite concretion	Carbonate only
RD14-373-1	Castle Cove	23.89	Calcite concretion	Carbonate only
RD14-373-2	Castle Cove	23.89	Calcite concretion	Carbonate only
RD14-373-3	Castle Cove	23.89	Calcite concretion	Carbonate only
RD14-373-4	Castle Cove	23.89	Calcite concretion	Carbonate only
RD14-373-5	Castle Cove	23.89	Calcite concretion	Carbonate only
RD14-373-5b	Castle Cove	23.89	Calcite concretion (whole rock)	Whole rock only, no carbonate
RD14-373-6	Castle Cove	23.89	Calcite concretion	Carbonate only
RD14-373-7	Castle Cove	23.89	Calcite concretion	Carbonate only
RD14-373-8	Castle Cove	23.89	Calcite concretion	Carbonate only
RD14-373-9	Castle Cove	23.89	Calcite concretion	Carbonate only
RD14-373-10	Castle Cove	23.89	Calcite concretion	Carbonate only
RD14-373-11	Castle Cove	23.89	Calcite concretion	Near rim, carbonate only
RD14-371 (1)	Castle Cove	23.89	Siderite concretion	Carbonate only
RD14-371 (1b)	Castle Cove	23.89	Siderite concretion (whole rock)	Whole rock only, no carbonate

RD14-371 (2)	Castle Cove	23.89	Siderite concretion	Carbonate only
JS-07	Cape Otway	26.29	Calcite vein	For mineralogy and porosity of fracture cements
HBSB01	Station Beach	28.33	Calcite vein	-
HBSB02	Station Beach	28.33	Calcite vein	-
LFPM01 (Ca)	Parker River Mouth	35.39	Calcite vein	Cross-cutting siderite, no crack-seal, tensile fracture behaviour
LFPM02(Ca)	Parker River Mouth	35.39	Calcite vein	Cross-cutting siderite, no crack-seal, tensile fracture behaviour
LFPM02 (Sid)	Parker River Mouth	35.39	Siderite vein	Cross-cutting siderite, no crack-seal, tensile fracture behaviour
8642-103b	Wild Dog Creek	46.70	Calcite concretion	Core, carbonate only
NDSC03	Skenes Creek	49.02	Calcite vein	-
HBSC01	Skenes Creek	49.02	Calcite vein	-
LFSK04	Skenes Creek	49.02	Siderite vein	-
LFCR01	Cumberland River	69.54	Siderite vein	Calcite cross-cuts siderite with ~100 µm offset, tensile fracture behaviour
LFCR02	Cumberland River	69.54	Calcite stained with siderite	Cataclastic deformation
LFL01	Lorne	72.14	Calcite vein	Crack-seal with calcite precipitation, cross-cutting siderite, tensile fracture behaviour

Stable isotopes and strontium isotopes data: concretions, veins, and sandstone

Sample	$\delta^{18}O_{VPDB}$ average	$\delta^{18}O_{VPDB}$ error	$\delta^{13}C_{VPDB}$ average	$\delta^{13}C_{VPDB}$ error	$\delta^{18}O_{SMOW}$ average	$\delta^{18}O_{SMOW}$ error	Sr average	Sr 2se error
8642-113A (repeat 1b)	-8.53	-	-2.64	-	22.1		-	-
LFWB02 (1)	-6.66	0.30	-16.74	0.18	24.1	0.31	-	-
LFWB02 (2)	-7.34	0.33	-16.79	0.22	23.4	0.35	-	-
LFWB04	-1.00	0.31	-11.20	0.19	29.9	0.32	0.705873	0.000005
RD14-378 (Loc 204)	-	-	-	-	-	-	0.706061	0.000002
RD14-378 (Hbl)	-	-	-	-	-	-	0.704761	0.000002
RD14-378 (Zeo)	-	-	-	-	-	-	0.705987	0.000004
LFMH01	-6.62	0.15	-12.99	0.04	24.1	0.16	-	-
LFMH04	-2.34	0.07	-24.14	0.11	28.5	0.07	-	-
JS-01	-1.91	0.14	-33.84	0.03	29.0	0.14	0.706090	0.000006
R25366a	-15.46	-	-8.60	-	15.0	-	0.708174	0.000004
R25366b	-15.46	-	-8.60	-	15.0	-	0.705733	0.000003
R25367a	-2.98	-	-10.91	-	27.8	-	0.706759	0.000003
R25367b	-2.98	-	-10.91	-	27.8	-	0.705960	0.000003
RD14-365	**-**	**-**	**-**	**-**	**-**	**-**	0.710463	0.000010
NDCC(Ca)01	-21.89	0.14	-0.67	0.05	8.4	0.14	0.704317	0.000005
LFCC02	-	-	-	-	-	-	0.709882	0.000004
RD14-372 (1) (core)	-19.50	0.03	3.99	0.05	10.8	0.03	-	-
RD14-372 (2) (mid)	-19.31	0.08	2.63	0.07	11.0	0.08	0.705874	0.000004
RD14-372 (3) (rim)	-19.52	0.11	2.20	0.02	10.8	0.11	-	-
RD14-373 (rim)	-18.54	0.12	-1.19	0.02	11.8	0.12	-	-
RD14-373-1	-18.85	0.09	2.26	0.03	11.5	0.09	-	-
RD14-373-2	-19.98	0.02	2.51	0.09	10.3	0.02	-	-
RD14-373-3	-19.94	0.06	2.88	0.04	10.4	0.06	-	-
RD14-373-4	-19.86	0.05	2.21	0.06	10.4	0.05	-	-
RD14-373-5	-19.62	0.08	2.62	0.03	10.7	0.08	0.705516	0.000003
RD14-373-5b	-	-	-	-	-	-	0.707373	0.000002
RD14-373-6	-19.71	0.05	2.03	0.07	10.6	0.05	-	-
RD14-373-7	-19.62	0.08	2.62	0.03	10.7	0.08	-	-
RD14-373-8	-20.15	0.05	2.31	0.05	10.1	0.05	-	-
RD14-373-9	-20.01	0.08	3.05	0.06	10.3	0.08	-	-
RD14-373-10	-19.59	0.10	2.55	0.04	10.7	0.10	-	-
RD14-373-11	-19.10	0.05	3.09	0.12	11.2	0.05	-	-
RD14-371 (1)	-1.73	0.21	-11.29	0.09	29.1	0.21	0.708858	0.000003
RD14-371 (1b)	-	-	-	-	-	-	0.707238	0.000003
RD14-371 (2)	-1.47	0.18	-11.22	0.07	29.4	0.18	-	-
JS-07	-24.77	0.06	2.24	0.05	5.4	0.06	0.704787	0.000003
HBSB01	-	-	-	-	-	-	0.707603	0.000003
HBSB02	-2.96	0.43	-14.56	0.15	27.9	0.44	-	-
LFPM01 (Ca)	-3.33	0.32	-9.56	0.23	27.5	0.33	-	-
LFPM02(Ca)	-1.30	0.20	-11.54	0.08	29.6	0.20	0.709327	0.000004
LFPM02 (Sid)	-4.03	0.11	-12.02	0.25	26.8	0.12	-	-

8642-103b	-23.00	-	0.36	-	7.2	-	-	-
NDSC03	-19.17	0.07	-1.59	0.06	11.2	0.07	-	-
HBSC01	-5.00	0.09	-38.82	0.08	25.8	0.09	0.706245	0.000003
LFSK04	-4.54	0.41	-3.74	0.13	26.2	0.42	0.705961	0.000003
LFCR01	-	-	-	-	-	-	0.709194	0.000003
LFCR02	-6.64	0.16	-3.34	0.11	24.1	0.16	0.705173	0.000003
LFL01	-5.32	0.08	-11.88	0.10	25.4	0.08	0.705009	0.000005

Pressure calcimeter and calculated burial depth data: concretions

Sample	Carbonate (%)	Burial depth (m) Calculation A	Burial depth (m) Calculation B
8642-113A (repeat 1b)	54.50	687.7	726.3
R25366a	34.1	1248.8	1257.9
R25367a	41.6	1012.1	1033.7
RD14-372 (1) (core)	37.31	1141.0	1155.8
RD14-372 (2) (mid)	39.12	1084.2	1102.0
RD14-372 (3) (rim)	38.69	1097.3	1114.4
RD14-373 (rim)	18.63	1971.5	1942.6
RD14-373-1	42.48	985.6	1008.6
RD14-373-2	44.42	932.1	957.9
RD14-373-3	44.63	926.5	952.6
RD14-373-4	45.04	915.5	942.2
RD14-373-5	48.08	837.5	868.3
RD14-373-5b	48.72	821.7	853.3
RD14-373-6	46.83	869.0	898.1
RD14-373-7	46.94	866.2	895.5
RD14-373-8	46.61	874.7	903.5
RD14-373-9	44.89	919.7	946.2
RD14-373-10	43.52	956.7	981.2
RD14-373-11	45.65	899.6	927.1
RD14-371 (1)	45.56	901.8	929.2
RD14-371 (1b)	37.31	1141.0	1155.8
RD14-371 (2)	39.12	1084.2	1102.0
8642-103b	25.40	1600.7	1591.3

Calculation A: Burial depth calculated by Natalie Debenham by converting sonic transit time to porosity from Tassone *et al.* 2014, where $y = -1196\ln(x) + 5469.5$ (y = depth (m), x = porosity (%)).

Calculation B: Burial depth calculated by Ian Duddy using measured porosity at different depths from Port Campbell-4 well completion report, assuming 1°C, where $y = -1133\ln(x) + 5256.3$.

APPENDIX 4

Chapter 5 data

Sample data: Veins

Sample	Location	W-E distance (km)	Mineralogy	Comments
BA01	Blue Anchor	0	Gypsum	Gypsum fracture, -10m East
BA02	Blue Anchor	0	Gypsum	Gypsum bedding/bedding-parallel fracture
DBF01	Warren Bay	2.2	Gypsum	Fracture 33 (Map 1)
DBF02 (1)	Warren Bay	2.2	Gypsum	Gypsum bedding with fracture 33 (Map 1)
DBF03 (1)	Warren Bay	2.2	Gypsum	Fracture 2 (Map 1)
DBF03 (2)	Warren Bay	2.2	Gypsum	Fracture 2 (Map 1)
DBF05 (1)	Warren Bay	2.2	Gypsum	Slickensides in fault core
W01	Warren Bay	2.28	Gypsum	Unit 1 (Meng et al. 2017 Fig. 2), fracture plane
W03	Warren Bay	2.46	Gypsum	Unit 2 (Meng et al. 2017 Fig. 2), fracture plane
W05	Warren Bay	2.6	Gypsum	Unit 3 (Meng et al. 2017 Fig. 2), fracture plane
W07	Warren Bay	2.75	Gypsum	Unit 4 (Meng et al. 2017 Fig. 2), fracture plane
QHF01	Quantock's Head	9.28	Calcite	Fracture plane, FW
QHF02	Quantock's Head	9.27	Calcite	Fault, slickensides
QHF03	Quantock's Head	9.26	Calcite	Fracture plane, HW
K01	Kilve	10.77	Calcite	Fracture 4 (with shale) (Map 2)
K02	Kilve	10.77	Calcite	Fracture left of fracture 40 with same orientations as 40 (Map 2)
K03	Kilve	10.77	Calcite	Fracture 31 (Map 2)
K04	Kilve	10.77	Calcite	Slickensides with HW and small folds toward fault core
K06	Kilve	10.75	Calcite	"Hydrofractures" of calcite (away from the fault)
K07 (1)	Kilve	10.58	Calcite	FW = 12/172, HW = 28/358
K07 (2)	Kilve	10.58	Calcite	FW = 12/172, HW = 28/358
K08	Kilve	10.6	Calcite	FW = 63/176, HW = 02/210, fault plane
K09	Kilve	10.62	Calcite	FW = 18/190, HW = 02/186
K10	Kilve	10.63	Calcite	FW = 23/197, HW = 02/241
K11	Kilve	10.65	Calcite	FW = 12/192, HW = 01/221 (horizontal)
K12	Kilve	10.67	Calcite	FW = 10/188, HW = 09/205
K13	Kilve	10.69	Calcite	FW = 08/176, HW = 13/213, fault plane
K15	Kilve	10.73	Calcite	FW = 13/187, HW = 17/197, fault plane
L04	Lilstock	13.93	Calcite	Fracture with orientation of fracture 33 (Map 3)
L08	Lilstock	15.48	Calcite	Sample of calcite near another fault, fracture plane

Stable isotopes and strontium isotopes data: veins

Sample	$\delta^{18}O_{VPDB}$ average	$\delta^{18}O_{VPDB}$ error	$\delta^{13}C_{VPDB}$ average	$\delta^{13}C_{VPDB}$ error	$\delta^{18}O_{SMOW}$ average	$\delta^{18}O_{SMOW}$ error	Sr average	Sr 2se error
BA01	-	-	-	-	-	-	0.709656	0.000004
BA02	-	-	-	-	-	-	0.709794	0.000004
DBF01	-	-	-	-	-	-	0.709182	0.000006
DBF02 (1)	-	-	-	-	-	-	0.709493	0.000005
DBF03 (1)	-	-	-	-	-	-	0.709028	0.000004
DBF03 (2)	-	-	-	-	-	-	0.708992	0.000005
DBF05 (1)	-	-	-	-	-	-	0.709047	0.000006
W01	-	-	-	-	-	-	0.709259	0.000005
W03	-	-	-	-	-	-	0.709248	0.000014
W05	-	-	-	-	-	-	0.709006	0.000003
W07	-	-	-	-	-	-	0.709079	0.000004
QHF01	-9.04	0.17	-0.55	0.13	21.6	0.17	0.708172	0.000003
QHF02	-10.87	0.25	-1.27	0.05	19.7	0.25	0.708229	0.000003
QHF03	-7.48	0.10	-0.13	0.04	23.2	0.11	0.708184	0.000004
K01	-10.37	0.23	-1.04	0.15	20.2	0.24	-	-
K02	-10.05	0.22	-0.68	0.14	20.6	0.22	-	-
K03	-9.93	0.18	-0.77	0.06	20.7	0.18	-	-
K04	-7.74	0.11	-0.26	0.04	22.9	0.12	0.708027	0.000003
K06	-11.38	0.18	-1.15	0.06	19.2	0.18	0.708194	0.000003
K07 (1)	-10.42	0.20	-0.24	0.09	20.2	0.20	0.708192	0.000003
K07 (2)	-10.33	0.13	-0.17	0.07	20.3	0.13	-	-
K08	-10.51	0.46	-0.35	0.04	20.1	0.48	0.708225	0.000004
K09	-10.84	0.09	-1.09	0.04	19.7	0.10	0.708212	0.000003
K10	-10.94	0.11	-0.78	0.07	19.6	0.12	0.708233	0.000003
K11	-10.63	0.12	-0.77	0.04	20.0	0.13	0.708158	0.000004
K12	-10.43	0.12	-0.15	0.09	20.2	0.13	0.708196	0.000004
K13	-10.66	0.09	-0.80	0.05	19.9	0.09	0.708171	0.000003
K15	-11.21	0.14	-0.69	0.07	19.4	0.14	0.708082	0.000003
L04	-3.16	0.12	-6.02	0.13	27.7	0.13	0.709465	0.000004
L08	-11.01	0.10	0.78	0.03	19.6	0.11	-	-